UNIVERSIDAD AUTÓNOMA DE BAJA CALIFORNIA

INSTITUTO DE INGENIERÍA

Maestría y Doctorado en Ciencias e Ingeniería

LA INTELIGENCIA DE LOS PRONÓSTICOS METEOROLÓGICOS COMO HERRAMIENTA EN LA PREDICCIÓN DE ENERGÍA SOLAR EN LA REGIÓN DESÉRTICA DEL NOROESTE DE MÉXICO.

Tesina que para obtener el grado de

Doctor en Ciencias presenta:

José Ernesto López Velázquez

Director de tesis:

Dr. Nicolás Velázquez Limón

Codirector de tesis:

Dr. Saúl Islas Pereda

Mexicali, Baja California, México.

Enero, 2025

INSTITUTO DE INGENIERÍA
Universidad Autónoma de Baja California
EXCELENCIA E INNOVACIÓN EN INGENIERÍA

Agradecimientos

Al doctor Nicolás Velázquez Limón, por su apoyo para realizar mi investigación de posgrado, así como por sumarme a su grupo de trabajo y brindarme toda su ayuda posible. También al doctor Rafael García Cueto, por su asesoría y apoyo aun a distancia. Al doctor Saúl Islas Pereda por materializar gran parte de la infraestructura para el trabajo de campo.

Un agradecimiento especial al Instituto de Ingeniería, al doctor Mario Curiel Álvarez por su apoyo al permitirme trabajar en mis actividades docentes y continuar con el desarrollo de mi formación profesional.

A la doctora Sara Ojeda y los integrantes del laboratorio de Ciencias Atmosféricas Aplicadas, David Flores y Néstor Santillán.

Al MYDCI y al CONACHYT por las facilidades brindadas para realizar esta investigación.

Resumen

El crecimiento y desarrollo de sistemas de energía solar acoplados a las redes eléctricas, han demostrado la importancia de contar con herramientas precisas para predecir su generación. Por lo que la variabilidad de los recursos renovables representa un desafío significativo para garantizar la estabilidad y confiabilidad del suministro de energía. Factores como el Cambio Climático, están estrechamente relacionados al aumento de las temperaturas extremas, las cuales influyen directamente en la variabilidad de la radiación solar. Por ejemplo, un aumento en la temperatura puede provocar una mayor evaporación, lo que a su vez afecta la formación de nubes y, en consecuencia, la cantidad de radiación solar que llega a la superficie terrestre. Estudios previos han demostrado que la variabilidad natural de la energía solar, debe ser dimensionada adecuadamente en escalas espaciales y temporales en función al evento meteorológico o climático que mayor influya durante el periodo de interés. Es decir, resulta necesario implementar predicciones a corto y largo plazo para mejorar la planeación y la operatividad de los sistemas de generación de energía.

Este trabajo explora dos metodologías de predicción atmosférica para las energías renovables: la primera se centra en analizar las alteraciones en las temperaturas extremas a lo largo de los últimos 30 años en distintas ciudades mexicanas con el propósito de revelar un patrón general de calentamiento a largo plazo, analizando las tendencias de temperaturas extremas en 12 ciudades mexicanas bajo un enfoque de clima no estacionario. En donde se encontró que la mayoría de las ciudades mexicanas muestran un calentamiento urbano, especialmente en las temperaturas mínimas, aunque existen variaciones significativas entre las ciudades, como el caso de Guadalajara que presenta una tendencia negativa en las temperaturas máximas. Mediante la distribución Generalizada de Valores Extremos (GEV) y pruebas estadísticas, se modelaron las temperaturas extremas y se estimaron los períodos de retorno para futuros escenarios climáticos. Los resultados indican que las temperaturas mínimas mostraron una tendencia más uniforme, el 90% de las ciudades se mostraron no-estacionarias con tendencia positiva, y solo un 10%, una zona metropolitana del Valle de México, y una ciudad costera del Golfo de México, mostraron una serie estacionaria. El segundo estudio, se enfoca en la predicción numérica computacional de la radiación solar a corto plazo, un recurso fundamental para la generación de energía solar en México. El estudio evalúa la capacidad del modelo meteorológico Weather Research Forecast (WRF) para predecir la irradiación solar global (GHI) en el noroeste de México durante la influencia de eventos frontales de invierno. A partir de diferentes configuraciones de radiación solar de onda corta y onda larga propuestas para la simulación en el modelo, se evaluaron estadísticamente los resultados y se determinó que dos configuraciones de parametrizaciones de radiación, fueron las que mejor desempeño mostraron. Los resultados mostraron una sobreestimación del modelo WRF durante la mayor parte de los periodos analizados; las predicciones más acertadas, obtuvieron valores de correlación entre 0.85 a 0.91 y un Error Medio Absoluto (EMA) entre los 15-45 $W.m^{-2}$.

Los periodos menos favorables de estimación de GHI , indican que se observó hasta un porcentaje máximo de sesgo promedio (Mbias) del 20%. La evaluación de las diferentes configuraciones propuestas, muestra las ventajas que la predicción de la GHI tiene principalmente con las parametrizaciones de radiación Dudiah de SW y Rapid Radiative Transfer Model (RRTM) de LW. Gran parte de los resultados obtenidos sugieren que el modelo WRF, con las configuraciones adecuadas, puede ser una herramienta útil para mejorar la operatividad a corto plazo de sistemas de generación de energía solar en regiones con alta variabilidad meteorológica durante inviernos.

Ambos estudios pintan un panorama complejo y desafiante al relacionar algunos índices de Cambio Climático en México con la predicción de tendencias en extremos de temperatura y su relación a la variabilidad de la irradiación a escalas más pequeñas. Sin embargo, también ofrecen valiosa información para tomar decisiones informadas en la planeación de proyectos futuros en el sector de las energías renovables y el desarrollando de estrategias de operatividad de los sistemas de aprovechamiento conectados a redes para optimizar su desempeño ante la variabilidad diaria ante eventos meteorológicos y mitigar los impactos del cambio climático a largo plazo.

Abstract

The expansion of solar energy systems coupled to electricity grids has demonstrated the importance of having accurate tools to predict their generation. Therefore, the variability of renewable resources represents a significant challenge to ensure the stability and reliability of energy supply. Factors such as climate change are closely related to rising temperature extremes, which directly influence the variability of solar radiation. For example, an increase in temperature can lead to increased evaporation, which in turn affects cloud formation and consequently the amount of solar radiation reaching the earth's surface. Previous studies have shown that the natural variability of solar energy must be adequately dimensioned on spatial and temporal scales according to the most influential meteorological or climatic event during the period of interest. In other words, it is necessary to implement short- and long-term forecasts to improve the planning and operation of power generation systems.

This paper explores two atmospheric forecasting methodologies for renewable energies: the first focuses on analysing changes in extreme temperatures over the last 30 years in different Mexican cities in order to reveal a general long-term warming pattern, analysing extreme temperature trends in 12 Mexican cities under a non-stationary climate approach. It was found that most Mexican cities show urban warming, especially in minimum temperatures, although there are significant variations among cities, such as Guadalajara, which shows a negative trend in maximum temperatures. Using the Generalised Extreme Value (GEV) distribution and statistical tests, extreme temperatures were modelled and return periods for future climate scenarios were estimated. The results indicate that minimum temperatures showed a more uniform trend, 90% of the cities were non-stationary with a positive trend, and only 10%, one metropolitan area in the Valley of Mexico, and one coastal city in the Gulf of Mexico, showed a stationary series. The second study focuses on the computational numerical prediction of short-term solar radiation, a fundamental resource for solar power generation in Mexico. The study evaluates the ability of the Weather Research Forecast (WRF) meteorological model to predict global solar irradiance (GHI) in northwestern Mexico during the influence of winter frontal events. From different configurations of shortwave and longwave solar radiation proposed for simulation in the model, the results were statistically evaluated and it was determined that two configurations of radiation parameterisations showed the best performance. The results showed an overestimation of the WRF model during most of the periods analysed; the most accurate predictions obtained correlation values between 0.85 and 0.91 and a Mean Absolute Error (MAE) between 15-45 W.m-2. The least favourable periods of GHI estimation indicate that up to a maximum mean percentage bias (Mbias) of 20% was observed.

The evaluation of the different proposed configurations shows the advantages that the GHI prediction has mainly with the SW Dudiah and LW Rapid Radiative Transfer Model (RRTM) radiation parameterisations. Much of the results obtained suggest that the WRF model, with the right settings, can be a useful tool for improving the short-term operability of solar power generation systems in regions with high meteorological variability during winters.

Both studies shows a complex and challenging picture by relating some indices of Climate Change in Mexico to the prediction of trends in temperature extremes and their relationship to irradiance variability at smaller scales. However, they also provide valuable information for informed decision-making in planning future projects in the renewable energy sector and developing operational strategies for grid-connected power systems to optimise their performance in the face of daily variability in weather events and mitigate the impacts of climate change in the long term.

Índice

1. Introducción al Proyecto

Con el aumento de la población mundial, también crece la demanda de electricidad; se espera que para el 2050 esta se duplique, y su generación cause efectos negativos en el sistema climático a nivel global, debido al aumento significativo de las emisiones de gases de efecto invernadero (GEI). El uso de combustibles fósiles ha causado un incremento en la concentración de GEI y a su vez el calentamiento del sistema climático. Las implicaciones de estas tendencias térmicas crecientes están impulsando los esfuerzos en la modelación para comprender el futuro del clima de la Tierra. Existen distintas propuestas que buscan la mitigación de concentraciones de GEI en el futuro, y la transición de combustibles fósiles a fuentes de energía renovables continúa siendo clave (Paulescu, 2016). En la actualidad, ha incrementado la colaboración de disciplinas de investigación dentro del área de energías renovables, y se proyecta un gran crecimiento del mercado para los próximo 10 años (DELOITTE, 2019). De acuerdo a la información de la Comisión Nacional Regulatoria de Energía (NERC, por sus siglas en ingles), durante el mes de abril del 2019 en los Estados Unidos, la generación a partir de recursos renovables, superó por primera vez en la historia a la producción media de energía eléctrica a partir de carbón; tan solo en el primer semestre del 2019, la suma de la producción eólica y solar, representó casi el 50% del total de energías renovables. En México, a pesar de que las políticas actuales de desarrollo impuestas por la Secretaría de Energía, han proyectado un crecimiento menor en el campo de las energías renovables en comparación a países del norte, se espera que una tendencia generalizada a cumplir con los compromisos internacionales en la disminución de emisiones, lleve al país a un gradual progreso en la innovación y la expansión de energías limpias. En una situación similar al panorama actual en México, la NERC prevé que, en los Estados Unidos, los clientes de energía eólica, continúen diversificando sus opciones de consumo, añadiendo peso a la generación solar y a los sistemas de almacenamiento de energía para lograr cumplir sus compromisos.

Se espera que las energías renovables, mantengan competitividad ante la producción de energía por combustibles fósiles en un futuro cercano. Para que exista este proceso de transición a las renovables, las futuras instalaciones de sistemas de aprovechamiento, deben contemplar que además de la disponibilidad suficiente del recurso, las condiciones meteorológicas y climáticas deben ser consideradas. Cuando estas condiciones no se conocen, es necesario proponer el desarrollo y la investigación en el campo de las energías renovables, con un enfoque en la mejora de proyectos futuros de generación de energía a partir de renovables, además de la búsqueda de optimizaciones en los ya operantes. Para el desarrollo de nuevos proyectos de generación de energía y redes eléctricas, la industria dedicada a la energía eólica y solar, ha mantenido una orientación hacia la innovación de mejoras en el diseño y eficiencia de las turbinas y sistemas fotovoltaicos, mientras que, en las ya operantes, las opciones se diversifican; la adaptabilidad y la optimización en los procesos de almacenamiento de energía y administración de las redes, resultan las opciones más viables.

Los pronósticos meteorológicos y climáticos, tienen como uno de sus objetivos principales, predecir la variabilidad de la atmósfera en un determinado sitio hacia el futuro (cada uno en diferentes escalas espaciales y temporales). Todos los días se realizan y analizan pronósticos del tiempo atmosférico que se utilizan como una herramienta de apoyo en toma de decisiones en actividades relacionadas a la industria del transporte, navegación, energía, agricultura, protección civil, etc. Esto genera a su vez, la necesidad de distintos tipos de pronósticos especializados que brinden una alta precisión, lo cual se traduce en un mayor interés en la búsqueda de mejoras en su desarrollo computacional y resolución.

Un desafío importante en la generación de pronósticos, es la obtención de datos medidos, por ejemplo, la modelación computacional de pronósticos meteorológicos, requiere definir los valores iniciales y de frontera de los modelos. Cuando un pronóstico se integra en el tiempo, la evolución de la atmósfera en un periodo futuro puede simularse a partir de las observaciones meteorológicas actuales y datos de las últimas horas previas al punto de inicio de la simulación (datos de condiciones iniciales), bajo la reserva de reproducir y propagar errores si estos valores iniciales no son actualizados conforme el tiempo avanza. Entonces, se asume que un modelo computacional es capaz de pronosticar adecuadamente si cumple con dos aspectos principales; en primer lugar, contar con precisión en las condiciones iniciales y, en segundo lugar, tener una representación física adecuada de los procesos que rigen el comportamiento de la atmósfera (Kalnay, 2003). En la representación física queda implícito otro aspecto importante en la modelación computacional: la topografía de la superficie terrestre. Se ha demostrado que la topografía influye significativamente en las regiones climáticas, así como en las interacciones entre las capas bajas de la atmósfera y la superficie (Kapos, et al., 2000), por lo que su representación física en los modelos computacionales resulta de gran importancia en la simulación de las variables meteorológicas a niveles bajos (Carvalho et al., 2012). De acuerdo al autor Arnold et al. (Arnold et al.,2012), un área de “terreno complejo” puede definirse como la superficie donde existe una importante variación del gradiente de altitud a lo largo de una corta extensión de kilómetros y, a la vez, confluyen diferentes formas topográficas, tales como colinas, montañas, planicies, valles, mesetas, etc; similar a las características topográficas de Baja California.

En el caso de los modelos climáticos, la necesidad de datos medidos en sitio, no es suficiente, pues se requiere disponer de series de tiempo extensas (óptimamente mayores a 30 años) que cumplan condiciones de calidad de datos y homogeneidad para poder ser procesadas. No todas las metodologías de predicción climática, residen en la simulación computacional, otras relevantes como el análisis de tendencias de variables climáticas e índices de Cambio Climático, resultan muy útiles en la predicción a largo plazo, lo que favorece en gran medida a proyectos de aprovechamiento de energías renovables que se encuentran en una de las primeras fases de desarrollo. Las herramientas climáticas de esta clase, no solo pueden brindar un mayor conocimiento del potencial del recurso en el sitio, sino también permiten conocer los eventos extremos a los que las instalaciones y los sistemas podrían exponerse a lo largo de años de operación basados en la climatología del lugar.

El clima desértico extremo de la zona fronteriza del sur de California, Estados Unidos y norte de Baja California, México, la disponibilidad de datos medidos en superficie por estaciones meteorológicas y el potencial de desarrollo en la instalación de sistemas de aprovechamiento solar, fueron el objeto principal de estudio en esta investigación. Este trabajo busca abonar a la incorporación de pronósticos climáticos en la planeación de posibles proyectos futuros de generación de energía solar, analizando mediante el estudio de tendencias de extremos de temperaturas e índices de Cambio Climático, las predicciones de escenarios extremos de temperaturas y variables atmosféricas relacionadas al aprovechamiento de la energía solar. Así como analizar el potencial de los pronósticos numéricos computacionales para realizar predicciones de la irradiación solar global a corto plazo en relación a la variabilidad del recurso solar en invierno. Ambos pronósticos, son herramientas de predicción a diferentes escalas temporales y espaciales, y por lo tanto con peso en la planeación de potenciales instalaciones y la operatividad diaria de sistemas en función.

1.1.1 Problemática de la predicción atmosférica en las Energías Renovables

Las redes eléctricas suelen tener problemas cuando existen periodos de interrupción no esperados. Tomando como ejemplo a las microrredes (MG), las cuales han sido propuestas como una solución complementaria que da mayor confiabilidad a una red (Huang et al., 2012), y son consideradas un sistema de generación eléctrica híbrido autónomo que consiste en un conjunto de cargas interconectadas y fuentes de energía distribuida que pueden ser operadas de forma aislada o coordinada y controlada a una red eléctrica (Marnay et al., 2015), se pueden considerar como un tipo de aplicación de redes eléctricas que se han posicionado a nivel mundial como opciones resilientes. La flexibilidad en su configuración, permite integrar distintas fuentes de energía renovables (Pascual et al., 2015); como muestra la Figura 1.1, una MG aislada puede ser compuesta por paneles PV, turbinas eólicas y generadores de diesel o gas. Una parte importante de la MG, es su sistema de gestión de energía. Este realiza las funciones de fijar el punto de operación de entrega de energía por parte de las baterías o generadores, administrar la potencia de carga utilizada y regular el intercambio de energía entre otras redes.

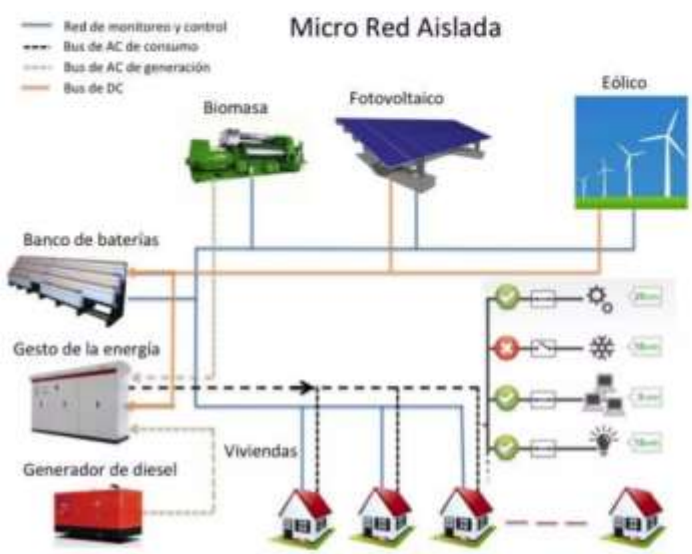

Figura 1.1. Microrred aislada. Fuente: González. (2016).

Existen condiciones atmosféricas bajo las cuales, el sistema de administración de energía necesita más información para optimizar su desempeño. Un ejemplo puede ser representado por los sistemas fotovoltaicos, conocidos por su casi instantáneo tiempo de respuesta para entregar energía y los abruptos cambios de radiación solar que se pueden registrar al paso de nublados bajos, provocando en estos, el conocido problema de “rampa de potencia”; donde al variar la incidencia de la radiación directa sobre los paneles, su desempeño se ve comprometido, y esto representa un obstáculo para la operación de la red si no ha sido previsto (Mills, 2009). Una respuesta a esta problemática es, contar con un pronóstico de la generación de energía en un horizonte temporal que puede ir desde pocos segundos, hasta horizontes mayores a 72 horas, de acuerdo a la necesidad de información y a la resolución temporal y espacial del modelo de pronóstico empleado (Figura 1.2). Sin embargo, como se mencionó antes, no sólo la predicción a corto plazo, brinda beneficios a la operatividad de un sistema de generación unido a una red. Resulta útil complementar con un pronóstico climático en un horizonte temporal mayor, destinado a brindar información de los parámetros atmosféricos máximos a registrar en el sitio de estudio.

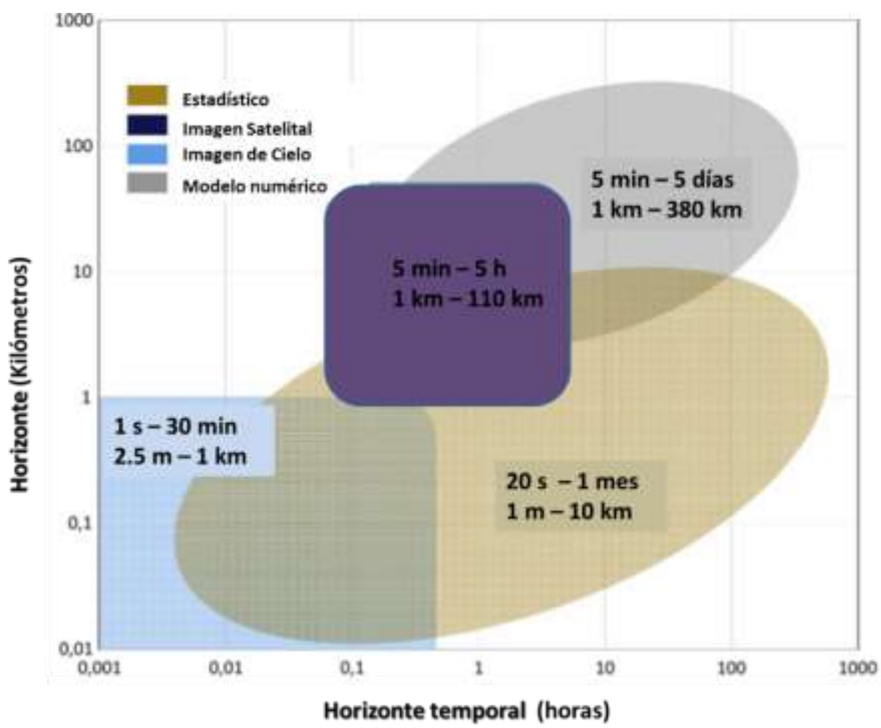

Figura 1.2 Horizonte temporal y resolución espacial de distintos métodos de pronóstico. Fuente: Antonanzas et al. 2016.

A nivel internacional, con el propósito de mejor los sistemas actuales o buscar nuevas alternativas de optimización, se han realizado trabajos relacionados a los temas de “Inteligencia de pronósticos para energías renovables”. La mayoría de estos se han enfocado a aspectos eléctricos, computacionales y de arquitectura del sistema, que tienen como objetivo principal una meta económica, pues existen algunos incentivos y sanciones monetarias impuestas por los operadores de las redes nacionales, que buscan evitar problemas en la congestión de las líneas y la estabilidad de la red (Rodriguez et al., 2018). En el caso particular de un sistema de generación de energía solar, reside en gran parte en los recursos renovables, el propósito principal en el diseño de una estrategia de manejo del sistema, se enfoca en mantener en funcionamiento a la MG en todo momento, restringiendo la salida de energía cuando es necesario, y en ocasiones haciendo uso de técnicas de manejo en la demanda, para evitar la descarga total del sistema de almacenamiento (baterías) y el colapso de la red (Pascual et al., 2015).

Como se mencionó anteriormente, existe una estrecha relación entre la variación de las condiciones de la atmósfera y el desempeño de las MG, es por esto que sus sistemas de control, deben monitorear constantemente información meteorológica para poder pronosticar dicha variabilidad y lograr ser más eficientes. Sin embargo, esto no resulta una tarea sencilla si no existe información climática y meteorológica confiable y de libre acceso, que propicie la aplicación de distintas metodologías de pronóstico (Chowdhury y Crossley, 2009). Además de considerar que cuando existen la influencia de múltiples variables y procesos, como ocurre en el sistema de manejo de una MG, el diseño de estrategias de optimización sugiere también un análisis multivariable para poder prever decisiones (Fu y Zhang, 2019). Como se muestra en la figura 1.2, la constitución de los diversos modelos de pronóstico meteorológico para la generación de energía solar y eólica, puede comprender técnicas de modelación estadística, numérica computacional o de análisis de imágenes, así como distintas fuentes de datos de entrada para su desarrollo y operación, con el fin de satisfacer diferentes horizontes temporales y espaciales de acuerdo a la necesidad de la red en estudio.

1.1.2 Servicios climáticos a disposición de redes eléctricas: estudios previos

La información meteorológica y climática es de gran importancia en la planeación de estrategias de manejo en una red eléctrica, esta ayuda a determinar la generación de energía de los recursos renovables, y en menor grado, la carga del sistema (Lorenz et al., 2012). Mediante los pronósticos meteorológicos, esta información puede ser obtenida en una primera fase, es decir, las variables meteorológicas como la temperatura, radiación solar, humedad relativa y velocidad del viento, se pronosticarán para un determinado horizonte de tiempo; posteriormente serán procesadas por un software de simulación de redes como Trnsys (Transient System Simulation Tool) o SAM (System Advisor Model), que a partir de la descripción técnica de la configuración del sistema de generación de la red, e información meteorológica del sitio, estimará la generación de energía para un determinado horizonte temporal.

Slusarewicz y Cohan en el 2018, propusieron integrar una herramienta capaz de reducir la variabilidad de producción de energía en una red alimentada principalmente por generadores eólicos y paneles PV en Texas, emplearon el modelo SAM de la NREL (National Renewable Energy Laboratory) para generar diversos escenarios de simulación a distintos horizontes de tiempo (30 min, 1 h y mayores para incluir la variabilidad interanual). En una primera fase, el estudio modeló la energía solar y eólica, y posteriormente contrastó los resultados con la base de datos de la red nacional de radiación solar de Estados Unidos. Las conclusiones mostraron que a pesar de los distintos experimentos, algunos valores máximos de producción no pudieron ser estimados con precisión; sin embargo, el experimento también demostró que las predicciones funcionaron mejor para específicas temporadas del año, por lo que alternar y diversificar sus fuentes de energía para alimentar a la red, era recomendable; además, otro problema fue que el modelo SAM, carece de la capacidad de configurar los procesos computacionales dinámicos que ajustan el pronóstico a un sitio de estudios con características climáticas y geográficas particulares, lo que puede generar una menor precisión en las predicciones.

En teoría, se esperaría que una alta precisión en el pronóstico de las variables meteorológicas, brindara una confiable estimación de la producción de energía, sin embargo, también existen errores de pronóstico que deben ser minimizados. Estos pueden ser disminuidos en la mayoría de los modelos de predicción meteorológica, mediante el ajuste adecuado de las parametrizaciones y la caracterización de procesos atmosféricos del sitio de estudio, lo cual se vuelve un proceso clave para reducir su incertidumbre. Esto coincide con lo señalado por Agüera-Perez et al. en el 2018, quien a nivel mundial realizó la revisión de cerca de 190 estudios asociados al manejo de MG y la implementación de pronósticos, y mostró una carencia generalizada en la descripción de las metodologías y la uniformidad de la evaluación, comparación e interpretación de los resultados meteorológicos obtenidos en las investigaciones. Por lo que extrapolar los estudios y replicar los métodos en una región distinta, no era posible. En diversos artículos revisados en esta publicación, también se señaló la aparente falta de robustez en las comparaciones y la duración de los experimentos de simulación, debido a que la mayoría de los estudios, realizaron pruebas para periodos no mayores a 24 horas y bajo condiciones “óptimas” de cielo despejado. Sin embargo, el desempeño de la predicción, no puede ser corroborado adecuadamente a menos de incluir dentro de estos periodos, lapsos de prueba mucho más extensos que incluyan condiciones meteorológicas diversas, como cielos nublados, precipitación ligera o vientos fuertes. En el mismo sentido de la falta de representatividad de la evaluación de escenarios, sólo poco menos de la tercera parte de los estudios revisados por Agüera-Perez, realizaron pruebas para periodos mayores a 24 horas y menores a 30 días, por lo cual la variabilidad estacional y anual, no fue evaluada en ninguno.

Se puede considerar que los métodos de pronóstico en redes eléctricas más utilizados en las investigaciones, son:

- *Arbitrarios*: pruebas a partir de datos sintéticos diseñados específicamente para el experimento o simulación, con un grado muy similar a los datos reales.
- *Históricos*: los pronósticos que se realizan a partir de largas series históricas, que pueden ser consideradas como un pronóstico perfecto o introducir variabilidad para simular errores.

- *Pronósticos locales*: son generados a partir de procesar la actualización de las mediciones de un sistema de operación, incluyendo las condiciones meteorológicas del sitio. En este caso, los modelos de pronóstico están basados en estadística y aplicaciones estadísticas de aprendizaje automático. En algunos casos, las series históricas son usadas para calibrar el modelo.
- *Pronósticos externos*: las predicciones son directamente recibidas de algún servicio público o privado. En algunos casos, bajo ciertos ajustes de parametrización, adecuados al sitio.

Este último caso, es actualmente uno los métodos con mayor flexibilidad y disponibilidad de información para modelar el pronóstico meteorológico de cualquier parte del mundo. Pues estos son obtenidos a partir de modelos globales de predicción numérica que permiten pronosticar a horizontes temporales entre 1 a 72 horas y que además pueden ser modificados en las condiciones iniciales para obtener diferencias en las simulaciones a futuro, y adecuar la configuración del modelo a las características del sitio estudiado. Por otra parte, los pronósticos locales e históricos, también han sido utilizados en la investigación, y brindan precisión aceptable cualitativamente en las predicciones, y suelen tener un mejor desempeño en pronósticos a corto plazo o bajo un análisis promedio a mediano o largo plazo.

1.2 Hipótesis

El desarrollo de un modelo de pronóstico meteorológico, basado en técnicas de modelación estadística y numérica computacional para variables atmosféricas como las temperaturas extremas y la variabilidad de la irradiación solar, contribuye a optimizar las estimaciones de generación de energía en sistemas de aprovechamiento solar.

1.3 Objetivo

Realizar un estudio enfocado en la inteligencia de pronósticos meteorológicos y climáticos, aplicado a energía solar, para generar información atmosférica a distintos horizontes temporales que contribuya a la predicción de la generación eléctrica y favorezca la toma de decisiones en la planeación, administración y gestión operativa del sector eléctrico.

1.4 Descripción del contenido

Esta tesina, es presentada de la siguiente manera: en la sección 2, se muestra una síntesis del trabajo realizado para el análisis de tendencias de temperatura extremas en ciudades de México (Predicción estadística). En esta sección se rescatan puntos clave de la metodología aplicada y algunos de los resultados obtenidos con mayor relevancia para la región de Baja California. En la sección 3, se presenta de manera similar, una síntesis del diseño de experimentos y la metodología para la evaluación del pronóstico computacional para eventos frontales en la región desértica de Baja California (Predicción numérica computacional). Se elabora en alguno de los resultados de mayor relevancia para el estudio y finalmente se mencionan algunas de las conclusiones obtenidas. Ambas secciones previamente mencionadas, se encuentran al final del documento como anexos en los correspondientes artículos arbitrados en donde las investigaciones fueron publicadas.

2. Implementación de un pronóstico basado en métodos estadísticos: Análisis de índices y extremos climáticos en México (artículo 1)

2.1 Introducción

Los fenómenos climáticos extremos (ECE) deben ser objeto de un seguimiento periódico y un análisis detallado, debido a su papel como agentes de alto impacto en la sociedad, el medio ambiente y los ecosistemas. Un evento extremo, climático o meteorológico, se refiere a la ocurrencia del valor de una variable climática o meteorológica por encima o por debajo de un valor umbral que está cerca de los límites superior (o inferior) del rango de valores observados de la variable (Seneviratne et al. 2012). Los ECE son importantes por sus impactos, pero son difíciles de cuantificar estadísticamente, ya que son poco frecuentes y se producen a múltiples escalas (Palmer y Räisänen 2002). Las definiciones de "raro" varían, pero un ECE sería normalmente tan raro como, o más raro que, el percentil 10 o 90 de la función de densidad de probabilidad observada. Es probable que diferentes ECE afecten a regiones específicas y se han detectado aumentos de frecuencia e intensidad en varias regiones del mundo (Brown et al. 2008, Almazroui et al. 2014, Chen et al. 2015; Wypych et al. 2017; Caloiero 2017). Se espera que estos ECE se intensifiquen en el futuro en respuesta a los cambios climáticos globales causados por la emisión de gases de efecto invernadero (Beniston et al. 2007; Lau y Nath 2012; Gao et al. 2012; Easterling et al. 2016; Grotjahn et al. 2016; Schoof y Robeson 2017).

Existen básicamente dos enfoques fundamentales para estudiar la ECE: Los Modelos de Circulación Global (MCG), y los modelos estadísticos, que utilizan la Teoría de los Valores Extremos (TVE). Los MCG contemporáneos, como los utilizados para el 5th Coupled Model Intercomparison Project (Taylor et al. 2012) son un componente clave de las proyecciones regionales del cambio climático, pero su limitada resolución espacial reduce su utilidad para estimar extremos locales o regionales sin un postprocesamiento sustancial (Schoff y Robeson 2016). Por otro lado, en la EVT la modelización de eventos extremos es su tema central y el principal objetivo de esta teoría es proporcionar modelos asintóticos para las colas de la distribución (Furió y Meneu 2011). Por lo tanto, la EVT tiene como objetivo derivar una distribución de probabilidad de eventos en el extremo más alejado de los rangos superiores o inferiores de las distribuciones de probabilidad (Coles 2001); su principal ventaja es que permite estimar y analizar la probabilidad de ocurrencia de eventos que están fuera del rango de datos observados (Raggad 2018). Por estas razones, la EVT es el enfoque que se ha elegido en esta investigación, y debido a su amplia aplicabilidad en diferentes campos que están relacionados con eventos meteorológicos y climáticos extremos y su impacto: en ecología (Moritz et al. 1997; Meehl et al. 2000; Dixon et al. 2005;

Katz et al. 2005; Friederichs 2010; Papalexiou y Koutsoyiannis 2013; Kim et al. 2015; Boucefiane 2019); y en daños a las comunidades que afectan a los agroecosistemas a través de cambios en la humedad del suelo y las tasas de evapotranspiración (Miralles et al. 2014; Whan et al. 2015; Guan et al. 2015; Hatfield y Prueger 2015).

Los cambios en los extremos de temperatura y precipitación se han evaluado en distintas regiones del mundo. Sin embargo, hasta el Cuarto Informe de Evaluación del Grupo Intergubernamental de Expertos sobre el Cambio Climático (Trenberth et al. 2007), las ciudades habían sido tratadas como entidades generadoras de "ruido" en las señales climáticas estudiadas a escala mundial. En el Quinto Informe de Evaluación del Grupo Intergubernamental de Expertos sobre el Cambio Climático (IPCC 2013), se dedicó un capítulo especial al tema de las ciudades y su papel en el cambio climático. Esto no es sorprendente, ya que aunque las ciudades contribuyen de manera muy importante al bienestar social y económico, requieren una fuente ininterrumpida de energía para todas sus actividades. Las ciudades consumen aproximadamente el 75% de la energía primaria mundial y emiten entre el 50% y el 60% de los gases de efecto invernadero (GEI) del planeta (Rosenzweig et al. 2011). Esta cifra puede elevarse hasta el 80% si se incluyen las emisiones indirectas generadas por los habitantes de las ciudades (ONU-Hábitat 2011; Kraussmann et al. 2017). Así pues, las ciudades favorecen el calentamiento global y contribuyen a aumentar la temperatura media de la superficie a nivel planetario.

Además de los efectos globales de los GEI, hay que tener en cuenta la tendencia mundial al alza del crecimiento urbano, tanto en población como en su extensión de área. Este crecimiento ha generado problemas ambientales, no sólo de contaminación atmosférica y residuos sólidos, sino también los relativos a un producto ambiental diferente, como es la génesis de un clima urbano. En particular, la principal connotación del clima urbano es la formación de una isla de calor urbana, que a su vez requiere agua y energía adicionales para mantener el confort térmico a través de espacios climatizados (Coutts et al. 2012; Wang et al. 2016; de Munck et al. 2018, Skelhorn et al. 2018). Así, las ciudades que ya son especialmente vulnerables a los ECE causados por el cambio climático global, ahora también deben considerar los efectos causados por el cambio climático local. Por tanto, se puede inferir que al ser una ciudad el espacio geográfico que aglutina una mayoría de población y prestación de servicios, será donde se manifiesten las mayores vulnerabilidades asociadas a los impactos del cambio climático (ONU-Hábitat 2011).

En México aproximadamente tres de cada cuatro personas (72.3%) viven en ciudades según la Fundación Centro de Investigación y Documentación de la Casa y Sociedad Hipotecaria Federal (CIDOC y SHF, 2011). Se espera que este porcentaje aumente en el mediano plazo, ya que, de acuerdo con proyecciones del Consejo Nacional de Población, el número de personas en 384 localidades del Sistema Urbano Nacional se incrementará en 16.6 millones (de 82.6 millones en 2010 a 99.3 millones en 2030) como resultado de una tasa de crecimiento promedio anual de 0.92% (Hernández et al. 2014). La proporción urbana de la población nacional aumentará a 77.9% (18.1 millones de nuevos habitantes urbanos). Esta tendencia de la dinámica geográfica de las ciudades es inequitativa con bajos niveles de calidad de vida y sustentabilidad urbana, y no todas las ciudades tienen el mismo potencial de desarrollo. Así pues, los retos para hacer frente a riesgos climáticos como las olas de calor y las inundaciones serán enormes si no se llevan a cabo estudios científicos cuantitativos.

En México se han realizado muy pocas investigaciones sobre valores climáticos extremos en entornos urbanos (Cavazos y Rivas 2004; Ríos-Alejandro 2011; Magaña et al. 2003; Magaña et al. 2012; García-Cueto et al. 2013, 2014, 2018; Martínez-Austria y Bandala 2017). Esto puede explicarse por un acceso limitado a los datos climáticos medidos, limitaciones en la cobertura geográfica de las redes de estaciones e interrupciones en las series climáticas por falta de datos. Ante ello, y dada la incertidumbre cuantitativa de los extremos climáticos mencionados a nivel urbano y su gran importancia para la evaluación de riesgos y propuestas de adaptación, en este estudio se seleccionan algunas ciudades de México con incrementos importantes en población y en extensión areal, que han sido afectadas recientemente por ECE.

Así, este estudio tiene tres objetivos principales: a) detectar el comportamiento térmico en algunas ciudades en crecimiento de México, b) modelar las temperaturas extremas a través de la EVT, y c) realizar proyecciones de niveles de retorno para temperaturas extremas en un futuro clima cambiante.

2.2 Los Índices de Cambio Climático, contexto y antecedentes

Se utilizaron los Índices de Cambio Climático (ICC) propuestos por el Grupo de Expertos en Detección e Índices de Cambio Climático (ETCCDI, por sus siglas en inglés). Este grupo coordinado por la Comisión de Climatología de la Organización Meteorológica Mundial en el proyecto sobre Predictibilidad Climática y Variabilidad Climática, y la Comisión Técnica de Oceanografía y Meteorología Marítima, propuso un conjunto de 27 índices para detectar modificaciones en el comportamiento de los extremos del clima. Estos índices se estiman a partir de la serie de datos diarios observados de temperatura y precipitación.

Los índices son estadísticamente robustos, cubren una amplia gama de climas, y tienen una alta relación señal-ruido. Algunos están basados en umbrales fijos que son de relevancia a aplicaciones particulares. En estos casos los umbrales son los mismos para todas las estaciones climáticas. Otros índices están basados en umbrales que varían de lugar a lugar, lo cual fue propuesto y realizado en este estudio.

Algunos índices incluidos son el número total de días al año con heladas y el número máximo de días secos consecutivos en un año. Otro tipo de índice estima los máximos o mínimos mensuales y/o anuales de temperatura diaria o cantidad máxima de precipitación diaria. Estos tipos de índices extremos han sido ampliamente utilizados en aplicaciones de ingeniería para inferir valores de diseño en estructuras. Hay un tipo de índice que involucra realizar el cálculo del número de días en un año que exceda umbrales específicos que tienen valores fijos, o umbrales que son relativos a un período climático base. Algunos otros se definen para estimar períodos de sequedad, humedad, calor o frío, o períodos de vernalización como en el caso de períodos de duración de la estación de crecimiento.

Ejemplos de índices de “conteo de días” con umbrales fijos son el número de días con temperatura mínima diaria inferior a 0 °C (es decir, los días con heladas) o el número de días con la cantidad de lluvia superior a 20 mm. Estos índices son menos adecuados para las comparaciones espaciales de los extremos que las basadas en umbrales de percentiles. La razón es que, en grandes áreas, los índices de conteo de días basándose en umbrales fijos pueden muestrear diferentes partes de las distribuciones de temperatura y precipitación. Por ejemplo, mientras que el número de días con una temperatura mínima por debajo de 0 °C puede ser un buen indicador de frío extremo en muchos climas de latitudes medias, en latitudes más altas, donde casi todas las noches de invierno están por debajo de 0 °C incluso en inviernos suaves, la variabilidad en el número anual de noches por debajo de 0 °C es impulsada en gran medida por las condiciones en primavera y otoño. Por otra parte, un índice como el número de días de verano por encima de 25 °C puede ser un indicador de calor anormal en un clima donde la media de temperatura máxima en verano es de 18 °C, pero de frío anormal en un clima donde la temperatura máxima media en verano es de 35 °C.

Muchos índices ETCCDI se basan en los percentiles con los umbrales establecidos para evaluar extremos moderados que ocurren típicamente unas pocas veces al año en lugar de los de alto impacto, que son eventos climáticos que ocurren una vez en una década. Para la temperatura, los umbrales de percentiles en los índices ETCCDI se calculan a partir de ventanas de cinco días centradas en cada día del calendario para tener en cuenta el ciclo medio anual. Para precipitación los umbrales percentiles en el ETCCDI se calculan de la muestra de todos los días húmedos en el período base sin consideración del ciclo anual. Tales índices permiten monitoreo directo de tendencias en la frecuencia o intensidad de eventos, que aunque no son particularmente extremas, potencialmente podrían causar estrés a los seres humanos o al medio ambiente. La razón para elegir umbrales de percentil es que el número de días que los superen se distribuye de manera más uniforme en el espacio y es significativo en todas las regiones. Los umbrales se establecen de manera que la frecuencia de cruce de umbral durante el período base, tal como 10% de todos los días registrados, es fija. Estos índices permiten comparaciones espaciales más sobre grandes regiones con topografía compleja debido a que muestrean la misma parte de la distribución de probabilidad de temperatura y precipitación en cada lugar. También pueden dar cuenta de los valores aislados que faltan de una manera relativamente sencilla.

Varios estudios han sido realizados aplicando los índices definidos en la tabla 2.1 (por ejemplo, Alexander et al., 2006; Christidis et al., 2005; Peterson et al., 2009; Donat et al., 2013). La tabla 2.1, presenta los índices que se estiman y analizan en el estudio.

Tabla 2.1 Índices Climáticos Extremos recomendados por el ETCCDI

Índice	Nombre de índice	Definición de Índice	Unidades
TMAXmean	Temperatura Máxima media	Valor medio de temperatura máxima media anual	°C
TMINmean	Temperatura Mínima media	Valor medio de temperatura mínima media anual	°C
TXx	Tmax MAX	Valor máximo mensual de temperatura máxima diaria	°C
TNx	Tmin MAX	Valor máximo mensual de temperatura mínima diaria	°C
TXn	Tmax MIN	Valor mínimo mensual de temperatura máxima diaria	°C
TNn	Tmin MIN	Valor mínimo mensual de temperatura mínima diaria	°C
TN10p	Noches Frías	% tiempo cuando la temperatura mínima diaria < P10	%
TX10p	Días Fríos	% tiempo cuando la temperatura máxima diaria < P10	%
TN90p	Noches Cálidas	% tiempo cuando la temperatura mínima diaria > P90	%
TX90p	Días Cálidos	% tiempo cuando la temperatura máxima diaria > P90	%
DTR	Rango diurno de temperatura	Diferencia mensual entre las temperaturas máximas y mínimas diarias	°C
GSL	Longitud de la estación de crecimiento (TG es la temperatura media diaria)	Conteo anual (1 enero a 31 diciembre en HN; 1 julio a 30 junio en HS) entre el primer lapso de al menos 6 días con TG > 5°C, y primer lapso después del 1 julio (1 enero en el HS) de 6 días con TG < 5°C	Días
FD0	Días con heladas	Conteo anual cuando la Tmin diaria < 0°C	Días
SU25	Días de verano	Conteo anual cuando la Tmax diaria > 25°C	Días
TR20	Noches tropicales	Conteo anual cuando la Tmin diaria > 20°C	Días
WSDI	Duración de período cálido	Conteo anual cuando al menos 6 días consecutivos de Tmax > P90	Días
CSDI	Duración de período frío	Conteo anual cuando al menos 6 días consecutivos de Tmin < P10	Días
RX1day	Máximo de precipitación en 1 día	Valor máximo anual de la precipitación diaria	mm
RX5day	Máximo de precipitación en 5 días	Precipitación máxima anual consecutiva de 5 días	mm
SDII	Índice simple de intensidad diaria	Relación de precipitación anual al número de días húmedos (≥ 1 mm)	mm/día
R10	Número de días de precipitación fuerte	Conteo anual cuando la precipitación es ≥ 10 mm	Días
R20	Número de días de precipitación muy fuerte	Conteo anual cuando la precipitación es ≥ 20 mm	Días
CDD	Días secos consecutivos	Número máximo de días consecutivos cuando la precipitación < 1 mm	Días
CWD	Días húmedos consecutivos	Número máximo de días consecutivos cuando la precipitación ≥ 1 mm	Días
R95p	Días muy húmedos	Precipitación total anual de días > P95	mm
R99p	Días extremadamente húmedos	Precipitación total anual de días > P99	mm
PRCPTOT	Precipitación total anual de días Húmedos	Precipitación total anual de días ≥ 1 mm	mm

2.3 Climatología de Temperaturas Extremas

Las Figuras 2.1 y 2.2 muestran los percentiles 10th y 90th de las temperaturas mínimas y máximas, respectivamente (Cavazos et al. 2013), para el periodo 1961-2000. De acuerdo con los índices climáticos extremos derivados del Reliability Ensemble Averaging (REA) (Fig. 2.1), los inviernos más fríos y su percentil 10th (P10) durante los meses invernales de diciembre, enero y febrero (DJF) para México se caracterizan por temperaturas mínimas por debajo de 0 °C en las tierras altas de la Sierra Madre Occidental y el Altiplano Mexicano, y entre 0 y 5 °C en gran parte del norte de México. La Figura 2.2 muestra que los valores extremos del percentil 90th (P90) de las temperaturas máximas durante los meses de verano de junio, julio y agosto (JJA) amplían el área cubierta por las isotermas de 25 y 40 °C a una franja más estrecha en la región fronteriza. Esta región de clima semiárido es la más extrema de México; por lo tanto, es la más susceptible a los impactos negativos causados por los aumentos de temperatura.

Los cambios climáticos proyectados a nivel nacional (Cavazos et al. 2013) coinciden con los obtenidos a nivel global (Alexander et al. 2006; Caesar et al. 2011; Song et al. 2014). En cuanto a los relacionados con el aumento en la frecuencia de los días de calor, las olas de calor y la variabilidad en la precipitación agravarán los problemas relacionados con los sistemas naturales y humanos (Ummenhofer y Meehl 2017). Si analizamos los percentiles 10^{th} y 90^{th} de temperaturas extremas a nivel nacional, es notable la falta de información confiable y oportuna a nivel regional y urbano para la evaluación de riesgos, y justifica el estudio aquí realizado.

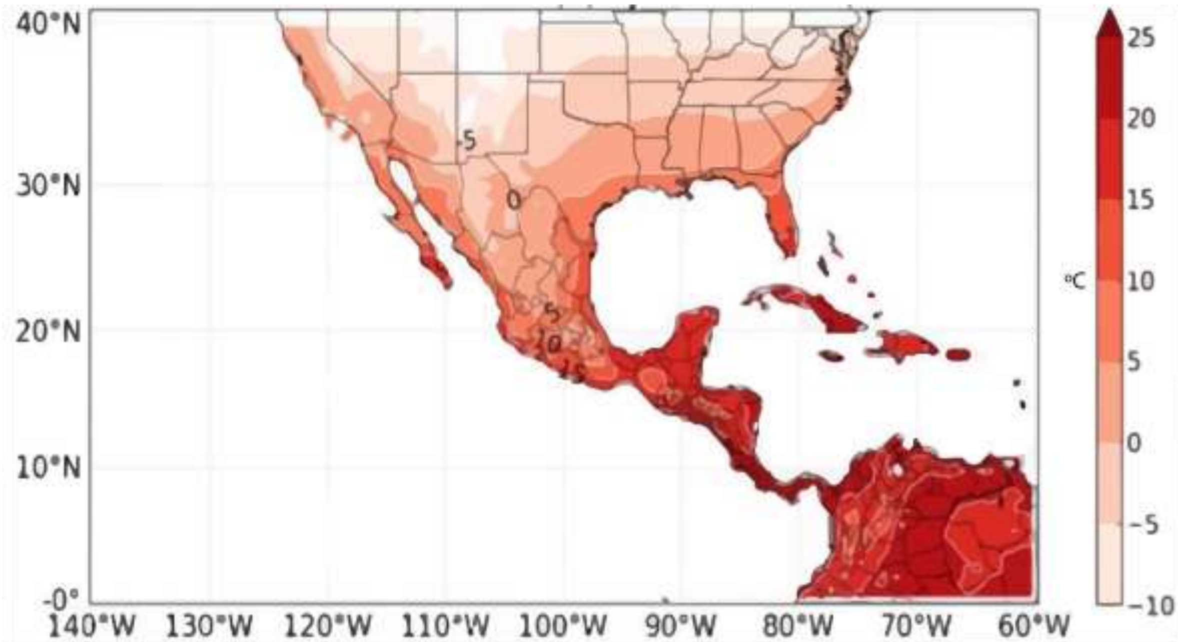

Figura 2.1 Umbrales de P10 de temperatura mínima (Tmin) de invierno, obtenidos con el ensemble del reliability ensemble averaging (REA) para 1961-2000 (Cavazos et al. 2013).

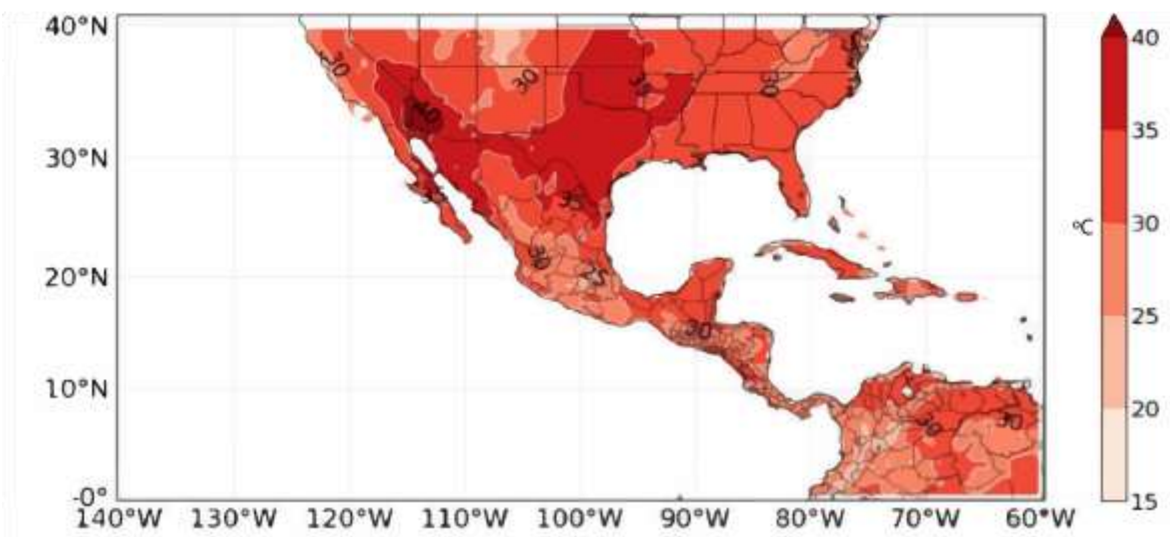

Figura 2.2 Umbrales de P90 de temperatura máxima (Tmax) de verano, obtenidos con el ensemble del REA para 1961-2000 (Cavazos et al. 2013).

2.4 Metodología

Posterior al análisis de calidad realizado a la información climatológica diaria de temperatura y precipitación, las ciudades y/o regiones que cumplieron los requerimientos estipulados para su estudio son las que se presentan en la tabla 2.2; en ésta se puede ver el número y nombre de estación climática disponibles para su análisis, de acuerdo al Servicio Meteorológico Nacional de México, el período inicial y final de información, y el período de datos útiles.

Tabla 2.2. Ciudades elegidas para el estudio de tendencias climáticas y eventos extremos, estaciones climáticas y período disponible de datos útiles.

Ciudad o Región	Número y nombre de estación climática	Inicio (año)	Final (año)	Período disponible (año)
Aguascalientes	01030 (Aguascalientes)	1972	2007	36
Mexicali	02033 (Mexicali)	1944	2012	69
Tijuana	02038 (Tijuana)	1950	2012	63
Tuxtla Gutiérrez	07165 (Tuxtla Gutiérrez)	1980	2010	31
Ciudad de México y ZMVM*	09014 (Santa Úrsula Coapa)	1971	2013	43
	09029 (Gran Canal)	1952	2010	59
	09032 (Milpa Alta)	1963	2012	50
	15002 (Aculco)	1970	2011	42
	15126 (Toluca)	1974	2011	38
	15170 (Chapingo)	1954	2010	57
León	11095 (León)	1959	2014	56
Guadalajara	14066 (Guadalajara)	1960	2013	54
Monterrey	19049 (Monterrey)	1950	2001	52
Puebla	21035 (Puebla)	1953	2013	61
Tlaxcala	29030 (Tlaxcala)	1969	2013	45
Veracruz	30192 (Veracruz)	1930	2014	85

*ZMVM significa Zona Metropolitana del Valle de México

La localización de estas estaciones en las ciudades o regiones en la República Mexicana se pueden ver en la Figura 2.3.

Una vez obtenida la base de datos diarios se procedió al cálculo de los ICC mediante la utilización del software Rclimdex (Zhang y Yang, 2004), que es un software libre (http://cccma.seos.uvic.ca/ETCCDI/software.shtml) que funciona bajo una plataforma R (http://www.r-project.org). Un nivel de confianza del 95% se propuso como umbral para que un índice se considerara estadísticamente significativo.

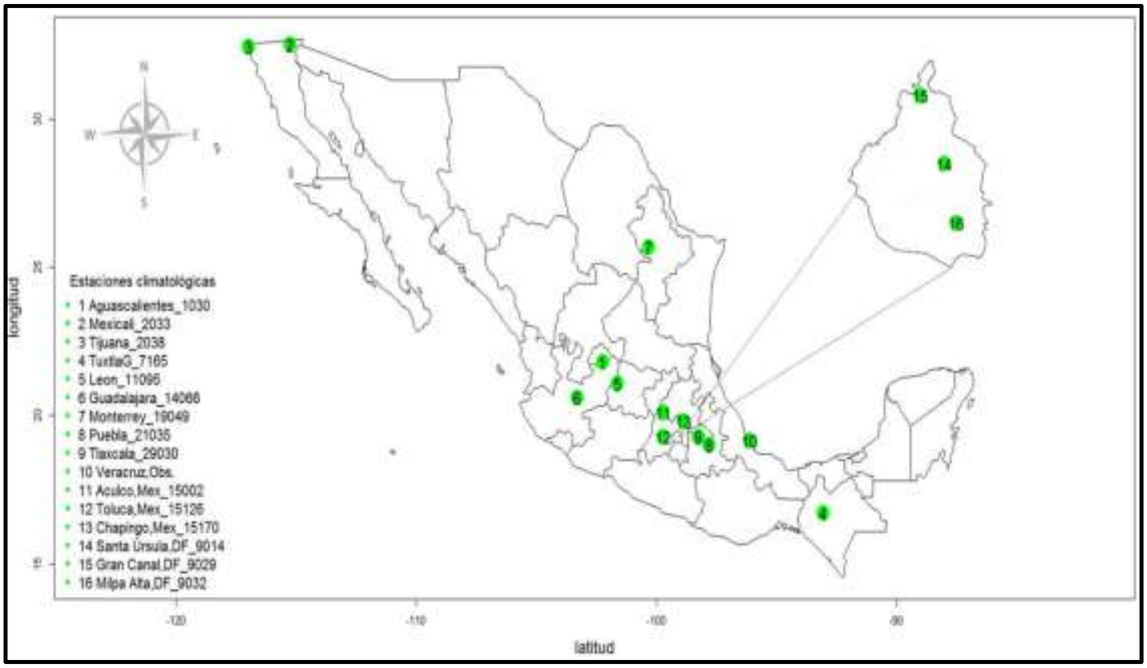

Figura 2.3 Localización de las estaciones climáticas seleccionadas

Debido a que muchos índices no son adecuados para calcularse tal cual ha propuesto el grupo del ETCCDI, se realizó una modificación de acuerdo a la realidad climatológica de cada ciudad o región estudiada. De tal suerte, los índices climáticos que fueron propuestos para estimarse en base a las normales climatológicas locales fueron los siguientes: a) SU (Summer Days/Días de Verano), estimado con el umbral superior de la temperatura máxima diaria; b) ID (Icing Days/Días de hielo), estimado con el umbral inferior de la temperatura máxima diaria; c) FD (Frost Days/Días de heladas), estimado con el umbral inferior de la temperatura mínima diaria; y d) TR (Tropical Nights/Noches tropicales), estimado con el umbral superior de la temperatura mínima diaria.

Para que este reporte fuera consistente y se pudieran comparar las tendencias entre ciudades, se utilizó el período de referencia de 1980 al 2010, aunque Aguascalientes y Monterrey no cumplieron este requisito, igual que en el caso de Toluca, Col. Santa Úrsula Coapa de la Delegación Coyoacán y Gran Canal de la Delegación Gustavo A. Madero de la ZMVM, pero que se dejaron porque su base de datos era de calidad adecuada, aunque su período de análisis fue un poco menor que el período base seleccionado.

2.5 Análisis de tendencias

Las detecciones de tendencias monotónicas de aumento o disminución de TXX y TNN en una serie temporal se analizaron mediante la prueba no paramétrica de Mann-Kendall (Mann 1945; Kendall 1975) y utilizando el método de Sen para las estimaciones de la pendiente (Sen 1968). La prueba de Mann-Kendall se basa en rangos y ha resultado ser una herramienta excelente para detectar tendencias en aplicaciones climáticas (Burn y Hag Elnur 2002; Mugume et al. 2016). Una de las ventajas de esta prueba es que no es necesario ajustar los datos a ninguna distribución. La segunda ventaja de esta prueba es su baja sensibilidad a las rupturas repentinas debidas a series temporales no homogéneas, valores extremos (valores atípicos) y tendencias no lineales (Helsel y Hirsch 1992; Tabari et al. 2011). Dada su solidez, la prueba de Mann-Kendall se ha hecho muy popular en la evaluación de tendencias en datos medioambientales y permite realizar comparaciones adecuadas entre regiones (Qiang et al. 2011; Fengjin y Lianchun 2011; Wang et al. 2013; Dumitrescu et al. 2015; Ongoma et al. 2016). El método de Sen utiliza un modelo lineal para estimar la pendiente de una tendencia, y la varianza de los residuos debe ser constante a lo largo del tiempo (Salmi et al. 2002). Muchos estudios (Taxak et al. 2014; Caloiero 2017; Raggad 2018; García-Cueto et al. 2018, entre otros) han descrito estos métodos de forma explícita.

2.6 Los valores GEV estacionarios y no estacionarios

El marco general de este estudio es una EVT estadística. La EVT pretende caracterizar los sucesos raros describiendo las colas de la distribución subyacente. La EVT se refiere al comportamiento estocástico asintótico de los estadísticos de orden extremo de una muestra aleatoria, como los valores máximo y mínimo de variables aleatorias independientes idénticamente distribuidas (Coles 2001). El postulado del Teorema de Fisher-Tippett (1928) establece que si la distribución del máximo normalizado de una secuencia de variables aleatorias converge, siempre converge a la distribución GEV, independientemente de la distribución subyacente. A este respecto, sea X_1 , ..., X_n una secuencia de variables aleatorias independientes idénticamente distribuidas con una función de distribución común F; la muestra máxima, M_n , siendo n el tamaño del bloque, se define como $M_n = \max \{X_1 , X_2 , ..., X_n \}$. X_i suele representar los valores máximos (o mínimos) medidos en una escala temporal regular o en bloques de tiempo, por lo que M_n representa los valores extremos del proceso en *n* unidades de tiempo de observación. Los bloques de datos en este estudio son secuencias de observaciones que tienen la duración de un año, es decir, el enfoque utiliza los valores máximos y mínimos por bloques anuales de temperatura.

Para estos datos, las distribuciones de M_n según la EVT pueden modelizarse como bloques de valores extremos idénticamente distribuidos con una distribución GEV definida por la ecuación (1), con una función de distribución acumulativa con tres parámetros dada por (Coles 2001):

$$G(z;\mu,\sigma,\xi) = \exp\left[-\left\{1 + {}^{\xi(z-\mu)}\!/_{\sigma}\right\}^{-1/\xi}\right] \qquad (1)$$

Esta distribución se define en el conjunto $\{z: 1 + \xi (z - \mu) / \sigma > 0\}$. Aquí, μ es el parámetro de localización ($-\infty < \mu < \infty$), σ es el parámetro de escala ($\sigma > 0$), y ξ es el parámetro de forma ($-\infty < \xi < \infty$) que determina la naturaleza del comportamiento de la cola de la distribución máxima. La justificación de la distribución GEV surge de un argumento asintótico. La distribución GEV combina las tres posibles distribuciones límite sobre valores extremos en datos muestrales en una única expresión. Es una familia de distribuciones de probabilidad continua desarrollada para combinar las tres distribuciones de valores extremos: Gumbel ($\xi = 0$), Fréchet ($\xi > 0$) y Weibull ($\xi < 0$), o distribuciones de valores extremos tipos I, II y III, respectivamente. Cada uno de los tres tipos de distribuciones tiene formas distintas de comportamiento en la cola. La Weibull *está acotada* por arriba, lo que significa que existe un valor finito que el máximo no puede superar. La distribución de Gumbel presenta una *cola ligera*, lo que significa que, aunque el máximo puede tomar valores infinitamente altos, la probabilidad de obtener tales niveles se hace exponencialmente pequeña. La distribución de Fréchet tiene una cola pesada y decae polinómicamente, de modo que los valores más altos del máximo se obtienen con mayor probabilidad, como ocurriría con una cola más ligera (Gilleland y Katz 2006). La flexibilidad de la GEV para describir los tres tipos de comportamiento de la cola en una única familia simplifica enormemente la aplicación estadística.

Como se menciona más adelante, las temperaturas extremas de varias ciudades analizadas muestran tendencias temporales, por lo que el supuesto de una serie de datos distribuidos de forma independiente e idéntica con propiedades constantes a lo largo del tiempo (estacionaria) debe modificarse para considerar los efectos del cambio climático a largo plazo. De hecho, cada vez hay más pruebas de que las series extremas, ya sean térmicas o hidroclimáticas, no son estacionarias, debido a la variabilidad climática natural o al cambio climático antropogénico (Jain y Lall 2001; Milly et al. 2008). La modelización de la no estacionariedad dentro del esquema de distribución GEV requiere modelos mejorados, en los que los parámetros del modelo se expresen en función del tiempo, y posiblemente con la incorporación de otras covariables (El Adlouni et al. 2007; Leclerc y Ouarda 2007; Panagoulia 2013; Parey et al. 2018).

Incorporamos la no estacionariedad permitiendo que el parámetro de localización (μ) de la distribución GEV dependa del tiempo (Renardt et al. 2013). Utilizando la notación (μ, σ, ξ) para denotar una distribución GEV con parámetros μ, σ, ξ, un modelo adecuado para las temperaturas extremas en el año t, Z_t , podría ser el presentado en la ecuación (2) (Furió y Meneu 2011):

$$Z_t \approx \text{GEV}\,[\mu(t), \sigma, \xi] \qquad (2)$$

En la ecuación (2), $\mu(t) = \mu_0 + \mu_1(t)$ para los parámetros μ_0 y μ_1 . De este modo, las variaciones temporales del proceso observado se modelizan como una tendencia lineal para el parámetro de localización del modelo de valores extremos, que en este caso es la distribución GEV. El parámetro μ_0 corresponde al valor de μ cuando t es el tiempo inicial, mientras que el parámetro μ_1 corresponde a la tasa anual de variación de las temperaturas extremas anuales.

2.7 Resultados

2.7.1 Índices de cambio climático para Mexicali (1980- 2010)

En el caso de la ciudad de Mexicali los índices que fueron estimados en base a valores climatológicos locales se mencionan a continuación: el índice SU42 (SUmmer days) fue fijado según las normales climatológicas de la estación en el umbral de 20-42º C en la temperatura máxima diaria, en lugar del propuesto por default de 25° C (SU25); ID20 (Icing Days), el umbral inferior de la temperatura máxima diaria se eligió de 20° C, en lugar de tomar el default de 0 °C (ID0). FD5 (Frost Days) fue seleccionado el umbral inferior de la temperatura mínima diaria, se eligió el valor de 5° C, en lugar del propuesto de 0°C; TR25 (Tropical Nights), el umbral superior de la temperatura mínima diaria se eligió con un valor de 25° C (en lugar del propuesto de 20° C TR20), que es el valor mayor en el umbral de las normales de temperatura mínima. En la tabla 2.3 se listan los índices climáticos que resultaron estadísticamente significativos ($\alpha = 0.05$) para la ciudad de Mexicali, B.C.

Tabla 2.3 Índices de cambio climático (ICC) estadísticamente significativos al 95% en Mexicali, B.C.Índices de cambio climático (ICC) estadísticamente significativos al 95% en Mexicali, B.C., tendencias lineales (Pendiente, Unidad/año), desviación estándar de la pendiente (DE, Unidad/año), y significancia estadística (p_value). Las unidades de los ICC, pueden ser revisadas a detalle en la tabla 2.1

ICC	Pendiente (Unidad/año)	DE (Unidad/año)	p_value
TMAXmean	0.06	0.02	0.001
TMINmean	0.05	0.01	0.000
SU42	1.00	0.32	0.004
FD5	-0.53	0.20	0.013
TNn	0.11	0.03	0.004
TX10p	-0.31	0.10	0.004
TX90p	0.24	0.09	0.016
TN10p	-0.39	0.08	0.000
TN90p	0.18	0.08	0.044
CSDI	-0.45	0.14	0.002

Los resultados mostraron una tendencia positiva en los siguientes índices climáticos: temperatura máxima media (TMAXmean, fig. 2.4), temperatura mínima media (TMINmean, fig. 2.5), frecuencia de días cuando la temperatura máxima diaria > 42° C (SU42, fig. 2.6), valor mínimo anual de la temperatura mínima diaria (TNn, fig. 2.8), porcentaje de días con temperatura máxima mayor a la del P90 (TX90p, fig. 2.10), y porcentaje de días con temperatura mínima diaria > P90 (TN90p, fig. 2.12)

De los índices con tendencia positiva, TX90P y SU42 son los que muestran el mayor aumento. El índice SU42 que relaciona el valor máximo normal de temperatura, muestra la mayor tendencia al aumento; a pesar de mostrar una disminución en la tendencia durante finales de los 80´s, en los últimos veinte años el incremento fue más evidente. También el índice TX90P, el cual es una importante referencia de los valores mayores de temperaturas máximas, muestra una clara tendencia positiva. A partir de los valores de estos dos importantes índices con tendencias positivas y los anteriormente mencionados como significativos con tendencia positiva pero con menores valores en la pendiente, se sugiere que podría existir evidencia estadística de un aumento significativo en los valores de temperaturas máximas a lo largo de la serie de tiempo.

Por otra parte entre los índices significativos que mostraron una tendencia al decremento, están la frecuencia de días cuando la temperatura mínima es < 5° C (FD5, fig. 2.7), el porcentaje de días con la temperatura máxima menor al percentil (TX10p, fig. 2.9), el porcentaje de días con la temperatura mínima menor al percentil 10 (TN10p, fig. 2.11), el porcentaje de días con la temperatura mínima diaria mayor a la del percentil 90 (TN90p, fig. 2.12), y el conteo de periodos de al menos 6 días consecutivos menor al percentil 10 de temperatura mínima (CSDI, fig. 2.13). Las tendencias negativas mayores, se mostraron en los índices FD5, CSDI y TN10p. El decremento en la frecuencia, porcentaje y número de días con temperaturas mínimas por debajo de los valores promedio mostrado en FD5, CSDI y TN10p, concuerda con el incremento de los días cálidos (SU42 y TX90p, mencionados anteriormente) y ratifica la tendencia al incremento en las temperaturas mínimas y máximas promedio en la ciudad de Mexicali.

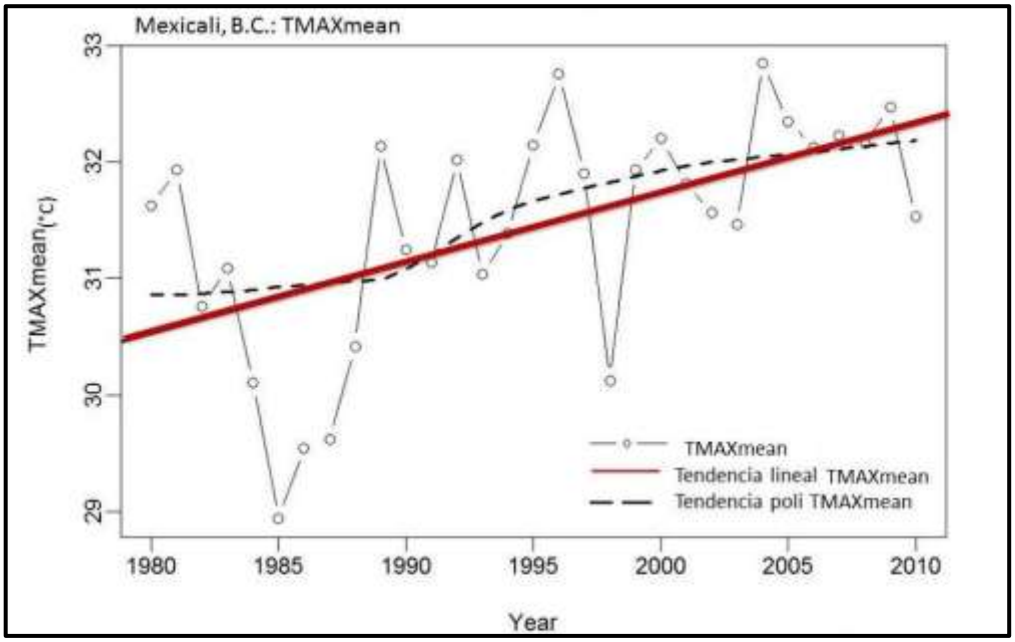

Figura 2.4 Tendencia de temperatura máxima media (°C) en Mexicali, B.C. (1980-2010)

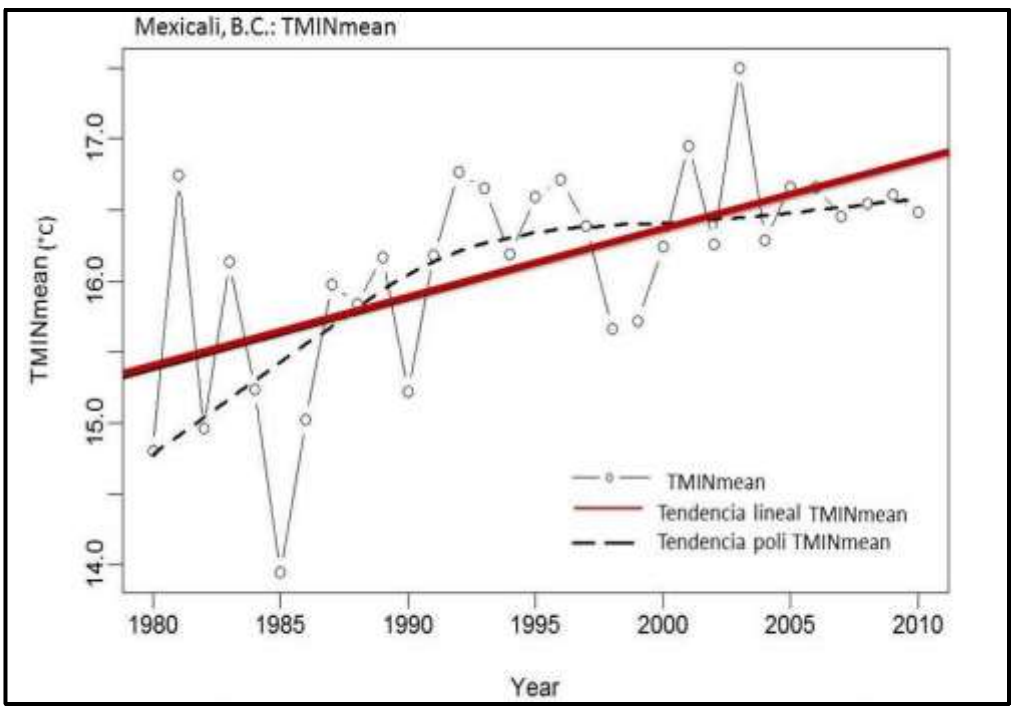

Figura 2.5 Tendencia de temperatura mínima media (°C) en Mexicali, B.C. (1980-2010)

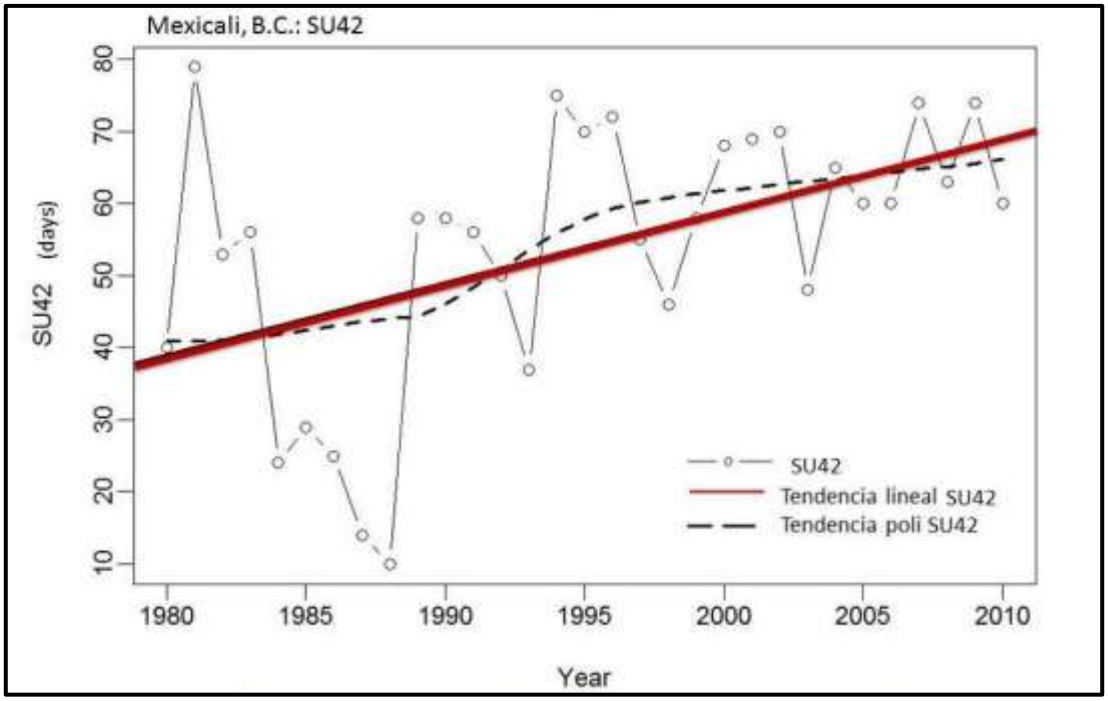

Figura 2.6 Tendencia de días cuando la temperatura máxima diaria es >42°C Mexicali, B.C. (1980- 2010)

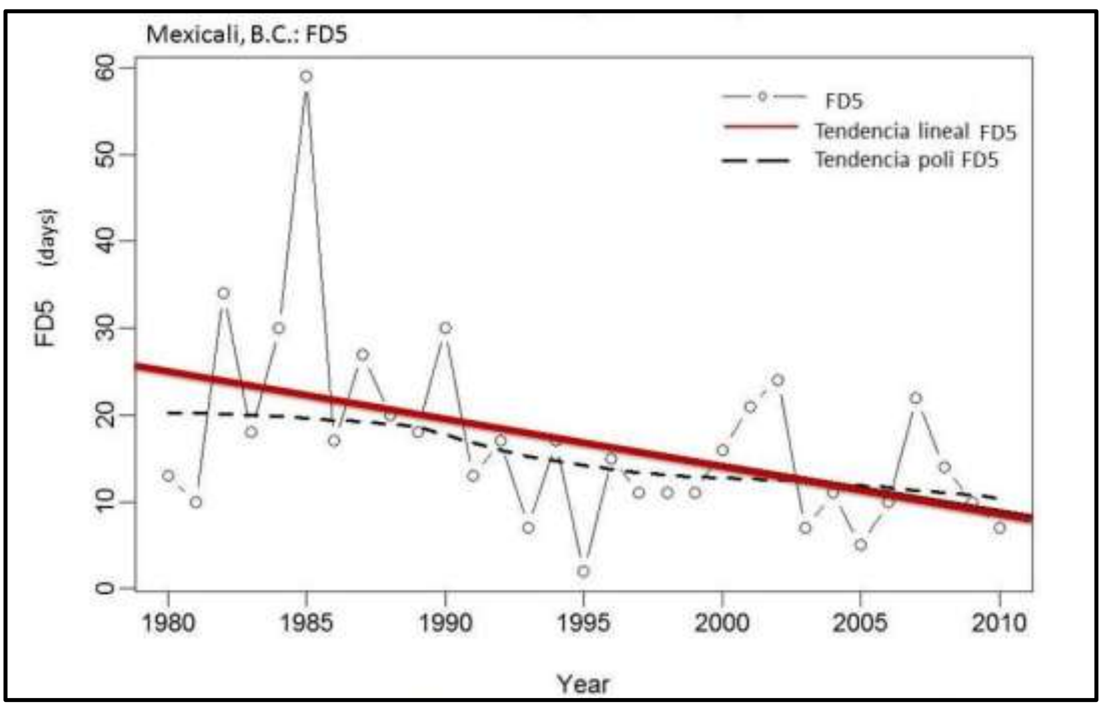

Figura 2.7 Tendencia de días cuando la temperatura mínima es < 5° C Mexicali, B.C. (1980-2010)

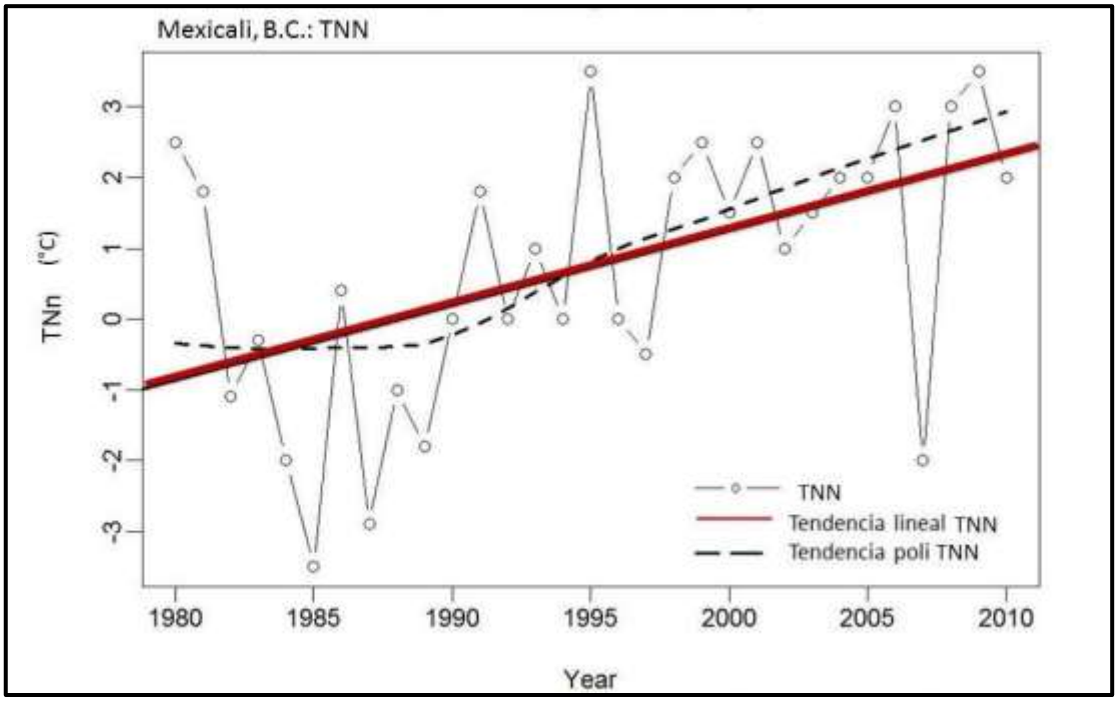

Figura 2.8 Tendencia de valores mínimos anuales de temperatura mínima diaria en Mexicali, B.C. (1980-2010)

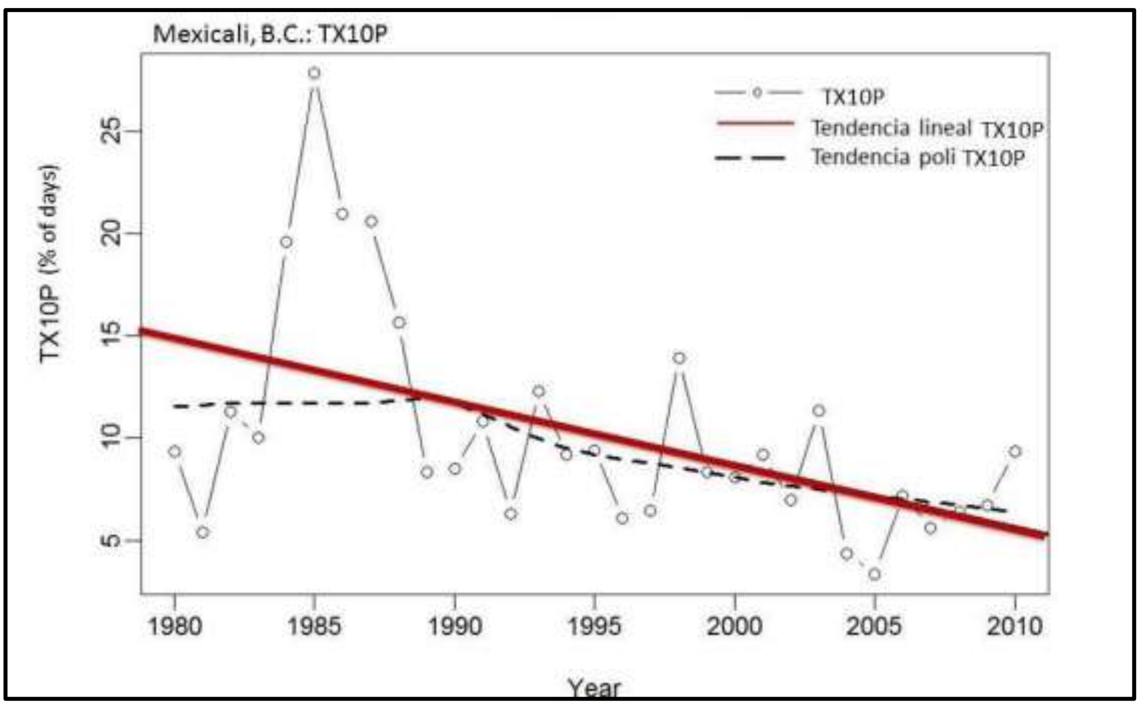

Figura 2.9 Tendencia de días con la temperatura máxima diaria menor al P10 en Mexicali, B.C. (1980-2010)

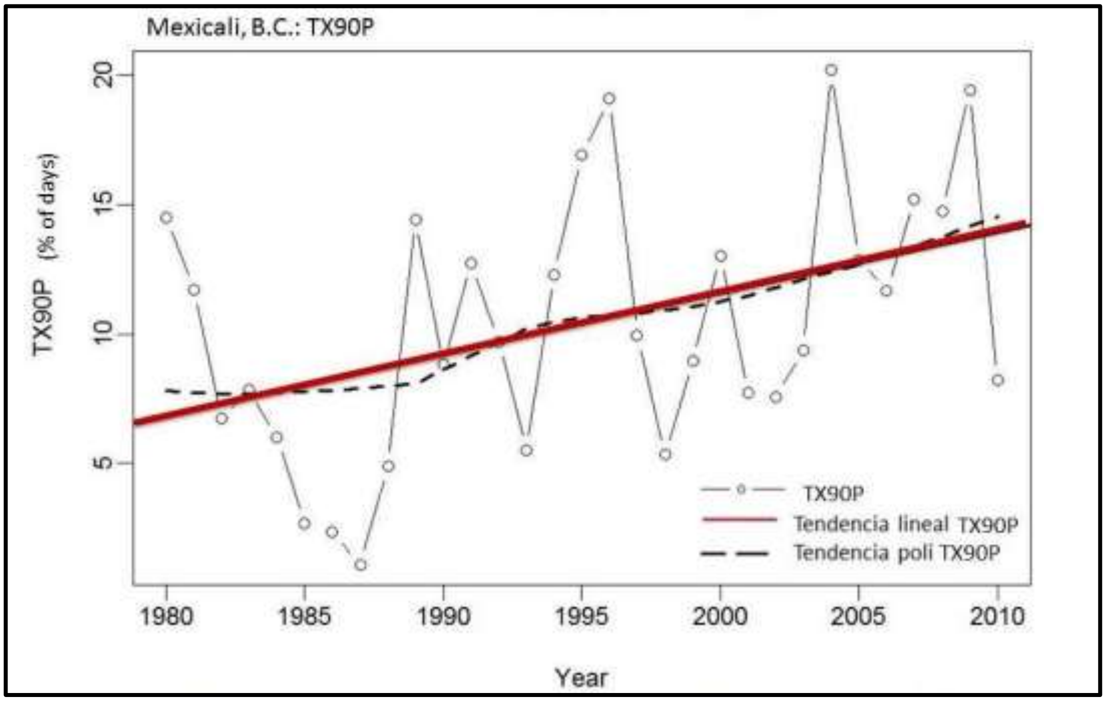

Figura 2.10 Tendencia de días con temperatura máxima superior al P90 en Mexicali, B.C. (1980- 2010)

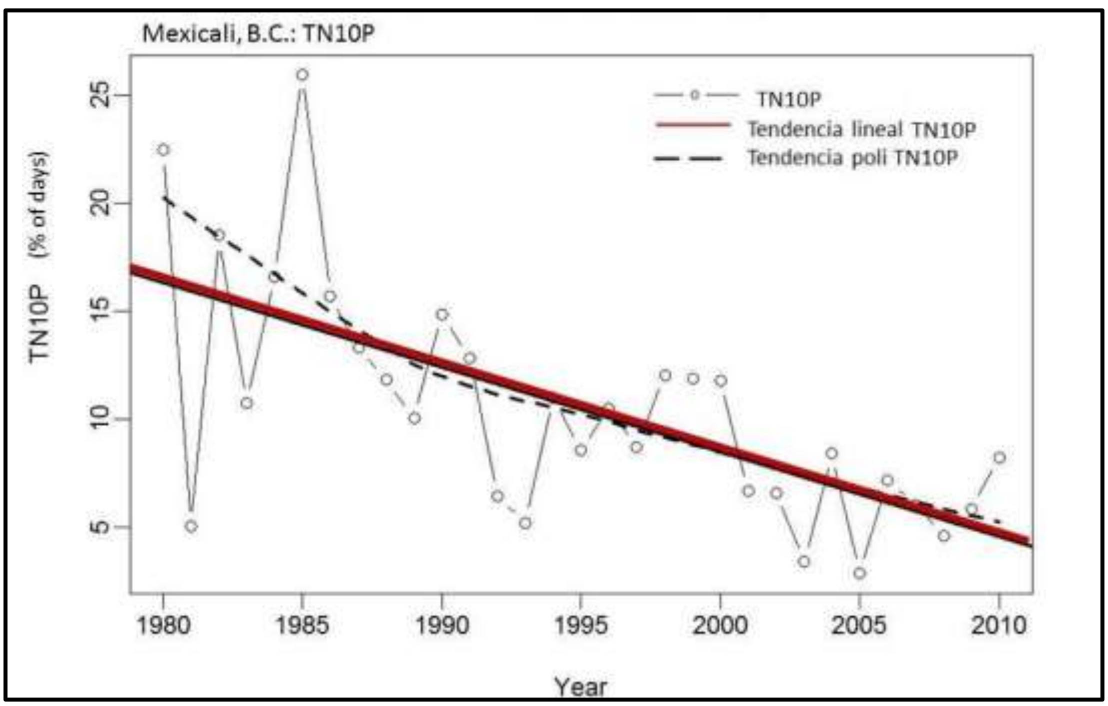

Figura 2.11 Tendencia de días con la temperatura mínima diaria menor al P10 en Mexicali, B.C. (1980-2010)

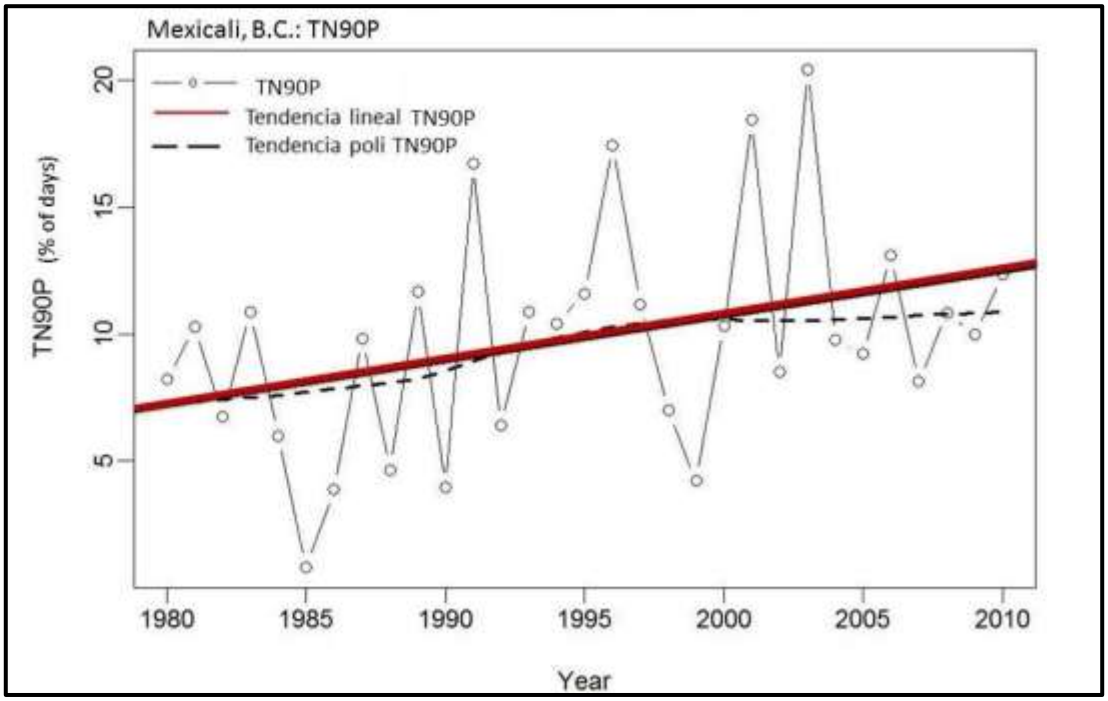

Figura 2.12 Tendencia de días con temperatura mínima superior al P90 Mexicali, B.C. (1980-2010)

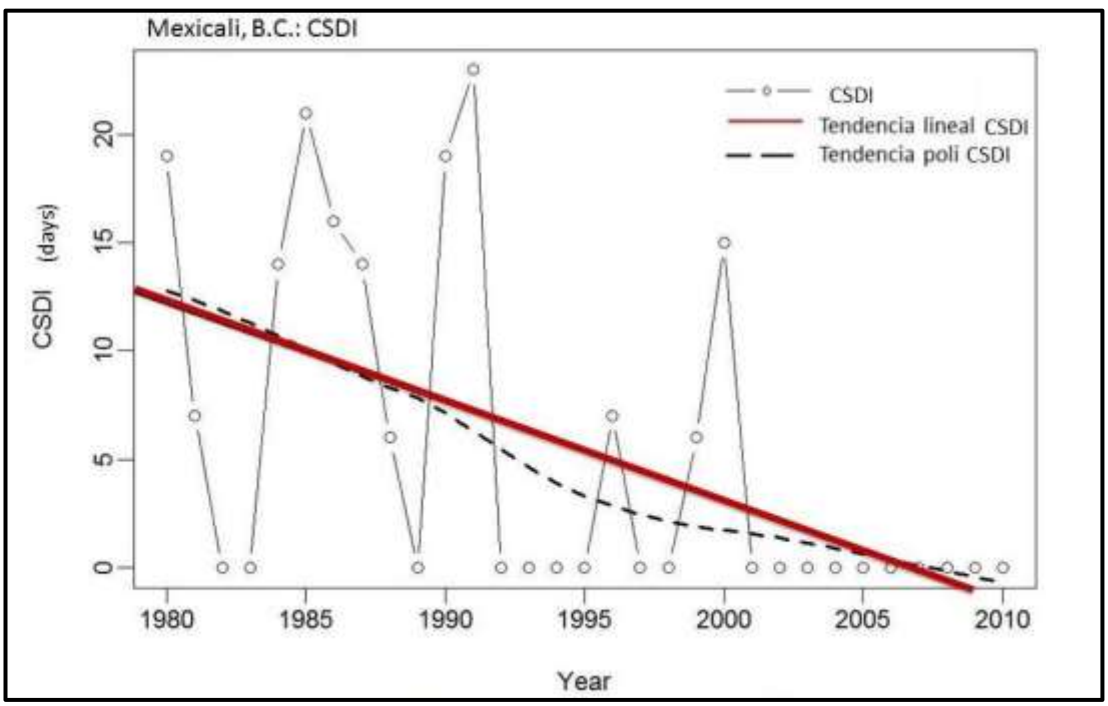

Figura 2.13 Número de días consecutivos (al menos 6 días) en que la temperatura mínima diaria < P10 en Mexicali, B.C. (1950-2010)

2.7.2 Estudio de Extremos Climáticos de Temperatura Máxima, Temperatura Mínima y Precipitación Pluvial para Mexicali, B.C.

2.7.2.1 Aplicación de la distribución GEV a valores máximos de Temperatura Máxima.

La información de valores máximos de temperaturas máximas, extraída de información diaria, fueron en total 62 datos, derivados de bloques máximos anuales de los años de 1950 al 2012. Previo a la aplicación de la función de Valores Extremos Generalizados (GEV, por sus siglas en inglés) se verificó que la serie de valores de temperatura máxima maximorum (TMAXmax) correspondiera a una serie estacionaria o no estacionaria, por la necesidad de insertar en el proceso de ajuste de la GEV una covariable adecuada que explique ese comportamiento, ya que esto se debe tomar en cuenta para la estimación de períodos de retorno. Tras analizar la tendencia de TMAXmax, resultó una *serie no estacionaria*. En estos casos, se obtiene un modelo ajustado por una GEV estacionaria, y posteriormente un segundo modelo con una GEV no estacionaria mediante la inclusión de la covariable que probablemente mejore el desempeño de la función de densidad propuesta. Como algunos valores de la GEV estacionaria se toman en cuenta para el cálculo de los períodos de retorno, se presentan algunos resultados útiles de este proceso.

La función de verosimilitud de la distribución GEV estacionaria para la temperatura máxima maximorum (TMAXmax), encontró que los valores para los estimadores, en °C, fueron (μ, σ, ξ)= (46.74, 1.37, -0.17), con errores estándar de 0.18, 0.12 y 0.06, respectivamente. Combinando los estimadores y errores estándar asociados, los intervalos de confianza al 95%, también en °C, son (46.56, 46.92) para μ, (1.25, 1.49) para σ, y (-0.23, -0.11) para ξ. Se observa que el valor del parámetro de forma (ξ) es negativo, por lo que se concluye que la distribución de Weibull ajusta bien a este conjunto de datos.

2.7.2.2 Incorporación de una covariable al modelo de TMAXmax en Mexicali, B.C.

Debido a la tendencia positiva de la TMAXmax se incorporó al modelo de distribución GEV. Las gráficas de diagnóstico para evaluar la precisión de la distribución GEV ajustada a la TMAXmax se muestran en la figura 2.14. Las gráficas de cuantiles de probabilidad (panel superior) muestran la validez del modelo ajustado: el conjunto de puntos sigue una conducta casi-lineal, a excepción de una ligera discrepancia en algunos valores más extremos. La correspondiente función de densidad es bastante consistente con la función empírica (panel inferior izquierdo). En el panel inferior derecho se muestran los niveles de retorno asociados con la variable respuesta TMAXmax que en este caso se refiere a la tendencia temporal incluida; obsérvese que de acuerdo a los niveles de retorno mostrados, la temperatura máxima va ligeramente en aumento de acuerdo al tiempo.

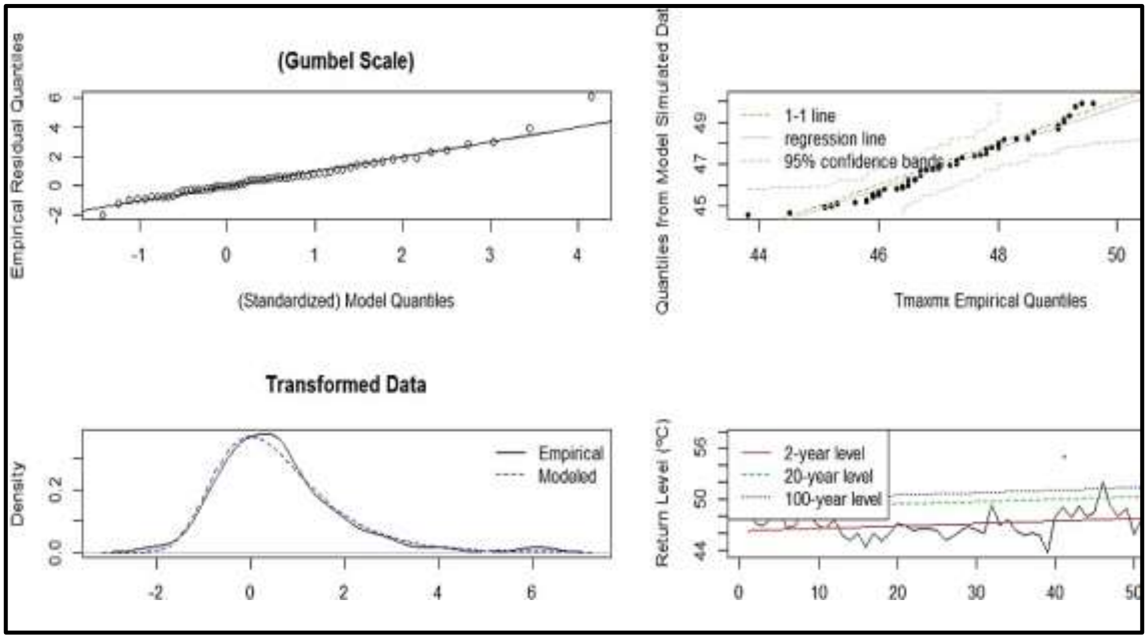

Figura 2.14 Gráficas de diagnóstico de la distribución GEV con la tendencia temporal como covariable para la TMAXmax de Mexicali, B.C., México. Los cuantiles y niveles de retorno están °C.

Como medida de la calidad relativa de los modelos, estacionario y no estacionario, se utilizó el criterio de Akaike y el criterio de Bayes, que mostraron que la incorporación de una covariable, en este caso el tiempo en años, mejoraba sustancialmente al modelo de ajuste propuesto inicialmente. Otra prueba estadística que se utilizó es la de prueba de razón de verosimilitud, cuyo valor de 7.36 es un valor más grande que el nivel crítico de $\chi^2_{1,1-0.05}$ que es de 3.84.

La inclusión de una tendencia lineal como covariable en el parámetro de ubicación (μ) de la distribución GEV, produjo una mejoría significativa (al nivel del 5%) al ajuste que sin la tendencia, por lo que se seleccionó este modelo para la estimación de la variabilidad de los períodos de retorno.

Específicamente, el modelo que se toma en cuenta es el siguiente:

$$\mu(t) = \mu_0 + \mu_1(t) = 46.74 + 0.028*(t) \qquad (3)$$

En la ecuación 3, μ_0 es el parámetro de ubicación (location = 46.74) de la distribución GEV estacionaria, mientras que μ_1 (mμ_1 = 0.028) es el parámetro estimado de la serie GEV no estacionaria, que se refiere a la inclusión como pendiente de la variable tiempo; en este caso t es el tiempo en años en los que se desea estimar el valor de μ(t), que indica que a nivel decadal se está experimentando un incremento de 0.28°C.

2.7.2.3 Estimación de Períodos de Retorno de $TMAX_{max}$ en Mexicali, B.C.

Aplicando la ecuación 3, si se desea, p.e., estimar el período de retorno de 5 años:

$$\mu(2017)= 46.74+ (0.028)*(2017-1950)= 48.61\ °C$$

Al valor anterior (48.61 °C) se le debe aplicar una corrección por ser una GEV no estacionaria. Se puede ver que conforme la variable t se incrementa, los valores del parámetro de ubicación también, indicando que los valores extremos de temperatura máxima, serán mayores conforme se incrementa el tiempo. La tabla 2.4 muestra los resultados finales de períodos de retorno con la corrección realizada a los niveles de retorno estimados con los intervalos de confianza al 95% de confiabilidad.

Tabla 2.4 Niveles estimados de retorno e intervalos de confianza al 95% para varios períodos de retorno, obtenidos con el modelo GEV no estacionario para la TMAXmax en Mexicali, B.C., México

Período de retorno (años)	Nivel de retorno (ºC)	Límite inferior (ºC)	Límite superior (ºC)
5	47.1	46.6	47.5
10	47.2	46.6	47.7
15	47.3	46.7	47.9
20	47.5	46.8	48.1
25	47.6	46.9	48.3
50	48.3	47.5	49.2
75	49.1	48.1	50.0
100	49.8	48.7	50.8

De acuerdo a los resultados encontrados con una tendencia lineal en el parámetro de ubicación (μ), se esperaría, p.e., que la $TMAX_{max}$ en Mexicali, B.C., México, en promedio con una probabilidad de 0.1 (período de retorno de 10 años) sea mayor de 47.2 ºC, y en el largo plazo, con una probabilidad de 0.01 (período de retorno de 100 años) el valor de $TMAX_{max}$ sea mayor a 49.8 ºC; los intervalos de confianza al 95%, en °C, para esos períodos de retorno son de 46.6 a 47.7 y de 48.7 a 50.8, respectivamente. En resumen, se observa que los valores de $TMAX_{max}$ en el futuro serán cada vez mayores, respecto a los valores actuales.

2.7.2.4 Aplicación de la distribución GEV a valores mínimos de Temperatura Mínima en Mexicali B.C.

La información de valores mínimos de temperaturas mínimas ($TMIN_{min}$), igual que para las temperaturas máximas, extraída de información diaria, fueron en total 62 datos, derivados de bloques mínimos anuales de los años de 1950 al 2012. Se verificó que la serie de valores de $TMIN_{min}$ correspondiera a una serie estacionaria o no estacionaria, con el propósito de insertar en el proceso de ajuste de la GEV una covariable adecuada que explicara ese comportamiento, ya que se debe tomar en cuenta para la estimación de períodos de retorno. En este caso, la $TMIN_{min}$ fue una *serie no estacionaria*. Como se ha mencionado, se obtiene primero un modelo ajustado por una GEV estacionaria, y posteriormente un segundo modelo con una GEV no estacionaria mediante la inclusión de la covariable que mejoraría el desempeño de la función de densidad propuesta. Ya que algunos valores de la GEV estacionaria se toman en cuenta para el cálculo de los períodos de retorno, se presentan algunos resultados útiles.

La función de verosimilitud de la distribución GEV estacionaria para la temperatura mínima minimorum ($TMIN_{min}$), encontró que los valores para los estimadores, en °C, fueron (μ, σ, ξ) = (-1.73, 2.91, -0,49), con errores estándar de 0.40, 0.32 y 0.10, respectivamente. Combinando los estimadores y errores estándar asociados, los intervalos de confianza al 95%, en el caso de la $TMIN_{min}$, son (-1.33, 2.13) para μ, (3.23, 2.59) para σ, y (-0.39, -0.59) para ξ. Se observa que el valor del parámetro de forma (ξ) es negativo, por lo que se concluye que la distribución de Weibull ajusta bien a este conjunto de datos. Esto significa que la $TMIN_{min}$ tiene un límite superior, por lo que hay valores finitos que no pueden ser excedidos.

2.7.2.5 Incorporación de una covariable al modelo de $TMIN_{min}$ en Mexicali, B.C.

Por la tendencia positiva de la $TMIN_{min}$ se decidió incorporarla al modelo de distribución GEV. Las gráficas de diagnóstico para evaluar la precisión de la distribución GEV ajustada a la $TMIN_{min}$ se muestran en la figura 2.15. Las gráficas y cuantiles de probabilidad muestran la validez del modelo ajustado: el conjunto de puntos sigue una conducta casi-lineal, aunque algunos de los valores más extremos discrepan, lo cual tiene explicación por la incertidumbre asociada. La correspondiente función de densidad es bastante consistente con la función empírica (panel inferior izquierdo). En el panel inferior derecho se muestran los niveles de retorno asociados con la $TMIN_{min}$, que en este caso se refiere a la tendencia temporal incluida; obsérvese que de acuerdo a los niveles de retorno mostrados, la temperatura mínima va siendo cada vez mayor de acuerdo al avance del índice anual.

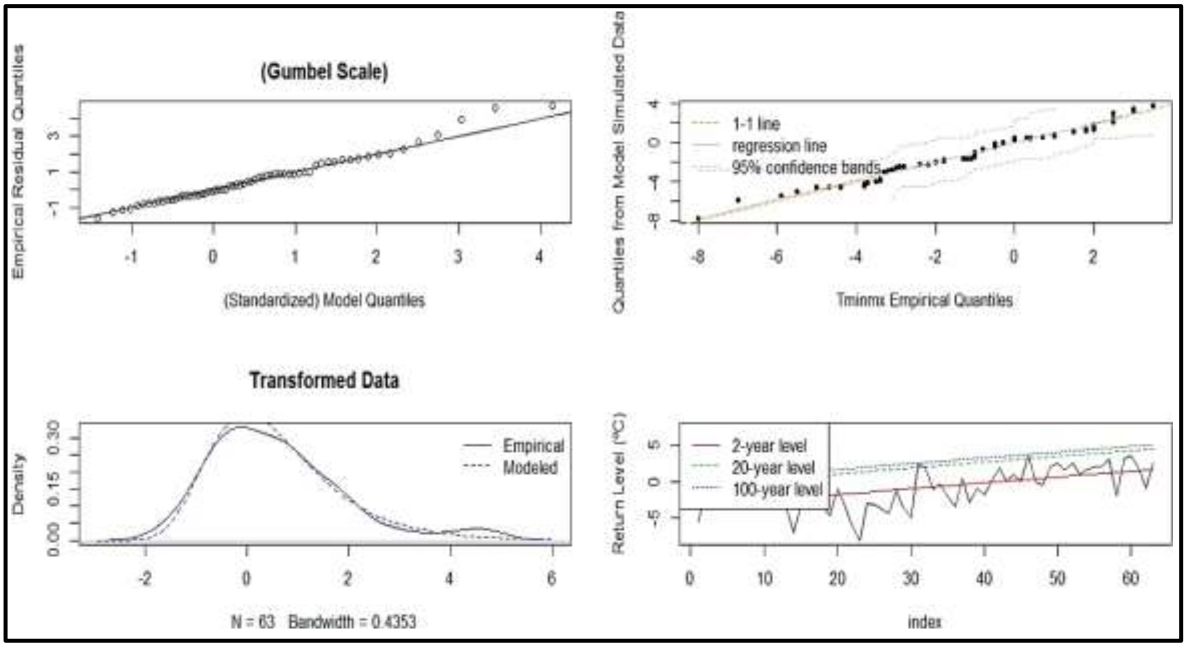

Figura 2.15 Gráficas de diagnóstico de la distribución GEV con la tendencia temporal como covariable para la TMINmin de Mexicali, B.C., México. Los cuantiles y niveles de retorno están °C.

Como medida de la calidad relativa de los modelos, estacionario y no estacionario, se utilizó el criterio de Akaike y el criterio de Bayes, los cuales mostraron que la incorporación de una covariable, en este caso el tiempo en años, mejoraba sustancialmente al modelo de ajuste propuesto inicialmente. Otra prueba estadística que se utilizó es la de prueba de razón de verosimilitud, cuyo valor de 31.40 es un valor mayor que el nivel crítico de $\chi^2_{1,1-0.05}$ que es de 3.84.

Por lo analizado, se concluye que la inclusión de la tendencia lineal como covariable en el parámetro de ubicación (μ) de la distribución GEV, produjo una mejoría significativa (al nivel del 5%) al ajuste que, sin la tendencia, por lo que se seleccionó el modelo GEV no estacionario para la estimación de los períodos de retorno.

El modelo que se toma en cuenta es el siguiente:

$$\mu(t) = \mu_0 + \mu_1(t) = -1.73 + 0.07*(t) \qquad (4)$$

En la expresión 4, μ_0 es el parámetro de ubicación (location = -1.73) de la distribución GEV estacionaria, μ_1 (mu1 = 0.07) es el parámetro estimado de la serie GEV no estacionaria, que se refiere a la pendiente del modelo GEV, y t es el tiempo en años en los que se desea estimar el valor de μ(t). A nivel decadal se estima un incremento de 0.7°C por el valor de la pendiente estimada.

2.7.2.6 Estimación de Períodos de Retorno de TMINmin en Mexicali, B.C., México

Con la aplicación de la ecuación 4, si queremos estimar el período de retorno de 5 años, se tiene lo siguiente:

$$\mu(2017) = -1.73 + (0.07)*(2017-1950) = 2.96\ °C$$

Al valor anterior (2.96 °C) se le debe aplicar una corrección por ser una GEV no estacionaria. Se puede ver que al incrementarse t, los valores del parámetro de ubicación también se incrementan, indicando que los valores extremos de temperatura mínima serán mayores conforme el tiempo avance. La tabla 2.5 muestra los resultados finales de períodos de retorno con la corrección realizada a los niveles de retorno estimados con los intervalos de confianza al 95% de confiabilidad.

Tabla 2.5 Niveles estimados de retorno e intervalos de confianza al 95% para varios períodos de retorno, obtenidos con el modelo GEV no estacionario para la TMINmin en Mexicali, B.C., México

Período de retorno (años)	Nivel de retorno (ºC)	Límite inferior (ºC)	Límite superior (ºC)
5	0.3	-0.4	0.9
10	0.7	0.1	1.2
15	1.1	0.5	1.6
20	1.5	0.9	2.0
25	1.8	1.3	2.4
50	3.8	3.2	4.5
75	5.8	5.1	6.5
100	7.8	7.0	8.6

De acuerdo a los resultados encontrados con una tendencia lineal en el parámetro de ubicación (μ), se esperaría, por ejemplo, que la TMINmin en Mexicali, B.C., México, en promedio con una probabilidad de 0.1 (período de retorno de 10 años) sea mayor a 0.7 ºC, y en el largo plazo, con una probabilidad de 0.01 (período de retorno de 100 años) el valor de TMINmin sea mayor a 7.8 ºC; los intervalos de confianza al 95%, en °C, para los períodos de retorno mencionados son de
01.4 a 1.2 y de 7.0 a 8.6, respectivamente. En resumen, se observa que los valores de TMINmin en el futuro serán cada vez más altos, respecto a los valores actuales.

2.7.2.7 Aplicación de la distribución GEV a valores máximos de Precipitación Pluvial en Mexicali, B.C.

Los datos extremos de precipitación pluvial de Mexicali, B.C., obtenidos de información diaria, fueron 62 datos, es decir 62 bloques de máximos anuales de los años de 1950 al 2012.La función de verosimilitud de la distribución GEV para la precipitación máxima maximorum ($PMAX_{max}$), debido a que no se encontró evidencia de tendencia, se realizó para una serie estacionaria.

La función de verosimilitud de la distribución GEV estacionaria para la $PMAX_{max}$, encontró que los valores para los estimadores de los parámetros fueron (μ, σ, ξ) = (15.06, 10.13, 0.14), con errores estándar de 1.49, 1.17 y 0.12, respectivamente. Combinando los estimadores y errores estándar asociados, los intervalos de confianza al 95%, en el caso de la $PMAX_{max}$, son (13.57, 16.55) para μ, (8.96, 11.30) para σ, y (0.02, 0.26) para ξ. En este caso se observa que el valor del parámetro de forma (ξ) es positivo, y su intervalo de confianza al 95% indica que la franja de valores puede ser positiva. Lo que se concluye es que la distribución de Fréchet ajusta a este conjunto de datos.

Las gráficas de diagnóstico resultante para evaluar la precisión de la distribución GEV ajustada a la $PMAX_{max}$ se muestran en la figura 2.16. La gráfica en la esquina superior izquierda muestra que los cuantiles empíricos contra los derivados de la función de densidad ajustada GEV, parecen agruparse razonablemente a lo largo de la línea recta y el modelo parece satisfacerse. La gráfica del panel superior derecho muestra la gráfica QQ para datos generados aleatoriamente de la función de densidad ajustada GEV contra los cuantiles empíricos de datos junto con bandas de confianza del 95%, una línea 1-1 y una línea de regresión ajustada; se puede observar como las bandas de confianza adquieren una forma cóncava. La gráfica de densidad en el panel inferior izquierdo muestra relativamente buena correspondencia entre la densidad empírica (línea sólida) y la función de densidad GEV ajustada (línea punteada). La gráfica del nivel de retorno (panel inferior derecho) muestra el aumento de los valores. Los niveles de retorno empíricos están situados sobre la banda de confianza del 95%.

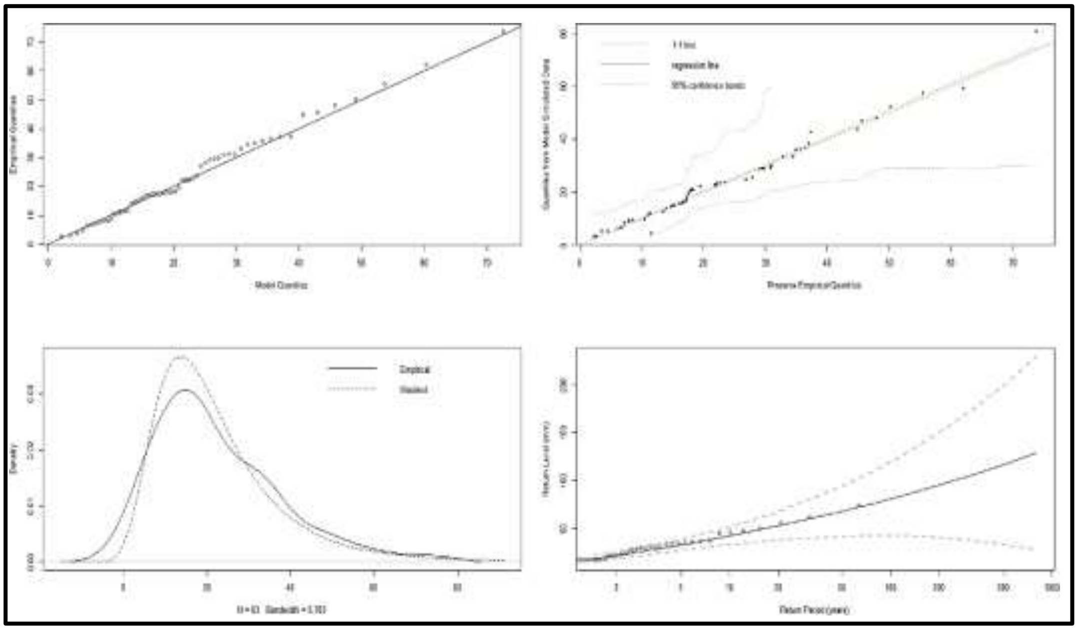

Figura 2.16 Gráficas de diagnóstico de la distribución GEV a la PMAXmax en Mexicali, B.C., México.Los cuantiles y niveles de retorno están en mm.

2.7.2.8 Estimación de Períodos de retorno de PMAX$_{max}$ en Mexicali, B.C.

Los períodos de retorno para la PMAX$_{max}$ se presentan a continuación. Esta gráfica se ha mostrado en el panel inferior derecho de la figura 2.16, junto con las bandas de confianza al 95%, estimada por el método delta. Este método, como se ha mencionado asume que los estimadores de los parámetros son simétricos, que no es siempre el caso para el parámetro de forma o períodos extremos de retorno. En el caso bajo análisis se optó, para la estimación de períodos de retorno, por el de bootstrap paramétrico. En la tabla 2.6 se muestran los períodos de retorno de 5 a 100 años, y los intervalos de confianza al 95%, con la distribución GEV para la PMAX$_{max}$.

Tabla 2.6 Niveles estimados de retorno e intervalos de confianza del 95% para varios períodos de retorno, obtenidos con el modelo GEV estacionario para la PMAXmax en Mexicali, B.C., México.

Período de retorno (años)	Nivel de retorno (mm)	Límite inferior (mm)	Límite superior (mm)
5	31.9	26.7	**37.7**
10	41.9	33.8	**51.4**
15	48.0	37.3	**61.6**
20	52.5	40.5	**67.4**
25	56.2	42.8	**73.5**
50	68.9	48.4	**101.0**
75	77.6	51.5	**118.4**
100	**82.9**	**52.6**	**128.1**

De acuerdo a los resultados de la tabla 7 se esperaría que la PMAXmax en Mexicali, B.C., México, en promedio, con una probabilidad de 0.1 (período de retorno de 10 años) excederá el valor de 41.9 mm, y en el largo plazo, con una probabilidad de 0.01 (período de retorno de 100 años) excederá el valor de 82.9 mm; los intervalos de confianza al 95%, en mm, para esos períodos de retorno son de 33.8 a 51.4, y de 52.6 a 128.1, respectivamente.

2.8 Conclusiones

Es importante resaltar que acuerdo a Gosling et al. (2011), México ha experimentado un calentamiento generalizado desde 1960. La frecuencia de días fríos ha disminuido y la de noches cálidas ha aumentado. También se ha producido un aumento generalizado de las temperaturas medias invernales en el país como consecuencia de las influencias humanas sobre el clima. Así, durante la estación invernal, los casos de temperaturas cálidas son más frecuentes, y los de temperaturas frías, menos. Así también, las tendencias significativas de las temperaturas máximas y mínimas extremas encontradas en muchas partes del mundo (Heim Jr. 2015; Easterling et al. 2016; Houngninou et al. 2017) refuerzan los resultados obtenidos en este trabajo.

La aplicación de una teoría de eventos extremos a la TXX y TNN en 16 estaciones climatológicas ubicadas en 12 zonas urbanas de México, en series de tiempo con diferentes periodos, mostró tendencias generales en el calentamiento urbano, especialmente nocturno. Sin embargo, los valores variaron de una ciudad a otra. Una señal de detección menos clara fue el calentamiento diurno. Aunque las causas de este comportamiento de tendencias heterogéneas para TXX y TNN pueden ser de origen puramente local y causadas por la dinámica de urbanización (cambio de uso de suelo, actividades antropogénicas), no se puede descartar que puedan ser causadas por algunos otros fenómenos climáticos de mayor escala. Por ejemplo, México podría estar expuesto a patrones de bloqueo, o modos de variabilidad climática, como El Niño Oscilación del Sur, la Oscilación Decadal del Pacífico, la Oscilación del Atlántico Norte, o la Oscilación Madden-Julian, entre otros. Estos podrían ser factores causales que contribuyan a las tendencias térmicas ya que en otras regiones del mundo han influido significativamente en el comportamiento de las temperaturas extremas. (Arblaster y Alexander 2012; Parker et al. 2014; Matsueda y Takaya 2015; Burgess y Klingaman 2015). Todos estos factores se consideran importantes para una posible atribución pero no son objeto de este estudio.

Las ciudades seguirán siendo los espacios geográficos más vulnerables, sobre todo en países en desarrollo como México, ya que suelen concentrar grandes poblaciones sin infraestructura adecuada. Así, el conocimiento de las regiones donde el clima es inestable (cambiante), y el saber que los eventos climáticos extremos no son controlables, servirá para generar algunas posibles estrategias de adaptación urbana para enfrentar las temperaturas extremas actuales y futuras. Por ejemplo, dichas temperaturas pueden abordarse rediseñando el espacio urbano, haciéndolo seguro, ecológico y aceptable, para reducir la vulnerabilidad y reforzar la seguridad hídrica urbana. Cada ciudad es un caso de análisis, y que un esquema adecuado de planeación urbana sustentable sólo puede lograrse mediante la participación de autoridades gubernamentales, sectores productivos, sector académico y actores locales.

En este estudio se modelaron las TXX y TNN registradas en 16 estaciones climatológicas correspondientes a 12 ciudades de México, para periodos que variaron de acuerdo con las series de datos disponibles. Mediante la aplicación de la prueba no paramétrica de Mann-Kendall y el método de Sen, se detectó una tendencia al calentamiento urbano, pero no se encontró un comportamiento homogéneo en todas las ciudades analizadas. Una observación importante fue la prevalencia significativa de series no estacionarias con la TXX en la mitad de las ciudades analizadas. En el centro-occidente del país, se presentó una tendencia negativa significativa, quizá debido al efecto de "oscurecimiento" por incrementos en la contaminación por aerosoles. Por lo tanto, las tendencias anuales del calentamiento diurno, representadas por el TXX, no son similares en todas las zonas urbanas seleccionadas de México. En el caso del TNN, relacionado con el calentamiento nocturno, el comportamiento fue más uniforme. Específicamente, 90% de las ciudades son no estacionarias con una tendencia positiva significativa, y sólo dos áreas presentaron una serie estacionaria. Con el ajuste de la distribución GEV no estacionaria al conjunto de datos e incorporando la tendencia del parámetro de localización, se estimaron las tendencias de los niveles de retorno de 10, 20, 50 y 100 años, manteniendo constantes los parámetros de forma y escala. Los resultados son muy similares a los de los métodos no paramétricos de detección de tendencias, tanto para TXX como para TNN. Esto confirma el comportamiento no estacionario de la mitad de las estaciones para TXX, y del 90% de las estaciones para TNN. Los periodos de retorno de los extremos térmicos estimados en un clima cambiante para muchas de las ciudades analizadas en este estudio varían significativamente, y la regularidad con la que se producen las temperaturas extremas es cada vez mayor. Por ello, la modelización estadística debe considerar este comportamiento, debido a su importancia para la evaluación de riesgos para la salud humana, la flora y la fauna, y las infraestructuras urbanas. El modelo GEV no estacionario propuesto ha proporcionado nueva e importante información relativa a los cambios en las temperaturas extremas, y mediante la estimación de los periodos de retorno, ha proporcionado su probabilidad de recurrencia. Algunos modos principales de variabilidad climática como mecanismos causales de atribución de temperaturas extremas no han sido estudiados, por lo que es una tarea pendiente.

3 Implementación del pronóstico computacional y la simulación de eventos de invierno (artículo 2)

3.1 Introducción

Los sistemas fotovoltaicos (SFV) aprovechan la irradiación solar global (GHI) y la convierten directamente a energía eléctrica a partir de la implementación de materiales semiconductores; la constante búsqueda por disminuir las emisiones de gases de efecto invernadero a nivel global, han favorecido el crecimiento de plantas solares y redes eléctricas mixtas que implementan tecnología que aprovecha diversas fuentes renovables. Se prevé que los SFV se conviertan progresivamente en tecnologías accesibles y costeables para cualquier usuario, continúen su expansión a gran escala por diferentes regiones geográficas y su investigación y desarrollo permanezcan vigentes en años futuros. Uno de los problemas operativos más importante que enfrenta la generación de energía solar, radica en la incertidumbre que la intermitencia y la variabilidad natural del recurso pueden generar. La predicción meteorológica, considera dos escalas temporales importantes para diferenciar la variabilidad que afecta a la predicción del recurso solar: **1**) la predicción a mediano plazo, la cual se ve influenciada principalmente por patrones meteorológicos de larga duración en la atmósfera, que pueden comprender periodos mayores a 120 horas, o corresponder a oscilaciones climáticas que regulan las condiciones meteorológicas de una región por largos periodos (ciclos anuales o mayores); otra escala de interés, y sobre la cual se enfoca el análisis de este trabajo, comprende una menor cobertura temporal y espacial, y se conoce como **2**) la predicción a corto plazo, la cual engloba las variaciones relacionadas a fenómenos meteorológicos de corta duración que pueden ir desde pocos minutos hasta días (aprox. 72 horas) y que su cobertura espacial comprende desde los 0.01 km – 100 km. Las variaciones que producen los fenómenos meteorológicos como, tormentas, tornados y frentes, se desarrollan dentro de los horizontes espaciales y temporales que un pronóstico meteorológico a corto plazo es capaz de prever (Figura.3.1). Los modelos climáticos son una herramienta fundamental en la investigación de variaciones atmosféricas a largo plazo, son capaces de representar patrones generales de temperatura, humedad y precipitación sobre una región extensa, sin embargo, su baja resolución dificulta el análisis de escalas espaciales menores a 100 km. Dentro de los métodos de predicción que son capaces de captar la variabilidad local, se encuentran los modelos estadísticos y los modelos numéricos computacionales de predicción meteorológica (NWP). Los modelos estadísticos requieren de una robusta base de datos climáticos y meteorológicos del sitio, a partir del cual se establecen relaciones estadísticas significativas para la predicción de las variables atmosféricas (Pirovano et al., 2014); los NWP pueden prescindir de información medida *in situ*, y optar por datos iniciales disponibles a partir de diversos modelos globales, datos satelitales e información de reanálisis, también permiten configurar dominios de alta resolución para una región específica, y cuentan con la opción de seleccionar distintas parametrizaciones físicas de los procesos atmosféricos, con fines de experimentación a pequeñas escalas.

En teoría, se espera que una adecuada predicción de la variable GHI obtenida del NWP, permitirá al usuario realizar una confiable estimación de la producción de energía a corto plazo basado en la capacidad instalada y las características de la tecnología del SFV, no obstante, los NWP cometen errores de predicción que deben ser analizados y evaluados, con el fin de proponer nuevas configuraciones que contribuyan a minimizarlos. El ajuste adecuado de las parametrizaciones y la caracterización de procesos atmosféricos del sitio de estudio, es un proceso clave para reducir la incertidumbre de las predicciones.

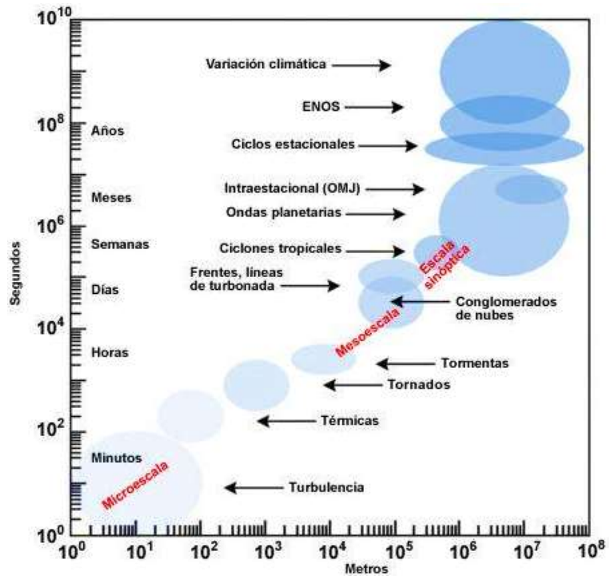

Figura 3.1 Diagrama de escalas meteorológicas con referencia a escalas espaciales y temporales de algunos fenómenos atmosféricos. (AEMET, 2018)

El objetivo del presente trabajo fue evaluar el desempeño del modelo meteorológico computacional WRF, mediante la simulación de un evento meteorológico de mesoescala en la región desértica del noroeste de México, para el periodo de invierno del 2017; el evento de interés fue elegido por haber generado a su paso sobre el sitio de estudio, cambios abruptos en la GHI y las variables de temperatura ambiente (Tamb) y humedad relativa (Hrel), así como haber favorecido nublados a diferentes alturas. Cada experimento fue ejecutado en el modelo WRF bajo 4 configuraciones distintas de parametrizaciones de radiación solar y los resultados obtenidos se compararon con las mediciones en superficie de estaciones meteorológicas automáticas y piranómetros solares. La comparación estadística de los valores pronosticados por el modelo y las mediciones en superficie, mostraron las configuraciones del modelo y los esquemas de parametrización solar que lograron estimar las variables de GHI, Tamb y Hrel con menores errores durante el paso del evento.

3.1.1 El modelo numérico computacional WRF

WRF es un modelo NWP y un sistema de simulación atmosférica diseñado para investigación y aplicaciones operacionales (Skamarock et al., 2008); representa el estado de la atmósfera en una malla tridimensional en términos de variables fundamentales, es considerado un modelo tipo no-hidrostático que resuelve las ecuaciones primitivas que controlan la circulación atmosférica, permite pronosticar variables meteorológicas con una alta resolución a partir de una condición inicial y una de frontera. Dentro del modelo existe la posibilidad de configurar parámetros que influyen en procesos atmosféricos físicos relacionados a la radiación, convección, microfísica de nubes, etc. Dichos procesos tienen lugar principalmente a niveles bajos de la atmósfera y son representados mediante módulos denominados parametrizaciones físicas, que consisten en algoritmos que calculan el efecto del fenómeno de manera indirecta a partir de las variables que el modelo si es capaz de resolver, y una vez resuelto, el efecto o tendencia se aplica a subyacentes campos del modelo (García-Diez, 2013).

3.2 Parametrizaciones de radiación solar

Las principales variaciones que afectan a la radiación solar a su paso por la atmósfera, se deben en su mayoría a los procesos de dispersión por nubosidad, sin embargo, la dispersión por aerosoles y la humedad, también juegan papel importante. Muchos modelos NWP, han minimizado las afectaciones debido a la dispersión por aerosoles, y se han limitado al uso de datos climáticos para sustituir la carencia de métodos de medición para obtener estos valores en el área modelada. Esta simplificación ha llevado a que los modelos cometan errores de hasta el 20% en sus predicciones (Ruiz-Arias et al. 2013). Actualmente, más modelos incluyen avanzados esquemas de parametrización de radiación solar. Muchos están basados en la solución de la teoría de transferencia radiativa para 2 y 4 corrientes en 14 bandas espectrales. Un ejemplo es el esquema RRTMG (Iacono et al., 2008) y su antecesor RRTM (Clough et al., 2005); estos esquemas conjuntan la necesidad de los modelos globales y regionales en la predicción solar. RRTMG se enfoca en la representación de variaciones debido al vapor de agua, dióxido de carbono, nitrógeno, aerosoles, dispersión de Raleigh y nubosidad. RRTMG y RRTM guardan gran similitud, pero su mayor diferencia radica en sus múltiples cálculos de dispersión y las parametrizaciones de nubosidad a subescalas. Bajo condiciones de cielos despejados, se puede esperar que RRTMG cometa un error de predicción cercano al 0.3% con respecto de RRTM (Iacono et al., 2008). Otro esquema importante es Goddard, desarrollado por la NASA en el Goddard Space Flight Center (Chou y Suarez, 1999) para su aplicación a modelos climáticos. Con similitud al esquema Goddard, Fu-Liou-Gu (FLG) (Gu et al., 2011), calcula el flujo a partir del método delta de 4 y 2 corrientes para 6 bandas espectrales; menos que cualquier otro esquema anterior. El modelo WRF cuenta con más de 10 esquemas en radiación de onda corta (SW) y larga (LW). Los cuatro esquemas de parametrización mencionados anteriormente, corresponden a la metodología utilizada por Incecik et al., en el 2019 para Turquía, y de acuerdo a su estudio, se consideran las opciones más relevantes por sus distintos algoritmos de cálculos de flujos, representaciones de numero de bandas espectrales y simulación de diversas fuentes de dispersión (gases y aerosoles); estas parametrizaciones destacan también por su exploración en estudios previos y su vigencia en el modelo.

3.3 Eventos meteorológicos en la zona de estudio

Mexicali, B.C., es una ciudad fronteriza localizada al extremo noroeste de México, colinda al norte con el estado de California y al noreste con Arizona y Sonora. Durante verano, promedia una temperatura máxima de 42 °C y máximas extremas de 45 °C; en invierno, durante los meses de diciembre a febrero, se pueden registrar temperaturas mínimas promedio de 9 °C y mínimas extremas de 2.5 °C (Urias et al., 2021). Es posible alcanzar una GHI máxima de 1200 W/m^2 en verano y 600 W/m^2 algunos días de invierno. Uno de los principales eventos meteorológicos que afectan a la región desértica del noroeste del país durante el invierno y generan intermitencia a corto plazo en la GHI, son los frentes fríos (FF). Cuando dos masas de aire, una fría y otra cálida, chocan entre sí, la masa de aire frío desplaza a la de aire cálido y la superficie que separa una de otra se denomina “frente frío” (Lazaridis, 2011). El desplazamiento de un FF, genera intensos desplazamientos verticales en la atmósfera, el aire forzado a ascender es enfriado adiabáticamente y como el ascenso del aire cálido es rápido y abrupto, no sólo hay formación de nubes bajas y medias sino también de grandes nubes de desarrollo convectivo, asociadas a tormentas, niebla o intensa lluvia, en periodos cortos. Los FF que se registran en el país, tienen origen cerca del polo norte, cruzan parte de la costa oeste de los E.U.A. y llegan al norte de México. Son por lo regular sistemas con duración de tres a siete días, usualmente generan lluvia moderada, favorecen la disminución de las temperaturas y el aumento de las velocidades del viento, su influencia también favorece la formación de nublados parciales, lo cual genera una gran variabilidad de la GHI que llega a superficie. Su ocurrencia va de septiembre a mayo y la mayoría acontece en temporada invernal. Por cumplir con las características de duración y variabilidad que genera la influencia de un caso típico de invierno en la región, se seleccionó como caso de estudio un evento frontal que afectó a la zona noroeste de México durante enero del 2017; periodo del cual se cuenta con registros de información meteorológica medida en superficie.

3.4 Metodología

3.4.1 Datos iniciales y observaciones

Para las condiciones iniciales del modelo WRF se utilizaron los datos de Análisis Global Operacional Final (FNL, por sus siglas en inglés) del Centro Nacional de Predicción y Medio Ambiente (NCEP, por sus siglas en inglés), tienen una resolución espacial de 1°x

1° y una resolución temporal de 6 horas, 26 niveles en la vertical y una cobertura global. Con la finalidad de realizar una comparación visual y estadística de las salidas obtenidas del modelo WRF, se utilizaron datos observados en superficie por estaciones meteorológicas automáticas modelo Davis Vantage Pro2 y un piranómetro Kipp&Zonnen CMP-10, instalados en el Instituto de Ingeniería UABC-Mexicali. Para contrastar los resultados de las simulaciones, también fueron recabados los datos horarios correspondientes en la base de información climática POWER de NASA y se añadió una comparación de control con los datos del “Pronóstico de persistencia”, el cual consiste en mantener los mismos valores medidos en un día, para las próximas 24 horas, es decir, prescindir de una predicción y esperar que las condiciones del día anterior se repitan.

3.4.2 Dominios y configuración del experimento

Se utilizaron tres dominios, un dominio madre (D01) y dos anidados o interiores (D02 y D03), como se detalla la figura 3.2. En estos dominios se mantuvo una relación en la resolución de 3:1, con la resolución mayor en el D03, centrada en el sitio de estudio. Los dominios fueron dimensionados de esta manera para poder captar la ocurrencia y el progresivo desplazamiento de los fenómenos de mesoescala que se desarrollan cerca de la costa al noroeste e ingresan por el oeste de la región.

El experimento comprendió un periodo de simulación de 120 horas (FF0:17/01/2017-21/01/2017). Las simulaciones se realizaron con el modelo WRF versión 4.3 (Skamarock et al., 2008) y se aplicaron 4 opciones distintas de configuración (Tabla 3.1). El enfoque de este trabajo hacia la mejora de la predicción de GHI, propuso variar principalmente las parametrizaciones de radiación en cuatro combinaciones de SW y LW, mientras que el resto de las parametrizaciones como Microfísica, Superficie y Cumulus sólo sufrieron cambios necesarios debido a la compatibilidad de las opciones entre sí. Los resultados fueron extraídos del dominio de mayor resolución (D03), de acuerdo a las coordenadas de la estación meteorológica de donde se obtuvieron las mediciones.

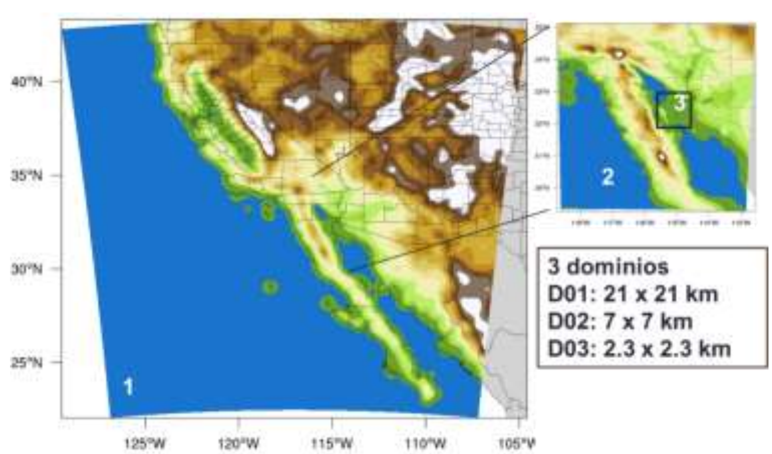

Figura 3.2 Dominios de las simulaciones del área de estudio. (Elaboración propia)

Tabla 3.1 Opciones de configuración utilizadas en las simulaciones del FF0.

Parametrización	op0	op1	op2	op3
Radiación SW/LW	*RRTMG/RRTM*	*FLG/FLG*	*Dudiah/RRTM*	*N Godard/N Godard*
Microfísica	WSM6	Thompson	WRF single	Godard ICE
Superficie	Monin Obukhov	Monin Obukhov	Monin Obukhov	Monin Obukhov
Cumulus	Kain Firtsch	Kain Firtsch	Kain Firtsch	Kain Firtsch

Para la evaluación de los resultados, se calcularon los errores estadísticos entre los datos simulados y los medidos de GHI, Tamb y Hrel, se utilizaron el Error Absoluto Medio (Mean Absolute Error, MAE), que representa la medida de la cercanía entre los valores medidos y estimados en términos de valor absoluto (Ec. 5), y el Porcentaje de Sesgo (Pbias%), que representa una medida de la tendencia media de los valores simulados a ser mayores o menores que los observados (Ec.6). También se utilizaron diagramas de Taylor; estos muestran un resumen estadístico de cómo los resultados de un modelo, coinciden en términos de dispersión (desviación estándar) y correlación (coeficiente de correlación de Pearson) entre sí. El diagrama compara entre valores modelados y observados. Los valores de referencia normalizados para GHI, Tamb y Hrel, corresponden a los valores medidos y se ubican en la parte central inferior del diagrama.

(5)

$$MAE = \sum_{i=1}^{N} \frac{|Xestimada - Xobservada|}{N}$$

(6)

$$Pbias\% = 100 * \frac{\sum_{i=1}^{N}(Xestimada - Xobservada)}{\sum_{i=1}^{N}(Xobservada)}$$

3.5 Discusión de resultados

Los principales resultados en términos de la comparación de los errores de predicción, se discutieron mediante los estadísticos MAE y Pbias% (Tabla 3.2). Los valores de MAE menores en la Tamb fueron simulados en la opt2 con un valor de 1.2 °C, similar al valor mostrado por el pronóstico de persistencia; la opt0 y los valores de NASA, fueron las opciones que presentaron un mayor error. Respecto a los valores simulados de Hrel, las opciones del modelo obtuvieron mejores resultados por encima de NASA y el pronóstico de persistencia, con apenas un delta de variación del MAE de 1.3% entre estas. Finalmente, la GHI mostró los valores menores de MAE en la Opt2 (32.2 W/m^2) y NASA (21.5 W/m^2). A diferencia del MAE, los valores del Pbias% pueden ser comparados entre variables distintas mediante un porcentaje que indica la sobreestimación o subestimación de los valores, sin embargo, es necesario considerar la magnitud de las variaciones diarias y el comportamiento nocturno de la GHI. Los valores de Pbias% muestra que los porcentajes menores correspondieron al pronóstico de persistencia (-1.2%), seguido por NASA (4.3%). De las opciones de configuración propuestas, la opt2 mostró los valores más favorables de Pbias% con un 14.6% en GHI, mientras que la opt1 obtuvo el mayor porcentaje de sesgo con 32.3%. También en la opt2, las variables Tamb y Hrel tuvieron una buena estimación con valores bajos de 1.6% y -2.9% respectivamente. Por último, es importante destacar que los datos NASA cometieron los mayores errores en ambos estadísticos para Tamb y Hrel.

Tabla 3.2 Resultados del MAE y Pbias% para cada opción de configuración de la simulación del FF0 comparadas con los datos medidos.

	Persistencia	opt0	opt1	opt2	opt3	NASA
			MAE			
T ambiente °C	1.2	1.7	1.4	1.2	1.3	2.4
H relativa %	13.9	11.4	12.3	11.7	11.0	15.8
GHI W/m^2	53.0	45.1	45.4	32.2	46.2	21.5
			Pbias %			
T ambiente °C	-0.7	10.0	7.3	1.6	6.1	-11.9
H relativa %	0.4	-13.8	-11.5	-2.9	-11.7	26.2
GHI W/m^2	-1.2	24.4	32.3	14.6	24.1	4.3

Los resultados de los valores simulados por las opciones de configuración, también fueron calificados gráficamente en términos de los valores del coeficiente de correlación de Pearson y la desviación estándar con un diagrama de Taylor (Figura 3.3); una de las predicciones con mayor similitud a los datos medidos, fue NASA en la variable GHI, seguido muy cerca por la configuración opt2; el resto de las opciones de la misma variable, se ubican muy cerca entre sí con valores que rondan una correlación de 0.92-0.94. La variable Tamb, rondó los valores de correlación 0.85-0.89 en las opciones de configuración, mientras que la NASA mostró el valor más bajo con 0.82. Finalmente, es posible observar que las predicciones de Hrel tienen los valores más bajos de correlación y más alejados de los valores de referencia.

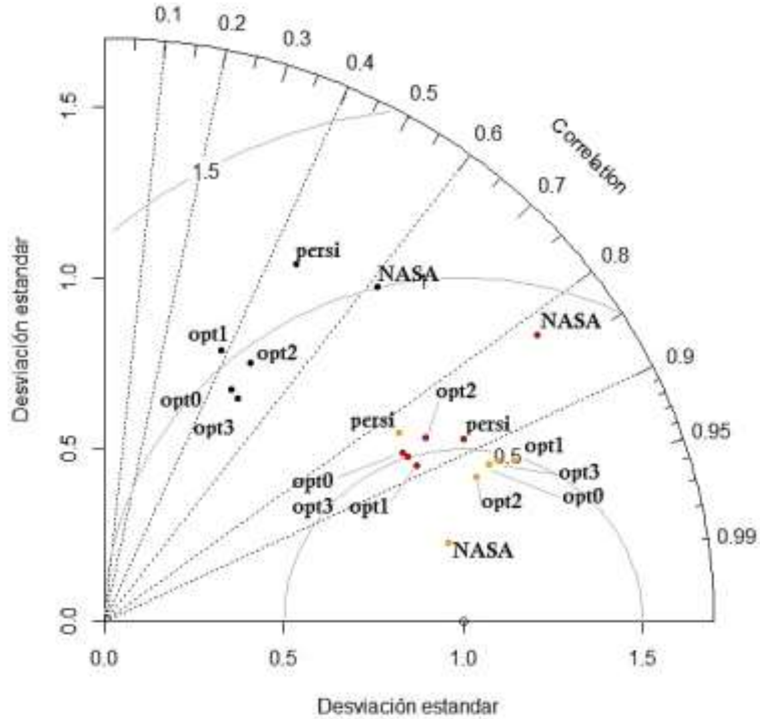

Figura 3.3 Diagrama de Taylor de los resultados de GHI (amarillo), Tamb (rojo) y Hrel (negro) para cada configuración, datos medidos de NASA y el pronóstico de persistencia (persi).

3.6 Conclusiones

Las predicciones de las variables GHI, Tamb y Hrel realizadas por el modelo WRF bajo 4 opciones de parametrización, mostraron en su evaluación, que son capaces de simular el comportamiento de las condiciones atmosféricas ante el paso de un sistema de invierno de mesoescala. En este trabajo, el objetivo principal se centró en mejorar las predicciones de GHI, sin embargo, se analizaron las variables de Tamb y Hrel por ser consideradas de gran variabilidad durante eventos de invierno, además de la búsqueda de una posible correlación entre la mejora de la predicción de estas con respecto a la GHI. Las predicciones que obtuvieron los errores menores, fueron las de la variable Tamb; de igual manera se reflejó una sobreestimación en los valores del Pbias%. Las predicciones de Hrel, mostraron valores diversos en los errores, sin embargo, no rebasaron el 13% de sobreestimación en los casos menos favorables. Que la variable Hrel haya respondido con valores bajos de correlación y un porcentaje de error relativamente alto, podría obedecer al comportamiento y la variabilidad natural de las mediciones en sitio, un ejemplo es la humedad relativa, pues registra cambios rápidos durante la llegada de una masa de aire frío y húmedo. Se puede concluir para la Hrel que el modelo no logró simular la magnitud de esta a lo largo de todo el periodo, sin embargo, si fue capaz de simular la variabilidad que produjo la influencia del sistema frontal.

Las simulaciones de GHI, destacaron por su favorable representación en la variabilidad y magnitud del evento. Fue durante los periodos de ingreso del sistema frontal sobre la región, cuando el modelo cometió algunos errores de sobreestimación y falta de sensibilidad a la rápida variabilidad generada por la nubosidad y humedad. Los datos NASA, destacaron como una herramienta potencial para ajustar los valores de las mediciones satelitales a futuros eventos frontales, pues como pronóstico a futuro, no son una herramienta con acceso a información actualizada en tiempo real.

La comparación del pronóstico de persistencia y las predicciones generadas, denotaron la capacidad del modelo y sus configuraciones, para mejorar la predicción del evento simulado; sin embargo, en el caso de la GHI, el análisis de resultados no demostró de manera clara el desempeño de las predicciones, debido a que en la evaluación estadística fueron considerados los periodos nocturnos de GHI=0 W/m^2, y que los periodos de variabilidad debido a nublados intermitentes representaron menos del 20% del total del periodo, por lo que en futuros ejercicios de simulación, se propone que esta variable sea evaluada excluyendo los periodos nocturnos. De manera generalizada y basado en la observación de los diagramas de Taylor y los estadísticos de error, se puede concluir que la configuración del modelo correspondiente a la opt2, tuvo el mejor desempeño en la predicción de la variabilidad de un sistema frontal en la región desértica. Este análisis brinda una configuración del modelo WRF que puede ser utilizada como una herramienta de predicción meteorológica operativa a corto plazo para sistemas fotovoltaicos y redes mixtas, ante la influencia de sistemas invernales en regiones desérticas. En investigaciones futuras, se propone que la configuración opt2 sea probada bajo distintas opciones de parametrizaciones de capa límite planetaria, se evalúe su desempeño en otras regiones climáticas similares y se incremente la muestra de eventos meteorológicos simulados.

Bibliografía

- Alexander LV, Zhang X, Peterson TC, Caesar J, Gleason B et al. 2006. Global observed changes in daily climate extremes of temperature and precipitation. Journal of Geophysical Resources 111: D05109. https://doi.org/10.1029/2005JD006290
- Almazroui M, Islam MN, Dambul R, Jones PD. 2014. Trends of temperature extremes in Saudi Arabia. *International Journal of Climatology* 34: 808-826. https://doi.org/10.1002/joc.3722
- Antonanzas, J., Osorio, N., Escobar, R., Urraca, R., Martinez-de-Pison, F. J., & Antonanzas-Torres, F. (2016). Review of photovoltaic power forecasting. *Solar Energy*, *136*, 78-111.
- Arblaster JM, Alexander LV. 2012. The impact of the El Nino-Southern Oscillation on maximum temperature extremes. *Geophysical Resource Letters* 39 (L20702). https://doi.org/10.1029/2012GL053409
- Beniston M, Stephenson DB, Christensen OB, Ferro AT, Frei Ch, Goyette S, Halsnaes K, Holt T, Jylhä K, Koffi B, Palutikof J, Schöll R, Semmler T, Woth K. 2007. Future extreme events in European climate: an exploration of regional climate model projections. *Climatic Change* 81 (Supl 1):71–95. https://doi.org/10.1007/s10584-006-9226-z
- Boucefiane A, Meddy M. 2019. Regional growth curves and extreme precipitation events estimation in the steppe area of northwestern Algeria. *Atmósfera* 32(4): 287-303. DOI: 10.20937/ATM.2019.32.04.03
- Brown SJ, Caesar J, Ferro CAT. 2008. Global changes in extreme daily temperature since 1950. Journal of Geophysical Research: *Atmosphere* 113(5): D05115.
- Burgess ML, Klingaman NP. 2015. Atmospheric circulation patterns associated with extreme cold winters in the UK. *Weather* 70(7):211-217.
- Burgman M, Franklin J, Keith RK, Hosack RG, Peters WG, Sisson AS. 2012. Modeling extreme risks in ecology. *Risk Analysis* 32(11): 1956-1966. DOI: 10.1111/j.1539-6924.2012.01871.x
- Burn DH, Hag Elnur AM. 2002. Detection of hydrological trends and variability. Journal of Hydrology 255:107–122. https://doi.org/10.1016/S0022-1694(01)00514-5
- Caesar J, Alexander LV, Trewin B, Tse-ring K, Sorany L, Vuniyayawa V, Keosavang N, Shimana A, Htay MM, Karmacharya J, Jayasinghearachchi DA, Sakkamart J, Soares E, Hung LT, Thuong LT, Hue CT, Dung NTT, Hung PV, Cuong HD, Cuong NM, Sirabaha S. 2011. Changes in temperature and precipitation extremes over the indo-Pacific region from 1971 to 2005. International Journal of Climatology 31:791–801. https://doi.org/10.1002/joc.2118
- Caloiero T. 2017. Trend of monthly temperature and daily extreme temperature during 1951–2012 in New Zealand. *Theoretical Applied of Climatology* 129:111–127. DOI: 10.1007/s00704-016-1764-3
- Cavazos T and Rivas D. 2004. Variability of extreme precipitation events in Tijuana, México. *Climate Research* 25: 229-243. DOI: 10.3354/cr025229
- Cavazos T, Salinas JA, Martínez B, Colorado G, De Grau P, Prieto Gonzalez R, Bravo ME. 2013. Actualización de escenarios de cambio climático para México como parte de los productos de la quinta comunicación nacional. Informe final. CICESE, IMTA, CCA UNAM. 150 pp.
- Chen W, Chen C, Li L, Xing L, Huang G, Wu C. 2015. Spatio-temporal analysis of extreme hourly precipitation patterns in Hainan Island, South China. *Water* **7**(5):2239–2253.
- Chen YR and Chu P-S. 2014. Trends in precipitation extremes and return levels in the Hawaiian Islands under a changing climate. *International Journal of Climatology* 34:3913-3925. DOI: 10.1002/joc.3950

- Chowdhury, S. P. & Crossley, P. (2009). Microgrids and Active Distribution Networks (Energy Engineering). *Published by The Institution of Engineering and Technology,(June 24, 2009)*.
- CIDOC, SHF. 2011. Current housing situation in Mexico 2011. Gobierno Federal, SHCP,-SEDESOL, México City.
- Coles S. 2001. *An Introduction to Statistical Modeling of Extreme Values*. Springer series in Statistics, 2nd edn, London.
- Cooley D, Nychka D, Naveau P. 2007. Bayesian spatial modeling of extreme precipitation return levels. *Journal of the American Statistical Association* 102:824–840
- Coutts MA, Tapper JN, Beringer J, Loughnan M, Demuzere M. 2012. Watering our cities: The capacity for Water Sensitive Urban Design to support urban cooling and improve human thermal comfort in the Australian context. *Progress in Physical Geography* 37(1):2–28. DOI: 10.1177/0309133312461032
- de Munck C, Lemonsu A, Masson V, Le Bras J, Bonhomme M. 2018. Evaluating the impacts of greening scenarios on thermal comfort and energy and water consumptions for adapting Paris city to climate change. *Urban Climate* 23:260-286. https://doi.org/10.1016/j.uclim.2017.01.003
- Della-Marta MP, Haylock RM, Luterbacher J, Wanner H. 2007. Doubled length of western European summer heat waves since 1880. *Journal of Geophysical Research* 112, D15103. DOI: 10.1029/2007JD008510
- Deloitte, Risk management, strategy and analysis (2019). “Expect more gains in renewable energy in 2020”. (20 de diciembre del 2019). Recuperado de: https://deloitte.wsj.com /riskandcompliance/2019/12/20/expect-more-gains-in-renewable-energy-in-2020/
- demanda eléctrica de una microrred híbrida aislada (Tesis de maestría). Universidad Autónoma de Baja California, México.
- Dixon P, Ellison A, Gotelli N. 2005. Improving the precision of estimates of the frequency of rare events. *Ecology* 86(5):1114-1123.
- Dumitrescu A, Bojariu R, Birsan M-V, Marin L, Manea A. 2015. Recent climatic changes in Romania from observational data (1961–2013). Theoretical Applied of Climatology 122:111–119. https://doi.org/10.1007/s00704-014-1290-0
- Easterling DR, Kunkel KE, Wehner MF, Sun L. 2016. Detection and attribution of climate extremes in the observed record. *Weather and Climate Extremes* 11: 17-27. http://dx.doi.org/10.1016/j.wace.2016.01.001
- El Adlouni S, Ouarda TBMJ, Zhang X, Roy R, Bobée B. 2007. Generalized maximum likelihood estimators for the nonstationary generalized extreme value model. *Water Resources Research* 43: W03410. DOI: 10.1029/2005WR004545
- Fengjin X, Lianchun S. 2011. Analysis of extreme low-temperature events during the warm season in Northeast China. *Natural Hazards* 58: 1333. https://doi.org/10.1007/s11069-011-9735-6
- Fisher RA, Tippett LHC. 1928. On the estimation of the frequency distributions of the largest or smallest member of a sample. Proceedings of the Cambridge Philosophical Society 24:180-190.
- Friederichs P. 2010. Statistical downscaling of extreme precipitation events using extreme value theory. *Extremes* 13: 109. https://doi.org/10.1007/s10687-010-0107-5
- Fu, X., & Zhang, X. (2019). Estimation of building energy consumption using weather information derived from photovoltaic power plants. *Renewable Energy*, *130*, 130-138.

- Furió D, Meneu V. 2011. Analysis of extreme temperatures for four sites across Peninsular Spain. *Theoretical and Applied Climatology* 104:83-99. DOI 10.1007/s00704-010-0324-5
- Gao Y, Fu JS, Drake JB, Liu Y, Lamarque J-F. 2012. Projected changes of extreme weather events in the eastern United States based on a high-resolution climate modeling system. *Environmental Research Letters*. DOI:10.1088/1748-9326/7/4/044025
- García-Cueto OR, Cavazos T, de Grau P, Santillán-Soto N. 2014. Analysis and modeling of extreme temperatures in several cities in northwestern Mexico under climate change conditions. *Theoretical and Applied Climatology* 116:211–225. DOI 10.1007/s00704-013-0933-x
- García-Cueto OR, Santillán-Soto N, López-Velázquez JE, Reyes-López J, Cruz-Sotelo S, Ojeda-Benítez S. 2018. Trends of climate change indices in some Mexican cities from 1980 to 2010. *Theoretical and Applied Climatology* 137:775-790. https://doi.org/10.1007/s00704-018-2620-4
- García-Cueto OR, Santillán-Soto N, Quintero-Núñez M, Ojeda-Benítez S, Velázquez-Limón N. 2013. Extreme temperature scenarios in Mexicali, México under climate change conditions. *Atmósfera* 26(4):509-520. https://doi.org/10.1016/S0187-6236(13)71092-0
- García-Cueto R, Tejeda-Martínez A, Jáuregui E. 2010. Heat waves and heat days in an arid city in the northwest of México: current trends and in climate change scenarios. *International Journal of Biometeorology* 54(4):335-345. DOI: 10.1007/s00484-009-0283-7
- García-Díez, M., Fernández, J., Fita, L., & Yagüe, C. (2013). Seasonal dependence of WRF model biases and sensitivity to PBL schemes over Europe. Quarterly Journal of the Royal Meteorological Society, 139(671), 501-514.
- Gilleland E, Katz R. 2005. Tutorial for the extremes toolkit: weather and climate applications of extreme value statistics. Available at http://www.assessement.ucar.edu/toolkit (accesed 2018 September 20).
- Gilleland E, Katz R. 2006. Analyzing seasonal to interannual extreme weather and climate variability with the extremes toolkit (extRemes). In: 18th Conference on Climate Variability and Change, 86th American Meteorological Society (AMS) Annual Meeting, 29 January - 2 February 2006, Atlanta, Georgia.
- Gilleland E, Katz, RW. 2013. in2extRemes: Into the R Package extRemes Extreme Value Analysis for Weather and Climate Applications. NCAR/TN-523+STR, NCAR, Technical Note. National Center for Atmospheric Research, Boulder, Colorado.
- Gonzalez-San Pedro, E., (2016). Desarrollo de un sistema de monitoreo y control de la
- Gosling SN, Dunn R, Carrol F, Christidis N, Fullwood J, de Gusmao D, Golding N, Good L, Hall T, Kendon L, Kennedy J, et al. 2011. Climate: observations, projections and impacts: México. UK Met Office. Nottingham ePrints: Nottingham UK.
- Grotjahn R, Black R, Leung R, Wehner FM, Barlow M, Bosilovich M, Gershunov A, Gutowski JW, Gyakum RJ, Katz RW, Lee Y-Y, Lim Y-K, Prabhat. 2016. North American extreme temperature events and related large-scale meteorological patterns: a review of statistical methods, dynamics, modeling, and trends. *Climate Dynamics* 46:1151–1184. DOI 10.1007/s00382-015-2638-6
- Gu, Y., Liou, K. N., Ou, S. C., & Fovell, R. (2011). Cirrus cloud simulations using WRF with improved radiation parameterization and increased vertical resolution. Journal of Geophysical Research: Atmospheres, 116(D6).

- Guan Y, Zhang X, Zheng F, Wang B. 2015. Trends and variability of daily temperature extremes during 1960–2012 in the Yangtze River Basin, China. *Global Planetary Change* 124:79–94.
- Hartmann DL, Klein Tank AMG, Rusticucci M, Alexander LV, Brönnimann S, Charabi, Y, Dentener FJ, Dlugokencky EJ, Easterling DR, Kaplan A, Soden BJ, Thorne PW, Wild M, Zhai PM. 2013. Observations: atmosphere and surface. In: Stocker TF, Qin D, Plattner G-K, Tignor M, Allen SK, Boschung, J, Nauels A, Xia Y, Bex V, Midgley PM, eds. *Climate Change 2013: The Physical Science Basis. Contribution of Working Group I to the Fifth Assessment Report of the Intergovernmental Panel on Climate Change*. Cambridge Uni- versity Press, Cambridge, United Kingdom and New York, NY, USA.
- Hatfield JL, Prueger JH. 2015. Temperature extremes: Effect on plant growth and development. *Weather and Climate Extremes* 10 (Part A):4-10. http://dx.doi.org/10.1016/j.wace.2015.08.001
- Heim Jr. RR. 2015. An overview of weather and climate extremes. *Weather and Climate Extremes* 10 (Part B):1-9. http://dx.doi.org/10.1016/j.wace.2015.11.001
- Helsel DR, Hirsch MR. 1992. *Statistical methods in water resources*. Elsevier, New York.
- Hernández AR, Galeana GJ, Villegas BI. 2014. La urbanización en México 2010-2030: un esbozo de los retos y oportunidades asociados al crecimiento urbano y regional. En: *La Situación Demográfica de México 2014*. Consejo Nacional de Población, México, D.F., 139-164.
- Houngninou BE, Allé CSU, Kougbéagbédè H, Guédjé KF. 2017. Changes in daily temperature extremes over benin between 1970 and 2015. *International Journal of Advances Research* 5(12):108-113. DOI: 10.21474/IJAR01/5944
- Huang, R., Huang, T., Gadh, R., & Li, N. (2012, November). Solar generation prediction using the ARMA model in a laboratory-level micro-grid. In *2012 IEEE third international conference on smart grid communications (SmartGridComm)* (pp. 528-533). IEEE.
- Iacono, M. J., Delamere, J. S., Mlawer, E. J., Shephard, M. W., Clough, S. A., & Collins, W. D. (2008). Radiative forcing by long-lived greenhouse gases: Calculations with the AER radiative transfer models. Journal of Geophysical Research: Atmospheres, 113(D13).
- Incecik, S., Sakarya, S., Tilev, S., Kahraman, A., Aksoy, B., Caliskan, E. & Odman, M. T. (2019). Evaluation of WRF parameterizations for global horizontal irradiation forecasts: A study for Turkey. Atmósfera, 32(2), 143-158.
- IPCC. 2013. Climate change 2013: the physical science basis. In: Stocker TF, Qin D, Plattner G.-K, Tignor M, Allen PM, Boschung J, Nauels A, Xia Y, Bex V, Midgley PM, eds. *Contribution of Working Group I to the Fifth Assessment Report of the Inter-governmental Panel on Climate Change*. Cambridge University Press, Cambridge, United Kingdom and New York, NY, USA.
- Jain S, Lall U. 2001. Magnitude and timing of annual maximum floods, trends and large scale climatic associations for the Black smith Fork River, Utah. *Water Resources Research* 36(12):3641–3651.
- Jentsch A, Kreyling J, Beierkuhnlein C. 2007. A new generation of climate change experiments: events, not trends. *Frontiers in Ecology and the Environment* 5(6): 315-324.
- Katz R, Brush G, Parlange M. 2005. Statistics of extremes: modeling ecological disturbances. *Ecology* 86(5):1124-1134.
- Katz R, Parlange M, Naveau P. 2002. Statistics of extremes in hydrology. *Advances in Water Resources* 25:1287-1304.

- Katz RW. 2013. Statistical methods for nonstationary extremes. In: AghaKouchak A, Easterling D, Hsu K, eds. *Extremes in changing climate: detection, analysis and uncertainty*. Springer.
- Kendall MG. 1975. *Rank Correlation Methods*. Charles Graffin, London.
- Kharin VV, Zwiers FW. 2005. Estimating extremes in transient climate change simulations. *Journal of Climate* 18:1156-1173.
- Kim YH, Min SK, Zhang X, Zwiers F, Alexander LV, Donat MG, Tung YS. 2015. Attribution of extreme temperature changes during 1951–2010. *Climate Dynamics* 1–14. http://dx.doi.org/10.1007/s00382-015-2674-2
- Koutsoyiannis D. 2004. Statistics of extremes and estimation of extreme rainfall: I. Theoretical investigation / Statistiques de valeurs extrêmes et estimation de précipitations extrêmes: I. Recherche théorique. *Hydrological Sciences Journal* 49(4). DOI: 10.1623/hysj.49.4.575.54430
- Krausmann F, Wiedenhofer D, Lauk Ch, Haas W, Tanikawa H, Fishman T, Miatto A, Schandl H, Haberl H. 2017. Global socioeconomic material stocks rise 23-fold over the 20th century and require half of annual resource use. PNAS 8(114): 1880-1885.
- Lau N-C, Nath MJ. 2012. A model study of heat waves over North America: meteorological aspects and projections for the twenty-first century. *Journal of Climate* 25:4761–4784. DOI: 10.1175/ JCLI-D-11-00575.1
- Lazaridis, M. (2011). First Principles of Meteorology. En First Principles of Meteorology and Air Pollution (pp. 81-82). Springer, Dordrecht.
- Leclerc M, Ouarda T. 2007. Non-stationary regional flood frequency analysis at ungauged sites. *Journal of Hydrology* 343:254–265.
- Liu G, Zhang L, He B, Jin X, Zhang Q, Razafindrabe B, You H. 2015. Temporal changes in extreme high temperature, heat waves and relevant disasters in Nanjing metropolitan region, China. *Natural Hazards* 76:1415. https://doi.org/10.1007/s11069-014-1556-y
- Lorenz, E., Kühnert, J., & Heinemann, D. (2012, September). Short term forecasting of solar irradiance by combining satellite data and numerical weather predictions. In *Proceedings of the 27th European PV Solar Energy Conference (EU PVSEC), Frankfurt, Germany* (Vol. 2428, p. 44014405).
- Magaña V, Pérez J, Méndez M. 2003. Diagnosis and prognosis of extreme precipitation events in the Mexico city basin. *Geofísica Internacional* 41(2):247-259.
- Magaña V, Zermeño D, Neri C. 2012. Climate change scenarios and potential impacts on water availability in northern Mexico. *Climate Research* 51:171–184. https://doi.org/10.3354/cr01080
- Mann HB. 1945. Nonparametric tests against trend. *Econometrica* 13:245–259.
- Marnay, C., Chatzivasileiadis, S., Abbey, C., Iravani, R., Joos, G., Lombardi, P., ... & von Appen, J. (2015, September). Microgrid evolution roadmap. In *2015 international symposium on smart electric distribution systems and technologies (EDST)* (pp. 139-144). IEEE.
- Martínez-Austria PF, Bandala ER. 2017. Temperature and Heat-Related Mortality Trends in the Sonoran and Mojave Desert Region. *Atmosphere* 8(53). DOI:10.3390/atmos8030053
- Matsueda S, Takaya Y. 2015. The global influence of the Madden–Julian Oscillation on extreme temperature events. *Journal of Climate* 28:4141-4151.
- Meehl G, Karl T, Easterling RD, Changnon S, Pielke R Jr., Changnon D, Evans J, Groisman YP, Knutson RT, Kunkel EK, Mearns OL, Parmesan C, Pulwarty R, Root T, Sylves TR, Whetton P, Zwiers F. 2000. An

Introduction to Trends in Extreme Weather and Climate Events: Observations, Socioeconomic Impacts, Terrestrial Ecological Impacts, and Model Projections. *Bulletin American of Meteorological Society* 81(3):413-416.

- Meehl G, Tebaldi C. 2004. More intense, more frequent, and longer lasting heat waves in the twenty-first century. *Science* 305:994–997.
- Mills, A. (2009). Understanding variability and uncertainty of photovoltaics for integration with the electric power system.
- Milly PCD, Betancourt J, Falkenmark M, Hirsch M, Kundzewicz ZW, Lettenmaier DP, Stouffer RJ. 2008. Stationarity is dead: whither water management? *Science* 319:573–574.
- Miralles DG, Teuling AJ, van Heerwaarden CC, de Arellano JVG. 2014. Mega-heatwave temperatures due to combined soil desiccation and atmospheric heat accumulation. *Nature Geoscience* **7**:345-349. http://dx.doi.org/10.1038/NGEO2141
- Mondal A, Mujumdar PP. 2015. Modeling non-stationarity in intensity, duration and frequency of extreme rainfall over India. *Journal of Hydrology* 521:217–231.
- Moritz AM. 1997. Analyzing Extreme Disturbance Events: Fire in Los Padres National Forest. *Ecological Applications.* https://doi.org/10.1890/1051-0761(1997)007 [1252: AEDEFI]2.0.CO;2
- Mugume I, Shen S, Tao S, Mujuni G. 2016. Analysis of temperature variability over desert and urban areas of northern China. *Climatology and Weather Forecasting* 4:162. https://doi.org/10.4172/2332-2594.1000162
- Ongoma V, Chen H, Omony GW. 2016. Variability of extreme weather events over the equatorial East Africa, a case study of rainfall in Kenya and Uganda. *Theoretical and Applied Climatology* 131(1–2):295–308. https://doi.org/10.1007/s00704-016-1973-9
- Palmer T, Räisänen J. 2002. Quantifying the risk of extreme seasonal precipitation events in a changing climate. *Nature* 415:512-514.
- Panagoulia D, Economou P, Caroni C. 2013. Stationary and nonstationary generalized extreme value modelling of extreme precipitation over a mountainous area under climate change. *Environmetrics* 25:29-43. DOI: 10.1002/env.2252
- Papalexiou SM, Koutsoyiannis D. 2013. Battle of extreme value distributions: A global survey on extreme daily rainfall. *Water Resources Research* 49:187–201. DOI:10.1029/2012WR012557
- Parey S, Hoang TTH, Dacunha-Castelle D. 2018. Future high-temperature extremes and stationarity. *Natural Hazards.* https://doi.org/10.1007/s11069-018-3499-1
- Parey S, Malek F, Laurent C, Dacunha-Castelle D. 2007. Trends and climate evolution: Statistical approach for very high temperatures in France. *Climatic Change* 81:331-352. DOI 10.1007/s10584-006-9116-4
- Parker TJ, Berry GJ, Reeder MJ, Nicholls N. 2014. Modes of climate variability and heat waves in Victoria, southeastern Australia. *Geophysical Research Letters* 41(19):6926-6934.
- Pascual, J., Barricarte, J., Sanchis, P., & Marroyo, L. (2015). Energy management strategy for a renewable-based residential microgrid with generation and demand forecasting. *Applied Energy*, *158*, 12-25.
- Paulescu, Eugenia, and Robert Blaga. (2016). "Regression models for hourly diffuse solar radiation." *Solar Energy* 125 (2016): 111-124.
- Pirovano, G., Faggian, P., Bonelli, P., Lacavalla, M., Marcacci, P., & Ronzio, D. (2014). Combining meteorological and electrical engineering expertise to solve energy management problems. In Weather

Matters for Energy (pp. 133-154). Springer, New York, NY.

- Qiang Z, Vijay PS, Suna P, Chend X. 2011. Precipitation and stream flow changes in China: changing patterns, causes and implications. Journal of Hydrology 410:204–216. https://doi.org/10.1016/j.jhydrol.2011.09.017
- Raggad B. 2018. Statistical assessment of changes in extreme maximum temperatures over Saudi Arabia, 1985-2014. *Theoretical and Applied Climatology* 132:1217-1235. DOI 10.1007/s00704-017-2155-0
- Renard B, Sun X, Lang M. 2013. Bayesian Methods for Non-stationary Extreme Value Analysis. In: AghaKouchak A, Easterling D, Hsu K, Schubert S, Sorooshian S, eds. Extremes in a Changing Climate. Water Science and Technology Library, vol 65. Springer, Dordrecht.
- Ríos-Alejandro JG. 2011. Temperaturas extremas en la ciudad de Monterrey, N.L., México. Rev Chapingo Serie Ciencias Forestales y del Ambiente 17(2):225-230.
- Rodríguez, F., Fleetwood, A., Galarza, A., & Fontán, L. (2018). Predicting solar energy generation through artificial neural networks using weather forecasts for microgrid control. *Renewable Energy*, *126*, 855-864.
- Rosenzweig C, Solecki W, Hammer SA, Mehrotra S, eds. *Climate Change and Cities (First Assessment Report of the Urban Climate Change Research Network)*. Cambridge, MA: Cambridge University Press; 2011.
- Ruiz-Arias, J. A., Dudhia, J., Santos-Alamillos, F. J., & Pozo-Vázquez, D. (2013). Surface clear-sky shortwave radiative closure intercomparisons in the Weather Research and Forecasting model. Journal of Geophysical Research: Atmospheres, 118(17), 9901-9913.
- Salmi T, Maata A, Antilla P, Ruoho-Airola T, Amnell T. 2002. Detecting trends of annual values of atmospheric pollutants by the Mann–Kendall test and Sen’s slope estimates – the excel template application Makesens. Finnish Meteorological Institute, Helsinki, pp 35.
- Schoof TJ, Robeson MS. 2016. Projecting changes in regional temperature and precipitation extremes in the United States. Weather and Climate Extremes 11: 28–40. http://dx.doi.org/10.1016/j.wace.2015.09.004
- Sen PK. 1968. Estimates of the regression coefficient based on Kendall's tau. Journal of American Statistical Associaton 63:1379–1389. https://doi.org/10.1080/01621459.1968.10480934
- Seneviratne SI, Nicholls N, Easterling D, Goodess CM, Kanae S, Kossin J, Luo Y, Marengo J, McInnes K, Rahimi M, Reichstein M, Sorteberg A, Vera C, Zhang X. 2012. Changes in climate extremes and their impacts on the natural physical environment. In: Field CB, Barros V, Stocker TF, Qin D, Dokken DJ, Ebi KL, Mastrandrea MD, Mach KJ, Plattner G.-K, Allen SK, Tignor M, Midgley PM, eds. *Managing the Risks of Extreme Events and Disasters to Advance Climate Change Adaptation*. A Special Report of Working Groups I and II of the Intergovernmental Panel on Climate Change. Cambridge University Press, Cambridge, United Kingdom and New York, NY, USA, 109-230.
- Shen L, Mickley JL, Gilleland E. 2016. Impact of increasing heat waves on U.S. ozone episodes in the 2050s: Results from a multimodel analysis using extreme value theory. *Geophysical Research Letters* 43:4017–4025. DOI: 10.1002/ 2016GL068432
- Skamarock, W. C., 2008: A Description of the Advanced Research WRF Version 3. NCAR Notas técnicas de NCAR/TN-475+STR
- Skelhorn CP, Lindley S, Levermore G. 2018. Urban greening and the UHI: seasonal trade-offs in heating and cooling energy consumption in Manchester, UK. Urban Climate 23:173-187. https://doi.org/10.1016/j.uclim.2017.02.010

- Smith R. 2001. Environmental Statistics. Department of Statistics, University of North Carolina, USA pp 377, Available from http://www.stat.unc.edu/postscript/rs/envnotes.ps
- Song X, Zhang Z, Chen Y, Wang P, Xiang M, Shi P, Tao F. 2014. Spatiotemporal changes of global extreme temperature events (ETEs) since 1981 and the meteorological causes. *Natural Hazards* 70:975. https://doi.org/10.1007/s11069-013-0856-y
- Tabari H, Marofi S, Ahmadi M. 2011. Long-term variations of water quality parameters in the Maroon River, Iran. *Environmental Monitoring and Assessment* 177:273–287. https://doi.org/10.1007/s10661-010-1633-y
- Tanarhte M, Hadjinicolaou P, Lelieveld J. 2015. Heat wave characteristics in the eastern Mediterranean and Middle East using extreme value theory. *Climate Research* 63:99-113. https://doi.org/10.3354/cr01285
- Taxak KA, Murumkar AR, Arya DS. 2014. Long term spatial and temporal rainfall trends analysis in Wainganga basin, Central India. *Weather and Climate Extremes* 4:50-61. http://dx.doi.org/10.1016/j.wace.2014.04.005
- Taylor KE, Stouffer RJ, Meehl GA. 2012. **An overview of CMIP5 and the experimental design.** Bull. Am. Meteorol. Soc., 93:485-498.
- Thiombiano AN, El Adlouni S, St-Hilaire A, Ouarda T, El-Jaabi N. 2017. Nonstationary frequency analysis of extreme daily precipitation amounts in Southeastern Canada using a peaks-over-threshold. *Theoretical and Applied Climatology* 129:413-426. DOI 10.1007/s00704-016-1789-7
- Trenberth KE, Jones PD, Ambenje P, Bojariu R, Easterling D, Klein Tank A, Parker D, Rahimzadeh F, Renwick JA, Rusticucci M, Soden B, Zhai P. 2007. Observations: surface and atmospheric climate change. In: Solomon S, Qin D, Manning M, Chen Z, Marquis M, Averyt KB, Tignor M, Miller HL, eds. *Climate Change 2007: The Physical Science Basis. Contribution of Working Group I to the Fourth Assessment Report of the Intergovernmental Panel on Climate Change*. Cambridge University Press, Cambridge, United Kingdom and New York, NY, USA.
- Ummenhofer CC, Meehl GA. 2017. Extreme weather and climate events with ecological relevance: a review. *Philos Trans R Soc* B 372: 20160135.
- UN-Habitat. 2011. *Cities and Climate Change* (Global Report on Human Settlements). London-Washington DC. Published by Earthscan.
- Urias, H. E., Cueto, O. R. G., & Morales, G. B. (2021). Identification and classification of local climate zones in a semi-arid city of northwestern Mexico. Vivienda y Comunidades Sustentables, (9), 45-60.
- Wang H, Chen Y, Chen Z, Li W. 2013. Changes in annual and seasonal temperature extremes in the arid region of China, 1960–2010. *Natural Hazards* 65:1913. https://doi.org/10.1007/s11069-012-0454-4
- Wang Z-H, Feng Y. 2010. *RHtestsV3 User Manual*. Climate Research Division. Atmospheric Science and Technology Directorate. Science and Technology Branch, Environment Canada, pp 24 Available at: http://cccma.seos.uvic.ca/ETCCDMI/software.shtml
- Wang Z-H, Zhao X, Yang J, Song J. 2016. Cooling and energy saving potentials of shade trees and urban lawns in a desert city. *Applied Energy* 161:437-444. http://dx.doi.org/10.1016/j.apenergy.2015.10.047
- Waylen PR, Keellings D, Qiu Y. 2012. Climate and health in Florida: changes in risks of annual maximum temperatures in the second half of the twentieth century. *Applied Geography* 33:73-81.
- Whan K, Zscheischler J, Orth R, Shongwe M, Rahimi M, Asare E, Seneviratne S. 2015. Impact of soil moisture on extreme maximum temperatures. *Weather and Climate Extremes* 9:57-67. https://dx.doi.org/10.1016/j.wace.2015.05.001

- Wypych A, Sulikowska A, Ustrnul Z, Czekierda D. 2017. Temporal Variability of Summer Temperature Extremes in Poland. *Atmosphere* 8(3), 51. DOI:10.3390/atmos8030051
- Zhang X, Yang F. 2004. *RClimDex (1.0) user manual*. Climate Research Branch Environment Canada, pp 22. Available at: http://cccma.seos.uvic.ca/ETCCDI/software.shtml.

Anexo A (artículo 1)

Trends in Temperature Extremes in Selected Growing Cities of México Under a Non-Stationary Climate

Revista: Atmósfera
34(3), 233-254 (2021)
https://doi.org/10.20937/ATM.52784

México es un país vulnerable a los eventos climáticos extremos, sin embargo, el impacto no es uniforme en todas sus regiones, por lo que se analizan y modelan las temperaturas extremas de 12 ciudades de México, bajo la suposición de un clima no-estacionario. A partir de la base climatológica disponible de temperaturas máximas y temperaturas mínimas, se estimó su tendencia temporal con las pruebas no-paramétricas de Mann-Kendall y el método de pendiente de Sen, y se utilizó la Distribución Generalizada de Valores Extremos (GEV), para modelar ambas temperaturas. Para evaluar la fortaleza de los modelos propuestos con la incorporación de una covariable, se utilizó la Prueba de Razón de Verosimilitud, y los Criterios de Información de Akaike y de Bayes, y se estimaron los niveles de retorno para escenarios temporales futuros. Se detectó una tendencia al calentamiento urbano, tanto con las pruebas no-paramétricas, como con la distribución GEV, aunque con comportamiento heterogéneo: en la serie de la temperatura máxima, la mitad de las ciudades analizadas se mostró no-estacionaria, de las cuales, la ciudad de Guadalajara, situada en el centro-occidente del país, presentó tendencia negativa. En el caso de las temperaturas mínimas su tendencia fue más uniforme, el 90% de las ciudades se mostraron no-estacionarias con tendencia positiva, y solo un 10%, una zona urbana al oriente de la zona metropolitana del Valle de México (Milpa Alta), y una ciudad costera del Golfo de México (Veracruz), mostraron una serie estacionaria. Se concluye que los períodos de retorno de extremos térmicos estimados en un clima cambiante, varían temporalmente, por lo que la modelación estadística debe tomar en cuenta ese comportamiento debido a su importancia para valoraciones de riesgos y propósitos de adaptación.

Atmósfera 34(3), 233-254 (2021)
https://doi.org/10.20937/ATM.52784

Trends in temperature extremes in selected growing cities of Mexico under a non-stationary climate

O. Rafael GARCÍA-CUETO[1]*, J. Ernesto LÓPEZ-VELÁZQUEZ[1], Gonzalo BOJÓRQUEZ-MORALES[2], Néstor SANTILLÁN-SOTO[1] and David Enrique FLORES-JIMÉNEZ[1]

[1]*Instituto de Ingeniería, Universidad Autónoma de Baja California, Blvd. Benito Juárez y C. de la Normal, Col. Insurgentes Este, 21280 Mexicali, Baja California, México.*
[2]*Facultad de Arquitectura y Diseño, Universidad Autónoma de Baja California, Churubusco e Ignacio López Rayón, Col. Insurgentes Este, 21280 Mexicali, Baja California, México.*
*Corresponding author; email: rafaelcueto@uabc.edu.mx

Received: October 7, 2019; accepted: June 10, 2020

RESUMEN

México es un país vulnerable a los eventos climáticos extremos; sin embargo, el impacto no es uniforme en todo el territorio, por lo que se analizan y modelan las temperaturas extremas de 12 ciudades de México con la suposición de que existe un clima no estacionario en todas las regiones del país. A partir de la base climatológica disponible de temperaturas máximas y temperaturas mínimas, se estimó una tendencia temporal con las pruebas no paramétricas de Mann-Kendall y el método de pendiente de Sen, y se utilizó la distribución generalizada de valores extremos (GEV) para modelar ambas temperaturas. Para evaluar la fortaleza de los modelos propuestos con la incorporación de una covariable, se utilizaron tanto la prueba de razón de verosimilitud como los criterios de información de Akaike y de Bayes, y se estimaron los niveles de retorno para escenarios temporales futuros. Se detectó una tendencia al calentamiento urbano, tanto con las pruebas no paramétricas como con la distribución GEV, aunque con comportamiento heterogéneo. En la serie de temperatura máxima, la mitad de las ciudades analizadas se mostró no estacionaria; de éstas, la ciudad de Guadalajara, situada en el centro-occidente del país, presentó tendencia negativa. En el caso de las temperaturas mínimas la tendencia fue más uniforme: 90% de las ciudades se mostraron no estacionarias con tendencia positiva y sólo el 10% (una zona urbana al oriente de la zona metropolitana del Valle de México [Milpa Alta] y una ciudad costera del Golfo de México [Veracruz]) mostraron una serie estacionaria. Se concluye que los periodos de retorno de extremos térmicos estimados en un clima cambiante varían temporalmente, por lo que la modelación estadística debe tomar en cuenta ese comportamiento en razón de su importancia para valoraciones de riesgos y propósitos de adaptación.

ABSTRACT

Mexico is vulnerable to extreme climatic events; however, their impact is not uniform in all the country. This study presents an analysis of extreme temperatures in 12 Mexican cities, modeled under the assumption of a non-stationary climate. Temporal trends were estimated from an available climatological base of maximum and minimum temperatures with the non-parametric tests of Mann-Kendall and Sen's slope method, and a generalized extreme value (GEV) distribution was used to model both temperatures. A likelihood ratio test and Akaike and Bayesian information criteria were used to evaluate the optimal model choice with incorporation of a covariate. Using the best model, return levels and confidence intervals for future scenarios were estimated. A trend towards urban warming was detected from both the non-parametric tests and the GEV distribution, although with heterogeneous behavior. In the series of the maximum temperatures, half of the cities analyzed were non-stationary, and of those, the city of Guadalajara, located in the center-west of the country had a negative trend. The trend for minimum temperatures was more uniform, as 90% of the cities were non-stationary with a positive trend, and only 10%, in an urban area to the east of the metropolitan area of the Valley of Mexico (Milpa Alta) and a coastal city of the Gulf of Mexico (Veracruz), showed stationary series. It is therefore concluded that return periods of thermal extremes estimated in a changing climate temporarily showed a significant variation, so statistical modeling must consider this behavior due to its importance for risk assessments and adaptation purposes.

Keywords: extreme temperatures, non-stationary climate, generalized extreme value distribution, return periods, cities of Mexico.

1. Introduction

Extreme climate events (ECE) must be periodically monitored and analyzed in detail, due to their role as high impact agents on society, environment, and ecosystems. An extreme climatic or meteorological event refers to the occurrence of a climatic or meteorological variable which value is above or below a threshold that is close to the upper (or lower) limits of the range of observed values of the variable (Seneviratne et al., 2012). ECE are important because of their impacts, but they are difficult to quantify statistically, as they are infrequent and occur at multiple scales (Palmer and Räisänen, 2002). The definitions of "rare" vary, but an ECE would normally be as rare as, or rarer than, the 10th or 90th percentile of the observed probability density function.

It is likely that different ECE affect specific regions and increases in their frequency and intensity have been detected in several regions of the world (Brown et al., 2008; Almazroui et al., 2014; Chen et al., 2015; Wypych et al., 2017; Caloiero, 2017). It is expected that these ECE will intensify in the future in response to global climate changes caused by the emission of greenhouse gases (Beniston et al., 2007; Gao et al., 2012; Lau and Nath, 2012; Easterling et al., 2016; Grotjahn et al., 2016; Schoof and Robeson, 2016).

There are basically two fundamental approaches to study ECE: global circulation models (GCMs), and statistical models using the extreme value theory (EVT). Contemporary GCMs, such as those used for the 5th Coupled Model Intercomparison Project (Taylor et al., 2012) are a key component of regional climate change projections, but their limited spatial resolution reduces their utility in estimating local or regional extremes without substantial post-processing (Schoof and Robeson, 2016). On the other hand, the central issue of EVT is the modeling of extreme events, and the main purpose of this theory is to provide asymptotic models for the distribution tails (Furió and Meneu, 2011). Therefore, EVT aims at deriving a probability distribution of events at the far end of the upper or lower ranges of the probability distributions (Coles, 2001); its main advantage is that it allows for estimating and analyzing the probability of occurrence of events that are outside of the observed data range (Raggad, 2018).

For these reasons, EVT is the approach that has been chosen in this research due to its wide applicability in different fields that are related to extreme weather and climate events and their impact: ecology (Moritz, 1997; Meehl et al., 2000; Dixon et al., 2005; Katz et al., 2005; Jentsch et al., 2007; Burgman et al., 2012); extreme temperatures and heat waves (Meehl and Tebaldi, 2004; Della-Marta et al., 2007; Parey et al., 2007; García-Cueto et al., 2010; Waylen et al., 2012; Tanarhte et al., 2015; Liu et al., 2015; Shen et al., 2016); extreme rainfall (Katz et al., 2002; Koutsoyiannis, 2004; Friederichs, 2010; Papalexiou and Koutsoyiannis, 2013; Kim et al., 2015; Boucefiane and Meddi, 2019); and damages to the communities that affect agroecosystems through changes in soil moisture and evapotranspiration rates (Miralles et al., 2014; Whan et al., 2015; Guan et al., 2015; Hatfield and Prueger, 2015).

Changes in extremes of temperature and precipitation have been evaluated in different regions of the world. However, until the Fourth Assessment Report of the Intergovernmental Panel on Climate Change (Trenberth et al., 2007), the cities had been treated as "noise-generating" entities in globally studied climatic signals. In the Fifth Assessment Report of the Intergovernmental Panel on Climate Change (IPCC, 2013), a special chapter was dedicated to the subject of cities, and their role in climate change. This is not surprising, as although cities are very important contributors to social and economic well-being, they require an uninterrupted source of energy for all their activities. Cities consume approximately 75% of global primary energy and emit between 50-60% of the greenhouse gases (GHG) on the planet (Rosenzweig et al., 2011). This figure can be raised to 80% when indirect emissions generated by inhabitants of the cities are included (UN-Habitat, 2011; Kraussmann et al., 2017). Thus, cities promote global warming, and contribute to an increase in average surface temperature at the planetary level.

In addition to the global effects of GHG, the worldwide upward trend of urban growth must be considered, both in population and in its areal extension. This growth has generated environmental problems, not only air pollution and solid waste, but also those concerning a different environmental product, such as the genesis of an urban climate. In particular, the main connotation of urban climate is the formation of an urban heat island, which in turn requires additional water and energy to maintain thermal comfort through air-conditioned spaces (Coutts et al., 2012; Wang et al., 2016; de Munck et al., 2018, Skelhorn et al., 2018). Thus, cities that are already particularly vulnerable to ECE caused by global climate change must now also consider the effects caused by local climate change. Therefore, it can be inferred that because a city is the geographical space that brings together a majority of the population and provision of services, it will be where the greatest vulnerabilities associated with the impacts of climate change manifest themselves (UN-Habitat, 2011).

In Mexico approximately three out of four people (72.3%) live in cities according to Fundación Centro de Investigación y Documentación de la Casa and Sociedad Hipotecaria Federal (CIDOC-SHF, 2011). This percentage is expected to increase in the medium term, as according to projections of the National Population Council the number of people in 384 localities of the National Urban System will increase by 16.6 million (from 82.6 million in 2010 to 99.3 million in 2030) as a result of an annual average growth rate of 0.92% (Hernández et al., 2014). The urban proportion of the national population will increase to 77.9% (18.1 million new urban inhabitants). This trend of the geographic dynamics of cities is inequitable with low levels of quality of life and urban sustainability, and not all cities have the same development potential. Thus, the challenges in facing climatic risks such as heat waves and floods will be massive if quantitative scientific studies are not carried out.

Very little research has been conducted in Mexico on extreme climate values in urban environments (Magaña et al. 2003, 2012; Cavazos and Rivas, 2004; Ríos-Alejandro, 2011; García-Cueto et al., 2013, 2014, 2018; Martínez-Austria and Bandala, 2017). This can be explained by a limited access to measured climate data, limitations in the geographical coverage of the networks of stations, and interruptions in climate series due to missing data. In view of this and given the quantitative uncertainty of the climate extremes mentioned at the urban level and their great importance for the assessment of risks and adaptation proposals, this study selects some cities in Mexico with important increases in population and in areal extension, which have recently been affectated by ECE.

Thus, this study has three main objectives: (a) to detect thermal behavior in some growing cities of Mexico, (b) to model extreme temperatures through the EVT, and (c) to make projections of return levels for extreme temperatures in a future changing climate.

This paper is organized as follows: section 2 presents the climatology of extreme values in Mexico; section 3 presents the study area and the climate data, and section 4 provides a theoretical outline of the methodology. The results and discussion are presented in section 5. In section 6, conclusions are drawn.

2. Climatology of extreme temperature values of Mexico

Figures 1 and 2 show the 10th and 90th percentiles of minimum and maximum temperatures, respectively (Cavazos et al., 2013), for the period 1961-2000; the methodology used in these figures is described in Colorado-Ruiz et al. (2018). According to extreme climate indices derived from reliability ensemble averaging (REA) (Fig. 1), the coldest winters and their 10th percentile (P10) during the winter months of December, January, and February (DJF) for Mexico are characterized by minimum temperatures below 0 ºC in the highlands of the Sierra Madre Occidental and the Mexican High Plateau, and between 0 and 5 ºC in much of northern Mexico. Figure 2 shows that the extreme values of the 90th percentile (P90) of the

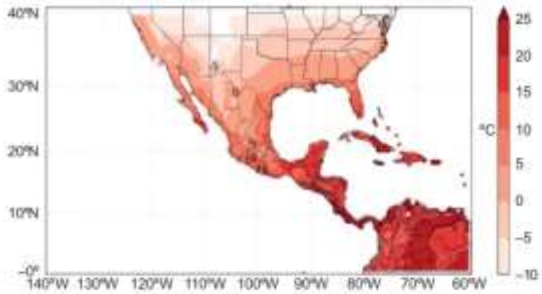

Fig. 1. Thresholds of P10 of minimum temperature for winter, obtained with the ensemble of the Reliability Ensemble Averaging (REA) for 1961-2000 (Cavazos et al., 2013).

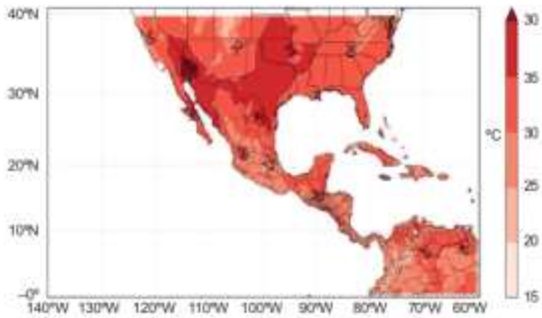

Fig. 2. Thresholds of P90 of maximum temperature for summer, obtained with the ensemble of the Reliability Ensemble Averaging (REA) for 1961-2000 (Cavazos et al., 2013).

maximum temperatures during the summer months of June, July, and August (JJA) expand the area covered by the isotherms of 25 and 40 °C to a narrower strip in the border region. This region of semiarid climate is the most extreme in Mexico; therefore, it is the most susceptible to negative impacts caused by increases in temperature.

The projected climate changes at a national level (Cavazos et al., 2013) agree with those obtained globally (Alexander et al., 2006; Caesar et al., 2011; Song et al., 2014). Regarding those related to the increase in the frequency of heat days, heatwaves and variability in precipitation will exacerbate problems related to natural and human systems (Ummenhofer and Meehl, 2017). If we analyze the 10th and 90th percentiles of extreme temperatures at the national level, there is a notable lack of reliable and timely information at the regional and urban levels for risk assessment, which justifies the study carried out herein.

3. Data and study area

A digital historical collection of daily temperature data for several cities in Mexico was possible using information from climatological stations operated by the Servicio Meteorológico Nacional (SMN, National Weather Service). Unfortunately, the selection of urban areas of interest faced some limitations, as not all climate stations have the same record length, and none had a strict data quality control. Based on a previous analysis of the growth of some cities in Mexico and the occurrence of climatic events that have affected them in important ways, 21 cities were selected in the first instance. However, an analysis of the quality of climate information limited the study to only 12 cities. These cities are heterogeneously distributed in the country because, as mentioned above, they were selected for their population growth and urban development. Data quality control was carried out for the daily information for each city, consisting of the following synthetic process.

The SMN database from the Climate Computing Project (CLICOM) was extracted in the .csv format, using Matlab and RClimdex software. The climatic information was explored, and quality control was performed for the original database. The daily meteorological values of maximum temperature (TXX) and minimum temperature (TNN) were selected with a computation routine; at the same time, a continuity of the time series was sought by adding missing dates and values, if possible, and adding a –99.99 label for missing data. Subsequently, the database was imported into the RClimdex program (Zhang and Yang, 2004), ensuring the internal and temporal consistency of the daily climatological information. This quality control validated the following: (1) internal coherence, by verifying that the maximum temperature was always greater than the minimum temperature; (2) identification of atypical values and changes in the seasonal cycle or variability of the data through visual inspection of the time series of TXX and TNN, and (3) identification of values located more than four standard deviations (σ) from the mean as outliers and possible errors. Finally, outliers were verified individually to determine if they had been caused by an atypical event or if the measurement was incorrect and had to be discarded.

Temporal homogeneity of the data was then evaluated using the RHtest V3 software (Wang and Feng, 2010) to identify abrupt jumps or change-points. This homogeneity test is based on a two-phase regression model with a linear trend for the entire series, applied to selected series for each of the cities.

The final selection included the following cities and/or intra-urban regions for the detailed analysis of extreme temperatures: Aguascalientes, Mexicali, Tijuana, Tuxtla Gutiérrez, Mexico City (with analysis of the climatological stations of Úrsula Coapa, Gran Canal, and Milpa Alta), León, Guadalajara, Monterrey, Puebla, Tlaxcala, Veracruz and the metropolitan area of the Valley of Mexico, including the urban areas of Toluca, Aculco and Chapingo (Table I). Their locations are presented in Figure 3 and, as can be seen, the analysis includes cities distributed in central Mexico (18-25° N latitude), a city in southeastern Mexico (Tuxtla Gutiérrez), another in northeastern Mexico (Monterrey), and two more in northwestern Mexico (Tijuana and Mexicali).

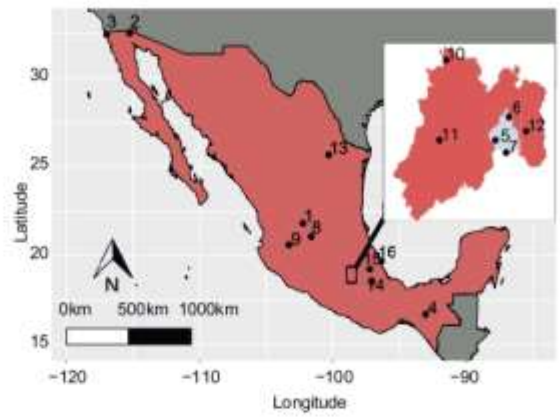

Fig. 3. Locations of intra-urban cities or regions according to Table I.

Table I. City or urban region, climatological station number, elevation, period of useful data, historical values of extreme maximum temperature, and extreme minimum temperature.

ID	City or urban region	Climatological station number[a]	Elevation (masl)	Period	TXX (°C)	TNN (°C)
1	Aguascalientes	01030	1889	1950-2015	40.0	−6.0
2	Mexicali	02033	4	1950-2012	52.0	−7.0
3	Tijuana	02038	120	1950-2012	45.0	0.0
4	Tuxtla Gutiérrez	07165	570	1980-2010	42.0	7.1
5	Úrsula Coapa, CDMX	09014	2256	1971-2013	34.5	−3.0
6	Gran Canal, CDMX	09029	2239	1952-2008	38.5	−7.5
7	Milpa Alta, CDMX	09032	2420	1963-2012	34.0	−2.5
8	León	11095	1828	1959-2014	39.5	−2.5
9	Guadalajara	14066	1550	1957-2013	47.0	−1.5
10	Aculco, ZMVM	15002	2490	1970-2011	32.0	−5.0
11	Toluca, ZMVM	15126	2726	1974-2009	33.6	−10.0
12	Chapingo, ZMVM	15170	2250	1954-2010	37.5	−8.5
13	Monterrey	19049	495	1949-2009	48.0	−7.5
14	Puebla	21035	2122	1955-2013	36.5	−6.0
15	Tlaxcala	29030	2230	1969-2013	39.2	−7.4
16	Veracruz	30192	16	1930-2014	42.7	7.9

[a]Climatological station number refers to the key that the National Weather Service (SMN) of Mexico manages in its files.

TXX: extreme maximum temperature; TNN: extreme minimum temperature; CDMX: Mexico City; ZMVM: metropolitan area of the Valley of Mexico.

Our study focused on ECE using a parametric non-stationary generalized extreme value (GEV) distribution model, which tacitly assumes that extreme events are changing over time as climate changes. Instead of the climate change indices used in García-Cueto et al. (2018), the current study directly applies extreme temperature values. In addition, the non-stationary GEV model is applied to investigate how the return levels of extreme temperatures might change in the future.

It is worth mentioning that for the city of Mexicali, due to the importance of extreme temperatures for human comfort and energy consumption for use in air conditioning, other studies have been carried out (García-Cueto et al., 2010, 2013). Unlike current research, in García-Cueto et al. (2010) warm days were modeled with the GEV and the maximum temperature was included as a covariate, without performing a temporal trend analysis of extreme temperatures. Their difference with respect to García-Cueto et al. (2013) is that the trends of extreme temperatures and their return periods are updated with a methodological process that requires a re-parameterization of the GEV model, which gives greater reliability in its estimation.

4. Methodology

In this section we present the techniques used for trend analysis and a brief review of the GEV distribution, to provide a basis for the modeling of extreme temperature events. As described in section 1, the GEV distribution is used to model extremes in atmospheric science and in many other scientific fields. Using the trends of annual temperature series, we describe the non-stationary models, the criteria for deciding which GEV model to use, the estimation of the parameters of the GEV distribution, and the return levels.

4.1 Trend analysis

The detections of monotonic trends of increase or decrease in TXX and TNN in a time series were analyzed using the Mann-Kendall non-parametric test (Mann, 1945; Kendall, 1975) and Sen's method for slope estimates (Sen, 1968). The Mann-Kendall test is based on ranges and has been found to be an excellent tool for detecting trends in climatic applications (Burn and Hag Elnur, 2002; Mugume et al., 2016). One of the advantages of this test is that the data does not need to be adjusted to any distribution. The second advantage of this test is its low sensitivity to sudden breaks owing to non-homogeneous time series, extreme values (outliers), and non-linear trends (Helsel and Hirsch, 1992; Tabari et al., 2011). Given its robustness, the Mann-Kendall test has become very popular in evaluating trends in environmental data and allows adequate comparisons across regions (Fengjin and Lianchun, 2011; Qiang et al., 2011; Wang et al., 2013; Dumitrescu et al., 2015; Ongoma et al., 2016). Sen's method uses a linear model to estimate the slope of a trend, and the variance of the residuals must be constant over time (Salmi et al., 2002). Many studies (Taxak et al., 2014; Caloiero, 2017; García-Cueto et al., 2018; Raggad, 2018, among others) have described these methods explicitly.

4.2 Generalized extreme values (GEV) stationary distribution

The general framework of this study is a statistical EVT. The EVT aims to characterize rare events by describing the tails of the underlying distribution. The EVT concerns the asymptotic stochastic behavior of the extreme order statistics of a random sample, such as the maximum and minimum values of identically distributed independent random variables (Coles, 2001).

The Fisher-Tippett theorem (1928) states that if the distribution of the normalized maximum of a sequence of random variables converges, it always converges to the GEV distribution, independently of the underlying distribution. In this regard, let X_1, ..., X_n be a sequence of identically distributed independent random variables with a common distribution function F; the maximum sample, M_n, with n being the size of the block, is defined as $M_n = \max \{X_1, X_2, ..., X_n\}$. X_i usually represents the maximum (or minimum) values measured on a regular time scale or blocks of time, so M_n represents the extreme values of the process in n units of observation time. The blocks of data in this study are sequences of observations having the length of a year, i.e., the approach uses the maximum and minimum values per annual blocks of temperature.

For these data, the distributions of M_n according to the EVT can be modelled as blocks of identically distributed extreme values with a GEV distribution as defined by Eq. (1), with a cumulative distribution function with three parameters given by (Coles, 2001):

$$G(z; \mu, \sigma, \xi) = \exp\left[-\{1 + \xi(z - \mu)/\sigma\}^{-1/\xi}\right] \qquad (1)$$

This distribution is defined on the set $\{z: 1 + \xi(z - \mu)/\sigma > 0\}$. Here, μ is the location parameter ($-\infty < \mu < \infty$), σ is the scale parameter ($\sigma > 0$), and ξ is the shape parameter ($-\infty < \xi < \infty$) that determines the nature of the behavior of the tail of the maximum distribution. The justification for the GEV distribution arises from an asymptotic argument.

The GEV distribution combines the three possible limiting distributions on extreme values in sample data in a single expression. It is a family of continuous probability distributions developed to combine the three distributions of extreme values: Gumbel ($\xi = 0$), Fréchet ($\xi > 0$), and Weibull ($\xi < 0$), or distributions of extreme values types I, II, and III, respectively. Each of the three types of distributions has distinct forms of behavior in the tail. The Weibull is *bounded* above, meaning that there is a finite value which the maximum cannot exceed. The Gumbel distribution yields a *light tail*, meaning that although the maximum can take on infinitely high values, the probability of obtaining such levels becomes exponentially small. The Fréchet distribution has a heavy tail and decays polynomially, so that higher values of the maximum are obtained with greater probability, as would be the case with a lighter tail (Gilleland and Katz, 2006). The flexibility of the GEV in describing all three types of tail behavior in a single family greatly simplifies the statistical implementation.

4.3 GEV non-stationary distribution

As we will see later, the extreme temperatures in several cities being analyzed show temporal trends, so the assumption of an independently distributed and identically distributed series of data with constant properties over time (stationary) needs to be modified to consider the effects of long-term climate change. In fact, there is increasing evidence that extreme series, whether thermal or hydroclimatic, are not stationary, due to natural climatic variability or anthropogenic climate change (Jain and Lall, 2001; Milly et al., 2008). Modeling of the non-stationarity within the GEV distribution scheme requires improved models, in which model parameters are expressed as a function of time, and possibly with the incorporation of other covariates (El Adlouni et al., 2007; Leclerc and Ouarda, 2007; Panagoulia et al., 2013; Parey et al., 2018).

We incorporate the non-stationarity by allowing the location parameter (μ) of the GEV distribution to be time dependent (Renardt et al., 2013). Using the notation (μ, σ, ξ) to denote a GEV distribution with parameters μ, σ, ξ, a suitable model for extreme temperatures in year t, Z_t, could be as presented in Eq. (2) (Furió and Meneu, 2011):

$$Z_t \approx GEV\left[\mu(t), \sigma, \xi\right] \qquad (2)$$

where $\mu(t) = \mu_0 + \mu_1(t)$ for parameters μ_0 and μ_1. In this way, temporal variations in the observed process are modeled as a linear trend for the location parameter of the extreme value model, which in this case is the GEV distribution. The parameter μ_0 corresponds to the value of μ when t is the initial time, whereas the parameter μ_1 corresponds to the annual rate of change in annual extreme temperatures.

4.4 Parameter estimation

Many techniques have been proposed for the estimation of parameters in extreme value models. The maximum likelihood method is a general and flexible estimation method for the unknown parameters μ, σ, and ξ within a family F. This technique estimates the parameters to give maximum probability to the observed values. In addition, the method allows for the inclusion of covariates such as time into the model (Katz et al., 2005). This approach is particularly attractive, due to its adaptability to complex constructions of models in techniques based on plausibility (Coles, 2001). It should be mentioned that this estimation technique has an inherent difficulty, in that the maximum likelihood estimators must be within certain limits, so that the conditions of regularity required by the asymptotic properties are valid. That is, if $\xi > -0.5$, the obtained parameter estimators are regular in the sense of having the usual asymptotic properties; when $-1 < \xi < -0.5$, the estimators can generally be obtained, but do not have standard asymptotic properties; and when $\xi < -1$, the estimators are unlikely to be obtained (Smith, 2001).

The maximum likelihood method was chosen in this study to estimate the parameters, mainly because: (a) the data sample for each climate station is sufficiently large (with the exception of Tuxtla Gutiérrez and Toluca, all of the other climate stations have series larger than 40 years), and accordingly it is comparable in performance to other methods; (b) it allows for the easy incorporation of covariate information (non-stationary distributions, which, as we will see, are frequently presented in this study), and (c) it is easier to obtain error limits than in most alternative methods. Eq. (1) assumes that the data are maximum or minimum annual blocks. The estimation of μ, σ, and ξ is performed using the maximum likelihood function for the independent maxima of annual blocks $z_1, ..., z_n$ according to Eq. (3):

$$L(\mu, \sigma, \xi) = \prod_{i=1}^{k} \frac{dG(z_i; \mu, \sigma, \xi)}{dz_i} \quad (3)$$

4.5 Return levels

When considering the extreme values of a random variable, the interest lies in determining the level of return of an extreme event, which is defined as a certain value z_p. In that regard, p is the probability that the z value is exceeded in a year or, alternatively, the level that is expected to be exceeded on average once every $1/p$ years ($1/p$ is often referred to as the return period). In the terminology of extreme values, z_p is the level of return associated with the return period $1/p$ (Cooley et al., 2007), and basically refers to the average waiting time until the z level is exceeded again.

The return level is obtained from the GEV distribution by the cumulative distribution function, which is equal to the desired probability/quantile ratio, 1-p. Estimates of the return levels for the distribution of maximum or minimum annual values can be obtained with Eq. (4), by obtaining estimators of their parameters by the maximum likelihood method:

$$z_p = \begin{cases} \mu - \frac{\sigma}{\xi}[1 - y_p^{-\xi}], \textit{for } \xi \neq 0 \\ \mu - \sigma \log y_p, \textit{for } \xi = 0 \end{cases} \quad (4)$$

where $p = -\log(1 - p)$. In addition, by the delta method (Eq. [5]):

$$Var(z_p) \cong \nabla z_p^T V \nabla z_p \quad (5)$$

where V is the variance-covariance matrix of (μ, σ, ξ), and with Eq. (6):

$$\nabla z_p^T = \left[\frac{\partial z_p}{\partial \mu}, \frac{\partial z_p}{\partial \sigma}, \frac{\partial z_p}{\partial \xi}\right] \quad (6)$$

The above is evaluated in (μ, σ, ξ). Caution should be exercised in interpreting inferences of return levels, especially for long periods of return; this is because the normal approximation to the distribution of the maximum likelihood estimator may be poor, and generally better approximations are obtained with the likelihood profile function. This methodology can be applied when it is required to make an inference regarding some combination of parameters. We can obtain confidence intervals for any z_p return level. This requires a reparameterization of the GEV model, so that z_p is one of the parameters of the model; the log-likelihood profile is obtained by maximization with respect to the remaining parameters in the usual way (Coles, 2001) and is obtained by means of Eq. (7):

$$\mu = z_p + \frac{\sigma}{\xi}\left[1 - \{-\log(1 - p)\}^{-\xi}\right] \quad (7)$$

In this way, the GEV model is expressed in terms of the parameters (z_p, σ, ξ). For the choice of the GEV model and to evaluate the strength of the evidence of more complex models (stationary or non-stationary), the criteria of the likelihood ratio test were applied, along with those of Akaike and Bayes.

4.6 Likelihood ratio test

By including more parameters in the model, the maximized likelihood function will necessarily increase (Coles, 2001), and this method confirms whether the improvement is statistically significant. The test compares two nested models, and thus one model, a base model, must be contained in another model with more parameters.

Formally, the likelihood ratio test (LRT) says that if you have two models, one called M_0 which is the simplest model adjusted to the extreme data set, and another called M_1 to which a covariate has been added to improve the behavior of the same extreme data, then a proof of the validity of the model M_0 relative to the model M_1 at the level of significance α is to reject M_0 in favor of M_1 if:

$$D = 2\{l_1(M_1) - l_0(M_0)\} > c_\alpha \quad (8)$$

where c_α is the quantile of the distribution. In Eq. (8), l_1 (M_1) is the maximized likelihood logarithm for the M_1 model, and l_0 (M_0) the maximized likelihood logarithm for the M_0 model.

4.7 Akaike and Bayes information criteria

Alternatives to the LRT for comparing the relative quality of a statistical model include the Akaike information criterion (AIC) and the Bayes information criterion (BIC), which were also used in the selection of the best model for adjustment. None of these criteria require a nested model as in the LRT. The AIC is defined according to Eq. (9):

$$\text{AIC (p)} = 2n_p - 2l \quad (9)$$

where n_p is the number of parameters in a model of order p, and l is its maximized value of log-likelihood (Thiombiano et al., 2017). The best model is the one with the smallest AIC value (Katz, 2013; Mondal and Mujumdar, 2015). Similarly, for the adjustment of a model of order p to data with a sample size of n, the BIC is determined with Eq. (10):

$$\text{BIC (p)} = n_p (\ln nn) - 2l \quad (10)$$

Both the AIC and BIC attempt to counteract the problem of over adjusting a model by adding more parameters, through the incorporation of a penalty based on the number of parameters (Panagoulia et al., 2013). The BIC is more parsimonious than the AIC. Among the candidate models, the model with the lowest AIC/BIC ratio is preferred.

Given that the database for each city appears to be sufficiently large (n > 30 years), the maximum likelihood method is confirmed for the estimation of the three parameters of the GEV distribution. This is basically because the method easily incorporates covariable information into the estimates of the parameters. Besides, it has a series of attractive properties and it seems to be more suitable for situations in which climate change within the sample analyzed cannot be ignored (Kharin and Zwiers, 2005).

The modeling was supported by the free software R and the in2extRemes package that is designed to be used in the analysis of extreme weather and climate events (Gilleland and Katz, 2005, 2013).

5. Results and discussion

In this section we present and analyze the results of the parametric approach based on the GEV distribution for modeling the maximum annual value of the TXX and TNN for each of the selected urban areas in Mexico. The data series are analyzed in each climatological station, the use of stationary and non-stationary models is evaluated, and a statistical evaluation of the changes in TXX and TNN is presented.

We modeled the data series through the GEV distribution of three parameters, using stationary and non-stationary models for periods that varied from 83 years (Veracruz) to 31 years (Tuxtla Gutiérrez); the other cities had intermediate periods (Table I). The inclusion of non-stationarity is plausible for our modeling approach, as can be visualized for many locations. As an example, time series of TXX (Figs. 4, 6, 8, and 10) and TNN (Figs. 5, 7, 9, and 11) are shown for four of the 12 urban areas (Tijuana, Guadalajara, Toluca, and Puebla), with a trend line using Sen's slope estimator. The graphs for several cities show a clear trend in the maximum and minimum annual data. The graphical analysis and results of the Mann-Kendall trend test justify the use of non-stationary GEV models over time as a covariate. The trends shown are statistically significant with a p-value < 0.05, except for the TXX of Toluca, whose trend is significant with a p-value < 0.1, and the TXX of Tijuana, whose trend is not significant.

The time series of TXX and TNN were used to estimate the parameters in the distribution of GEV with and without trends, as well as the periods of

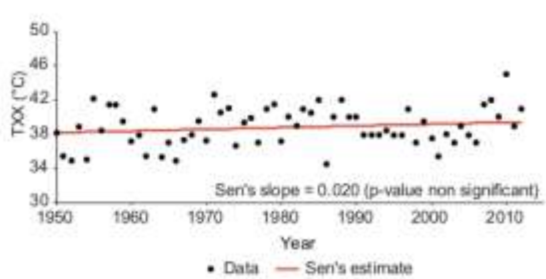

Fig. 4. Trend of extreme maximum temperature (TXX) in Tijuana from 1950 to 2012.

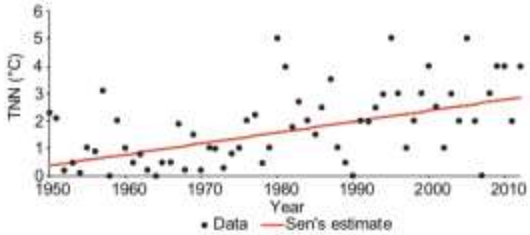

Fig. 5. Trend of extreme minimum temperature (TNN) in Tijuana from 1950 to 2012.

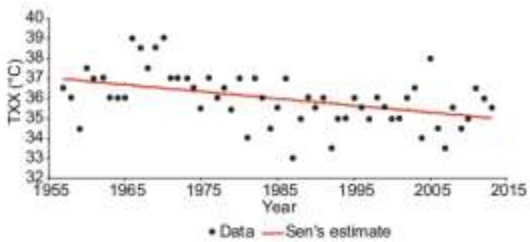

Fig. 6. Trend of extreme maximum temperature (TXX) in Guadalajara from 1957 to 2013.

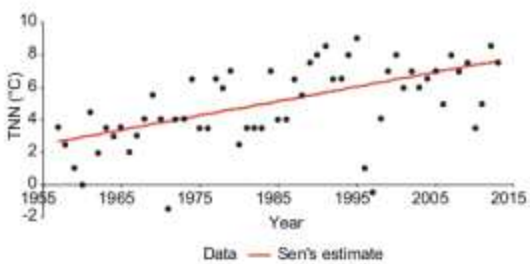

Fig. 7. Trend of extreme minimum temperature (TNN) in Guadalajara from 1957 to 2013.

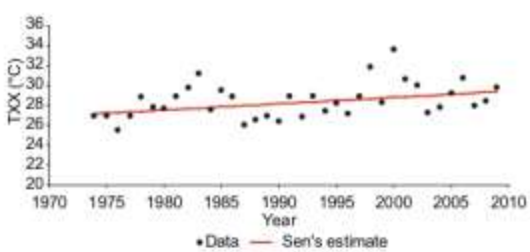

Fig. 8. Trend of extreme maximum temperature (TXX) in Toluca from 1974 to 2009.

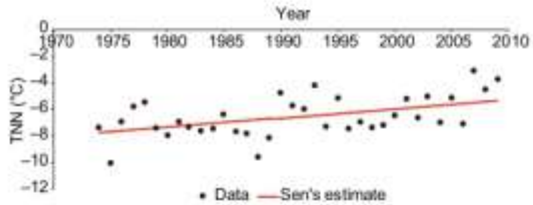

Fig. 9. Trend of extreme minimum temperature (TNN) in Toluca from 1974 to 2009.

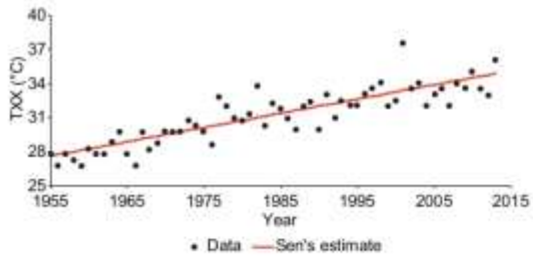

Fig. 10. Trend of extreme maximum temperature (TXX) in Puebla from 1955 to 2013.

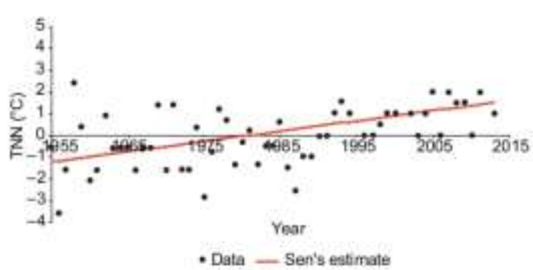

Fig. 11. Trend of extreme minimum temperature (TNN) in Puebla from 1955 to 2013.

return. The models were adjusted to the maximum annual temperature and minimum annual temperature of each of the 16 climate stations using the maximum likelihood (ML) method.

An attempt was made to improve the modeling approach by allowing the location parameter (μ) to depend on time. As mentioned, three model selection criteria (AIC, BIC, and LRT) were used to select the best model from a collection of nested models. The best adjustment models for TXX and TNN through the GEV distributions, as selected by the criteria separately listed for each urban area, are summarized in Table II.

Table II. Parameter estimates and criteria of the constant and linear models for μ in the generalized extreme values (GEV) model applied to temperature extreme data.

City	GEV parameters	TXX	TNN
Aguascalientes	Constant model: μ, σ, ξ, AIC, BIC	34.25, 1.37, –0.066, 251.19, 257.76	–2.29, 2.26, –0.35, 296.46, 303.03
	Linear model: $\mu_0, \mu_1, \sigma, \xi$, AIC, BIC, LRT	33.9, 0.009, 1.33, –0.028, 252.31, 261.07, 0.88	–4.4, 0.073, 1.90, –0.57, 259.54, 268.3, 38.9*
Mexicali	Constant model: μ, σ, ξ, AIC, BIC	46.74, 1.38, –0.17, 231.76, 238.19	–1.73, 2.91, –0.49, 305.21, 311.6
	Linear model: $\mu_0, \mu_1, \sigma, \xi$, AIC, BIC, LRT	45.87, 0.03, 1.31, –0.18, 226.39, 234.91, 7.36*	–4.13, 0.08, 2.28, –0.49, 275.81, 284.38, 31.4*
Tijuana	Constant model: μ, σ, ξ, AIC, BIC	38.03, 2.17, –0.23, 285.58, 292.01	1.14, 1.06, 0.04, 215.85, 222.28
	Linear model: $\mu_0, \mu_1, \sigma, \xi$, AIC, BIC, LRT	37.14, 0.03, 2.10, –0.24, 283.71, 292.29, 3.87*	027, 0.03, 1.05, –0.14, 202.9, 211.48, 14.95*
Tuxtla Gutiérrez	Constant model: μ, σ, ξ, AIC, BIC	40.29, 1.27, –0.70, 94.30, 98.61	10.48, 1.46, –0.45, 111.66, 115.96
	Linear model: $\mu_0, \mu_1, \sigma, \xi$, AIC, BIC, LRT	40.33, –0.003. 1.25, 96.13, 101.86, 0.18	9.06, 0.09, 1.17, –0.47, 99.10, 104.84, 14.55*
Úrsula Coapa (CDMX)	Constant model: μ, σ, ξ, AIC, BIC	32.22, 1.58, –0.36, 162.98, 168.27	0.57, 1.55, –0.15, 171.35, 176.63
	Linear model: $\mu_0, \mu_1, \sigma, \xi$, AIC, BIC, LRT	31.53, 0.03, 1.46, –0.27, 163.25, 170.3, 1.73	–0.71, 0.061, 1.32, –0.10, 161.25, 168.3, 12.1*
Gran Canal (CDMX)	Constant model: μ, σ, ξ, AIC, BIC	32.1, 1.23, –0.04, 206.15, 212.28	
	Linear model: $\mu_0, \mu_1, \sigma, \xi$, AIC, BIC, LRT	32.32, –0.008, 1.21, –0.032, 207.33, 215.5, 0.81	
Milpa Alta (CDMX)	Constant model: μ, σ, ξ, AIC, BIC	28.59, 1.49, –0.15, 167.85, 173.13	–0.50, 1.66, –0.43, 163.89, 169.17
	Linear model: $\mu_0, \mu_1, \sigma, \xi$, AIC, BIC, LRT	29.19, –0.03, 1.38, –0.08, 167.29, 174.33, 2.56	0.22, –0.04, 1.48, –0.26, 164.35, 171.39, 1.54
León	Constant model: μ, σ, ξ, AIC, BIC	35.03, 1.39, –0.19, 207.23, 213.31	1.47, 1.83, –0.34, 228.35, 234.42
	Linear model: $\mu_0, \mu_1, \sigma, \xi$, AIC, BIC, LRT	34.53, 0.02, 1.35, –0.17, 207.23, 213.21, 2.1	–0.46, 0.08, 1.58, –0.56, 198.74, 206.84, 31.6*
Guadalajara	Constant model: μ, σ, ξ, AIC, BIC	35.48, 1.27, –0.24, 197.58, 203.71	4.35, 2.62, –0.53, 261.87, 268.0
	Linear model: $\mu_0, \mu_1, \sigma, \xi$, AIC, BIC, LRT	36.61, –0.04, 1.16, –0.28, 186.47, 194.64, 13.1*	1.61, 0.10, 2.19, –0.61, 238.0, 246.17, 25.9*
Aculco (ZMVM)	Constant model: μ, σ, ξ, AIC, BIC		–2.15, 2.09, –0.61, 171.99, 177.2
	Linear model: $\mu_0, \mu_1, \sigma, \xi$, AIC, BIC, LRT		0.93, –0.13, 1.66, –0.79, 145.48, 152.43, 28.5*
Toluca (ZMVM)	Constant model: μ, σ, ξ, AIC, BIC	27.71, 1.39, –0.04, 141.63, 146.38	–7.1, 1.46, –0.25, 136.5, 141.25
	Linear model: $\mu_0, \mu_1, \sigma, \xi$, AIC, BIC, LRT	26.61, 0.06, 1.18, 0.047, 136.14, 142.47, 7.5*	–8.4, 0.08, 1.27, –0.34, 126.02, 132.35, 12.5*
Chapingo (ZMVM)	Constant model: μ, σ, ξ, AIC, BIC	32.18, 1.39, –0.15, 213.29, 219.42	–3.73, 2.07, –0.35, 245.61, 251.74
	Linear model: $\mu_0, \mu_1, \sigma, \xi$, AIC, BIC, LRT	30.87, 0.05, 1.17, –0.17, 194.2, 202.37, 21.1*	–5.65, 0.07, 1.75, –0.39, 226.11, 234.28, 21.5*
Monterrey	Constant model: μ, σ, ξ, AIC, BIC	40.19, 1.91, –0.16, 263.31, 269.65	–1.25, 3.39, –0.51, 311.1, 317.42
	Linear model: $\mu_0, \mu_1, \sigma, \xi$, AIC, BIC, LRT	40.49, –0.01, 1.89, –0.16, 264.84, 273.29, 0.47	–2.64, 0.06, 3.84, –0.73, 299.38, 307.83, 13.7*
Puebla	Constant model: μ, σ, ξ, AIC, BIC	30.25, 2.37, –0.25, 277.3, 283.53	–0.46, 1.46, –0.24, 220.31, 226.55
	Linear model: $\mu_0, \mu_1, \sigma, \xi$, AIC, BIC, LRT	27.1, 0.12, 0.99, –0.07, 187.62, 195.92, 91.7*	–1.96, 0.05, 1.15, –0.15, 200.58, 208.89, 21.7*
Tlaxcala	Constant model: μ, σ, ξ, AIC, BIC	31.64, 1.19, 0.11, 169.51, 174.93	–2.51, 1.63, –0.49, 166.1, 171.5
	Linear model: $\mu_0, \mu_1, \sigma, \xi$, AIC, BIC, LRT	31.53, 0.005, 1.19, 0.10, 171.3, 178.5, 0.21	–3.53, 0.05, 1.5, –0.66, 153.47, 160.7, 14.6*
Veracruz	Constant model: μ, σ, ξ, AIC, BIC	34.5, 1.46, 0.10, 349.1, 356.4	12.41, 1.73, –0.44, 323.97, 331.3
	Linear model: $\mu_0, \mu_1, \sigma, \xi$, AIC, BIC, LRT	33.01, 0.04, 1.12, 0.14, 310.55, 320.32, 40.5*	12.32, 0.002, 1.73, –0.44, 325.8, 335.57, 0.17

TXX: extreme maximum temperature; TNN: extreme minimum temperature; CDMX: Mexico City; ZMVM: metropolitan area of the Valley of Mexico; AIC: Akaike information criteria; BIC: Bayes information criteria; LRT: likelihood ratio test.

μ_0, μ_1, σ, ξ are parameters of the GEV distribution defined in Eqs. (1) and (2).

*Significance at the 95% confidence level.

In total, 58 models were generated. Table II shows the resulting estimators and the criteria for selecting the best model to be used in the estimation of return periods. According to this table, for the temporal trend of TXX, significant at a 95% confidence level, it can be seen that: (a) 44% of locations (seven urban areas) show a significant trend, (b) 50% of locations (eight urban areas) have no significant trend, and (c) 6% of locations (one urban area) show no trend. For the temporal trend of TNN, also significant at the 95% confidence level, it was found that: (a) 82% of locations (13 urban areas) show a significant trend, (b) 12% of locations (two urban areas) show no significant trend, and (c) 6% of locations (one urban area) show no trend.

According to the shape parameter (ξ), and by performing a detailed analysis, it was found that for the case of TXX, 63% of the climatic stations were adjusted to the Weibull distribution ($\xi < 0$), 25% were adjusted to the Gumbel distribution, 6% were adjusted to the Fréchet distribution, and 6% did not fit any of the three distributions. In the case of TNN, 94% of the analyzed climatic stations were adjusted to the Weibull distribution, and only 6% did not adjust to any of the distributions.

In the case of TXX, which exhibits a significant temporal trend, it was found that 72% was adjusted to the Weibull distribution, 14% to the Gumbel distribution, and 14% to the Fréchet distribution. For TNN, it was found that those that show a significant temporal trend (82%) and those that are stationary (12%) conformed to the Weibull distribution.

Overall, for both extreme temperatures TXX and TNN, it was found that the 57% following the Weibull distribution are statistically significant to the temporal trend at the 95% confidence level. One of the properties of this distribution, which may even be controversial because of the trend found, is that both extreme temperatures have an upper limit that cannot be exceeded.

Figures 12 and 13 describe the temporal trend pattern of decadal trends for the location parameter (μ) of the maximum and minimum temperatures according to non-stationary GEV models (Table II). About the TXX (Fig. 12), the most significant positive trend occurred in the center and east regions (Toluca, Chapingo, Puebla and Veracruz), whereas the lowest trends occurred in the northwest regions (Tijuana and Mexicali).

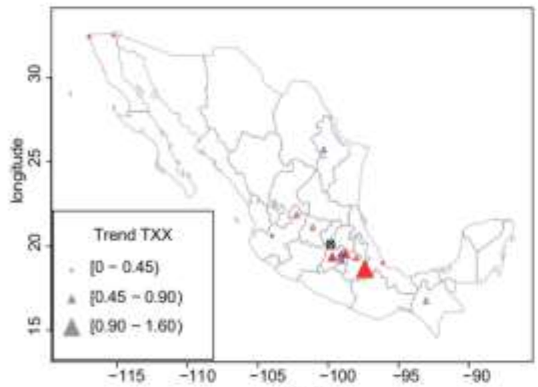

Fig. 12. Spatial patterns of trends of the location parameter (μ) for the maximum temperature. Red (blue) triangles mean positive (negative) values. Full triangles mean significant trends at the 5% level. The symbol ⊗ indicates without change.

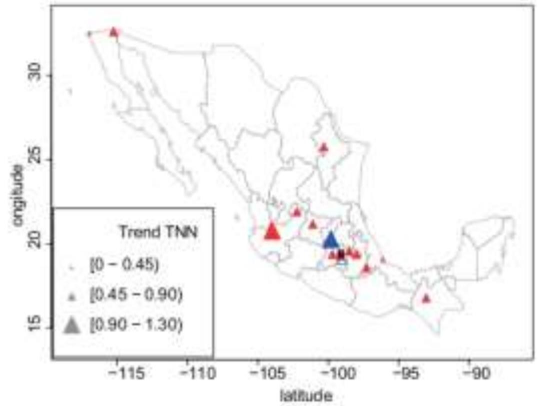

Fig. 13. Spatial patterns of trends of the location parameter (μ) for the minimum temperature. Red (blue) triangles mean positive (negative) values. Full triangles mean significant trends at the 5% level.

Respect to the TNN (Fig. 13), the most significant positive trends were most relevant in different geographical areas of the country, i.e., higher in the west center (Guadalajara and León), southeast (Tuxtla Gutiérrez), some urban areas located in the central part (Úrsula Coapa, Toluca, Chapingo, Tlaxcala and

Puebla), and in the northeast and northwest (Monterrey and Mexicali), whereas the lowest positive trend occurred in the urban area of Tijuana (with a value of 0.30). The most significant negative trend occurred in an urban area.

Once the best models were selected, the return levels of the extreme, maximum, and minimum temperatures were estimated. Tables III and IV present the estimators and confidence intervals for return levels to 10, 20, 50, and 100 years, for both stationary and non-stationary models. The stationary return levels for TXX in Table III, indicate that the values increase for increasingly larger periods (10, 20, 50, and 100 years), except for the urban area of Tuxtla Gutiérrez. In addition, the confidence intervals were increasingly wider as the periods of return increased. In Aguascalientes the TXX can be expected to progressively exceed 37.1 ºC on average every 10 years, 37.9 ºC on average every 20 years, 38.9 ºC on average every 50 years, and 39.7 ºC on average every 100 years. The 95% confidence intervals for these return periods, in ºC, were 36.4-37.8, 37.0-38.9, 37.5-40.4, and 37.8-41.5, respectively.

Among the locations considered in that block, and in the context of the stationary return levels, Monterrey (in the northeast of the country) was associated with the highest return levels, and Milpa Alta (in the metropolitan area of the Valley of Mexico in the center of the country) had the lowest return levels. Based on the 95% confidence interval and according to Table III, we can expect that the largest TXX event recorded for Milpa Alta could reappear for the next 10 years. Moreover, there is a high probability that the annual TXX will exceed the maximum historical value in the next 50 years, except in the sites Gran Canal and Monterrey.

The estimated return levels assume stationarity, meaning that the level of return for a return period is the same for the successive years. This implies that the statistical properties of the parameters μ, σ, and ξ are constant.

In a non-stationary case, the parameters of the GEV distribution vary over time, and the return levels of extreme temperatures will also follow that temporal trend. Under a changing climate, the return value can be interpreted as an extreme quantile of a

Table III. Stationary and non-stationary return levels for extreme maximum temperature and its 95% confidence levels (in parentheses).

Urban zone	Return levels (10 years)	Return levels (20 years)	Return levels (50 years)	Return levels (100 years)
		Stationary return levels (ºC)		
Aguascalientes	37.1 (36.4-37.8)	37.9 (37.0-38.9)	38.9 (37.5-40.4)	39.7 (37.8-41.5)
Tuxtla Gutiérrez	41.7 (41.5-42.0)	41.9 (41.7-42.0)	42.0 (41.8-42.2)	42.0 (41.8-42.2)
Úrsula Coapa	34.7 (34.2-35.2)	35.1 (34.6-35.6)	35.5 (35.0-36.1)	35.8 (35.1-36.4)
Gran Canal	34.7 (34.0-35.4)	35.5 (34.6-36.5)	36.5 (35.1-37.9)	37.2 (35.4-39.1)
Milpa Alta	31.4 (30.7-32.2)	32.2 (31.2-33.1)	33.0 (31.8-34.2)	33.6 (32.0-35.1)
León	37.6 (37.0-38.1)	38.2 (37.5-38.9)	38.9 (37.9-39.8)	39.3 (38.8-40.4)
Monterrey	43.8 (43.0-44.6)	44.7 (43.8-45.6)	45.7 (44.6-46.9)	46.4 (45.0-47.7)
Tlaxcala	34.7 (33.6-35.8)	35.8 (34.1-37.6)	37.5 (34.4-40.5)	38.8 (34.5-43.2)
		Non-stationary return levels (ºC)		
Mexicali	48.5 (48.0-49.1)	49.4 (48.8-50.1)	50.9 (50.1-51.7)	52.7 (51.7-53.7)
Tijuana	41.1 (40.3-41.8)	42.2 (41.3-43.0)	43.9 (42.8-45.0)	45.9 (44.5-47.2)
Guadalajara	38.2 (37.8-38.7)	38.3 (37.7-38.8)	37.6 (36.9-38.3)	36.1 (35.2-36.9)
Toluca	30.0 (28.9-31.0)	31.5 (30.1-32.9)	34.6 (32.4-36.8)	38.6 (35.7-41.5)
Chapingo	33.5 (32.9-34.1)	34.5 (33.8-35.3)	36.6 (35.6-37.6)	39.5 (38.2-40.7)
Puebla	30.2 (29.4-31.0)	32.0 (31.0-32.9)	36.3 (35.1-37.5)	42.8 (41.4-44.2)
Veracruz	36.3 (35.3-37.3)	37.9 (36.2-39.5)	40.7 (37.9-43.5)	44.0 (40.0-48.1)

Table IV. Stationary and non-stationary return levels for extreme minimum temperature and its 95% confidence levels (in parentheses).

Urban zone	Return levels (10 years)	Return levels (20 years)	Return levels (50 years)	Return levels (100 years)
		Stationary return levels (ºC)		
Milpa Alta	1.9 (1.4-2.3)	2.3 (1.8-2.7)	2.6 (2.2-3.1)	2.8 (2.3-3.3)
Veracruz	14.9 (14.6-15.2)	15.3 (15.0-15.6)	15.6 (15.3-16.0)	15.8 (15.5-16.2)
		Non-stationary return levels (ºC)		
Aguascalientes	–1.3 [–1.9-(–0.7)]	-0.3 [–1.0-(0.4)]	2.1 (1.3-3.0)	5.9 (4.9-7.0)
Mexicali	–0.3 [–0.9-(0.3)]	1.0 (0.4-1.6)	3.8 (3.1-4.5)	8.0 (7.1-8.8)
Tijuana	2.6 (1.8-3.4)	3.4 (2.2-4.7)	5.0 (2.8-7.3)	7.1 (3.9-10.3)
Tuxtla Gutiérrez	11.5 (11.1-12.0)	12.7 (12.3-13.2)	15.8 (15.2-16.3)	20.6 (19.9-21.2)
Úrsula Coapa	2.5 (1.7-3.3)	3.8 (2.9-4.8)	6.5 (5.3-7.8)	10.2 (8.6-11.8)
León	2.3 (1.7-2.8)	3.3 (2.7-3.8)	5.8 (5.2-6.5)	9.8 (9.0-10.5)
Guadalajara	5.2 (4.7-5.7)	6.5 (6.1-7.0)	9.8 (9.3-10.2)	14.9 (14.4-15.4)
Aculco	2.6 (2.2-2.9)	2.6 (2.3-2.9)	2.3 (1.9-2.7)	1.7 (1.3-2.1)
Toluca	–5.7 [–6.4-(–5.0)]	–4.6 [–5.3-(–3.8)]	–1.9 [–2.9-(–0.8)]	2.2 (1.0-3.4)
Chapingo	–2.4 [–3.0-(–1.8)]	–1.2 [–1.8-(–0.6)]	1.3 (0.6-2.0)	5.1 (4.3-5.9)
Monterrey	2.1 (1.5-2.8)	3.1 (2.5-3.7)	5.1 (4.5-5.6)	8.0 (7.5-8.6)
Puebla	0.7 (0.2-1.2)	1.8 (1.2-2.4)	3.9 (3.2-4.7)	6.9 (6.0-7.8)
Tlaxcala	–1.3 [–1.7-(–1.0)]	–0.6 [–1.0-(–0.3)]	1.0 (0.6-1.3)	3.5 (3.1-3.9)

temperature distribution that varies over time (for example, a return value of 20 years can be interpreted as a value that has a 5% probability to be exceeded in a particular year).

It is now possible to estimate return levels for any year, which are also presented in Table III. For example, note that the average return levels (in ºC) for Mexicali for 10, 20, 50, and 100 years, are 48.5, 49.4, 50.9 and 52.7, respectively. The confidence intervals at 95% (in ° C) are 48.0-49.1, 48.8-50.1, 50.1-51.7, and 51.7-53.7, respectively. The differences in return levels between stations is remarkable, both in the stationary GEV models and in the non-stationary models. Mexicali, in the northwest of Mexico, is associated with the highest return levels, whereas Milpa Alta, a metropolitan area in Mexico City, has the lowest return levels.

With respect to TNN, Table IV shows that only stations Milpa Alta and Veracruz have stationary return levels, and that the values increase slightly for increasingly large return periods (10, 20, 50, and 100 years). In addition, the confidence intervals remain nearly constant as the periods of return increase. For example, Milpa Alta could expect the TNN to exceed 1.9 ºC on average every 10 years, 2.3 ºC on average every 20 years, 2.6 ºC on average every 50 years, and 2.8 ºC on average every 100 years. The confidence intervals, at 95% (in ºC) are 1.4-2.3, 1.8-2.7, 2.2-3.1, and 2.3-3.3, respectively.

As already mentioned, the estimated return levels assume stationarity, meaning that the level of return for a return period is the same for successive years. This also implies that the statistical properties, as mentioned for TXX, keep the parameters μ, σ, y, and ξ constant.

In a non-stationary case (as with TXX), the parameters vary in time and the return levels of extreme temperatures will follow a similar temporal trend. It is possible to estimate return levels for any year of interest in a time period. The return levels for the non-stationary TNN series are presented in Table IV. Note that the average return levels of 10, 20, 50, and 100 years (in ºC) for Aguascalientes are –1.3, –0.3, 2.1, and 5.9, respectively, whereas their confidence intervals, at 95% and in ºC, progress from –1.9 to –0.7, –1.0 to 0.4, 1.3 to 3.0, and 4.9 to 7.0, respectively.

In the case of a non-stationary series, for both TXX and TNN, a positive trend of the location parameter (μ_1) will be reflected in the positive trend of the return levels (Chen and Chu, 2014). This means that with greater magnitudes of the trend return levels will increase considerably, and threshold values of return levels will contain greater variation over time. As examples of estimators of return levels, the time series of return levels for TXX for the city of Puebla (Fig. 14) and for TNN for the city of Guadalajara (Fig. 15) are plotted, according to the GEV adjustment non-stationary model. The difference in the return level for 2 years for the city of Puebla from the beginning of the period (1955) to the end (2013) is approximately 5 ºC, whereas the difference in the return level of 2 years for the city of Guadalajara from the beginning of the period (1957) to the end (2013) is approximately 3 ºC.

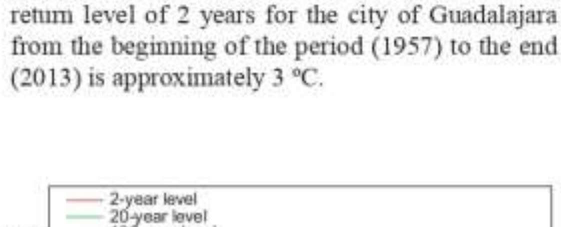

Fig. 14. Time series of extreme maximum temperature (TXX) return levels in Puebla in accordance with the non-stationary generalized extreme value (GEV) model. The red, green, and blue lines represent the return levels of 2, 20, and 100 years, respectively. The black line represents observed values.

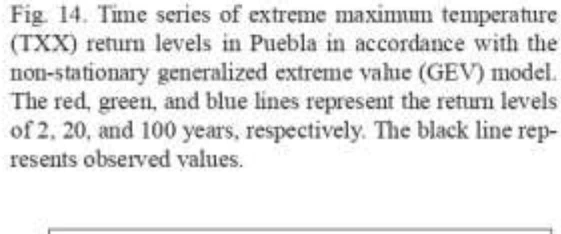

Fig. 15. Time series of extreme minimum temperature (TNN) return levels in Guadalajara in accordance with the non-stationary GEV model. The red, green, and blue lines represent the return levels of 2, 20, and 100 years, respectively. The black line represents observed values.

The application of the stationary and non-stationary GEV distributions has allowed this study to model the behavior of extreme temperatures in some cities of Mexico. Due to the lack of reliable data, only 16 climate stations were used, focusing on 12 urban areas. The latitudinal dispersion of these climatic stations ranged from 16º 45' (Tuxtla Gutiérrez) to 32º 39' (Mexicali), and with altitudes above sea level varying from 4 m (Mexicali) to 2726 m (Toluca). This resulted in several types of climates according to the geographical location (García-Cueto et al. 2018), making the analysis by chosen city even more interesting. This is particularly true for those cities that show significant trends and periods of return that could put the adaptation of people and the urban ecosystem at risk, particularly the fauna and flora. We found that the TXX is increasing in Mexicali, Tijuana, Toluca, Chapingo, Puebla and Veracruz, and no significant changes were detected in the other 10 urban zones. A larger number of climatological stations indicate increasing TNN compared to TXX, namely Aguascalientes, Mexicali, Tijuana, Tuxtla Gutiérrez, Úrsula Coapa, León, Guadalajara, Aculco, Toluca, Chapingo, Monterrey, Puebla and Tlaxcala. Non significant increases were detected in only two stations, i.e., Milpa Alta and Veracruz.

A comparison of the obtained results with those from studies using the ETCDDI indices shows similarities and some differences. For example, García-Cueto et al. (2018) used the same database herein and found a statistically significant increasing trend in the TX90 (warm days) and TN90 (warm nights) indices for Aguascalientes, whereas for Milpa Alta, both indices (TX90 and TN90) decreased significantly. The difference is between the TXX (stationary in this study) and TX90 (increasing trend) for Aguascalientes; in the case of Milpa Alta, there are coincidences in both indices (TXX with TX90 and TNN with TN90) that show decreasing trends.

At the country level, according to Gosling et al. (2011), Mexico has experienced a generalized warming since 1960. The frequency of cold days has decreased, and the frequency of warm nights has increased. There has also been a general increase in average winter temperatures in the country as a result of human influences on climate. Thus, during the winter season, the occurrences of warm temperatures are more frequent, and those of cold temperatures are less frequent. For the A1B emissions scenario, the projected temperature increases of the Coupled Model Intercomparison Project Phase 3 (CMIP3) over Mexico are approximately 4 ºC near the US border, with increases in the rest of the country between 2.5 and 3.5 ºC. This implies that the influence of GHGs will have an additive effect on the potential warming caused by urbanization. This can become a major problem affecting city dwellers both positively and negatively, depending on their latitudinal location.

Significant trends in extreme maximum and minimum temperatures found in many parts of the world (Heim Jr., 2015; Easterling et al., 2016; Houngninou et al., 2017) reinforce the results obtained here. In the US, extremely hot maximum and minimum temperatures have shown increasing trends between the 20th and 21st centuries and during the last four decades (1971-2013), whereas the presence of extremely low and minimum temperatures has decreased during these periods (Hartmann et al., 2013).

The application of a theory of extreme events to the TXX and TNN in 16 climatological stations located in 12 urban areas of Mexico, in time series with different periods, showed general trends in urban warming, especially at night. However, values varied from city to city. A less clear detection signal was the diurnal heating. Although the causes for this behavior of heterogeneous trends for TXX and TNN may be of purely local origin and caused by the dynamics of urbanization (land use change, anthropogenic activities), it cannot be ruled that they could be caused by some other climatic phenomena of a greater scale. For example, Mexico could be exposed to blocking patterns, or modes of climate variability, such as the El Niño Southern Oscillation, Pacific Decadal Oscillation, North Atlantic Oscillation, or the Madden-Julian Oscillation, among others. These could be causal factors that contribute to thermal trends since in other regions of the world they have significantly influenced the behavior of extreme temperatures (Arblaster and Alexander, 2012; Parker et al., 2014; Burgess and Klingaman, 2015; Matsueda and Takaya, 2015). All these factors are considered important for possible attribution but are not the object of this study.

It is well known that cities will remain the most vulnerable geographic spaces, especially in developing countries such as Mexico, as they often concentrate large populations without adequate infrastructure. Thus, knowledge of regions where the climate is unstable (changing), and the knowledge that extreme climate events are not controllable, but have showed signals of an increasing trend, will serve to generate some potential urban adaptation strategies for facing current and future extreme temperatures. For example, such temperatures can be addressed by redesigning the urban space (making it safe, ecological and acceptable) to reduce vulnerability and strengthen urban water security. It should be noted that each city is a case of analysis, and that an adequate scheme of sustainable urban planning can only be accomplished through the participation of governmental authorities, productive sectors, academics, and local actors.

6. Conclusions

This study modeled the TXX and TNN recorded in 16 climatological stations corresponding to 12 cities in Mexico, for periods that varied according to the series of available data. The longest record corresponded to Veracruz with 85 years (1930-2014), and the shortest to Tuxtla Gutiérrez with 31 years (1980-2010). Through the application of the non-parametric Mann-Kendall test and the Sen method, a trend towards urban warming was detected, but no homogeneous behavior in all cities analyzed was found. An important observation was the significant prevalence of non-stationary series with the TXX in half of the cities analyzed; only Guadalajara, located in the center-west of the country, presented a significant negative trend, perhaps due the effect of "diming" by increases in aerosol pollution (Fonseca-Hernández et al., 2018). Therefore, the annual trends in daytime warming, represented by TXX, are not necessarily identical in all selected urban areas of Mexico. In the case of the TNN, which is related to night warming, the behavior was more uniform. Specifically, 90% of the cities are non-stationary with a significant positive trend, and only two areas presented a stationary series: one urban area located to the east of the metropolitan area of the Valley of Mexico (Milpa Alta), and another on the coast of the Gulf of Mexico (Veracruz). With the adjustment of the non-stationary GEV distribution to the data set and by incorporating the trend of the location parameter, the trends of the return levels of 10, 20, 50, and

100 years were estimated, while keeping the shape and scale parameters constant.

The results are very similar to those from non-parametric trend detection methods, both for TXX and TNN. This confirms the non-stationary behavior of half of the stations for TXX, and 90% of the stations for TNN. Return periods of the thermal extremes estimated in a changing climate for many of the cities analyzed in this study vary significantly, and the regularity with which extreme temperatures are occurring is becoming more frequent. Thus, statistical modeling should consider this behavior, due to its importance for risk assessments for human health, flora and fauna, and urban infrastructure. The proposed non-stationary GEV model has provided new and important information concerning changes in extreme temperatures, and by estimating return periods, it has provided their probability of recurrence. Some main modes of climate variability as causal mechanisms of attribution of extreme temperatures have not been studied, making it a pending task.

Acknowledgments
The authors thank the United Nations Development Program and the National Institute of Ecology and Climate Change of Mexico for supporting this research. We would also like to thank the National Meteorological Service of Mexico for providing daily climate information for this study.

References
Alexander LV, Zhang X, Peterson TC, Caesar J, Gleason B, Klein Tank AMG, Haylock M, Collins D, Trewin B, Rahimzadeh F, Tagipour A, Rupa Kumar K, Revadekar J, Griffiths G, Vincent L, Stephenson DB, Burn J, Aguilar E, Brunet M, Taylor M, New M, Zhai P, Rusticucci M, Vázquez-Aguirre JL. 2006. Global observed changes in daily climate extremes of temperature and precipitation. Journal of Geophysical Resources 111: D05109. https://doi.org/10.1029/2005JD006290

Almazroui M, Islam MN, Dambul R, Jones PD. 2014. Trends of temperature extremes in Saudi Arabia. International Journal of Climatology 34: 808-826. https://doi.org/10.1002/joc.3722

Arblaster JM, Alexander LV. 2012. The impact of the El Nino-Southern Oscillation on maximum temperature extremes. Geophysical Resource Letters 39: L20702. https://doi.org/10.1029/2012GL053409

Beniston M, Stephenson DB, Christensen OB, Ferro AT, Frei Ch, Goyette S, Halsnaes K, Holt T, Jylhä K, Koffi B, Palutikof J, Schöll R, Semmler T, Woth K. 2007. Future extreme events in European climate: An exploration of regional climate model projections. Climatic Change 81: 71-95. https://doi.org/10.1007/s10584-006-9226-z

Boucefiane A, Meddi M. 2019. Regional growth curves and extreme precipitation events estimation in the steppe area of northwestern Algeria. Atmósfera 32: 287-303. https://doi.org/10.20937/ATM.2019.32.04.03

Brown SJ, Caesar J, Ferro CAT. 2008. Global changes in extreme daily temperature since 1950. Journal of Geophysical Research: Atmosphere 113: D05115. https://doi.org/10.1029/2006JD008091

Burgess ML, Klingaman NP. 2015. Atmospheric circulation patterns associated with extreme cold winters in the UK. Weather 70: 211-217. https://doi.org/10.1002/wea.2476

Burgman M, Franklin J, Keith RK, Hosack RG, Peters WG, Sisson AS. 2012. Modeling extreme risks in ecology. Risk Analysis 32: 1956-1966. https://doi.org/10.1111/j.1539-6924.2012.01871.x

Burn DH, Hag Elnur AM. 2002. Detection of hydrological trends and variability. Journal of Hydrology 255: 107-122. https://doi.org/10.1016/S0022-1694(01)00514-5

Caesar J, Alexander LV, Trewin B, Tse-ring K, Sorany L, Vuniyayawa V, Keosavang N, Shimana A, Htay MM, Karmacharya J, Jayasinghearachchi DA, Sakkamart J, Soares E, Hung LT, Thuong LT, Hue CT, Dung NTT, Hung PV, Cuong HD, Cuong NM, Sirabaha S. 2011. Changes in temperature and precipitation extremes over the Indo-Pacific region from 1971 to 2005. International Journal of Climatology 31: 791-801. https://doi.org/10.1002/joc.2118

Caloiero T. 2017. Trend of monthly temperature and daily extreme temperature during 1951-2012 in New Zealand. Theoretical Applied of Climatology 129: 111-127. https://doi.org/ 10.1007/s00704-016-1764-3

Cavazos T, Rivas D. 2004. Variability of extreme precipitation events in Tijuana, Mexico. Climate Research 25: 229-243. https://doi.org/10.3354/cr025229

Cavazos T, Salinas JA, Martínez B, Colorado G, de Grau P, Prieto González R, Bravo ME. 2013. Actualización de escenarios de cambio climático para México como parte de los productos de la quinta comunicación nacional. Informe final. CICESE-IMTA-CCA UNAM, 150 pp. Available at: https://www.researchgate.net/publication/321274898 (last accessed on June 1, 2019).

Chen YR, Chu P-S. 2014. Trends in precipitation extremes and return levels in the Hawaiian Islands under a changing climate. International Journal of Climatology 34: 3913-3925. https://doi.org/10.1002/joc.3950

Chen W, Chen C, Li L, Xing L, Huang G, Wu C. 2015. Spatio-temporal analysis of extreme hourly precipitation patterns in Hainan Island, South China. Water 7: 2239-2253. https://doi.org/10.3390/w7052239

CIDOC-SHF. 2011. Current housing situation in Mexico 2011. Fundación Centro de Investigación y Documentación de la Casa-Sociedad Hipotecaria Federal. Available at: http://doc.shf.gob.mx/English/Press/Publications/Documents/EAVM%20INGLES%20 2011.pdf (last accessed on June 15, 2019).

Coles S. 2001. An introduction to statistical modeling of extreme values. 2nd ed. Springer Series in Statistics, London.

Colorado-Ruiz G, Cavazos T, Salinas JA, De Grau P, Ayala R. 2018. Climate change projections from Coupled Model Intercomparison Project phase 5 multi-model weighted ensembles for Mexico, the North American monsoon and the mid-summer drought region. International Journal of Climatology 38: 5699-5716. https://doi.org/10.1002/joc.5773

Cooley D, Nychka D, Naveau P. 2007. Bayesian spatial modeling of extreme precipitation return levels. Journal of the American Statistical Association 102: 824-840. https://doi.org/10.1198/016214506000000780

Coutts MA, Tapper JN, Beringer J, Loughnan M, Demuzere M. 2012. Watering our cities: The capacity for water sensitive urban design to support urban cooling and improve human thermal comfort in the Australian context. Progress in Physical Geography 37: 2-28. https://doi.org/10.1177/0309133312461032

De Munck C, Lemonsu A, Masson V, Le Bras J, Bonhomme M. 2018. Evaluating the impacts of greening scenarios on thermal comfort and energy and water consumptions for adapting Paris city to climate change. Urban Climate 23: 260-286. https://doi.org/10.1016/j.uclim.2017.01.003

Della-Marta MP, Haylock RM, Luterbacher J, Wanner H. 2007. Doubled length of western European summer heat waves since 1880. Journal of Geophysical Research 112: D15103. https://doi.org/10.1029/2007JD008510

Dixon P, Ellison A, Gotelli N. 2005. Improving the precision of estimates of the frequency of rare events. Ecology 86: 1114-1123. https://doi.org/10.1890/04-0601

Dumitrescu A, Bojariu R, Birsan M-V, Marin L, Manea A. 2015. Recent climatic changes in Romania from observational data (1961-2013). Theoretical Applied Climatology 122: 111-119. https://doi.org/10.1007/s00704-014-1290-0

El Adlouni S, Ouarda TBMJ, Zhang X, Roy R, Bobée B. 2007. Generalized maximum likelihood estimators for the nonstationary generalized extreme value model. Water Resources Research 43: W03410. https://doi.org/10.1029/2005WR004545

Easterling DR, Kunkel KE, Wehner MF, Sun L. 2016. Detection and attribution of climate extremes in the observed record. Weather and Climate Extremes 11: 17-27. https://doi.org/10.1016/j.wace.2016.01.001

Fengjin X, Lianchun S. 2011. Analysis of extreme low-temperature events during the warm season in Northeast China. Natural Hazards 58: 1333. https://doi.org/10.1007/s11069-011-9735-6

Fisher RA, Tippett LHC. 1928. Limiting forms of the frequency distribution of the largest or smallest member of a sample. Proceedings of the Cambridge Philosophical Society 24: 180-190. https:// doi.org/10.1017/S0305004100015681

Fonseca-Hernández M, Tereshchenko I, Mayor Y, Figueroa-Montaño A, Cuesta-Santos O, Monzón C. 2018. Atmospheric pollution by PM_{10} and O_3 in the Guadalajara metropolitan area, Mexico. Atmosphere 9: 243. https://doi.org/10.3390/atmos9070243

Friederichs P. 2010. Statistical downscaling of extreme precipitation events using extreme value theory. Extremes 13: 109. https://doi.org/10.1007/s10687-010-0107-5

Furió D, Meneu V. 2011. Analysis of extreme temperatures for four sites across Peninsular Spain. Theoretical and Applied Climatology 104: 83-99. https://doi.org/10.1007/s00704-010-0324-5

Gao Y, Fu JS, Drake JB, Liu Y, Lamarque J-F. 2012. Projected changes of extreme weather events in the eastern United States based on a high-resolution climate modeling system. Environmental Research Letters 7: 1-12. https://doi.org/10.1088/1748-9326/7/4/044025

García-Cueto R, Tejeda-Martínez A, Jáuregui E. 2010. Heat waves and heat days in an arid city in the northwest of México: current trends and in climate change scenarios. International Journal of Biometeorology 54: 335-345. https://doi.org/10.1007/s00484-009-0283-7

García-Cueto OR, Santillán-Soto N, Quintero-Núñez M, Ojeda-Benítez S, Velázquez-Limón N. 2013. Extreme temperature scenarios in Mexicali, México under climate change conditions. Atmósfera 26: 509-520. https://doi.org/10.1016/S0187-6236(13)71092-0

García-Cueto OR, Cavazos T, de Grau P, Santillán-Soto N. 2014. Analysis and modeling of extreme temperatures in several cities in northwestern Mexico under climate change conditions. Theoretical and Applied Climatology 116: 211-225. https://doi.org/10.1007/s00704-013-0933-x

García-Cueto OR, Santillán-Soto N, López-Velázquez JE, Reyes-López J, Cruz-Sotelo S, Ojeda-Benítez S. 2018. Trends of climate change indices in some Mexican cities from 1980 to 2010. Theoretical and Applied Climatology 137: 775-790. https://doi.org/10.1007/s00704-018-2620-4

Gilleland E, Katz R. 2005. Extremes toolkit (extRemes): Weather and climate applications of extreme value statistics. Available at: https://www.lmd.jussieu.fr/~li/atelier_cc/tutorial_extremes.pdf (last accessed on September 20, 2018).

Gilleland E, Katz R. 2006. Analyzing seasonal to interannual extreme weather and climate variability with the extremes toolkit (extRemes). In: 18th Conference on Climate Variability and Change, 86th American Meteorological Society (AMS) Annual Meeting, Atlanta, Georgia, January 29-February 2. Available at: https://ams.confex.com/ams/Annual2006/techprogram/paper_101830.htm (last accessed on April 15, 2019).

Gilleland E, Katz, RW. 2013. in2extRemes: Into the R Package extRemes extreme value analysis for weather and climate applications. NCAR/TN-523+STR Technical Note. National Center for Atmospheric Research, Boulder, Colorado. Available at: https://opensky.ucar.edu/islandora/object/technotes%3A534/datastream/PDF/view (last accessed on May 2, 2019).

Gosling SN, Dunn R, Carrol F, Christidis N, Fullwood J, de Gusmao D, Golding N, Good L, Hall T, Kendon L, Kennedy J, et al. 2011. Climate: Observations, projections and impacts: Mexico. UK Met Office. Nottingham ePrints, Nottingham, UK. Available at: http://www.unscn.org/files/NutCC/Mexico.pdf (last accessed on August 24, 2019).

Grotjahn R, Black R, Leung R, Wehner FM, Barlow M, Bosilovich M, Gershunov A, Gutowski JW, Gyakum RJ, Katz RW, Lee Y-Y, Lim Y-K, Prabhat. 2016. North American extreme temperature events and related large-scale meteorological patterns: A review of statistical methods, dynamics, modeling, and trends. Climate Dynamics 46: 1151-1184. https://doi.org/10.1007/s00382-015-2638-6

Guan Y, Zhang X, Zheng F, Wang B. 2015. Trends and variability of daily temperature extremes during 1960-2012 in the Yangtze River Basin, China. Global Planetary Change 124: 79-94. https://doi.org/10.1016/j.gloplacha.2014.11.008

Hartmann DL, Klein Tank AMG, Rusticucci M, Alexander LV, Brönnimann S, Charabi, Y, Dentener FJ, Dlugokencky EJ, Easterling DR, Kaplan A, Soden BJ, Thorne PW, Wild M, Zhai PM. 2013. Observations: atmosphere and surface. In: Climate Change 2013: The Physical Science Basis. Contribution of Working Group I to the Fifth Assessment Report of the Intergovernmental Panel on Climate Change (Stocker TF, Qin D, Plattner G-K, Tignor M, Allen SK, Boschung, J, Nauels A, Xia Y, Bex V, Midgley PM, Eds.). Cambridge University Press, Cambridge, United Kingdom and New York, NY, USA.

Hatfield JL, Prueger JH. 2015. Temperature extremes: Effect on plant growth and development. Weather and Climate Extremes 10: 4-10. https://doi.org/10.1016/j.wace.2015.08.001

Heim Jr. RR. 2015. An overview of weather and climate extremes. Weather and Climate Extremes 10: 1-9. https://doi.org/10.1016/j.wace.2015.11.001

Helsel DR, Hirsch MR. 1992. Statistical methods in water resources. Elsevier, New York.

Hernández AR, Galeana GJ, Villegas BI. 2014. La urbanización en México 2010-2030: un esbozo de los retos y oportunidades asociados al crecimiento urbano y regional. En: La situación demográfica de México 2014. Consejo Nacional de Población, México, 139-164.

Houngninou BE, Allé CSU, Kougbéagbédé H, Guédjé KF. 2017. Changes in daily temperature extremes over Benin between 1970 and 2015. International Journal of Advances Research 5: 108-113. https://doi.org/10.21474/IJAR01/5944

IPCC. 2013. Climate change 2013: The physical science basis. Contribution of Working Group I to the Fifth Assessment Report of the Inter-governmental Panel on Climate Change (Stocker TF, Qin D, Plattner G.-K, Tignor M, Allen PM, Boschung J, Nauels A, Xia Y, Bex V, Midgley PM, Eds.). Cambridge University Press, Cambridge, United Kingdom and New York, NY, USA.

Jain S, Lall U. 2001. Magnitude and timing of annual maximum floods, trends and large-scale climatic associations for the Blacksmith Fork River, Utah. Water Resources Research 36: 3641-3651. https://doi.org/10.1029/2000WR900183

Jentsch A, Kreyling J, Beierkuhnlein C. 2007. A new generation of climate change experiments: Events, not trends. Frontiers in Ecology and the Environment 5: 315-324. https://doi.org/10.1890/1540-9295(2007)5[365:ANGOCE]2.0.CO;2

Katz R, Parlange M, Naveau P. 2002. Statistics of extremes in hydrology. Advances in Water Resources 25: 1287-1304. https://doi.org/10.1016/S0309-1708(02)00056-8

Katz R, Brush G, Parlange M. 2005. Statistics of extremes: Modeling ecological disturbances. Ecology 86: 1124-1134. https://doi.org/10.1890/04-0606

Katz RW. 2013. Statistical methods for nonstationary extremes. In: Extremes in changing climate (Aghakouchak A, Easterling D, Hsu K, Schubert S, Sorooshian S, Eds.). Water Science and Technology Library, vol 65, Springer, Dordrecht, 15-37.

Kharin VV, Zwiers FW. 2005. Estimating extremes in transient climate change simulations. Journal of Climate 18: 1156-1173. https://doi.org/10.1175/JCLI3320.1

Koutsoyiannis D. 2004. Statistics of extremes and estimation of extreme rainfall: I. Theoretical investigation/ Statistiques de valeurs extrêmes et estimation de précipitations extrêmes: I. Recherche théorique. Hydrological Sciences Journal 49: 575-590. https://doi.org/10.1623/hysj.49.4.575.54430

Kendall MG. 1975. Rank correlation methods. Charles Graffin, London.

Kim YH, Min SK, Zhang X, Zwiers F, Alexander LV, Donat MG, Tung YS. 2015. Attribution of extreme temperature changes during 1951-2010. Climate Dynamics 46: 1769-1782. https://doi.org/10.1007/s00382-015-2674-2

Krausmann F, Wiedenhofer D, Lauk Ch, Haas W, Tanikawa H, Fishman T, Miatto A, Schandl H, Haberl H. 2017. Global socioeconomic material stocks rise 23-fold over the 20th century and require half of annual resource use. PNAS 8: 1880-1885. https://doi.org/10.1073/pnas.1613773114

Lau N-C, Nath MJ. 2012. A model study of heat waves over North America: Meteorological aspects and projections for the twenty-first century. Journal of Climate 25: 4761-4784. https://doi.org/10.1175/ JCLI-D-11-00575.1

Leclerc M, Ouarda T. 2007. Non-stationary regional flood frequency analysis at ungauged sites. Journal of Hydrology 343: 254-265. https://doi.org/10.1016/j.jhydrol.2007.06.021

Liu G, Zhang L, He B, Jin X, Zhang Q, Razafindrabe B, You H. 2015. Temporal changes in extreme high temperature, heat waves and relevant disasters in Nanjing metropolitan region, China. Natural Hazards 76: 1415. https://doi.org/10.1007/s11069-014-1556-y

Magaña V, Pérez J, Méndez M. 2003. Diagnosis and prognosis of extreme precipitation events in the Mexico City basin. Geofísica Internacional 41: 247-259.

Magaña V, Zermeño D, Neri C. 2012. Climate change scenarios and potential impacts on water availability in northern Mexico. Climate Research 51: 171-184. https://doi.org/10.3354/cr01080

Mann HB. 1945. Nonparametric tests against trend. Econometrica 13: 245-259. https://doi.org/0012-9682(194507)13:3<245:NTAT>2.0.CO;2-U p. 245-259.

Martínez-Austria PF, Bandala ER. 2017. Temperature and heat-related mortality trends in the Sonoran and Mojave Desert region. Atmosphere 8. https://doi.org/10.3390/atmos8030053

Matsueda S, Takaya Y. 2015. The global influence of the Madden-Julian Oscillation on extreme temperature events. Journal of Climate 28: 4141-4151. https://doi.org/10.1175/JCLI-D-14-00625.1

Meehl G, Karl T, Easterling RD, Changnon S, Pielke R Jr., Changnon D, Evans J, Groisman YP, Knutson RT, Kunkel EK, Mearns OL, Parmesan C, Pulwarty R, Root T, Sylves TR, Whetton P, Zwiers F. 2000. An introduction to trends in extreme weather and climate events: Observations, socioeconomic impacts, terrestrial ecological impacts, and model projections. Bulletin American of the Meteorological Society 81: 413-416. https://doi.org/10.1175/1520-0477(2000)081<0413:AITTIE>2.3.CO;2

Meehl G, Tebaldi C. 2004. More intense, more frequent, and longer lasting heat waves in the twenty-first century. Science 305: 994-997. https://doi.org/10.1126/science.1098704

Milly PCD, Betancourt J, Falkenmark M, Hirsch M, Kundzewicz ZW, Lettenmaier DP, Stouffer RJ. 2008. Stationarity is dead: Whither water management? Science 319: 573-574. https://doi.org/10.11267/science.1151915

Miralles DG, Teuling AJ, van Heerwaarden CC, de Arellano JVG. 2014. Mega-heatwave temperatures due to combined soil desiccation and atmospheric heat accumulation. Nature Geoscience 7: 345-349. https://doi.org/10.1038/NGEO2141

Mondal A, Mujumdar PP. 2015. Modeling non-stationarity in intensity, duration and frequency of extreme rainfall over India. Journal of Hydrology 521: 217-231. https://doi.org/101016/j.jhydrol.2014.11.071

Moritz AM. 1997. Analyzing extreme disturbance events: Fire in Los Padres National Forest. Ecological Applications 7: 1252-1262. https://doi.org/10.1890/1051-0761(1997)007[1252:AEDEFI]2.0.CO;2

Mugume I, Shen S, Tao S, Mujuni G. 2016. Analysis of temperature variability over desert and urban areas of northern China. Climatology and Weather Forecasting 4: 162. https://doi.org/10.4172/2332-2594.1000162

Ongoma V, Chen H, Omony GW. 2016. Variability of extreme weather events over the equatorial East Africa, a case study of rainfall in Kenya and Uganda. Theoretical and Applied Climatology 131: 295-308. https://doi.org/10.1007/s00704-016-1973-9

Palmer T, Räisänen J. 2002. Quantifying the risk of extreme seasonal precipitation events in a changing climate. Nature 415: 512-514. https://doi.org/10.1038/415512a

Panagoulia D, Economou P, Caroni C. 2013. Stationary and nonstationary generalized extreme value modelling of extreme precipitation over a mountainous area under climate change. Environmetrics 25: 29-43. https://doi.org/10.1002/env.2252

Papalexiou SM, Koutsoyiannis D. 2013. Battle of extreme value distributions: A global survey on extreme daily rainfall. Water Resources Research 49: 187-201. https://doi.org/10.1029/2012WR012557

Parey S, Malek F, Laurent C, Dacunha-Castelle D. 2007. Trends and climate evolution: Statistical approach for very high temperatures in France. Climatic Change 81: 331-352. https://doi.org/10.1007/s10584-006-9116-4

Parey S, Hoang TTH, Dacunha-Castelle D. 2018. Future high-temperature extremes and stationarity. Natural Hazards 98: 1115.1134. https://doi.org/10.1007/s11069-018-3499-1

Parker TJ, Berry GJ, Reeder MJ, Nicholls N. 2014. Modes of climate variability and heat waves in Victoria, southeastern Australia. Geophysical Research Letters 41: 6926-6934. https://doi.org/10.1002/2014GL061736

Qiang Z, Vijay PS, Suna P, Chend X. 2011. Precipitation and stream flow changes in China: Changing patterns, causes and implications. Journal of Hydrology 410: 204-216. https://doi.org/10.1016/j.jhydrol.2011.09.017

Renardt B, Sun X, Lang M. 2013. Bayesian methods for non-stationary extreme value analysis. In: Extremes in a changing climate (AghaKouchak A, Easterling D, Hsu K, Schubert S, Sorooshian S, Eds.). Water Science and Technology Library, vol. 65, Springer, Dordrecht, 39-95.

Raggad B. 2018. Statistical assessment of changes in extreme maximum temperatures over Saudi Arabia, 1985-2014. Theoretical and Applied Climatology 132: 1217-1235. https://doi.org/10.1007/s00704-017-2155-0

Ríos-Alejandro JG. 2011. Temperaturas extremas en la ciudad de Monterrey, N.L., México. Revista Chapingo Serie Ciencias Forestales y del Ambiente 17: 225-230. https://doi.org/10.5154/r.rchscfa.2010.06.036

Rosenzweig C, Solecki W, Hammer SA, Mehrotra S. 2011. Climate change and cities: First assessment report of the Urban Climate Change Research Network. Cambridge University Press, Cambridge, MA.

Salmi T, Maata A, Antilla P, Ruoho-Airola T, Amnell T. 2002. Detecting trends of annual values of atmospheric pollutants by the Mann-Kendall test and Sen's slope estimates – The excel template application Makesens. Finnish Meteorological Institute, Helsinki. Available at: https://www.researchgate.net/publication/259356944 (last accessed on May 15, 2019).

Schoof TJ, Robeson MS. 2016. Projecting changes in regional temperature and precipitation extremes in the United States. Weather and Climate Extremes 11: 28-40. https://doi.org/10.1016/j.wace.2015.09.004

Sen PK. 1968. Estimates of the regression coefficient based on Kendall's tau. Journal of the American Statistical Association 63: 1379-1389. https://doi.org/10.1080/01621459.1968.10480934

Seneviratne SI, Nicholls N, Easterling D, Goodess CM, Kanae S, Kossin J, Luo Y, Marengo J, McInnes K, Rahimi M, Reichstein M, Sorteberg A, Vera C, Zhang X. 2012. Changes in climate extremes and their impacts on the natural physical environment. In: Managing the risks of extreme events and disasters to advance climate change adaptation. A special report of Working Groups I and II of the Intergovernmental Panel on Climate Change (Field CB, Barros V, Stocker TF, Qin D, Dokken DJ, Ebi KL, Mastrandrea MD, Mach KJ, Plattner G-K, Allen SK, Tignor M, Midgley PM, Eds.). Cambridge University Press, Cambridge, United Kingdom and New York, NY, USA.

Shen L, Mickley JL, Gilleland E. 2016. Impact of increasing heat waves on U.S. ozone episodes in the 2050s: Results from a multimodel analysis using extreme value theory. Geophysical Research Letters 43: 4017-4025. https://doi.org/10.1002/ 2016GL068432

Skelhorn CP, Lindley S, Levermore G. 2018. Urban greening and the UHI: Seasonal trade-offs in heating and cooling energy consumption in Manchester, UK. Urban Climate 23: 173-187. https://doi.org/10.1016/j.uclim.2017.02.010

Smith R. 2001. Environmental statistics. Department of Statistics, University of North Carolina, USA. Available at: http://www.stat.unc.edu/postscript/rs/envnotes.ps (last accessed on May 30, 2019).

Song X, Zhang Z, Chen Y, Wang P, Xiang M, Shi P, Tao F. 2014. Spatiotemporal changes of global extreme temperature events (ETEs) since 1981 and the meteorological causes. Natural Hazards 70: 975. https://doi.org/10.1007/s11069-013-0856-y

Tabari H, Marofi S, Ahmadi M. 2011. Long-term variations of water quality parameters in the Maroon River, Iran. Environmental Monitoring and Assessment 177: 273-287. https://doi.org/10.1007/s10661-010-1633-y

Tanarhte M, Hadjinicolaou P, Lelieveld J. 2015. Heat wave characteristics in the eastern Mediterranean and Middle East using extreme value theory. Climate Research 63: 99-113. https://doi.org/10.3354/cr01285

Taxak KA, Murumkar AR, Arya DS. 2014. Long term spatial and temporal rainfall trends analysis in Wainganga basin, Central India. Weather and Climate Extremes 4: 50-61. https://doi.org/10.1016/j.wace.2014.04.005

Taylor KE, Stouffer RJ, Meehl GA. 2012. An overview of CMIP5 and the experimental design. Bulletin of the American Meteorological Society 93, 4: 485-498. https://doi.org/10.1175/BAMS-D-11-00094.1

Thiombiano AN, El Adlouni S, St-Hilaire A, Ouarda T, El-Jaabi N. 2017. Nonstationary frequency analysis of extreme daily precipitation amounts in Southeastern Canada using a peaks-over-threshold. Theoretical and Applied Climatology 129: 413-426. https://doi.org/10.1007/s00704-016-1789-7

Trenberth KE, Jones PD, Ambenje P, Bojariu R, Easterling D, Klein Tank A, Parker D, Rahimzadeh F, Renwick JA, Rusticucci M, Soden B, Zhai P. 2007. Observations: surface and atmospheric climate change. In: Climate Change 2007: The Physical Science Basis. Contribution of Working Group I to the Fourth Assessment Report of the Intergovernmental Panel on Climate Change (Solomon S, Qin D, Manning M, Chen Z, Marquis M, Averyt KB, Tignor M, Miller HL, Eds.). Cambridge University Press, Cambridge, United Kingdom and New York, NY, USA.

Ummenhofer CC, Meehl GA. 2017. Extreme weather and climate events with ecological relevance: a review. Philosophical Transactions of the Royal Society B 372: 20160135. http://doi.org/10.1098/rstb.2016.0135

UN-Habitat. 2011. Cities and climate change: Global report on human settlements. Earthscan, London, Washington DC. Available at: https://unhabitat.org/global-report-on-human-settlements-2011-cities-and-climate-change (accessed on May 5, 2019).

Wang H, Chen Y, Chen Z, Li W. 2013. Changes in annual and seasonal temperature extremes in the arid region of China, 1960-2010. Natural Hazards 65: 1913. https://doi.org/10.1007/s11069-012-0454-4

Wang XL, Feng Y. 2010. RHtestsV3 user manual. Climate Research Division, Environment Canada, Toronto, Canada, 24 pp. Available at: http://groupware.sinanet.isprambiente.it/scidip/library/ts-homogeneization_repinfo/r-scritp-user-manual/download/1/RHtestsV3_UserManual.pdf (last accessed on June 10, 2019).

Wang Z-H, Zhao X, Yang J, Song J. 2016. Cooling and energy saving potentials of shade trees and urban lawns in a desert city. Applied Energy 161: 437-444. https://doi.org/10.1016/j.apenergy.2015.10.047

Waylen PR, Keellings D, Qiu Y. 2012. Climate and health in Florida: Changes in risks of annual maximum temperatures in the second half of the twentieth century. Applied Geography 33: 73-81. https://doi.org/10.1016/j.apgeog.2011.06.007

Whan K, Zscheischler J, Orth R, Shongwe M, Rahimi M, Asare E, Seneviratne S. 2015. Impact of soil moisture on extreme maximum temperatures. Weather and Climate Extremes 9: 57-67. https://dx.doi.org/10.1016/j.wace.2015.05.001

Wypych A, Sulikowska A, Ustrnul Z, Czekierda D. 2017. Temporal variability of summer temperature extremes in Poland. Atmosphere 8: 51. https://doi.org/10.3390/atmos8030051

Zhang X, Yang F. 2004. RClimDex (1.0) user manual. Climate Research Branch, Environment Canada, 22 pp. Available at: https://acmad.net/rcc/procedure/RClimDexUserManual.pdf (last accessed on June 2, 2019).

Anexo B (artículo 2)

An Assessment of the Weather Research and Forecasting Model for Solar Irradiance Forecasting under the Influence of Cold Fronts in a Desert in Northwestern Mexico

Revista: Atmosphere, October 2024
DOI: 10.3390/atmos15111300

Los pronósticos meteorológicos son una herramienta útil para prever las variaciones a corto plazo de la irradiación solar provocadas por cambios en las condiciones atmosféricas a mesoescala y mejorar la operatividad en sistemas de generación eléctrica activados por energía solar. Gran parte del noroeste de México comprende un clima desértico con altos niveles de recurso solar; los cielos despejados y bajos niveles de humedad durante la mayor parte del año, propician condiciones favorables para su aprovechamiento. Sin embargo, en invierno el desplazamiento de masas de aire frío provenientes de latitudes polares, generan cambios abruptos en el comportamiento de las variables atmosféricas, lo que incrementa el error de los pronósticos a corto plazo. Este trabajo se enfoca en la evaluación del modelo WRF para el pronóstico de la irradiación solar global (GHI) considerando distintas parametrizaciones de radiación solar de onda corta (SW) y larga (LW), durante la influencia de cinco frentes fríos (FF) que afectaron a la región desértica del noroeste de México entre el 2017 y 2020. El FF fue simulado bajo cuatro principales configuraciones de SW: Rapid Radiative transfer Model for GCMs (RRTMG), Fu-Liou-Gu (FLG), Dudiah y New Goddard. Los resultados se evaluaron con datos medidos en superficie e información climática del proyecto de Predicción Global e Recursos Renovables (POWER) de NASA. La GHI pronosticada con la configuración Dudiah (SW), mostró que existe una sobreestimación del modelo WRF durante la mayor parte de los periodos analizados; las predicciones más acertadas, obtuvieron valores de correlación entre 0.85 a 0.91 y un Error Medio Absoluto (EMA) entre los 15-45 $W.m^{-2}$. En lapsos en donde la intermitencia de nublados predominó, el porcentaje de sesgo (Mbias), aumentó hasta casi un 20%. La evaluación de las diferentes configuraciones propuestas, muestra las ventajas que la predicción de la GHI tiene principalmente con las parametrizaciones de radiación Dudiah de SW y Rapid Radiative Transfer Model (RRTM) de LW; esto brinda una herramienta meteorológica útil para mejorar la planeación y regulación de la generación eléctrica de las centrales activadas por energía solar ante el paso de sistemas meteorológicos invernales de mesoescala.

atmosphere

Article

An Assessment of the Weather Research and Forecasting Model for Solar Irradiance Forecasting under the Influence of Cold Fronts in a Desert in Northwestern Mexico

Jose Ernesto López-Velázquez [1,*], Nicolás Velázquez-Limón [2,*], Saúl Islas-Pereda [2], David Enrique Flores-Jiménez [1], Néstor Santillan-Soto [1] and Juan Ríos-Arriola [2]

1 Laboratorio de Ciencias Atmosféricas Aplicadas, Instituto de Ingeniería, Universidad Autónoma de Baja California, Mexicali 21280, Mexico; david.flores80@uabc.edu.mx (D.E.F.-J.); nsantillan@uabc.edu.mx (N.S.-S.)
2 Centro de Estudios de las Energías Renovables, Instituto de Ingeniería, Universidad Autónoma de Baja California, Mexicali 21280, Mexico; islass@uabc.edu.mx (S.I.-P.); riosj9@uabc.edu.mx (J.R.-A.)
* Correspondence: ernesto.lopez16@uabc.edu.mx (J.E.L.-V.); nicolas.velazquez@uabc.edu.mx (N.V.-L.); Tel.: +52-686-551-82-22 (J.E.L.-V.)

Abstract: Northwestern Mexico has a desert climate with high solar resources. Clear skies and low humidity during most of the year favor their use. In winter, the arrival of cold air masses from the polar latitudes cause instability and abrupt changes in atmospheric variables, increasing the error of short-term forecasts. This work focuses on the evaluation of the Weather Research and Forecasting (WRF) model for predicting the global horizontal irradiance (GHI), considering different parameterizations of shortwave and longwave solar radiation during the influence of five cold fronts that affected the desert region of northwestern Mexico. The simulation was carried out under four main shortwave configurations and the results were evaluated with surface measurements and compared with climate information from NASA-POWER. The GHI predicted with the Dudhia parameterization showed an overestimation of the WRF model during most of the analyzed events; the most accurate predictions obtained correlation values between 0.85 and 0.91 and a mean absolute error between 15 and 45 W m^{-2}. In periods where intermittent clouds prevailed, the mean error increased by almost 20%. An evaluation of the different proposed configurations shows advantages with the shortwave Dudhia and longwave RRTM parameterizations, providing a useful meteorological tool for predicting short-range variations in the GHI to improve the operability of solar power generation systems.

Keywords: desert climate; WRF; cold fronts; global horizontal irradiation; operational forecast; solar radiation variability

check for updates

Citation: López-Velázquez, J.E.; Velázquez-Limón, N.; Islas-Pereda, S.; Flores-Jiménez, D.E.; Santillan-Soto, N.; Ríos-Arriola, J. An Assessment of the Weather Research and Forecasting Model for Solar Irradiance Forecasting under the Influence of Cold Fronts in a Desert in Northwestern Mexico. *Atmosphere* **2024**, *15*, 1300. https://doi.org/10.3390/atmos15111300

Academic Editor: Eugene Rozanov

Received: 23 August 2024
Revised: 27 September 2024
Accepted: 4 October 2024
Published: 29 October 2024

1. Introduction

Solar power plants are a promising solution to reduce greenhouse gas emissions into the atmosphere. Some studies have shown that the influence of cloudiness, ambient temperature, and humidity are closely related to the accurate prediction of solar irradiance variability, which directly affects power generation (e.g., Refs. [1–4]). Concentrated solar power (CSP) uses direct solar irradiation to heat fluid until it vaporizes, then introduces the vapor into an expander to generate mechanical work, which in turn drives an electrical generator; photovoltaic (PV) technologies harness global solar irradiance and convert it into electrical energy from semiconductor materials. In both cases, the prediction of solar irradiance is crucial for the operability of power grids, allowing for better planning and regulation of variable power generation [5]. In the residential, commercial, agricultural, and industrial sectors, it is expected that solar-activated power generation systems (SGESs) will gradually become accessible and affordable technologies for any user; they will continue their large-scale expansion in various climatic regions, and will see sustained research and development in the coming years. Therefore, the prediction of solar power generation will become increasingly necessary in the short range [6,7].

However, one of the greatest vulnerabilities of SGESs lies in the uncertainty of the intermittency and natural variability the resource can generate, especially during mesoscale meteorological events and extreme events; in the United States alone, it has been reported that between 2000 and 2021, approximately 83% of interruptions in the electric grid were attributed to extreme meteorological events, which annually affect the safety and public health of citizens, in addition to causing damage to the electric infrastructure. Severe weather events such as high winds and storms (58%), winter weather events (22%), and tropical cyclones (15%) were among the top causes of power outages. Texas, Michigan, and California stood out as the states with the most weather-related power outages [8].

For example, in 2010, a cold snap in France caused a spike in natural gas demand, with approximately every degree Celsius drop in temperature resulting in an increase of 100 GWh in daily natural gas consumption. In January 2017, Spain experienced a three-day period with a minimum temperature of 1.8 °C, which, combined with winter weather conditions, market restrictions, and the need to supply electricity to France due to the failure of its nuclear power plants, drove prices up to EUR 112.8 per MWh, the highest ever recorded in the Spanish region [9].

The need for adequate weather forecasting to increase the reliability of electricity generation in power plants supplied by renewable resources has become relevant in North America. In February 2021 in Texas, USA, the slow movement of an intense cold front associated with an Arctic air mass caused several events that interrupted the electricity supply to almost 10 million people for several days. During the influence of the weather system, the generation of the main energy sources in Texas (natural gas, wind, coal, nuclear, and solar) decreased, which, in a cascading effect resulting from the extreme winter conditions, led to a significant deficit in the generation of natural gas, causing an over-demand of the available energy; as well as the death of 111 people due to the impact of the winter system [10].

In the western United States, southern California, Arizona, and part of the desert area of northwestern Mexico between Baja California and Sonora, there is a region of extreme desert climate that is of particular interest for study due to its interaction with extreme weather events in winter; according to the Climate and Weather Disaster Report for California and Arizona from 1980 to 2024, severe storms, freezes, and floods during the winter season can cause significant stress on energy demand in the region [11].

Over the southwestern United States and northwestern Mexico, winter frontal systems occur between September and May, with an average of 55 events per season, according to historical weather reports from the National Meteorological Service of Mexico (SMN) over the past 10 years. Considering the historical data on the occurrence of winter frontal systems based on the synoptic analysis of the Weather Prediction Center [12] archives, approximately 40% of the total frontal systems each season enter the western and southwestern United States, affecting Southern California and Baja California.

Weather forecasting considers two important time scales to differentiate the variability that affects the prediction of the solar resource: (1) Medium-range forecasts, which are mainly influenced by long-term weather patterns in the atmosphere that may include periods longer than 120 h or correspond to climatic oscillations that regulate the meteorological conditions of a region for long periods as annual cycles or longer [13]. The second scale of interest, which is the focus of this analysis, involves a smaller temporal and spatial coverage and is known as (2) short-range forecasting. This scale includes variations related to meteorological phenomena lasting from a few minutes to about 72 h and with spatial coverage ranging from 0.01 km to 100 km. Some meteorological phenomena, such as storms, tornadoes, and cold fronts, produce variations in solar irradiance that develop within the spatial and temporal horizons that can be predicted by short-range weather forecast [14], as shown in Figure 1.

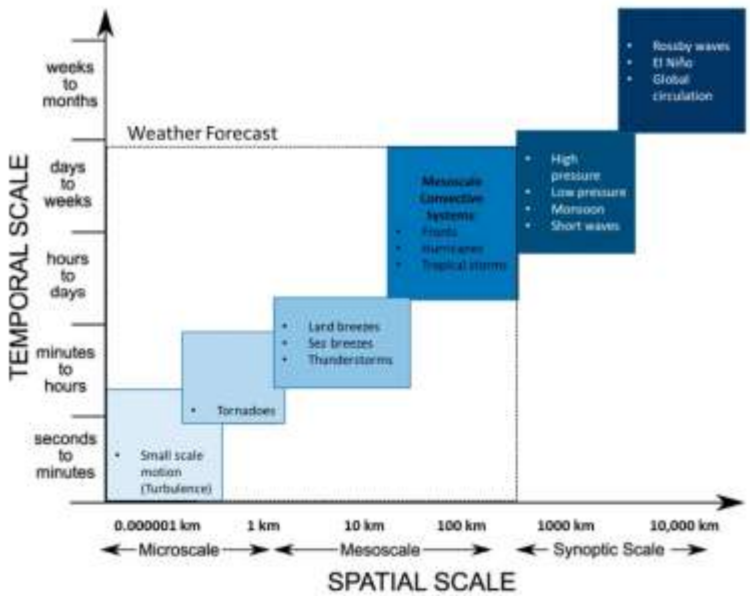

Figure 1. Time scales of weather and climate prediction with reference to the spatial and temporal horizons of some atmospheric phenomena (modified from [15]).

Climate models are a fundamental tool in the investigation of long-range atmospheric variations; they are capable of representing general patterns of temperature, humidity, and precipitation over a large region; however, their low resolution makes it difficult to analyze spatial scales smaller than 100 km. Among the forecasting methods capable of capturing local variability are statistical models (SMs) and numerical weather prediction (NWP) computational models. Statistical models require a robust climate and meteorological database of the site, from which meaningful statistical relationships are established for the prediction of atmospheric variables [16]. NWP can be based on initial data available from different global models, satellite data, and reanalysis information. They also allow for the configuration of high-resolution domains for a specific region and offer the possibility of selecting different physical parameterizations of atmospheric processes for small-scale experimental purposes. Among the studies that have focused their interest on the short-range prediction of solar irradiance at sites with potential for solar energy harvesting, we can mention [17], whose authors conducted an evaluation of the Weather Research and Forecasting (WRF) model in the region of Andalusia, Spain, using three-day periods throughout 2007 and 2008 to collect clear, partially covered and cloudy days in different seasons of the year. The results of the model showed that there was a greater number of successes in the prediction of solar irradiance during spring and summer, while fall and winter showed greater inaccuracies. Cohen et al. [18] conducted a review of planetary boundary layer (PBL) parameterization schemes, such as Yonsei University (YSU), Quasi-Normal Scale Elimination (QNSE), Mellor–Yamada–Janjic (MYJ), Asymmetric Convective Model 2 (ACM2), and Medium-Range Forecast Model (MRF), by simulating a cold season in the southeastern United States (winter–spring), where the simulation of humidity and temperature meteorological variables under severe convective weather conditions was analyzed. The results showed the advantages and disadvantages of local and non-local parameterizations during the influence of mesoscale systems, where the implementation of the YSU parameterization in the PBL was particularly notable. In a similar effort to evaluate parameterization schemes, in 2016, the authors of [4] conducted a study over a large region of Greece, characterized by a Mediterranean climate. This study involved the simulation and analysis of one year of horizontal solar irradiance measurements, focusing on the variation in shortwave parameterization schemes in the WRF model for clear day cases and "all cases", which included different cloudiness conditions. The statistical results showed that clear days were satisfactorily predicted under the Dudhia parameterizations, but in the rest of the cases, different parameterizations stood out according to the seasons of the year. In 2019, Ref. [5] evaluated different WRF model parameterizations for global solar irradiance prediction in a Mediterranean climate in the southeastern region of Turkey. The study simulated different periods of the year to characterize the model's behavior in different seasons. Among its results, the study highlighted the favorable performance of the shortwave FLG and RRTMG parameterizations, and it retained YSU as its only variation in the PBL parameterizations.

In 2020, the authors of [19] performed a short-range forecast in Australia with the WRF-Solar model, with an emphasis on the simulation of solar irradiance and meteorological variables for 24–48 h periods, which they called "high solar intermittency days"; these were selected over a year of on-site measurements based on the determination of the clearness index, which partially related the interaction with the influencing cloudiness. Among their most outstanding results, the authors pointed out that the prediction errors in wind speed and direction were closely related to the cloudiness circulation. These results gave rise to works such as the one carried out by the authors of [20], in which, under the continuation of the search for improvements for short-range solar prediction and the influence of other meteorological variables related to the interaction with cloudiness, they selected several periods of temperate climate for the northeastern region in Germany, which were considered relevant to their variability on that time scale. They simulated periods in which the region was influenced by cold, warm, and occluded frontal systems. The RRTMG and Dudhia schemes were used, and it was found that the most favorable prediction results were obtained with RRTMG for almost all cases, except for occluded fronts.

Based on the background information, which shows that no studies have been conducted to predict solar irradiance in desert climates during winter seasons, this paper presents an evaluation of the WRF model for the prediction of the global horizontal irradiance (GHI) by simulating five cold fronts over the desert region of northwestern Mexico, recorded between 2017 and 2020. The events were selected for having registered abrupt changes in GHI, ambient temperature (Tamb), and relative humidity (Hrel), in addition to having a similar duration and having generated clouds at different times of the day.

Each experiment was run under four different configurations of solar radiation settings of the WRF model. The results obtained were compared with surface measurements from automatic weather stations, solar pyranometers, satellite data, and a reference to a persistence forecast. The Dudhia and RRTMG parameterizations of the WRF allow for a more accurate estimation of the behavior of the GHI variable during the passage of the cold fronts, which can be used to make a better short-term prediction of the electricity generation of the solar power plants in the event of short-range meteorological events, as well as allowing for the planning and definition of operational strategies in solar power plants.

2. Materials and Methods

In order to predict the variability of solar irradiance during the influence of winter frontal systems in the desert region of northwestern Mexico, the following steps were carried out: an analysis of the synoptic behavior of mesoscale systems, a selection of the case study sample (winter cold fronts), configuration of the WRF computational model, definition of domains, and selection of the solar radiation parameterizations. Finally, the results were statistically evaluated to analyze the performance of each proposed configuration and to identify which conditions showed the best results for evaluated frontal systems. The methodology used is shown in detail below.

2.1. Geographical and Climatological Description of the Study Area

The area of focus for this study is the desert zone of northwestern Mexico, with the city of Mexicali, Baja California, selected as a representative point, given its exposure to the extreme events characteristic of this region. The city of Mexicali is situated on the border with the United States, in the extreme northwest of Mexico (N 32°30′18.468″, W −115°8′51.756″). It is bordered to the north by the US state of California and to the northeast by the US states of Arizona and Sonora. During the summer months, the average maximum temperature is 42 °C, with occasional readings reaching 45 °C. In contrast, the average minimum temperature during the winter months (December to February) is 9 °C, with occasional readings reaching 2.5 °C [21]. During the summer months, the maximum GHI reaches 1200 W m^{-2}, with 600 W m^{-2} recorded on some winter days. One of the primary meteorological phenomena affecting the northwestern desert region during the winter season is the occurrence of cold fronts, which span from September to May, with the majority occurring between December and March. As [22] notes, frontogenesis occurs when two air masses, one cold and the other warm, collide. The cold air mass displaces the warm air mass, and the surface separating both is called a "cold front". A cold front (CF) generates significant vertical displacement within the atmosphere. The air forced to rise is cooled adiabatically, resulting in the formation of low and medium clouds, as well as large convective clouds. These clouds are associated with storms, fog, or heavy rain, and they can occur in a relatively short period of time. Additionally, maximum temperatures decrease and wind speeds increase as a result of cold fronts. As illustrated in Figure 2, the CF events documented in the study region have their origin in the vicinity of the North Pole. They commonly traverse a portion of the west coast of the United States and reach northern Mexico, where they may either move southward within the country or eastward across the southeastern border region. They may also traverse the northern and central regions of the United States before reaching Mexican territory or approach lower latitudes to the east, ultimately entering the Gulf of Mexico. A synoptic situation of particular interest for this study can also occur, in which a CF with characteristics of a maritime polar (mP) or tropical maritime (mT) air mass moves over the west coast of the United States, acquires a greater influence of Pacific Ocean moisture, and enters northwestern Mexico (Figure 2). The duration of these mesoscale systems in northwestern Mexico can vary from one to four days, similar to that described by the authors of [23] in their study of the passage of cold fronts over the northwestern coasts of the Gulf of Mexico. They are typically associated with moderate rainfall, a decrease in maximum temperatures, and an increase in wind speeds. Their influence can also result in the formation of partial clouds, which contributes to a significant short-range variability of the GHI.

To meet the duration and variability criteria for a typical winter event in the study region, Table 1 presents a selection of five cold fronts that affected the northwestern area of Mexico between 2017 and 2020. These events were identified using data from the Mexicali, Baja California meteorological station and NASA data base viewer [24]. As this study classifies frontal systems according to the characteristics of the cold air masses associated with them, including polar maritime (mP), tropical maritime (mT), and polar continental (cP) air masses, it was essential to observe the displacement of each frontal system in historical synoptic maps at least 48 h prior to its arrival in the study region. This classification allows for the association of an additional descriptive characteristic in relation to each event.

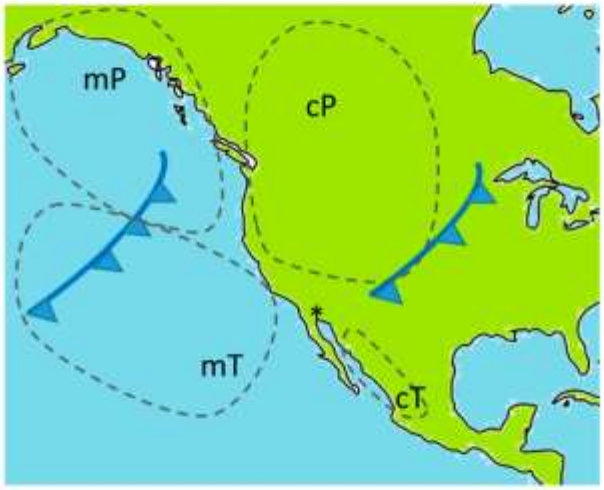

Figure 2. Graphical representation of the air masses associated with winter frontal systems affecting northwestern Mexico, depending on their origin: maritime tropical (mT), maritime polar (mP), continental polar (cP) and continental tropical (cT). Own elaboration. The symbol "*" indicates the location of Mexicali, Baja California (own reproduction).

Table 1. Events (cold fronts) simulated in the experiments.

Event	Air Mass-Associated	Year	Date
CF01	Maritime polar (humid)	2017	January 17 to 21
CF02	Maritime polar and tropical (humid)	2017	February 15 to 19
CF03	Maritime polar (humid)	2018	January 18 to 22
CF04	Continental polar (dry)	2018	December 20 to 24
CF05	Maritime polar and tropical + post Tropical storm influence (humid)	2020	November 5 to 9

2.2. Measured Data

The initial conditions of the WRF model are based on the Final Operational Global Analysis (FNL) data from the National Center for Prediction and the Environment (NCEP). This dataset has a spatial resolution of $1^{\circ} \times 1^{\circ}$ and a temporal resolution of 6 h, 26 vertical levels, and global coverage [25]. To validate the results obtained with the WRF model, they were statistically compared using data measured by an automatic weather stations model Davis Vantage Pro2 and a pyranometer model CMP-10 (Kipp & Zonen, Delft, The Netherlands), installed at the UABC Engineering Institute, Mexicali, Baja California, as representative of the study region (Figure 2). To verify the accuracy of the simulation results, corresponding hourly data were also collected from the NASA-POWER climate database, which is a satellite/reanalysis model [24] and has been used in some studies to estimate weather variables and test their reliability against meteorological measurements [26,27]. Additionally, the results were compared with data from the persistence forecast, which is a term used in weather forecasting to indicate that there is no change in the weather from one day to the next. As noted by [28], forecasters frequently identify instances where a forecast model exhibits suboptimal performance and hypothesize the presence of a persistent error in the model when similar conditions occur again. To this end, it is essential to quantify the discrepancy of a suboptimal forecast model across successive days, regardless of the prevailing meteorological conditions. This enables forecasters to assess the potential for model enhancement and identify the critical areas of divergence within the simulation [29].

2.3. Model Setup and Parameterizations

WRF is a numerical weather prediction (NWP) model and an atmospheric simulation system designed for research and operational applications [30]. It represents the state of the atmosphere in a three-dimensional grid in terms of fundamental variables and is considered a non-hydrostatic model that solves the primitive equations that describe the atmospheric circulation. It also allows for forecasting meteorological variables with a high resolution from initial and boundary conditions. Within the model, there is the possibility of configuring parameters that influence physical atmospheric processes related to radiation, convection, and cloud microphysics, among others. These processes take place mainly at low levels of the atmosphere and are represented by modules called physical parameterizations, which consist of algorithms that calculate the effect of the phenomenon indirectly from the variables that the model is able to resolve, and once resolved, the effect or trend is applied to underlying fields of the domain proposed for a study area in the model [31].

The main variations that affect solar radiation during its passage through the atmosphere are mostly due to cloud scattering processes; however, aerosol scattering and humidity also play an important role. Many NWP models have minimized the effects of aerosol scattering, and have limited themselves to the use of climate data to substitute for the lack of measurement methods to obtain these values in the modeled area. This simplification has led models to make errors of up to 20% in their predictions [32].

More and more models include advanced shortwave (SW) solar radiation parameterizations based on two-stream or four-stream solvers of the radiative transfer equation (RTE) in multiple spectral bands [33]. The RRTMG [34] and its predecessor RRTM schemes [35], used in this research, are examples of schemes that combine the need for global and regional models in solar prediction. The RRTMG scheme focuses on the representation of variations due to water vapor, carbon dioxide, nitrogen, aerosols, Rayleigh scattering, and cloudiness; this scheme and RRTM have great similarity, but their major difference lies in their multiple scattering calculations and subscale parameterizations of cloudiness.

Under clear sky conditions, RRTMG can be expected to have a prediction error of about 0.3% with respect to RRTM [34]. The Goddard scheme, used in this research, was developed by NASA at the Goddard Space Flight Center for application to climate models [36]. Goddard is similar to the Fu-Liou-Gu (FLG) scheme, also implemented in the modeling proposed in this research, since it calculates the radiative flux from the 4- and 2-stream delta methods for 6 spectral bands, less than any other previous scheme [37]. The WRF model has more than 10 schemes in SW and longwave (LW) radiation. The four parameterization schemes mentioned for SW (RRTMG, RRTM, FLG, and Goddard) partially correspond to the methodology used by [5] for Turkey, where it was implemented under different cloud cover conditions with the purpose of identifying the best model configuration that favored the GHI prediction, as they implement different algorithms for radiative flux calculations, the representation of different numbers of spectral bands, and the simulation of different scattering sources such as gases and aerosols. Some similar configurations of SW solar parameterizations for WRF also stood out for their exploration in previous studies and their validity in the model (e.g., Refs. [4,19,20]).

2.4. Domains and Configuration

Three domains were used, a parent domain (D01) and two nested or interior domains (D02 and D03), as detailed in Figure 3. In these domains, a 3:1 resolution ratio was maintained, with the highest resolution in D03 having a grid spacing of 2.3 km, centered at the point of surface measurements. The domains were sized in this way in order to capture the occurrence and progressive displacement of the CF developing offshore to the northwest and entering from the west of the region.

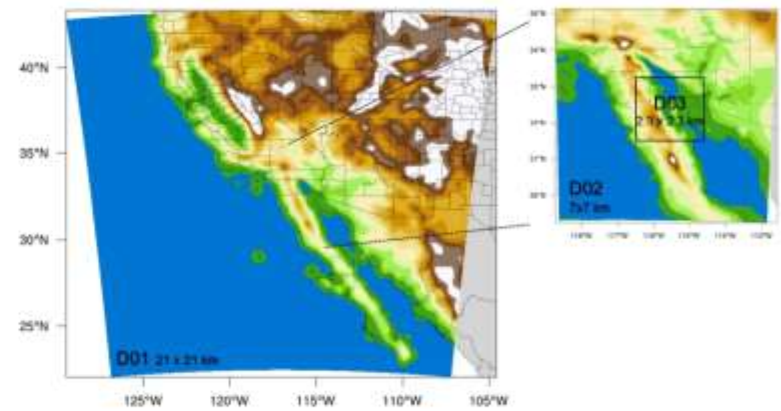

Figure 3. Domains of the simulations of the study area. D01 and D02 consider the southwestern United States, northern Mexico, and part of the Pacific Ocean and the Gulf of California; and D03 contains the representative area of Mexicali, Baja California (own preparation).

All experiments comprised a simulation period of 120 h (Table 1). The simulations were performed with the WRF-Solar model version 4.3 [30] and four different configurations were applied, as shown in Table 2. The focus of this work on improving the GHI prediction proposed mainly varied the radiation parameterizations in four combinations of SW and LW, while the rest of the parameters such as microphysics, surface, and cumulus only underwent necessary changes due to the compatibility of the options with each other. In the parameterization of the planetary boundary layer (PBL), YSU was used, based on the results that showed the experimentation performed for a winter–spring season in the southeastern United States by [18]. The results of all simulations were extracted from the highest resolution domain (D03), according to the coordinates of the meteorological station from which the measurements were obtained.

Table 2. Configurations used in the simulation of each event.

Parameterization	Option 0	Option 1	Option 2	Option 3
Radiation SW/LW	RRTMG / RRTM	FLG / FLG	Dudhia / RRTM	N Goddard / N Goddard
Microphysics	WSM6	Thompson	WSM6	Goddard ICE
Surface Layer	Monin Obukhov	Monin Obukhov	Monin Obukhov	Monin Obukhov
Surface Physics	Noah	Noah	Noah	Noah
Cumulus	Kain Firtsch	Kain Firtsch	Kain Firtsch	Kain Firtsch
PBL	YSU	YSU	YSU	YSU

2.5. Statistical Metrics

For the evaluation of the results, the statistical errors between the simulated data in D03 (Figure 3) and the measured data of GHI, ambient temperature (Tamb), and relative humidity (Hrel) were calculated with a total number of data $N = 720$ for each event. The mean absolute error (MAE) represents the measure of the closeness between the measured and simulated values in terms of absolute value (1). The mean bias (MBIAS) is represented in units of the variable measure of the mean trend of the simulated and measured values, where values close to zero are the most favorable, positive values indicate an overestimate, and negative values an underestimate (2). The root-mean-squared error (RMSE) was also calculated, which gives more weight to the mean dispersion of the errors individually (3) [38].

A Taylor diagram compares modeled and observed values, and several of which are used to show a statistical summary of how the results of a model's output agree in terms of dispersion and correlation with each other; standard deviation is shown in the x- and y-axes and Pearson's correlation coefficient is pointed out at the circumference of the diagram [39]. The normalized reference values for GHI, Tamb, and Hrel correspond to the measured values and are located at the bottom center of the figure.

$$MAE = \sum_{i=1}^{N} \frac{|Xmeasured - Xforecasted|}{N} \quad (1)$$

$$MBIAS = \frac{1}{N}\left(\sum_{i=1}^{N}(Xmeasured - Xforecasted)\right) \quad (2)$$

$$RMSE = \sqrt{\frac{1}{N}\sum_{i=1}^{N}(Xmeasured - Xforecasted)^{2}} \quad (3)$$

3. Analysis and Discussion of Results

This paper presents the forecast results of the GHI in a WRF model for cold frontal systems in a desert region. In order to perform the simulation of the selected events, four different configurations of physical parameterizations were tested, opt0, opt1, opt2, and opt3, which were proposed for the prediction of short-term irradiance variability due to the influence of other meteorological variables and cloud circulation by mesoscale events, as mentioned previously in Table 2. Given the extent of the statistical comparison performed for the five frontal events and the similarity of the results obtained for events CF01, CF02, CF03, and CF04, only the prediction errors of the most favorable case (CF01) and the least favorable case (CF05) are discussed and compared. Furthermore, the analysis of these two cases is of great interest in the evaluation of the WRF model due to the contrasting characteristics under which the frontal systems were classified: the first (CF01), as a "wet" event, is mainly associated with a polar maritime air mass, and the second (CF05) is mainly associated with a tropical maritime air mass and the influence of synoptic conditions particular to the transition season from autumn to winter in the study region, as mentioned above in Table 1.

3.1. Variability of Cold Fronts in a Case Study

In order to analyze the correlation and variability of the forecast with respect to the observed data, the forecasted data series of frontal systems CF01 and CF05 were plotted by variables in scatter plots. They were differentiated into diurnal (10:00 am to 5:30 pm) and nocturnal (6:00 p.m. to 9:30 a.m.) periods as shown in Figures 4 and 5. In Figure 4, corresponding to CF01, it is possible to observe that the GHI showed a behavior with a marked linear trend and the greatest dispersion of points graphed was observed from values above 500 W m^{-2} for most of the options, i.e., a large number of the predictions commit a similar estimation error. Within the GHI, it can be highlighted that some data points corresponding to opt1 are located further apart from the data cloud than the rest, mainly in overestimates in the range of 400–700 W m^{-2}. With a similar behavior, in the range of 300–700 W m^{-2}, the points corresponding to opt3 showed overestimates. The scatter plot for the GHI shows coherent results for the predicted values in the night period, ranging from 0 to 30 W m^{-2}. Tamb groups most of its values within a linear trend and shows a greater scatter of points at values above 12.5 °C. The lower temperature values, in the range of 7.5 to 11 °C, show a good correlation with respect to the measured values, and the night periods predominate. Temperatures between 11 and 20 °C show that the points are dispersed to the left of the data cloud as an underestimation of the day and night data of opt2, and to the right, in the same range as a diurnal, an overestimation of opt0 and opt3. In the Hrel variable, it is observed that the lowest dispersion of points is located between the values in the range of 20 and 40%, mainly in diurnal periods; while the rest of the values show a gradual increase in dispersion as they approach values greater than 60%. In the Hrel values, the daytime and nighttime periods are homogeneously dispersed in the 40–60% range, showing an overestimation, and this behavior is highlighted in the axis of the predicted values upon observing the dispersion of points in the 60–80% range for opt2; in the same range, but in the axis of the measured values, most of the options in daytime and nighttime periods are an underestimation.

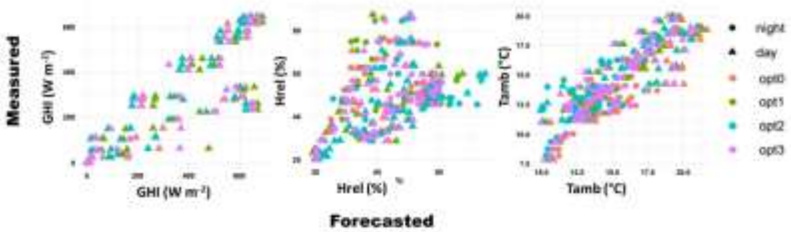

Figure 4. Scattering points differentiated in night and day periods of the solar radiation, relative humidity, and ambient temperature variables (**left** to **right**) with respect to the data predicted in the CF01 event.

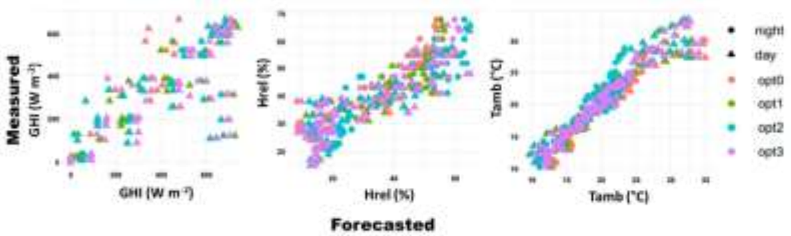

Figure 5. Scattering points differentiated in night and day periods, of the solar radiation, relative humidity, and ambient temperature variables (**left** to **right**) with respect to the data predicted in the CF05 event.

Figure 5, corresponding to event CF05, shows that the GHI is the variable with the greatest dispersion in the point cloud and that the estimates show a greater dispersion within the range of 400–700 W m^{-2}. It is possible to distinguish its positive linear trend; however, the errors that the prediction makes by overestimating or underestimating values equal to or greater than 600 W m^{-2} in most of the options stand out. With regard to the overestimates, opt2 and opt3 stand out, while for the underestimates, it is opt0. The Tamb is generally grouped with a clear positive trend and little dispersion of points in the data. The highest values in the range of 30–35 °C in diurnal periods, which show possible overestimates at values above 30 °C, stand out for their greater dispersion. The Hrel also shows a dispersion of data that tends to a linear correlation. The data cloud is more dispersed in the area of the minima and maxima values of the series, although underestimates predominate. However, although the differentiation between daytime and nighttime data is not clear, since they are homogeneously distributed in the data cloud, a normal pattern of behavior can be observed by locating a majority of nighttime points in the region of maximum values (greater than 50%), and of daytime periods in the region of the graph with the minimum values (below 30%). Both the overestimates shown by the GHI and Tamb could be due to the variability generated by the meteorological event upon arrival at the study point, which generated a significant error in the model's prediction due to the abrupt change in these variables by influencing the humid air mass, which is reflected in the diurnal underestimates. The overestimation of the Hrel conditions of CF01 was what marked the main difference with respect to CF05, in addition to favoring a greater variability of Tamb of the former with respect to the latter. The conditions of underestimation of the GHI for CF05 were not present in CF01 in a significant way.

3.2. Taylor Diagrams

The results obtained with the different proposed configurations were also compared graphically in terms of Pearson's correlation coefficient values and standard deviation, normalized with a Taylor diagram as shown in Figures 6 and 7. In Figure 6, corresponding to event CF01, it is observed that the variable with the highest similarity to the observed data was the GHI in the data measured by NASA, with correlation values around 0.98, followed very closely by the opt2 configuration prediction in the same variable. The rest of the forecast options for the GHI variable were very close to each other with values around a Pearson's correlation of between 0.92 and 0.94 and a standard deviation close to 1. The persistence forecast representing the variability with respect to the previous day, as expected due to the influence of the frontal event, was the least favorable prediction, with correlation values close to 0.82. The predictions of the Tamb variable showed Pearson's correlation values between 0.85 and 0.89 in the proposed configuration options (opt0, opt1, opt2, and opt3), which were grouped with similar values and a standard deviation close to 1. The values measured by NASA in Tamb obtained one of the lowest correlation values with 0.82 and a standard deviation of approximately 1.50, which could be due to the differences in resolution in the mesh of the model. The persistence forecast showed correlation values of 0.88, similar to the prediction options, which showed that there was no significant ambient temperature variability during the frontal event. The Hrel predictions in CF01 presented the least favorable correlation values compared to the rest of the normalized variables, as well as a higher standard deviation with values close to 2. The correlation values in Hrel were less than 0.60 in all the proposed options; opt0, opt2, and opt3 showed very similar values between them, ranging between correlations of 0.40 and 0.55. Given the characteristics of CF01, favorable values were obtained in the prediction of solar irradiance, followed by the Tamb variable, with the least favorable prediction being Hrel.

From Figure 7, corresponding to the Taylor diagram of event CF05, it is possible to observe that one of the best-predicted variables was Tamb, with correlation values that ranged from 0.85 to 0.97. The Hrel and GHI variables showed similarity, with most of their predictions ranging from 0.75 to 0.9 and standard deviations between 1.5 and 2; however, opt1 in both variables can be considered as the most favorable results for Hrel and GHI, followed closely by opt2 with similar values. In this same comparison, the data measured by NASA were favorable in the prediction of the GHI and Tamb, but not so for Hrel, where, despite showing a correlation higher than 0.9, a standard deviation close to 2 was obtained. This is possibly associated with local conditions of moisture transport at low levels of the atmosphere, which NASA measurements failed to represent. As mentioned above, it is important to note that in event CF05, the GHI predictions were less favorable than in CF01, i.e., the local humidity factor at the study site during the passage of the frontal system generated errors in the model predictions. The results of the GHI predictions in the two frontal events showed that the proposed prediction options were more favorable in the CF01 event, which is associated with a polar maritime air mass; in the prediction of event CF05, the standard deviation values were higher, possibly due to the influence of the tropical maritime air mass with the influence of ODALYS, a weak and short-lived tropical storm that remained over the western portion of the Eastern Pacific basin from 3 to 8 November with a peak on 4 November and low remnants from 5 to 8 November [40].

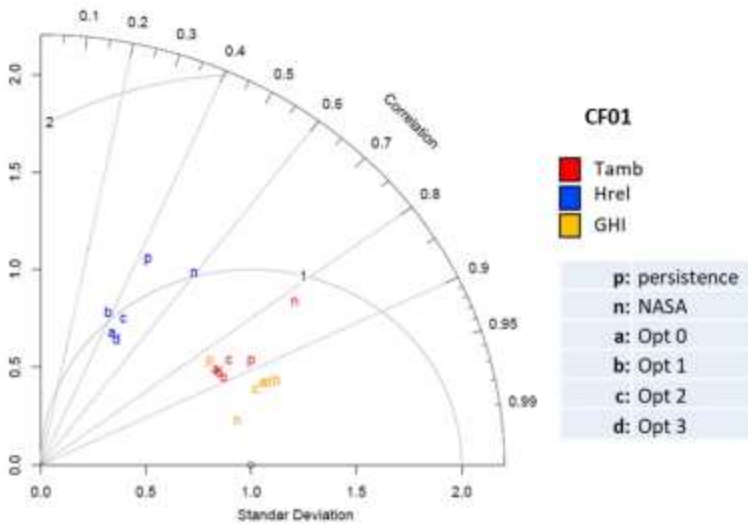

Figure 6. Taylor diagram of the results of the GHI (yellow), Tamb (red), and Hrel (blue) for the CF01 event.

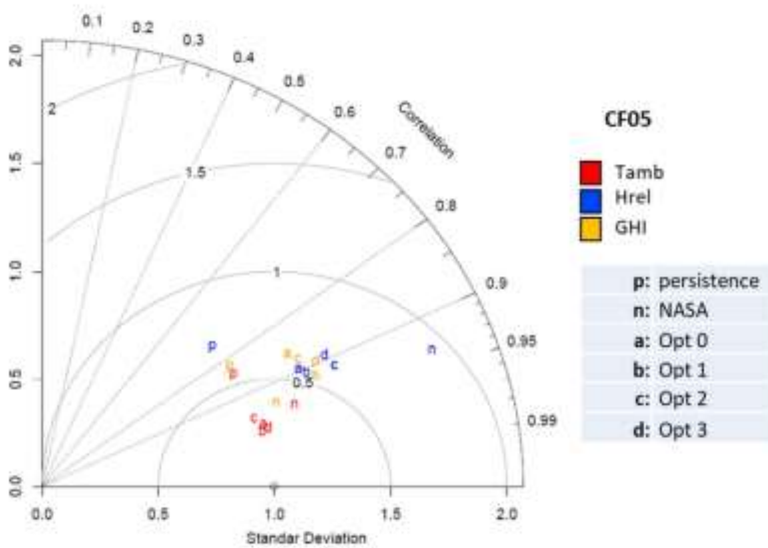

Figure 7. Taylor diagram of the results of the GHI (yellow), Tamb (red), and Hrel (blue) for event CF05.

3.3. Analysis of Statistical Values

Table 3 shows the statistical values of the CF01 forecast classified as a system with greater influence of a polar maritime air mass. Considering the characteristics of each statistic used to quantify the error in the simulations, it is necessary to analyze and discuss every result for each of the variables. In the statistical results, it is observed that opt2 predominates over the rest of the configurations for most of the simulated variables.

Table 3. Results of R^2, MAE, MBIAS, and RMSE for the prediction results for each configuration option for event CF01.

CF01	opt0	opt1	opt2	opt3	NASA	Persistence	
GHI	0.86	0.86	0.87	0.86	0.94	0.69	R^2
Tamb	0.74	0.78	0.73	0.75	0.67	0.78	
Hrel	0.2	0.143	0.21	0.23	0.35	0.19	
GHI W m^{-2}	41.15	40.65	35.66	42.13	22.4	53.12	MAE
Tamb °C	1.7	1.36	1.23	1.32	2.42	1.19	
Hrel %	13.12	13.11	12.26	12.44	14.3	14.57	
GHI W m^{-2}	−29.1	−39.21	−16.2	−28.6	−2.96	4.96	MBIAS
Tamb °C	−1.43	−1.04	−0.22	−0.88	1.72	0.1	
Hrel %	10.57	9.45	5.27	9.54	−8.96	−0.34	
GHI W m^{-2}	92.3	101.5	81.36	95.06	48.5	116.7	RMSE
Tamb °C	2.05	1.7	1.56	1.68	2.99	1.51	
Hrel %	17.96	18.53	15.75	16.92	18	17.77	

For the GHI variable, the determination coefficient R^2 shows values between 0.69 and 0.94. The values measured by NASA obtained the most favorable estimate with an R^2 of 0.94; however, there was no significant difference between the proposed prediction options, which ranged between 0.86 and 0.87. The persistence forecast showed the lowest coefficient value with an R^2 of 0.69, suggesting an attribution to the daily variability generated by the event. A similar pattern of correlation was observed in the statistical results for the Tamb and Hrel variables, where the R^2 of the simulation options showed values between 0.73 and 0.78, and 0.14 and 0.23, respectively. The R^2 values for the Hrel variable were the least favorable of the proposed configuration options.

In the MAE statistic, the GHI simulation option corresponding to opt2 was considered the best result because its values were the lowest among the options with 35.66 W m^{-2} and with an error 18% lower than the rest; in the measured data from NASA, the lowest value was obtained with 22.35 W m^{-2}, which represents a difference of only 35% with respect to the opt2 simulation. For the Tamb and Hrel variables, the MAE values in the opt2 configuration options were also the most favorable with a difference of approximately 40% in Tamb and 9% in Hrel with respect to the rest of the options.

For the GHI variable, all the proposed simulation configurations showed a negative MBIAS: opt2 with a value of −16.22 W m^{-2}, while the rest had higher negative values up to −39 W m^{-2}, in contrast to opt1. The RMSE statistic showed a similar pattern for opt2, where, with a value of 81.36 W m^{-2}, it was the best evaluated configuration option. The MBIAS values were the most favorable across the board, i.e., the lowest values of this statistic for the GHI were from NASA were from NASA and the persistence forecasts with a value of −2.96 and 4.96 W m^{-2}, respectively; however, with only a difference of −13.2 W m^{-2}, opt2 was the best of the predictions. Of the proposed configuration options, opt2 showed the most favorable values for most of the statistics, except for R^2, where the predictions were evaluated with values that were similar to each other with only a difference of one-tenth.

The variables Tamb and Hrel obtained a favorable estimation with low values in most of the statistics. Tamb showed R^2 values between 0.67 and 0.78, with the highest value in opt1, similar to that of the persistence forecast and slightly different from opt2 with 0.73, which dominated in the rest of the statistics. Finally, it is important to note that the measured NASA data, for the R^2, MAE, MBIAS, and RMSE statistics in Tamb and Hrel, made errors that, at times, in the statistical evaluation, resulted in scores that were a less favorable "prediction" than some of the proposed options.

The statistical results of the CF05 event, classified as wet and with the influence of a tropical cyclone prior to its displacement in the study area, are shown in Table 4. The GHI variable showed the most favorable values of R^2 in the opt1 with 0.86, while the opt0 was the least favorable, with 0.77 followed by the persistence forecast with a value of 0.68. In MAE, a similar pattern to the previous event could be observed, since according to the values, the best evaluated option was opt1 with 47.14 W m^{-2}, followed only by opt2 with 47.55 W m^{-2}; the MBIAS values remained negative in all options, where opt2 showed a lower bias with −22.81 W m^{-2}, in contrast to the highest bias, corresponding to opt3, with −43.95. W m^{-2}. The RMSE reflected that the values of 104.35 W m^{-2} and 108.33 W m^{-2} for opt1 and opt2, respectively, were the most favorable and did not show a large difference between them. As can be seen in the CF05 statistics, it is not possible to appreciate a clear trend towards any of the proposed options; however, relevant values were identified in almost all the options except opt0.

Table 4. Results of R^2, MAE, MBIAS, and RMSE for the prediction results for each configuration option for event CF05.

CF05	opt0	opt1	opt2	opt3	NASA	Persistence	
GHI	0.77	0.86	0.82	0.83	0.94	0.68	R^2
Tamb	0.93	0.93	0.91	0.94	0.89	0.67	
Hrel	0.78	0.79	0.79	0.78	0.84	0.42	
GHI W m^{-2}	55.98	47.14	47.55	55.51	20.94	51.63	MAE
Tamb °C	1.14	1.16	1.52	1.08	2.13	3.38	
Hrel %	7.92	7.37	6.91	7.67	9.7	9.27	
GHI W m^{-2}	−29.62	−34.53	−22.81	−43.95	−5.95	−2.09	MBIAS
Tamb °C	−0.4	0.06	0.91	0.18	0.98	−2.45	
Hrel %	6.72	6.17	3.7	5.05	−1.53	3.53	
GHI W m^{-2}	120.58	104.35	108.33	119.63	49.07	126.61	RMSE
Tamb °C	1.66	1.57	2.01	1.53	2.67	4.39	
Hrel %	9.83	9.54	9.12	9.7	11.84	11.34	

The Tamb and Hrel variables showed a satisfactory estimation in most of the statistics for each of the configuration options. However, according to the small differences shown in the evaluation, it could be complicated to define an optimal option. The Tamb variable showed good results, especially in opt3, where R^2, MAE, and RMSE were the most favorable among the configuration options. For the Hrel variable, it can be highlighted that there are unfavorable statistical values compared to the rest of the variables; this was generally the least accurate prediction in the CF05 event; however, opt2 stood out as the configuration with the best statistical results. Its highest R^2 value was obtained in opt1 and opt2 with 0.79.

4. Conclusions

In this work, four proposed configurations of the WRF model's physical parameterizations are generated and evaluated, focused on the prediction of the GHI for five frontal systems in the study region. The Tamb and Hrel are of great variability during this type of winter events, so they were considered in the discussion of the predicted GHI behavior. Based on the dispersion analysis of the point series, the evaluation of statistical errors between measured and calculated values, and their respective correlations, it can be concluded that the predictions of the GHI, Tamb, and Hrel variables within a range no larger than two standard deviations were able to simulate the behavior of atmospheric conditions during the passage of a winter frontal system. However, according to the evaluation of the statistical results obtained in all the case studies, the opt2 configuration corresponding to the Dudhia and RRTM solar radiation parameterizations was the most favorable for most of the events.

During the period of influence of the frontal systems analyzed in the study region, it was perceived that the WRF model made errors of underestimation and showed a lack of sensitivity to the rapid variability generated by possible clouds and humidity at low levels of the atmosphere, which was visible during the first 12 h, in which the cold front entered the study region. For the most part, it is clear that opt2 dominated with the most favorable statistical prediction values. Predictions of the Tamb variable obtained the lowest errors despite a general overestimation evidenced in the MBIAS values. The predictions of Hrel showed different values in the errors; however, they did not exceed the MAE of 13% nor the 10.6% overestimation in the less favorable cases. The fact that the Hrel variable responded with low correlation values and a relatively high error percentage could be closely related to the behavior and natural variability of the on-site measurements. Given the characteristics of the CF05 study event, this analysis suggests that the WRF model has difficulty in predicting the variability of the humidity of a cold front associated with a tropical maritime air mass and its interaction with Pacific upwelling moisture associated with the passage of tropical cyclones that transport moist air masses from latitudes to the south.

The results of the data measured by NASA stood out as a potential tool for the adjustment of the case studies analyzed, mainly due to the low errors shown in their measurements when recording the Hrel and GHI variables during the influence of frontal events associated with humid air masses.

The comparison between the persistence forecast and the predictions generated by the four WRF model parameterization configurations showed the capacity of the model to improve the prediction of atmospheric variables under the influence of cold fronts. Based on the observation of the Taylor diagrams and the analysis of the statistical errors, it can be concluded that the model configuration corresponding to the opt2 had the best performance in the prediction of the variability of the solar irradiance GHI, under the influence of a frontal system in the desert region of northwestern Mexico. It was also possible to observe the importance of associating humidity characteristics to frontal systems as a potential factor that hindered model predictions in this study area. This analysis provides a configuration of the WRF model that can be used as a meteorological prediction tool to directly associate the variability of solar irradiation in the estimation of short-term electric power generation in solar-activated plants, under the influence of winter systems in desert regions. It is proposed in future work that the opt2 configuration be tested under different planetary boundary layer parameterization options, where its performance will be evaluated in other similar climatic regions, and the sample of frontal events with humidity characteristics associated with tropical maritime air masses be increased.

Author Contributions: Conceptualization, J.E.L.-V. and N.V.-L.; methodology, J.E.L.-V.; software, J.E.L.-V. and D.E.F.-J.; validation, J.E.L.-V., D.E.F.-J. and S.I.-P.; investigation, J.E.L.-V. and N.V.-L.; resources, N.S.-S.; data curation, J.E.L.-V., J.R.-A. and S.I.-P.; writing—original draft preparation, J.E.L.-V.; writing—review and editing, N.V.-L., S.I.-P. and D.E.F.-J.; visualization, J.E.L.-V. and S.I.-P.; supervision, N.V.-L. and N.S.-S.; project administration, N.V.-L. and N.S.-S. All authors have read and agreed to the published version of the manuscript.

Funding: This research received no external funding.

Institutional Review Board Statement: Not applicable.

Informed Consent Statement: Not applicable.

Data Availability Statement: Data available on request due to restrictions privacy.

Acknowledgments: The authors are grateful to the Engineering Institute of the Autonomous University of Baja California for the support given to carry out this project. To the National Council of Science and Technology (CONAHCYT) for the grant given to José Ernesto López Velázquez (559433). The authors acknowledge the Autonomous University of Baja California for the support received from (111/6/C/19/23) within the framework of the call "23a. Convocatoria Interna".

Conflicts of Interest: The authors declare no conflict of interest.

References

1. Pedro, H.T.C.; Coimbra, C.F.M. Assessment of forecasting techniques for solar power production with no exogenous inputs. *Sol. Energy* **2012**, *86*, 2017–2028. [CrossRef]
2. Diagne, M.; David, M.; Boland, J.; Schmutz, N.; Lauret, P. Post-processing of solar irradiance forecasts from WRF model at Reunion Island. *Sol. Energy* **2014**, *105*, 99–108. [CrossRef]
3. Neves, D.; Brito, M.C.; Silva, C.A. Impact of solar and wind forecast uncertainties on demand response of isolated microgrids. *Renew. Energy* **2016**, *87*, 1003–1015. [CrossRef]
4. Zempila, M.-M.; Giannaros, T.M.; Bais, A.; Melas, D.; Kazantzidis, A. Evaluation of WRF shortwave radiation parameterizations in predicting Global Horizontal Irradiance in Greece. *Renew. Energy* **2016**, *86*, 831–840. [CrossRef]
5. Incecik, S.; Sakarya, S.; Tilev, S.; Kahraman, A.; Caliskan, E.; Topcu, S.; Kahya, C.; Odman, M.T. Evaluation of WRF parameterizations for global horizontal irradiation forecasts: A study for Turkey. *Atmosfera* **2019**, *32*, 143–158. [CrossRef]
6. Hayat, M.B.; Ali, D.; Monyake, K.C.; Alagha, L.; Ahmed, N. Solar energy—A look into power generation, challenges, and a solar-powered future. *Int. J. Energy Res.* **2019**, *43*, 1049–1067. [CrossRef]
7. Enríquez-Velásquez, E.A.; Benitez, V.H.; Obukhov, S.G.; Félix-Herrán, L.C.; Lozoya-Santos, J.D.J. Estimation of Solar Resource Based on Meteorological and Geographical Data: Sonora State in Northwestern Territory of Mexico as Case Study. *Energies* **2020**, *13*, 6501. [CrossRef]
8. Dubey, A. Preparing the Power Grid for Extreme Weather Events: Resilience Modeling and Optimization. In *Women in Power: Research and Development Advances in Electric Power Systems*; Tietjen, J.S., Ilic, M.D., Bertling Tjernberg, L., Schulz, N.N., Eds.; Springer International Publishing: Cham, Switzerland, 2023; pp. 209–243. [CrossRef]
9. Añel, J.A.; Fernández-González, M.; Labandeira, X.; López-Otero, X.; la Torre, L. Impact of Cold Waves and Heat Waves on the Energy Production Sector. *Atmosphere* **2017**, *8*, 209. [CrossRef]
10. Busby, J.W.; Baker, K.; Bazilian, M.D.; Gilbert, A.Q.; Grubert, E.; Rai, V.; Rhodes, J.D.; Shidore, S.; Smith, C.A.; Webber, M.E. Cascading risks: Understanding the 2021 winter blackout in Texas. *Energy Res. Soc. Sci.* **2021**, *77*, 102106. [CrossRef]
11. Smith, A.B. 2022 U.S. Billion-Dollar Weather and Climate Disasters in Historical Context. Available online: https://www.climate.gov/news-features/blogs/beyond-data/2022-us-billion-dollar-weather-and-climate-disasters-historical (accessed on 7 May 2024).
12. National Oceanic and Atmospheric Administration. National Centers for Environmental Prediction, Weather Prediction Center. Available online: https://www.wpc.ncep.noaa.gov/dailywxmap/index.html (accessed on 14 June 2024).
13. West, S.R.; Rowe, D.; Sayeef, S.; Berry, A. Short-term irradiance forecasting using skycams: Motivation and development. *Sol. Energy* **2014**, *110*, 188–207. [CrossRef]
14. Steyn, D.G.; Oke, T.R.; Hay, J.E.; Knox, J.L. On scales in meteorology and climatology. *Climatol. Bull.* **1981**, *39*, 1–8.
15. Brisch, J.; Kantz, H. Power law error growth in multi-hierarchical chaotic systems—A dynamical mechanism for finite prediction horizon. *New J. Phys.* **2019**, *21*, 93002. [CrossRef]
16. Balzarini, A.; Angelini, F.; Ferrero, L.; Moscatelli, M.; Perrone, M.G.; Pirovano, G.; Riva, G.M.; Sangiorgi, G.; Toppetti, A.M.; Gobbi, G.P.; et al. Sensitivity analysis of PBL schemes by comparing WRF model and experimental data. *Geosci. Model Dev. Discuss.* **2014**, *7*, 6133–6171. [CrossRef]
17. Lara-Fanego, V.; Ruiz-Arias, J.A.; Pozo-Vázquez, D.; Santos-Alamillos, F.J.; Tovar-Pescador, J. Evaluation of the WRF model solar irradiance forecasts in Andalusia (southern Spain). *Sol. Energy* **2012**, *86*, 2200–2217. [CrossRef]
18. Cohen, A.E.; Cavallo, S.M.; Coniglio, M.C.; Brooks, H.E. A Review of Planetary Boundary Layer Parameterization Schemes and Their Sensitivity in Simulating Southeastern U.S. Cold Season Severe Weather Environments. *Weather Forecast* **2015**, *30*, 591–612. [CrossRef]
19. Prasad, A.A.; Kay, M. Assessment of Simulated Solar Irradiance on Days of High Intermittency Using WRF-Solar. *Energies* **2020**, *13*, 385. [CrossRef]
20. Mierzwiak, M.; Kroszczyński, K.; Araszkiewicz, A. On Solar Radiation Prediction for the East–Central European Region. *Energies* **2022**, *15*, 3153. [CrossRef]
21. Urias, H.E.; Cueto, O.R.G.; Morales, G.B. Identification and classification of local climate zones in a semi-arid city of northwestern Mexico. *Vivienda Comunidades Sustentables* **2021**, *9*, 45–60. [CrossRef]
22. Lazaridis, M. Atmospheric Circulation. In *First Principles of Meteorology and Air Pollution*; Springer: Dordrecht, The Netherlands, 2011; pp. 119–149. [CrossRef]
23. Romero-Arteaga, A.; Ruiz de Alegría-Arzaburu, A.; Rivas, D.; Juarez, B. Nearshore current variations during the passage of cold fronts in NW Gulf of Mexico. *Cont. Shelf Res.* **2022**, *238*, 104697. [CrossRef]
24. NASA POWER Prediction of Worldwide Energy Resources. National Aeronautics and Space Administration. Available online: https://power.larc.nasa.gov (accessed on 14 June 2024).
25. National Centers for Environmental Prediction National Weather Service NOAA U.S. Department of Commerce. NCEP GDAS/FNL 0.25 Degree Global Tropospheric Analyses and Forecast Grids. Research Data Archive at the National Center for Atmospheric Research, Computational and Information Systems Laboratory, Boulder, CO, USA. 2015. Available online: https://rda.ucar.edu/datasets/dsd083003/ (accessed on 10 September 2023).
26. Kheyruri, Y.; Sharafati, A.; Ahmadi Lavin, J. Performance assessment of NASA POWER temperature product with different time scales in Iran. *Acta Geophys.* **2024**, *72*, 1175–1189. [CrossRef]

27. Rodrigues, G.C.; Braga, R.P. Evaluation of NASA POWER Reanalysis Products to Estimate Daily Weather Variables in a Hot Summer Mediterranean Climate. *Agronomy* **2021**, *11*, 1207. [CrossRef]
28. Sauter, B. *A Case Study of the Persistence of Weather Forecast Model Errors*; Army Research Laboratory: Adelphi, MD, USA, 2005.
29. Mittermaier, M.P. The Potential Impact of Using Persistence as a Reference Forecast on Perceived Forecast Skill. *Weather Forecast* **2008**, *23*, 1022–1031. [CrossRef]
30. Skamarock, W.C.; Klemp, J.B. A time-split nonhydrostatic atmospheric model for weather research and forecasting applications. *J. Comput. Phys.* **2008**, *227*, 3465–3485. [CrossRef]
31. García-Díez, M.; Fernández, J.; Fita, L.; Yagüe, C. Seasonal dependence of WRF model biases and sensitivity to PBL schemes over Europe. *Q. J. R. Meteorol. Soc.* **2013**, *139*, 501–514. [CrossRef]
32. Perez, R.; Lorenz, E.; Pelland, S.; Beauharnois, M.; Van Knowe, G.; Hemker, K., Jr.; Heinemann, D.; Remund, J.; Müller, S.C.; Traunmüller, W.; et al. Comparison of numerical weather prediction solar irradiance forecasts in the US, Canada and Europe. *Sol. Energy* **2013**, *94*, 305–326. [CrossRef]
33. Ruiz-Arias, J.A.; Dudhia, J.; Santos-Alamillos, F.J.; Pozo-Vázquez, D. Surface clear-sky shortwave radiative closure intercomparisons in the Weather Research and Forecasting model. *J. Geophys. Res. Atmos.* **2013**, *118*, 9901–9913. [CrossRef]
34. Iacono, M.J.; Delamere, J.S.; Mlawer, E.J.; Shephard, M.W.; Clough, S.A.; Collins, W.D. Radiative forcing by long-lived greenhouse gases: Calculations with the AER radiative transfer models. *J. Geophys. Res. Atmos.* **2008**, *113*. [CrossRef]
35. Clough, S.A.; Shephard, M.W.; Mlawer, E.J.; Delamere, J.S.; Iacono, M.J.; Cady-Pereira, K.; Boukabara, S.; Brown, P.D. Atmospheric radiative transfer modeling: A summary of the AER codes. *J. Quant. Spectrosc. Radiat. Transf.* **2005**, *91*, 233–244. [CrossRef]
36. Chou, M.-D.; Suarez, M.J. *A Solar Radiation Parameterization for Atmospheric Studies, NASA Tech. Rep. Series on Global Modeling and Data Assimilation, NASA/TM-1999-104606*; NASA Goddard Space Flight Center: Greenbelt, MD, USA, 1999; Volume 15.
37. Gu, Y.; Liou, K.N.; Ou, S.C.; Fovell, R. Cirrus cloud simulations using WRF with improved radiation parameterization and increased vertical resolution. *J. Geophys. Res. Atmos.* **2011**, *116*. [CrossRef]
38. Marquez, R.; Coimbra, C.F.M. Proposed metric for evaluation of solar forecasting models. *J. Sol. Energy Eng.* **2013**, *135*, 11016. [CrossRef]
39. Taylor, K.E. Summarizing multiple aspects of model performance in a single diagram. *J. Geophys. Res. Atmos.* **2001**, *106*, 7183–7192. [CrossRef]
40. Pasch, R.J. National Hurricane Center, Tropical Cyclone Report:Tropical Storm Odalys (EP-202020). April 2021. Available online: https://www.nhc.noaa.gov/data/tcr/EP202020_Odalys.pdf (accessed on 13 June 2023).

Anexo C (artículos coautoría)

Numerical modeling of soil temperature variation under an extreme desert climate

Revista: Geothermics
julio del 2023
https://doi.org/10.1016/j.geothermics.2023.102731

Influence of mixing height and atmospheric stability conditions on correlation of NO_2 columns and surface concentrations in a Mexico-United States border region

Revista: Atmospheric Science Letters
11 mayo del 2021
https://doi.org/10.1002/asl.1024

Geothermics 112 (2023) 102731

Contents lists available at ScienceDirect

Geothermics

journal homepage: www.elsevier.com/locate/geothermics

Numerical modeling of soil temperature variation under an extreme desert climate

J. Ríos-Arriola[a,*], E. Gómez-Arias[b,*], I. Zavala-Guillén[c], N. Velázquez-Limón[a], G. Bojórquez-Morales[d], J.E. López-Velázquez[e]

[a] *Centro de Estudio de las Energías Renovables (CEENER), Instituto de Ingeniería, Universidad Autónoma de Baja California, Mexicali, 21280, Mexico*
[b] *CONACYT - Centro de Investigación Científica y de Educación Superior de Ensenada, Ensenada, BC, 22860, Mexico*
[c] *Centro de Investigación Científica y de Educación Superior de Ensenada, Ensenada, BC, 22860, Mexico*
[d] *Facultad de Arquitectura, Universidad Autónoma de Baja California, Mexicali 21280, Mexico*
[e] *Laboratorio de Meteorología y Climatología, Instituto de Ingeniería, Universidad Autónoma de Baja California, Mexicali B.C., 21280, Mexico*

ARTICLE INFO

Keywords:
Soil temperature variation
Extreme climate
Soil temperature measurements
Soil surface water content

ABSTRACT

The soil temperature profile is useful for different engineering, architecture, and agriculture areas. In recent years, the growth of direct uses of geothermal energy has increased the interest in soil temperature prediction models. This research paper numerically models the soil temperature variation under extreme desert climate conditions and compares it with experimental data measured on-site to evaluate the reliability of numerical models based on the one-dimensional transient state heat conduction equation as a tool for the evaluation of low enthalpy geothermal resource using meteorological data and soil thermal properties. From the study results, it can be concluded that the numerical models present temperature values close to those measured experimentally. The model that presents the more significant mismatches concerning the experimental data is the 1 m model, presenting the following statistical values; R^2 of 0.97, mean absolute error of 0.61 °C, RMSE of 0.76 °C, NRMSE of 3.01%, and a MBIAS of 0.23. Although the numerical models present values are close to those measured, some coefficients, such as the soil surface water content greatly influence the model's accuracy regardless of depth.

1. Introduction

Soil is a natural heat source or sink because its thermophysical properties are different from those of the ambient air, which causes a slower response to heat transfer mechanisms caused by the daily and annual variation of meteorological conditions at the soil surface. This variation of properties between soil and ambient air establishes a temperature differential called *soil thermal inertia*. This thermal behavior varies according to the weather conditions, soil type, and local conditions such as type of cover (e.g. grass, concrete), moisture content, or thermal anomalies.

In recent years, the direct uses of geothermal energy have increased its worldwide installed capacity (Lund and Toth, 2021). One of its main applications is the air conditioning of buildings, which has driven the interest and the need to develop or improve predictive models that allow estimating shallow depth soil temperature variations. Due to the economic and technical costs involved in the experimental temperature measurement in a well or excavation, different mathematical models have been developed that describe the periodic variation of the soil temperature for a given time and depth.

Hillel (1982) assumed that the time variation of the soil temperature at any depth can be represented as a sine wave oscillating around the average value of the ambient temperature "T_m". His equation is expressed so that the amplitude of the sinusoidal wave decreases as the depth increases at a rate that depends on the thermophysical properties of the soil, until the point at which the soil temperature reaches the average ambient temperature value and maintains constant throughout the year.

Krarti et al. (1995) proposed an analytical model to predict soil temperature at different depths, their model assumes that the temperature variation in the soil is a purely sinusoidal wave but does not use the annual average of the ambient temperature to obtain the value of "T_m" instead, it considers an energy balance where it takes into account the variation of meteorological factors to calculate it. Its results were validated with experimental measurements with an uncertainty of 10%.

Sándor and Fodor, (2012) compared the CERES model, a modified

* Corresponding authors.
E-mail addresses: riosj9@uabc.edu.mx (J. Ríos-Arriola), gomezar@cicese.mx (E. Gómez-Arias).

https://doi.org/10.1016/j.geothermics.2023.102731
Received 4 January 2023; Received in revised form 30 March 2023; Accepted 25 April 2023
Available online 28 April 2023
0375-6505/

version of the CERES model, and the HYDRUS-1D model for soil temperature calculation, the authors measured soil temperature at 0.05, 0.1, 0.2, 0.4, and 0.6 m depth in 8 parcels with different treatments: fertilized, unfertilized, irrigated and non-irrigated. The authors conclude that vegetation reduces the average soil temperature and its diurnal amplitude; therefore, they recommend considering the vegetation area in soil temperature prediction models.

Ozgener et al. (2013) used the analytical sine-wave model to estimate the daily soil temperature variation in Izmir, Turkey. Their model is based on data calculated from annual ambient temperatures, such as annual mean temperature T_m and temperature wave amplitude A_s. Their results were compared with experimental measurements at 0.05, 0.1, 0.2, and 3 m depth, reporting error percentages of 10.78%, 10%, 10.26%, and 14.95%, respectively. The authors state that their simplified heat transfer model can be useful for design applications in agriculture and engineering.

Chalhoub et al. (2017) proposed a numerical model describing heat and mass transfer in soils exposed to moderate climates to predict the soil temperature at shallow depths. Their model includes the influence of soil moisture content to calculate their thermo-physical properties. The authors validated their model with experimental temperature measurements at 0.14, 0.5, 1 and 1.5 m depth and reported a maximum average error of 1.63 °C corresponding to the depth closest to the soil surface.

Naranjo-Mendoza et al. (2018) carried out a comparative study between two analytical models and two numerical models to predict soil temperature. The results of the four models were compared with experimentally measured data at 0.75, 1.25, 1.75, and 2.75 m depth. The authors conclude that the analytical models have a higher error generated by the influence of uncertainties in the soil undisturbed temperature that has a great influence on the analytical sinusoidal equation. The authors compared the effectiveness of their numerical model by establishing first-type (known temperature) and third-type (energy balance) boundary conditions at the upper boundary node and first-type boundary conditions at the last node, obtaining an RMSE of 1.99 and 11.56 °C, respectively. Therefore, the authors conclude that the numerical model solved with the first-type boundary condition at the upper boundary node provides the best estimates for their case study..

Fang et al. (2021) studied changes in soil temperature (ST) and soil moisture (SM) on the Tibetan Plateau using the Community Soil Model (CLM4.5) instead of situ observation and/or satellite products. The authors report that by considering gravel content in the CLM4.5 organic matter and thermal conductivity calculations, the numerical simulation tends to reasonably reproduce ST and SM variations over long time series. Their results show that soil warming and wetting reached maximum values of 0.31 °C/decade and 0.77%/decade since 1960.

In summary, different models have been proposed to predict the variation of the soil temperature profile. The numerical models proposed in the last five years have performed better predictions with respect to the analytical models (which have been widely used). However, most of the authors mentioned above state that there are some areas of opportunity, such as considering the variation of soil thermal properties according to the irrigation and/or precipitation behavior as a function of time to reduce the uncertainty of the estimation models. Similarly, evaluating the accuracy of numerical models in other study areas under different extreme climates could increase their reliability.

In this work, the main objective was to model the annual variation of the soil temperature profile for a desert area with high levels of solar radiation and extreme variation of daily temperature range throughout the year using the one-dimensional transient state heat conduction equation which was discretized using the finite volume method (FVM) and subsequently solved with a direct algebraic method (TDMA). At the upper boundary node, a third-type boundary condition was established that considers an energy balance between the heat transfer mechanisms occurring at the soil surface. A first-type boundary condition was established at the computational domain bottom, which assumes that its temperature will be equal to the annual average of the ambient temperature. The meteorological data used as input data for the numerical model, and the experimental soil temperature data (used to validate the numerical model results at different depths) were measured in the study area at a shallow deep of four meters.

2. Study area

The city of Mexicali, Baja California is located in northwestern Mexico (32.65°N, 115.45°W), in a desert zone with a hot arid, and dry climate according to the Köppen classification, adapted by García (2004) to the conditions of the Mexican Republic. Mexicali has extreme thermal variability. During the summer, the ambient temperature can reach maximum values close to 50 °C and, during the winter, minimums of up to 0 °C, while the average annual temperature is close to 23 °C (García-Cueto et al., 2013). Its rainy season is from August to February; however, annual precipitation does not exceed 80 mm. The maximum solar radiation levels occur in the May-June period, with values that can reach 1200 W/m^2. The average maximum radiation during the summer corresponds to 937 W/m^2 and 345 W/m^2 for the winter; relative humidity levels range between 60 and 70% during the year, with maximum values of up to 100% during September and October (Urias-Barrera et al., 2021). Fig. 1 shows the study area where the well (used to measure temperature at 1, 2, 3, and 4 m depth) and the meteorological station are located, both in the surroundings of the Engineering Institute of the Autonomous University of Baja California (UABC).

3. Materials and methods

3.1. Experimental soil temperature profile

A shallow vertical borehole with a depth of 4 m was drilled in the surroundings of the Engineering Institute of the UABC to measure the annual soil temperature variation. The depth of 4 m (it is worth mentioning that in areas with a natural thermal gradient ~35 °C/km from 4 m depth, the temperature variation between the maximum and the mean value is less than 10% (Acuña et al., 2017; Stylianou et al., 2019).

During drilling, samples were recovered from the different lithological identified in the soil. A total of nine samples were extracted and stored in sealed metal containers (to preserve their thermophysical, mechanics, and geological properties), which were analyzed in the laboratory, where the water content and texture analysis in each sample were estimated.

Experimental temperature data were obtained with four sensors model TMCx-HD (50 ft, with an uncertainty of ±0.15 °C) water/soil placed at 1, 2, 3, and 4 m depth in the vertical well. A HOBO model UX120-006 M 4-channel analog data logger was used for data acquisition. The temperature sensors were calibrated with Polyscience PD07R-20-A11B equipment before their installation in conjunction with the data logger. The maximum temperature difference (precision) was ±0.2 °C.

3.2. Meteorological data

For the measurement of the ambient temperature (dry bulb temperature), solar radiation, relative humidity, and wind speed during the year 2020 in Mexicali, Baja California, Mexico, a Davis model Vantage Pro-weather station was used, located at 16 m above ground level in the Engineering Institute of the UABC (30°21′19.7″ N and 114°38′26.3″ W).

3.3. Soil thermal properties

Thermal diffusivity α (m^2/s) is the ratio between thermal conductivity k (W/m °C) and the product of specific heat C_p (J/kg °C) multiplied

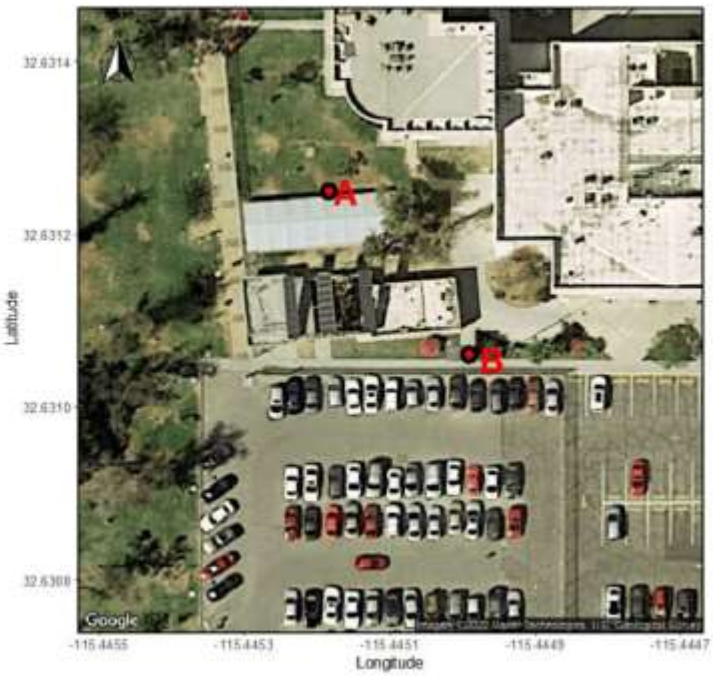

Fig. 1. Location of the well (A) and the meteorological station (B).

by density ρ (kg/m^3). In the absence of instruments to directly measure these four variables, we used experimental correlations reported in the literature.

Textural class and water content data were used to estimate thermal diffusivity from an experimental correlation (Eq. (1)), developed for different textural classes as a function of water content θ reported by Arkhangelskaya and Lukyashchenko (2017):

$$\alpha(\theta) = \alpha_0 + \gamma \exp\left[-0.5\left(\frac{\ln\left(\frac{\theta}{\theta_0}\right)}{\nu}\right)^2\right] \tag{1}$$

where α_0 is the thermal diffusivity corresponding to a determined soil type without water, γ is the difference between the highest thermal diffusivity at the optional water content θ_0 and the diffusivity without water content, and ν is a constant depending on the type of soil.

3.4. Mathematical model

The undisturbed soil temperature profile can be modeled by the one-dimensional transient heat conduction Equation (Carslaw and Jaeger, 1959);

$$\frac{\partial^2 T(z,t)}{\partial z^2} = \frac{1}{\alpha}\frac{\partial T(z,t)}{\partial t} \tag{2}$$

where α is the soil thermal diffusivity (m^2/s), z is the depth (m) and t is the time (s). To solve Eq. (2), an energy balance equation at the soil surface must be considered as the boundary condition (Mihalakakou et al., 1997).

$$\alpha \frac{\partial T}{\partial z}\Big|_{z=0} = SR - LR + CE - LH \tag{3}$$

where SR is the solar radiation absorbed by the soil surface, LR is the long-wave radiation emitted by the soil surface, CE is the convective energy exchanged between the air and the soil surface, and LH is the latent heat of evaporation (when moisture is present in the soil surface). The shortwave solar radiation absorbed by the soil surface can be calculated according to the solar radiation analysis of Kreith et al. (2011) using the following Equation:

$$SR = \beta_{soil} S_{rad} \tag{4}$$

were β_{soil} represents the soil absorptivity coefficient and S_{rad} the short-wave solar radiation incident on the soil surface (W/m^2). The long-wave radiation emitted from the soil surface to the sky is calculated by Eq. (5):

$$LR = \epsilon_{soil} \Delta R \tag{5}$$

where ϵ_{soil} is the emissivity of the soil surface (dimensionless value). The term ΔR represents the long-wave thermal radiation which depends directly on the soil surface temperature T_s and the sky temperature T_{sky}, and can be calculated using the empirical correlation reported by Singh and Sharma (2017):

$$\Delta R = \sigma\left[(T_s + 273.15)^4 - (T_{sky} + 273.15^4)\right] \tag{6}$$

The σ variable represents the Stefan-Boltzmann constant (5.67×10^{-8} W/m^{2}K^4). The sky temperature T_{sky} can be calculated using the Eq. (7) reported by Kröger (2022):

$$T_{sky} = 0.0552 T_{air}^{1.5} \tag{7}$$

The convective energy exchanged between the ambient air and the soil surface is calculated by means of the Eq. (8).

$$CE = h_c(T_{air} - T_r) \tag{8}$$

where T_{air} is the dry bulb ambient air temperature (°C), T_r is the soil temperature at the surface (°C), and h_c is the convective heat transfer coefficient by convection between the soil surface and the air in contact with it (W/m^2 °C); according to McAdams (1985) it can be calculated as follows:

$$h_c = 5.7 + 3.8W_{sp} \tag{9}$$

where W_{sp} is the wind speed (m/s) of the air in contact with the soil surface. Penman (1948) found that the latent heat flux in the soil surface due to evaporation of their moisture content can be calculated using Eq. (10):

$$LH = 0.0168fh_c[(\omega T_r + \theta) - H_{rel}(\omega T_{air} + \theta)] \tag{10}$$

where H_{rel} is the relative humidity of the ambient air in contact with the soil surface and f is a fraction that depends mainly on the water content of the soil surface and the presence of soil cover, ω=103 (Pa/K) and θ=609 (Pa) are constant values. The f typical values reported in the literature are for saturated soil are between 0.9 and 1.0, for wet soils from 0.6 to 0.8, for moist soil from 0.4 to 0.5, for arid soils between 0.1 to 0.2, and for dry soils f value is equal to 0 since no evaporation occurs. For soils covered by grass, the f value, can be calculated by multiplying the values described above by a coefficient of 0.7 (Penman, 1948).

Finally, a first-class boundary condition was established at the last node located at the bottom of the computational domain, which assumes that its temperature will be known, constant, and equivalent to the annual average of the ambient temperature T_m.

$$T_{i=n} = T_m \tag{11}$$

3.5. Numerical model

Fig. 2 shows the flow diagram used to calculate the soil temperature

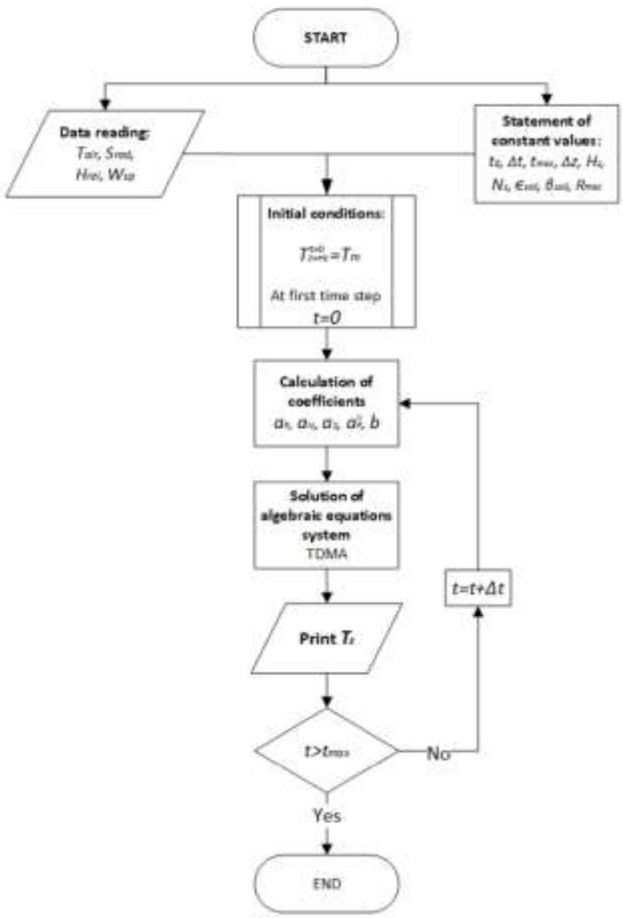

Fig. 2. Algorithm for soil temperature modeling.

profile from the one-dimensional transient heat conduction equation solution, which was discretized using the finite volume method (FVM) and subsequently solved with a direct algebraic method (TDMA) (Patankar, 1980; Versteeg and Malalasekera, 2000). The FVM discretization method requires dividing the system under study (in this case, the soil) into a finite number of non-overlapping control volumes (CV) so that each CV can be assigned a node of the mesh. The total volume of the domain is equal to the sum of the CV's considered (Xamán and Gijón-Rivera, 2015).

3.5.1. Conceptual model

The unidimensional physical model under study is the soil in the surroundings of the study area, which is considered a non-homogeneous finite medium with known physical properties. Fig. 3 shows the location of the temperature sensors and the type of soil corresponding to each one according to its depth (Fig. 3a). It also shows the physical representation of the nodes and control volumes (CV) that compose the numerical model (Fig. 3b).

3.5.2. Numerical solution

The integration of Eq. (1) over each CV is possible using Gauss's divergence theorem to substitute a volume integral for a surface integral and, subsequently, the half-point rule to express the flow at the center of the interface (Xamán and Gijón-Rivera, 2015).

The exact form of the discretized equation depends on the value of φ which is a pondered weight factor whose value varies between 0 and 1. Different values of φ can be interpreted in terms of the variation of T_P in the time interval between t_0 and $t+\Delta t$. A fully implicit scheme was used for this case, which considers $\varphi=1$. Therefore, the Equation to calculate the temperature T_P at each of the internal nodes reduces to:

$$a_P T_P = a_N T_N + a_S T_S + b \tag{12}$$

where "a" are the coefficients of the discretized equation, calculated with the following equations:

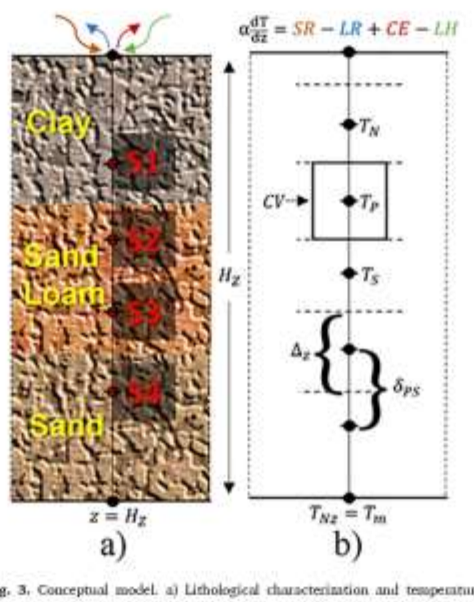

Fig. 3. Conceptual model. a) Lithological characterization and temperature sensors location. b) Computational domain in the "z" axis.

$$a_P = a_N + a_S + a_P^0 \tag{13}$$

$$a_N = \frac{\alpha_N}{\delta_{NP}} \quad a_S = \frac{\alpha_S}{\delta_{PS}} \quad b = a_P^0 T_P^* \quad a_P^0 = \frac{\Delta z}{\Delta t} \tag{14}$$

where δ is the distance between computational nodes (m), Δz is the control volume thickness (m) and Δt the time step (s) (the symbol * indicates that this value belongs to the previous iteration). Discretizing Eq. (3) at the upper boundary node, we obtain:

$$\alpha\frac{T_P - T_S}{\delta_{PS}} = \beta_{soil} S_{rad} - \epsilon_{soil}\Delta R + h_c(T_{air} - T_P) - 0.0168 f h_c[(\omega T_P + \theta) - H_{rel}(\omega T_{air} + \theta)] \tag{15}$$

Consequently, the coefficients at the upper boundary node are calculated as follows:

$$a_P = \frac{\alpha_P}{\delta_{PS}} + h_c + 0.0168 f h_c \omega \qquad a_N = 0 \qquad a_S = \frac{\alpha_P}{\delta_{PS}} \tag{16}$$

$$b = \beta_{soil} S_{rad} - \epsilon_{soil}\Delta R + h_c(T_{air}) - 0.0168 f h_c[(\theta) - H_{rel}(\omega T_{air})] \tag{17}$$

For the lower boundary node, it results:

$$a_P = 1 \qquad a_N = \frac{\alpha_P}{\delta_{NP}} \qquad a_S = 0 \tag{18}$$

$$b = T_m \tag{19}$$

In order to model the one-dimensional temperature profile in transient state as indicated in this section, a numerical code was developed in C++ computer language. Soil absorptivity (β_{soil}=0.73) and emissivity (β_{soil}=0.73) values were measured on site. The time step, computational domain depth, number of nodes, control volume thickness and convergence criterion correspond to Δt=3600 s, z=20 m, N_z=200, Δz=0.1 m and R_{max}=1.0 × 10^{-3}, respectively. Table 1 shows the thermal diffusivities (α) and the water content of the soil at the surface (f) values considered in this study for different depth and season.

3.6. Statistical metrics

In order to evaluate the accuracy of the numerical model compared with the experimental data, the following statistical indicators were used; Coefficient of determination (R^2), Mean Absolute Error (MAE), Root Mean Square Error (RMSE), Normalized Root Mean Square Error (based on the mean; NRMSE) and Mean Bias Error (MBIAS). These indicators are calculated as shown in the following Eqs. (20)-(23).

$$MAE = \sum_{i=1}^{n}\frac{|e_i - m_i|}{n} \tag{20}$$

$$RMSE = \sqrt{\frac{\sum_{i=1}^{n}(e_i - m_i)^2}{n}} \tag{21}$$

$$NRMSE = \frac{RMSE}{\overline{m_i}} \tag{22}$$

Table 1
Thermal diffusivities (α) and f values were used for modeling the one-dimensional soil temperature profile.

	Season Winter	Spring	Summer	Autumn
f	0	0.1	0.1	0
$\alpha_{0-1.7\ m}(m^2/s)$	2.5 × 10^{-7}	2.5 × 10^{-7}	2.5 × 10^{-7}	2.5 × 10^{-7}
$\alpha_{1.7-2.4\ m}(m^2/s)$	4.4 × 10^{-7}	4.4 × 10^{-7}	4.4 × 10^{-7}	4.4 × 10^{-7}
$\alpha_{2.4-3\ m}(m^2/s)$	4.4 × 10^{-7}	4.4 × 10^{-7}	4.4 × 10^{-7}	4.4 × 10^{-7}
$\alpha_{3-20\ m}(m^2/s)$	7.5 × 10^{-7}	7.5 × 10^{-7}	7.5 × 10^{-7}	7.5 × 10^{-7}

$$MBIAS = \sum_{i=1}^{n} \frac{e_i - m_i}{n} \tag{23}$$

where e_i and m_i represents the estimated and measured value for each time step "i". The variable n represent the number of total time steps and $\overline{m_i}$ is the average of the measured values.

4. Results and discussion

Fig. 4 shows soil temperature variation at 1 m depth in the city of Mexicali, Baja California, Mexico using the data measured in the vertical well of the study area and the data obtained with the numerical model. The model that most accurately predicted the temperature variation for 1 m depth was obtained considering different values of f for each weather season (f variable; see Table 1). This model presents a coefficient of determination (R^2) of 0.9745, MAE of 0.61 °C, RMSE of 0.76 °C, NRMSE (based on the mean) of 3.01%, and a MBIAS of 0.2319, concerning the experimentally measured data. The statistical metrics obtained using f variable values or constant values of f=0 and f=0.1 throughout the year are shown in Table 2. Furthermore, the Figure also shows that the numerical model at 1 m depth is sensitive to the heat transfer mechanisms that occur at the soil surface because it has abrupt temperature increases/decreases, even greater than those presented by the experimental data at this depth.

Fig. 5 shows soil temperature variation at 2 m depth from the data measured experimentally and those obtained with the numerical model. The results of the most accurate model for 2 m depth (also with f variable values; see Table 1) present a coefficient of determination (R^2) of 0.9827, MAE of 0.33 °C, RMSE of 0.43 °C, NRMSE (based on the mean) of 1.69%, and a MBIAS of 0.0852 respect to the experimentally measured data. Table 2 shows the statistical metrics obtained using f variable values or constant values of f=0.1 and f=0 throughout the year. The higher inaccuracy of the numerical model at 2 m depth occurs at around 5952 h, which corresponds to the beginning of September when the experimental data present their maximum value, which the model underestimates. This behavior also occurs with the numerical model at 1 m depth.

Fig. 6 shows soil temperature variation at 3 m depth from measured data and the data obtained with the numerical model. Using the different values of f for each weather season (f variable; see Table 1), the results of the numerical model present a coefficient of determination (R^2) of 0.9920, MAE of 0.14 °C, RMSE of 0.19 °C, NRMSE (based on the mean) of 0.77% and a percentage deviation MBIAS of −0.0706, with respect to the experimentally measured data. The statistical metrics obtained for numerical models with f variable values or f constant values equal to 0.1 and 0 throughout the year are shown in Table 2.

Table 2
Statistical metrics for the numerical models using different values of f compared with experimental data.

Depth (m)	f	R^2	MAE (°C)	RMSE (°C)	NRMSE (%)	MBIAS
1	f_v	0.974	0.61	0.77	3.01	0.23
	0.1	0.947	3.09	3.99	15.67	−3.00
	0	0.991	4.04	4.63	18.22	4.00
2	f_v	0.983	0.33	0.43	1.70	0.09
	0.1	0.899	2.00	2.41	9.47	−1.99
	0	0.980	2.78	3.32	13.06	2.77
3	f_v	0.992	0.15	0.20	0.77	−0.07
	0.1	0.887	1.54	1.76	6.91	−1.54
	0	0.977	1.93	2.45	9.63	1.87
4	f_v	0.990	0.23	0.27	1.04	−0.23
	0.1	0.846	1.27	1.41	5.48	−1.27
	0	0.944	1.24	1.69	6.59	1.10

Finally, Fig. 7 shows soil temperature variation at 4 m depth from measured data and estimated data with the numerical models. The results of the most accurate numerical model (considering f variable values) for 4 m depth present a coefficient of determination (R^2) of 0.9900, MAE of 0.23 °C, RMSE of 0.26 °C, NRMSE (based on the mean) of 1.04% and a deviation percentage MBIAS of −0.2307, with respect to the experimentally measured data. Table 2 shows the statistical metrics for numerical models considering f variable values or f constant values equal to 0.1 and 0 throughout the year.

The results obtained with the numerical model at 3 m depth showed higher similarity to the experimental data compared to the results obtained by the numerical model at the other depths. Although the coefficient of determination R^2 presented a value close to the obtained with the numerical model at 4 m depth, the rest of the statistical metrics show that at 3 m depth, the numerical model had a better response because the MAE, RMSE, NRMSE, and the MBIAS are 36.72, 26.13, 25.67 and 69.4% lower, with respect to the numerical model at 4 m depth.

The statistical metrics resulting from the comparison between the

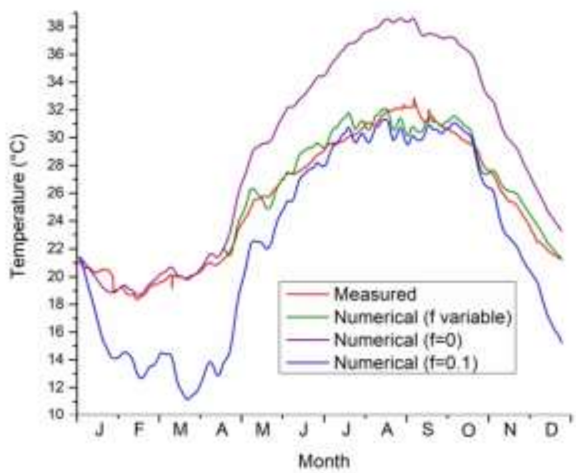

Fig. 4. Soil temperature variation at 1 m depth in Mexicali (study area) during the year 2020.

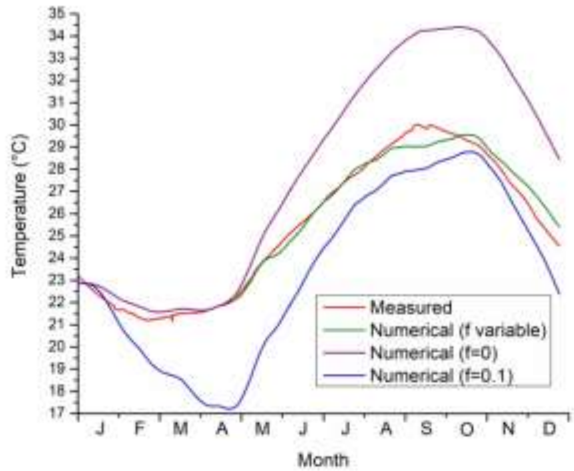

Fig. 5. Soil temperature variation at 2 m depth in Mexicali during the year 2020.

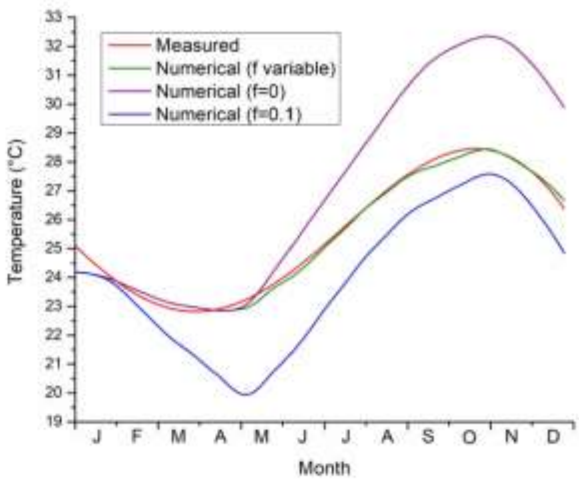

Fig. 6. Soil temperature variation at 3 m depth in Mexicali during the year 2020.

values estimated by the numerical models and the values measured on-site at 1, 2, 3, and 4 m depth are shown in Table 2.

Fig. 8 shows the dispersion of the statistical metrics obtained to evaluate the fit quality between the results obtained from the numerical models with the experimental data. Fig. 8a shows the distribution of the values of the coefficient R^2 corresponding to all depths (1 to 4 m) for each value of f (see Table 2), where the best values are obtained when the value of the parameter f is variable (f_v). This behavior is also observed in Figs. 8b (MAE), 8c (RMSE), 8d (NRMSE), and 8e (MBIAS), where the lowest residuals correspond to a f_v.

The soil surface ($z = 0$ m) moisture content factor "f" significantly impacts the numerical model results at any depth. Based on the annual soil temperature averages, the "f" factor with a value of 0.1 causes decreases of 3.00, 1.98, 1.53, and 1.26 °C at 1, 2, 3, and 4 m depth, respectively. Considering a factor f with a value of 0, the annual soil temperature averages at 1, 2, 3, and 4 m depth present increases of 3.99, 2.77, 1.86, and 1.09 °C respectively. This is because the lack of moisture at the soil surface ($f=0$) prevents latent heat transfer by evaporation from the soil surface to the environment; it is known that the latent heat required to evaporate water has a value of ≈2400 kJ/kg. Therefore, it has significant effects on the energy balance (Eq. (3)) at the soil surface ($z = 0$) and subsequently on the behavior of the soil temperature.

Since the measured soil temperature profiles present values close to those estimated by the numerical model, we proceeded to project the temperature profiles at greater depths without experimental data, to find the depth at which the temperature remains constant throughout the year. Fig. 9 shows the projection of temperature profiles against depth. Although the temperature, variation decreases with increasing

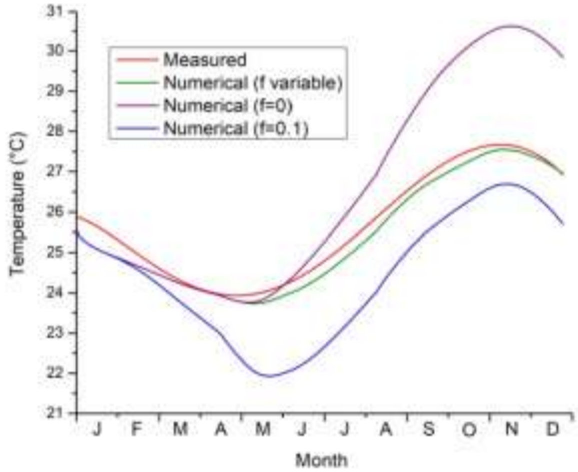

Fig. 7. Soil temperature variation at 4 m depth in Mexicali during the year 2020.

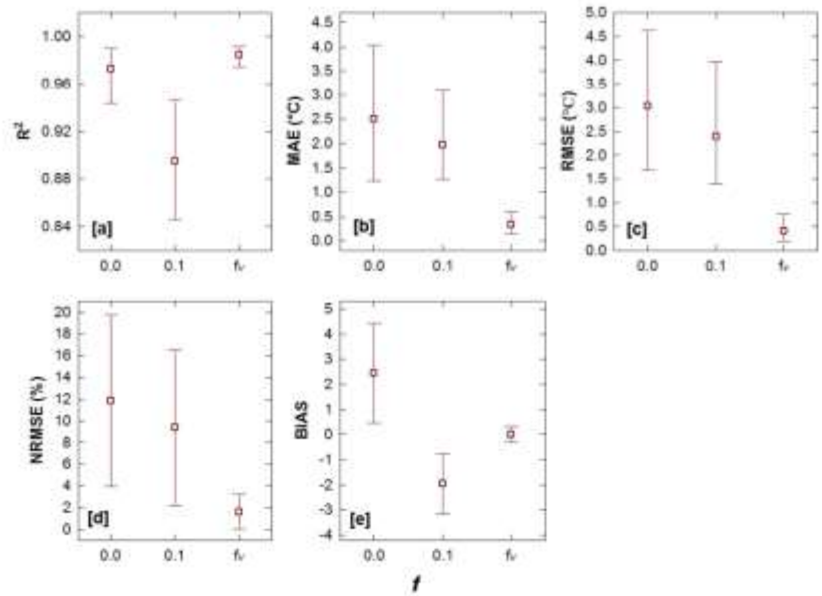

Fig. 8. Box-plot diagrams of the statical metrics between the numerical models and experimental data.

depth, the Figure indicates that at 10 m depth variations in soil temperature exist (≈0.24 °C).

The months of February, June, August, and December were selected because they represent the characteristic thermal behaviors of the temperature versus depth profiles that occur throughout the year. The results show that at 13 m depth, the variation of soil temperature throughout the year presents a difference of 0.0967 °C between its maximum and minimum, so it is determined that at this depth the soil temperature is undisturbed by weather conditions.

4. Conclusion

This research paper numerically models the soil temperature variation under extreme desert climate conditions and compares it with experimental data measured on-site in order to evaluate the reliability of numerical models based on the one-dimensional transient state heat

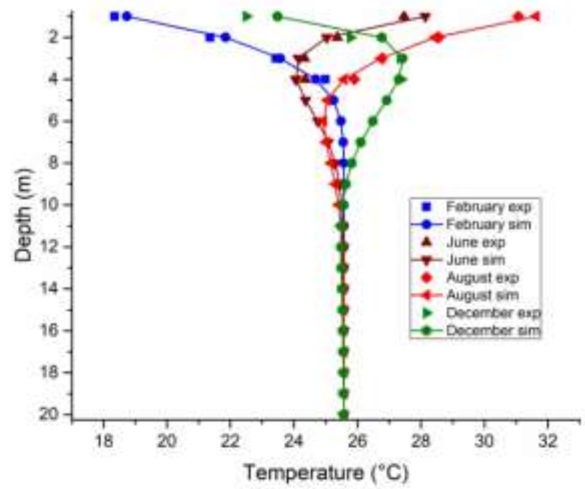

Fig. 9. Soil temperature variation with depth for each weather season.

conduction equation as a tool for the evaluation of low enthalpy geothermal resource using meteorological data (ambient temperature, relative humidity, solar radiation, and wind speed) and soil thermal properties (thermal diffusivity). Based on the results of the study, it can be concluded that the numerical models present temperature values close to those measured experimentally. The model that presents the greater mismatches with respect to the experimental data is the shallower model (1 m depth), presenting the following statistical values; R^2 of 0.9745, mean absolute error of 0.61 °C, RMSE of 0.76 °C, NRMSE of 3.00%, and a MBIAS of 0.2319. This can be attributed to the fact that at a shallower depth, the soil is more sensitive to the meteorological conditions, which, being an area with an extreme climate, presents marked diurnal and seasonal variations, mainly in the ambient temperature, that present considerable differences between the maximum and minimum daily and annual temperatures. Although the numerical model's present values are close to those measured, certain coefficients such as the surface soil moisture content factor "f" have a great influence on the accuracy of the model regardless of depth. In this work, values for f of 0 and 0.1 were considered, which are typical for arid regions; however, considering these values constant throughout the year induces a significant error. For this reason, the seasonal variation of the f coefficient between values of 0 and 0.1 was considered. This can be attributed to the fact that, during the spring and summer seasons when solar radiation levels increase, the frequency and intensity of water irrigation in the study area also increases, with the purpose of preserving the flora.

Declaration of Competing Interest

The authors declare that they have no known competing financial interests or personal relationships that could have appeared to influence the work reported in this paper.

Data availability

Data will be made available on request.

Acknowledgement

The authors would like to acknowledge "Consejo Nacional de Ciencia y Tecnología (CONACYT)" for the scholarship granted to Juan Ríos-Arriola (CVU 984076) to carry out his PhD studies. Thanks to the constructive comments and suggestions of the anonymous reviewers to improve the quality of this manuscript.

References

Acuña, A., Lara, F., Rosales, P., Suastegui, J., Velázquez, N., Ruelas, A., 2017. Impact of a vertical geothermal heat exchanger on the solar fraction of a solar cooling system. Int. J. Refrig. 76, 63–72. https://doi.org/10.1016/j.ijrefrig.2017.02.007.

Arkhangelskaya, T., Lukyashchenko, K., 2017. Estimating soil thermal diffusivity at different water contents from easily available data on soil texture, bulk density, and organic carbon content. Biosyst. Eng. 168, 83–95. https://doi.org/10.1016/j.biosystemseng.2017.06.011.

Carslaw, H.S., Jaeger, J.C., 1959. Conduction of Heat in Solids, 2nd edition. Oxford University Press, p. 520.

Chalhoub, M., Bernier, M., Coquet, Y., Philippe, M., 2017. A simple heat and moisture transfer model to predict ground temperature for shallow ground heat exchangers. Renew. Energy 103, 295–307. https://doi.org/10.1016/j.renene.2016.11.027.

Fang, X., Luo, S., Lyu, S., Cheng, C., Li, Z., Zhang, S., 2021. Numerical modeling of the responses of soil temperature and soil moisture to climate change over the Tibetan Plateau, 1961–2010. Int. J. Climatol. 41, 4134–4150. https://doi.org/10.1002/joc.7062.

García, E., 2004. Modificaciones al Sistema Climático Köppen. http://www.igeograf.unam.mx/sigg/utilidades/docs/pdfs/publicaciones/geo_siglo21/serie_lib/modific_al_sis.pdf.

García-Cueto, O.R., Soto, N.S., Quintero-Núñez, M., Ojeda-Benítez, S., Limón, N.V., 2013. Extreme temperature scenarios in Mexicali, Mexico under climate change conditions. Atmósfera 26, 509–520. https://www.revistascca.unam.mx/atm/index.php/atm/article/view/32108.

Hillel, D., 1982. Introduction to Soil Physics. Academic Press, Amherst, Massachusetts. https://doi.org/10.1016/C2009-0-03052-9.

Krarti, M., Claridge, D.E., Kreider, J.F., 1995. Analytical model to predict nonhomogeneous soil temperature variation. J. Sol. Energy Eng. Trans. ASME 100–107. https://doi.org/10.1115/1.2870825.

Kreith, F., Manglik, R.M., Bohn, M.S., 2011. Principles of heat transfer. Cengage Learn. 784.

Kröger, D.G., 2002. Convection heat transfer between a horizontal surface and the natural environment. R D J. 18 (3), 49–54. https://cdn.yazam.com/www.saimeche.org.za/resource/collection/A9416D0D-99A6-4534-B5C5-15E8475524FE/Sc_jm-2002_01_600_dpi_-_2002_18_3__49-54.pdf.

Lund, J.W., Toth, A.N., 2021. Direct utilization of geothermal energy 2020 worldwide review. Geothermics 90, 101915. https://doi.org/10.1016/j.geothermics.2020.101915.

McAdams, W.H., 1985. Heat Transmission, 3rd edition. McGraw-Hill Book Company, Inc.

Mihalakakou, G., Santamouris, M., Lewis, J.O., Asimakopoulos, D.N., 1997. On the application of the energy balance equation to predict ground temperature profiles. Solar Energy 60, 181–190. https://doi.org/10.1016/S0038-092X(97)00012-1.

Naranjo-Mendoza, C., Wright, A.J., Oyinlola, M.A., Greenough, R.M., 2018. A comparison of analytical and numerical model predictions of shallow soil temperature variation with experimental measurements. Geothermics 76, 38–49. https://doi.org/10.1016/j.geothermics.2018.06.003.

Ozgener, O., Ozgener, L., Tester, J.W., 2013. A practical approach to predict soil temperature variations for geothermal (ground) heat exchangers applications. Int. J. Heat Mass Transf. 62, 473–480. https://doi.org/10.1016/j.ijheatmasstransfer.2013.03.031.

Patankar, S.V., 1980. Numerical Heat Transfer and Fluid Flow. Hemisphere Publishing Corporation, Taylor & Francis Group, New York, p. 200.

Penman, H.L., 1948. Natural evaporation from open water, bare soil and grass. Proc. Roy. Soc. A. 158 (285), 120–145. https://doi.org/10.1098/rspa.1948.0037.

Sándor, R., Fodor, N., 2012. Simulation of soil temperature dynamics with models using different concepts. Sci. World J. 2012, 590287 https://doi.org/10.1100/2012/590287.

Singh, R.K., Sharma, R.V., 2017. Numerical analysis for ground temperature variation. Geotherm. Energy 5, 22. https://doi.org/10.1186/s40517-017-0082-z.

Stylianou, I.I., Tassou, S., Christodoulides, P., Aresti, L., Florides, G., 2019. Modeling of vertical ground heat exchangers in the presence of groundwater flow and underground temperature gradient. Energy Build. 192, 15–30. https://doi.org/10.1016/j.enbuild.2019.03.020.

Urias-Barrera, H.E., Garcia-Cueto, O.R., Bojórquez-Morales, G., 2021. Identification and classification of local climate zones in a semi-arid city of northwestern Mexico. Vivienda y Comunidades Sustentables (2021), 9. https://doi.org/10.32870/rvcs.v0i9.163.

Versteeg, H.K., Malalasekera, W., 2008. An Introduction to Computational Fluid Dynamics The Finite Volume Method, 2nd ed. Pearson, Prentice Hall, England.

Zamán, J., Gijón-Rivera, M., 2015. Dinámica De Fluidos Computacional Para Ingenieros. Palibrio, Bloomington, US.

(página en blanco)

Received: 14 August 2020 | Revised: 5 January 2021 | Accepted: 6 January 2021
DOI: 10.1002/asl.1024

RESEARCH ARTICLE

Atmospheric Science Letters RMetS

Influence of mixing height and atmospheric stability conditions on correlation of NO_2 columns and surface concentrations in a Mexico-United States border region

David E. Flores-Jiménez[1] | O. Rafael García-Cueto[1] | Néstor Santillán-Soto[1] | J. Ernesto López-Velázquez[1] | Adriana Camargo-Bravo[2]

[1]Institute of Engineering (Instituto de Ingeniería), Autonomous University of Baja California (Universidad Autónoma de Baja California), Mexicali, Baja California, Mexico

[2]Faculty of Nursing (Facultad de Enfermería), Autonomous University of Baja California (Universidad Autónoma de Baja California), Mexicali, Baja California, Mexico

Correspondence
David E. Flores-Jiménez, Institute of Engineering (Instituto de Ingeniería), Autonomous University of Baja California (Universidad Autónoma de Baja California), Blvd. Benito Juárez y Calle de la Normal s/n, Col. Insurgentes Este, Mexicali, Baja California, 21280, Mexico.

Abstract
The objective was to analyze how representative tropospheric NO_2 column densities are of surface NO_2 measurements under different atmospheric stability conditions in the air basin of two border cities: Calexico, United States, and Mexicali, Mexico. NO_2 columns were measured by the Ozone Monitoring Instrument (OMI) on the NASA Aura satellite. NO_2 concentrations and meteorological parameters were also measured on the surface for comparison. Specifically, the correlations between OMI and surface NO_2 concentrations under different atmospheric stability conditions according to the Pasquill-Gifford (P-G) and Monin-Obukhov (M-O) classification schemes were determined for 2017 and 2018. During the passage of the satellite through the study area (11:00–13:00 UTC−8), unstable conditions were documented in both years. Good correlation was found between the surface NO_2 and OMI NO_2 column observations in the second semester of each year, particularly under unstable conditions as diagnosed by the P-G and M-O schemes applied in the first and second year, respectively. However, a weakening of these conditions occurs during the autumn–winter period. In both cases, the highest determination coefficients were found for Calexico, with values of 0.48 and 0.36 in 2017 and 2018, respectively; for Mexicali, the determination coefficients were 0.23 and 0.35, respectively. Under each atmospheric stability scheme, the mechanical and convective turbulence caused a decreasing trend in wind speed and solar radiation over the course of second semester of 2017 and in friction velocity, temperature, and sensible heat flux over the course of the same period for 2018. The negative trend of these parameters during the analyzed time frames helped to reduce the influence of unstable atmospheric conditions, favoring better correlations between satellite and surface NO_2 measurements. The methodology applied and results obtained herein can enable us to better understand the representativeness of OMI NO_2 data in arid border zones with extreme meteorological conditions.

KEYWORDS

convective turbulence, Monin-Obukhov, OMI NO_2, Pasquill-Gifford, wind speed

1 | INTRODUCTION

Atmospheric stability conditions play an important role in the mixing of air pollutants. This is more markedly observed under extreme weather conditions or during the changes in the convective process that occur from season to season (Szep *et al*., 2017; Yuval *et al*., 2020). One example of this phenomenon occurred in winter 2004 in Logan, Utah, United States: Temperatures reached −23.6°C, favoring thermal inversion and causing the worst air pollution episode ever recorded in the country (Malek *et al*., 2006). In other metropolitan zones such as Mexico City (Mexico), Los Angeles (United States), and the Kathmandu Valley (Nepal), the transport of pollutants has been shown to be affected by variability in temperature, wind speed, solar radiation, and relative humidity (Shaw *et al*., 2007; Cohan *et al*., 2011; Mues *et al*., 2017).

The generation of nitrogen dioxide (NO_2) by anthropogenic emissions on the Earth's surface and its involvement in chemical reactions in the atmosphere affects the creation of tropospheric ozone (O_3) during photochemical reactions. Specifically, in urban areas, solar radiation and wind speed conditions impact available energy and pollutant levels (Sillman, 1999; Habeebullah *et al*., 2015). Both of these latter parameters can modify the mixing layer height of pollutants and, consequently, their concentration levels.

Satellite data on pollutants have enabled a greater understanding of their behavior and distribution at different temporal and spatial scales. Previously, these data were integrated with surface NO_2 data in Central Mexico in order to generate tropospheric NO_2 columns with greater representativeness of the spatial distribution of this pollutant near the surface (Rivera *et al*., 2013). The sensitivity of NO_2 data from the Ozone Monitoring Instrument (OMI) to vertical atmospheric conditions has been studied in recent years. In Hamilton, Canada, OMI and surface NO_2 data were compared: The highest regression coefficients were found during inversion days ($R^2 = 0.35$) under stable atmospheric conditions (Wallace and Kanaroglou, 2009). One study showed good correlations (R) between the seasonal variation of both measurements in the European cities of Berlin (0.86), Madrid (0.81), and Paris (0.69) (Paraschiv *et al*., 2017).

The air basin of Mexicali in Baja California, Mexico, and neighboring Calexico in California, United States, is shared due to the similar orographic conditions of these cities. Wind conditions can cause pollution episodes in either city throughout the year, mostly in winter and summer (Kelly *et al*., 2010; Secretaría de Protección al Ambiente, Baja California [SPABC], 2011a). One case study (Mendoza *et al*., 2011) showed that, in August 2001 (summer), an influence area of nitrogen oxides (NO_x) originating in Mexicali spread to the Imperial Valley of California and Arizona. Also, in January 2002, $PM_{2.5}$ originating in Los Angeles, California, and Las Vegas, Nevada, was transported to the air basin of Mexicali and Calexico (MXL-CLX).

Pollutant concentrations are monitored in both Mexicali and Calexico by the California Air Resources Board (CARB; "IADAM Air Quality Data Statistics") and Subsecretaría de Protección al Ambiente (SPABC), respectively (California Air Resources Board, n.d.; SPABC, 2011b). However, there is not enough information on the mixing height of pollutants and the influence of atmospheric stability on vertical NO_2 tropospheric columns. The present study first aimed to estimate (a) the height of the mixing layer and (b) local atmospheric stability. Then, it aimed (c) to evaluate how representative OMI NO_2 values are of surface NO_2 measurements under different atmospheric stability conditions in 2017 and 2018.

2 | STUDY AREA AND DATA

The city of Mexicali is located in northwestern Mexico near the border with the United States. It has a total area of 149 km^2 (Figure 1) and an arid climate. The average maximum temperature in the summer is 42°C, and the average annual rainfall is 75 mm. The wind comes mainly from northwest, west-northwest (winter, spring, and autumn), and south-southeast (summer) (SPABC, 2011b; Canales-Rodríguez *et al*., 2015; Villanueva-Solis, 2017). One of the main climate hazards during the summer is heat waves during which temperatures significantly higher than the average are presented for several days. The heat waves occur more frequently within the city limits (Instituto Nacional de Estadística y Geografía [INEGI], 2009; García Cueto *et al*., 2015).

The neighboring city of Calexico is located in southern Imperial County, California, United States. Its climatic conditions are extremely similar to Mexicali, except for perceptible differences in wind behavior (Kelly *et al*., 2010). The Mexicali Valley-Imperial Valley area is an important economic zone, with Mexicali spanning 58% of

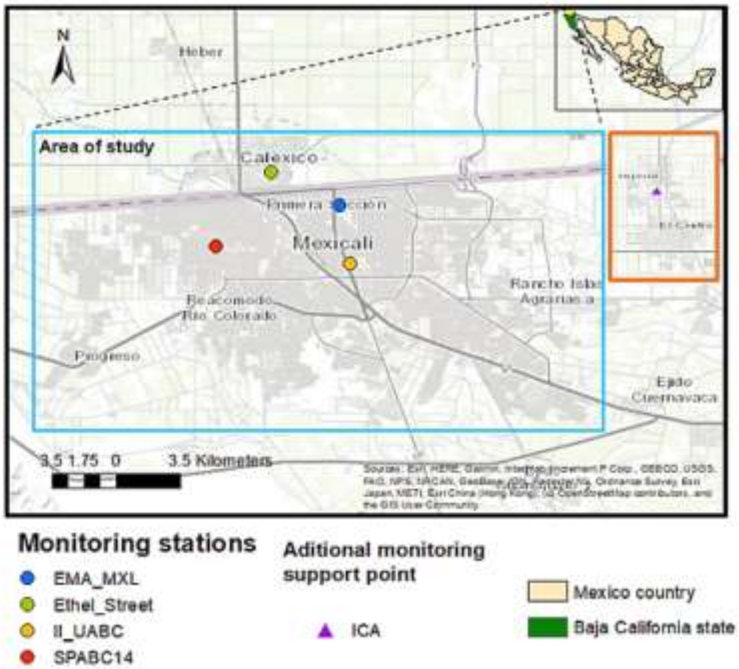

FIGURE 1 Map of the study area of Mexicali and Calexico (inside blue border) and monitoring stations. The orange border shows the location of the ICA station, in El Centro, CA, United States. ESRI satellite imagery database for Basemap (2020)

the total area (Figure 1) (Mungaray-Moctezuma and Calderón Ramírez, 2015). The average elevation above sea level of Calexico and Mexicali is 8 m and 156 m, respectively, although some elevations below sea level are presented in northern Imperial County and western Mexicali. The main NO_2 emission sources in this region are the result of combustion processes, including the burning of agricultural crops, vehicles, and power plants (San Diego County Air Pollution Control District [SDAPCD], 2012; Sánchez-Duque *et al.*, 2015; Montero *et al.*, 2018).

Ground-level data were obtained from meteorological and air quality monitoring stations for the following meteorological parameters: wind speed and friction velocity ($m{\cdot}s^{-1}$), solar radiation ($W{\cdot}m^{-2}$), relative humidity (%), and temperature (°C). These data were obtained from the monitoring stations indicated in Figure 1: (a) the EMA_MXL station administrated by the National Meteorological Service (SMN for its acronym in Spanish; smn.conagua.gob.mx/es/estaciones-meteorologicas-automaticas), (b) the II_UABC station located in the Engineering Institute of the Autonomous University of Baja California (UABC for its acronym in Spanish), and (c) the ICA station (Imperial County Airport) belonging to the CARB (www.arb.ca.gov/adam/index.html) located around 18 km north of Calexico. Local sensible heat flux values (Q_H, in $W{\cdot}m^{-2}$) and friction velocity were measured at the II_UABC station. No data were available for some months for these last parameters; thus, surface measurements from the ICA station were used to estimate its respective value using the AERMET model (United States Environmental Protection Agency [US-EPA], 2019).

The sensor used to obtain the friction velocity and sensible heat flux in the UABC station, was a Campbell Scientific CSAT3 sonic anemometer (Haro-Rincón *et al.*, 2013), which, through its temperature sensor (T) and the vertical component of the velocity (w), calculates the sensible heat flux with the equation $Q_H = \rho C_p\ (wT)$ (Burns *et al.*, 2012). The friction velocity is obtained by the sensor using their components of the velocity through the covariance values (Grare *et al.*, 2016).

Given the similarity of the air temperature distribution in the cities of Mexicali and Calexico (García-Cueto *et al.*, 2007, 2009), it is inferred that the sensible heat flux must be extremely similar; This seems to be caused because the ground cover materials, native and anthropogenic, keep a similar proportion, in such a way that the amount of heat absorbed and released by the surfaces, which depends on the thermal properties of those surfaces (Oke, 1988), in diurnal and seasonal cycles are similar. Regarding the friction speed (u_*), which was estimated for unstable conditions by an iterative process using the AERMET model, the correlation that was found between the measured values of II-UABC and the values estimated in ICA, was 0.70, which as a first approximation is considered an acceptable result. The values of u_* are less than one; the maximum overestimated magnitude was 0.33, and the minimum underestimated was 0.45. Since u_* is cubed to estimate the Monin-Obhukov Longitude, the error made when using the estimated values is very small, and therefore they are considered to be representative of air quality monitoring sites.

The vertical column densities (VCDs) of NO_2, in molecules·cm^{-2} units (from now on as: molec·cm^{-2}), were measured by the OMI instrument (OMI NO_2) administrated by the National Aeronautics and Space Administration (NASA) at a spatial resolution of 13×24 km at nadir. Their values represent the number of NO_2 molecules from the surface to the top of the troposphere in grids of $0.25° \times 0.25°$. These were obtained from Goddard Earth Sciences Data and Information Services Center (Giovanni) for cloud radiance fractions less than 30% (giovanni.gsfc.nasa.gov/giovanni/). The NO_2 sensor measures the vertical column of this pollutant in the corresponding swath of the study area once per day, in some moment between the local time interval of 11:00 to 13:00 hr (UTC−8). Accordingly, the daily averages of all considered parameters were obtained during this time. About 40% of the OMI measurements were missing due to anomalies caused by the partial blocking of the measuring instrument. A detailed explanation can be found at the following website: http://projects.knmi.nl/omi/research/product/rowanomaly-background.php. However, valid data were available for 215 and 219 days in 2017 and 2018, respectively. NO_2 surface concentrations (ppb) were obtained from the air quality monitoring stations of SPABC14 (Mexicali) (www.spabc.gob.mx/calidad-del-aire/) and Ethel_Street (Calexico) (www.arb.ca.gov/adam/index.html) (Figure 1).

The vertical column densities (VCDs) of NO_2, in molecules·cm^{-2} units (from now on as: molec·cm^{-2}), were measured by the OMI instrument (OMI NO_2) administrated by the National Aeronautics and Space Administration (NASA) at a spatial resolution of 13×24 km at nadir. Their values represent the number of NO_2 molecules from the surface to the top of the troposphere in grids of $0.25° \times 0.25°$. These were obtained from Goddard Earth Sciences Data and Information Services Center (Giovanni) for cloud radiance fractions less than 30% (giovanni.gsfc.nasa.gov/giovanni/). The NO_2 sensor measures the vertical column of this pollutant in the corresponding swath of the study area once per day, in some moment between the local time interval of 11:00 to 13:00 hr (UTC−8). Accordingly, the daily averages of all considered parameters were obtained during this time. About 40% of the OMI measurements were missing due to anomalies caused by the partial blocking of the measuring instrument. A detailed explanation can be found at the following website: http://projects.knmi.nl/omi/research/product/rowanomaly-background.php. However, valid data were available for 215 and 219 days in 2017 and 2018, respectively. NO_2 surface concentrations (ppb) were obtained from the air quality monitoring stations of SPABC14 (Mexicali) (www.spabc.gob.mx/calidad-del-aire/) and Ethel_Street (Calexico) (www.arb.ca.gov/adam/index.html) (Figure 1).

As might be expected in a hot arid dry climate, representative of the urban areas Mexicali-Calexico, of the available energy (Q^*) it was found that 56% is used to heat urban air (QH), followed by storage (QS) in the urban fabric (33%), leaving only 11% for evaporation (QE) from vegetated areas (Garcia-Cueto *et al.*, 2004); The above indicates that, given the lack of vegetation in the study area, the humidity distribution does not seem to be relevant, or it is only marginally important. On the other hand, according to studies carried out on the spatial distribution of air temperature for the urban areas of Mexicali-Calexico (Garcia-Cueto *et al.*, 2007; 2009), thermal differences were found from 0.2°C to 0.9°C in an annual period taking into account extreme values. Regarding the wind, given the similarity of the urban layout between Mexicali and Calexico, its homogeneity in the vertical sense (two-level constructions are common), wide streets (urban canyon ratio $H/W = 0.5$), and proximity between the sites of the air quality monitoring stations and the meteorological stations (the maximum distance is 3.5 km), it is inferred that the magnitude of the wind speed should not be significantly different. Therefore, it is considered that the error caused by not having simultaneous measurements in the same place, of NO_2 and meteorological, should not be significant, and that it could even be within the sensitivity errors of the measurement instruments.

2.1 | Meteorological conditions and local NO_2 data

From January to February of 2017, winter storms were recorded, favoring humid conditions and low temperatures. In summer (July, August, and September), temperatures above 40°C were recorded, which are not unusual during this season. In 2018, the winter storms and cold fronts lasted until May, resulting in humidity levels of 40–50%. In summer and early fall of the same year, the North American Monsoon brought moisture to the state of Baja California. From October to December, synoptic events continued to favor humid conditions (60%), causing short periods of rain (Comisión Nacional del Agua [CONAGUA], 2017; 2018).

Increases in humidity and temperature, which occurred frequently during winter season in 2018, favor a reduction in NO_2 concentrations (Wu and Chen, 2012; Habeebullah *et al*., 2015). In the Mexicali-Calexico (MXL-CLX) air basin, the minimum NO_2 values are shown hourly in Figure 2, with the lowest values being presented in 2018. Overall, Mexicali had the highest pollutant levels. In both cities, the maximum NO_2 concentrations were reached in the morning and evening, while the minimum concentrations occurred from 10:00 to 15:00 hr.

3 | METHODOLOGY

The atmospheric stability classes were determined in two ways using (a) the modified Pasquill-Gifford stability analysis scheme and (b) the inverse of the Monin-Obukhov length ($\frac{1}{L}$) (Essa *et al*., 2013). Both methods consider mechanical and convective turbulence and have diurnal stage classes. This was relevant because the OMI data corresponded with specific hours of the day in the study area (Table 1). In the Pasquill-Gifford classification, net radiation and wind speed values are considered (Asharafi and Hoshyaripour, 2010). In the Monin-Obukhov classification, the length L was estimated as follows:

$$L = -\frac{\rho C_p T u_*^3}{k g Q_H} \tag{1}$$

where ρ is the density of dry air (1.2 kg·m^{-3}), T (K) is the temperature, C_p (1,010 J·kg^{-1}·K^{-1}) is the specific heat of air at constant pressure, k (0.4) is the Von Karman constant, and g (9.81 m·s^{-2}) is the gravitational acceleration (Bonan, 2015; Haro Velastegui *et al*., 2018). The temperature and sensible heat flux (Q_H) were obtained from the meteorological station of II_UABC (Figure 1).

In 2018, Q_H and u_* values were incomplete and complemented with estimations from the AERMET model. In this latter model, the input meteorological data were obtained from ICA station (Figure 1).The net radiation estimation require solar radiation, temperature, and cloud cover data. Q_H is estimated through a parameterization of this parameter and air temperature according to the methodology of Holtslag and Van Ulden (1983). Friction velocity was estimated with a iterative procedure that depends of Q_H and Monin-Obukhov length described by Paine (1987). In the AERMET, both methods can be use because surface meteorological data are available (US-EPA, 2019).

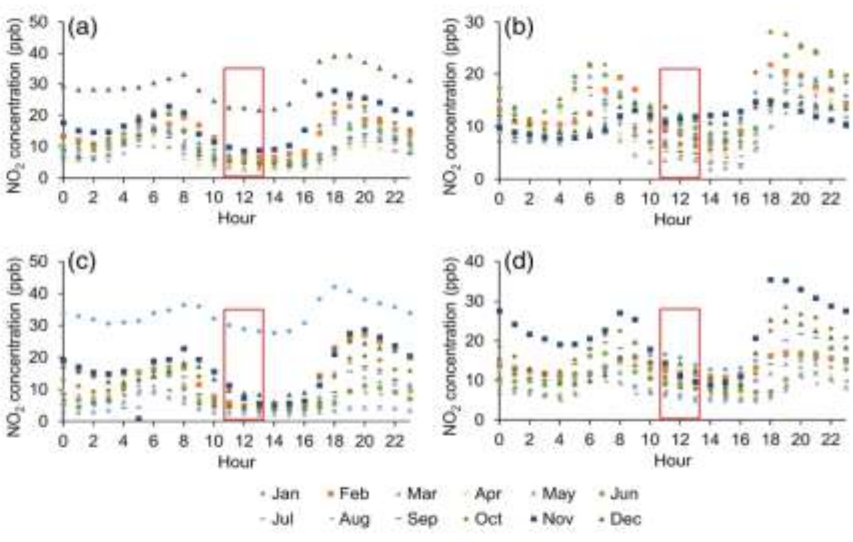

FIGURE 2 Average hourly concentrations of NO_2 in Calexico (left column) and Mexicali (right column) during 2017 (a, b) and 2018 (c, d), respectively. The red rectangles identify the study period

TABLE 1 Modified Pasquill-Gifford stability classes for the diurnal period

	Daytime incoming solar radiation ($W \cdot m^{-2}$)		
Wind speed ($m \cdot s^{-1}$)	**Strong (>600)**	**Moderate (300–600)**	**Slight (<300)**
≤2	A	A–B	B
2–3	A–B	B	C
3–5	B	B–C	C
5–6	C	C–D	D
>6	C	D	D

Note: Their correspondence with the inverse of Monin-Obukhov length established for letter A: very unstable atmosphere ($1/L < -0.056$); B: moderate unstable ($-0.056 < 1/L < -0.016$); C: slightly unstable ($-0.016 < 1/L < -0.004$); and D: neutral ($-0.004 < 1/L < -0.002$).

Previous studies in Oklahoma City, United States, and different regions of Cuba show that the AERMET model produces reliable results for these parameters during the diurnal period (Simpson *et al.*, 2007; Turtos Carbonell *et al.*, 2013; Rodríguez Valdés *et al.*, 2015).

The atmospheric stability directly affects the mixing height (MH) because this parameter depends on the convective process and wind dynamics (Aliabadi *et al.*, 2016). MH was calculated using the Lagrangian HYSPLIT 4 model in the VMIXING program (https://www.ready.noaa.gov/HYSPLIT_vmixing.php). This model calculates the MH from potential temperature data, locating the height at each grid point of NAM12 data (North American mesoscale model) every 3 hr at a horizontal resolution of 12 km. It is assumes the mixing layer height to be equal to the height at which the potential temperature first exceeds the surface value by 2 K. The temperature profile is analyzed from the surface up to determine the height of the mixed layer. This kind of data have been used to evaluate the confidence of planet boundary layer estimations (Garcia *et al.*, 2007; Yu *et al.*, 2010; Coniglio *et al.*, 2013).

The periods with the highest determination coefficients (R^2) between the tropospheric OMI NO_2 columns and surface NO_2 concentrations were identified at each air quality monitoring station (SPABC14 and Ethel_Street) (Boersma *et al.*, 2008; Kim *et al.*, 2016). This let to know the reliability of the data extracted from the satellite images. Also, the monitoring station that was best represented was determined considering that both stations are located in the same satellite observation area. Finally, the stability classes under which the best correspondence was found between both parameters were recognized.

4 | RESULTS AND DISCUSSION

Considering for this estimation only the diurnal period of 11–13 hr (UTC−8), the atmospheric basin of Mexicali and Calexico had and average monthly mixing height ranged between 753–1774 magl and 748–1785 magl, respectively, in 2017 and 716–1,615 magl and 735–1,598 magl, respectively, in 2018. The results obtained are comparable with those that were estimated for the daytime period by Bei *et al.* (2013) in 2010 at the Parque Morelos in Tijuana, and also with the values obtained by Salcido *et al.* (2020) in Mexicali Valley for July 2010, January 2012, and October 2016. The maximum values in 2017 were reached during May and August and in 2018 during July and August, which correspond with the months of highest atmospheric instability according to the Pasquill-Gifford (A, A-B) and Monin-Obukhov (A, B) classifications (Figure 3a,d,g,j). The increasing temperature trend before and during these latter months favors convective turbulence and the vertical mixing of pollutants, causing a decrease in the NO_2 concentrations (Figure 3c,i) below the annual average of 6.53 ppb in Calexico and 7.56 ppb in Mexicali in 2017 and 6.65 ppb in Calexico and 9.93 ppb in Mexicali in 2018.

The OMI and surface NO_2 concentrations in Calexico and Mexicali show a similar average monthly trend, with a determination coefficient (R^2) of 0.41 and 0.74 for 2017 and 2018, respectively, at a significance level of $\alpha = 0.05$ and p value < 0.05. Specifically, the VCD of NO_2 in the troposphere (OMI NO_2) had a similar behavior as the surface NO_2 measurements during both years, mostly around mid-year (June–July) and in the final third (October–November) (Figure 3c,i). The unstable atmospheric cases were higher in 2017 than in 2018 (Figure 3a,d,g,j). It has been found that during the periods of major convective turbulence, the largest mixing height favor the OMI NO_2 detection in the troposphere (Boersma *et al.*, 2007; Schaap *et al.*, 2013; Laughner *et al.*, 2016).

From January–May and June–November 2017, Mexicali showed a lag in reaching the highest daily values near 30 ppb in comparison to Calexico, whose

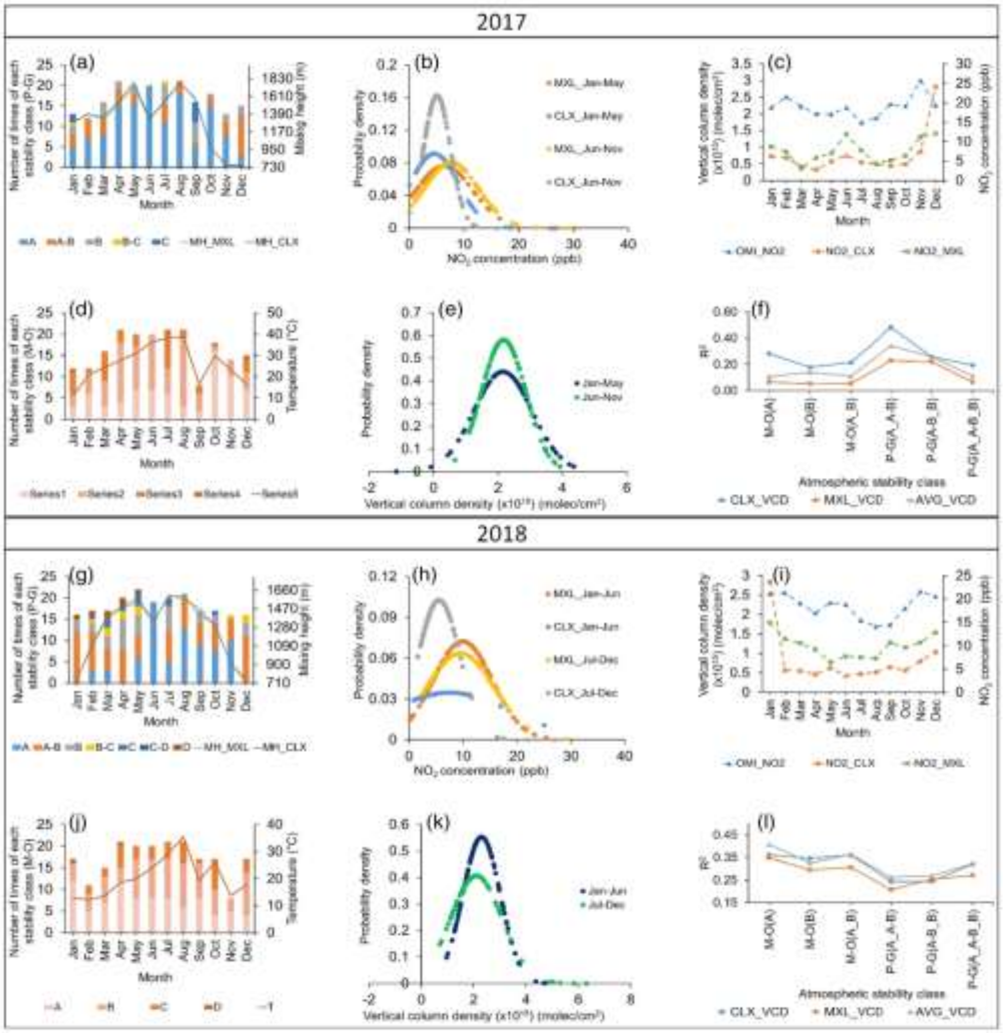

FIGURE 3 Count of different atmospheric conditions according to the Pasquill-Gifford (P-G) and Monin-Obukhov (M-O) classification methods (left column); probability densities of OMI and surface concentrations of NO_2 (central column); monthly averages of OMI and surface NO_2 concentrations and R^2 values under the atmospheric stability schemes (right column)

maximum values ranged from 10 to 20 ppb (Figure 3b). From January–June and July–December 2018, similar high values were found (Figure 3h). In the first year, the maximum daily values were reached in December in Calexico and Mexicali, corresponding with of 31 ppb and 59 ppb, respectively, which could negatively affect the correlation between OMI and surface NO_2 concentrations, because they are the furthest values in the data distribution.

The OMI NO_2 data distribution indicated that the highest levels in 2017 and 2018 occurred in June–November and January–June, respectively. The decrease of minimum values during the second semester of each year, according to the probability density graphs (Figure 3e,k), favored higher determination coefficients between the VCDs of OMI NO_2 levels and surface NO_2 concentrations. Specifically, the higher determination coefficients were found on days characterized by the A and B stability classes according to the Monin-Obukhov (M-O) method and the A, A-B, and B classes according to the Pasquill-Gifford (P-G) method. In particular, in 2017, the highest R^2 was found for the P-G atmospheric classes during days with combined A and A–B conditions in Calexico (0.48) and Mexicali (0.23) and considering the average of NO_2 concentrations between both cities (0.34) (Figure 3f). In 2018, the highest R^2 was found for the M-O classes during days with A conditions with the averages (AVG) concentrations between both cities (0.41), followed by Calexico (0.36) and Mexicali (0.35). Overall, in 2018, similar R^2 values were found under the combined A and B classes in each city (Figure 3l).

In 2017, the P-G classification was more sensitive: The best correlation between OMI NO_2 and surface NO_2 concentrations was identified under this classification scheme. In 2018, the highest correlation was identified under the M-O (A) classification scheme. In each year, it was important to reduce the influence of the minimum concentrations. The highest concentrations occurred in 2017. Atmospheric synoptic phenomena affected the study area differently, directly influencing the variability of the physical and meteorological parameters used to determine the atmospheric stability classes (Jiang et al., 2013).

As previously mentioned, in 2017, the highest R^2 was identified for the June–November period using the P-G classification. The correlation was highest at 12:00 hr from October to November, with Calexico having the highest R^2 (0.41) (Figure 4a). At this hour, the mechanical and convective turbulence in both cities were governed by similar wind patterns and a decreasing trend of solar radiation, respectively (Figure 4b). Although the latter parameter was only measured in Mexicali, the proximity of both border cities and their location in a single atmospheric basin (SPABC, 2011a) allowed us to explore its behavior. The highest number of emission sources due to combustion processes is located in Mexicali (Kelly et al., 2010), and pollutants in this city have a lower mixing height on average during the June–

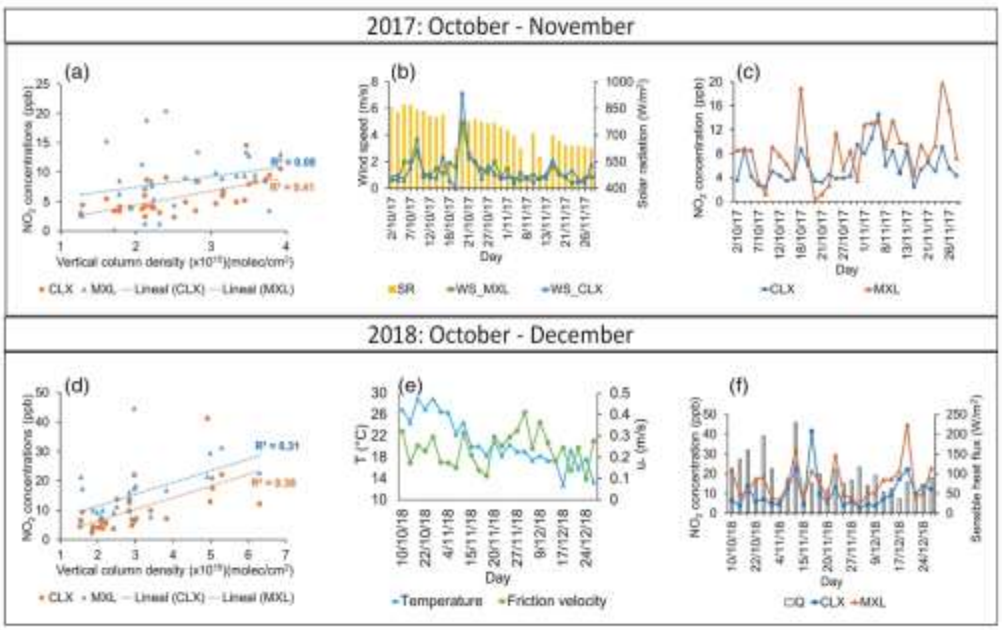

FIGURE 4 Regression of vertical column density of OMI NO_2 versus surface NO_2 concentrations (left column) (a, d); time series of solar radiation and wind speed (b) and NO_2 surface concentrations (c); and time series of temperature and friction velocity (e) and NO_2 surface concentrations in relation to sensible heat flux (f)

November period (Figure 3a), causing higher daily concentrations in most cases (Figure 4c) and the lowest R^2 value.

In 2018, the M-O classification was more sensitive, enabling a better correlation to be detected during the July–December period. This result reflects the concentrations measured at 11:00 hr from October to December in which R^2 values of 0.38 and 0.31 were obtained for Calexico and Mexicali, respectively (Figure 4d). In the M-O classification, mechanical and convective turbulence can be analyzed by identifying decreasing trends of friction velocity and temperature, respectively (Figure 4e). The convective behavior is influenced by the sensible heat flux due to more unstable atmospheric conditions, mostly during October. However, there were two dates in November during which the sensible heat flux (Q) decreased and NO_2 concentration increased in both cities (Figure 4f). A previous study on heat islands in the study zone showed that the spatial temperature distribution favors higher Q values in Mexicali, allowing for major heat transfer from the surface to the atmosphere (García-Cueto *et al*., 2007).

In other border cities such as Tijuana and San Diego, the orographic conditions are not as homogenous as Mexicali and Calexico, and different atmospheric stability conditions are observed. For example, wind speeds of around 1–4 $m \cdot s^{-1}$ have been documented in Tijuana. Although Calexico and Mexicali have a similar range of wind speeds, the relief is more homogeneous, and the meteorological conditions are more extreme (Vanoye and Mendoza, 2009; Rivera *et al*., 2015). In Ontario, Canada, significant correlations were found between OMI and surface NO_2 concentrations during days of thermal inversion ($R^2 = 0.35$) when wind speeds fluctuated between 1.3 and 4.4 $m \cdot s^{-1}$. In comparison with the study case, better correlations were found during more stable atmospheric conditions (Wallace and Kanaroglou, 2009).

5 | CONCLUSIONS

In Mexicali and Calexico, the highest mixing heights were founded during 2017, 1774 magl and 1785 magl, respectively. For both years, Calexico had the highest. Atmospheric instability during the analyzed time frame (11:00–13:00, GMT−8) was strong to moderate. The minimum NO_2 concentrations in both Mexicali and Calexico were found during these hours. The variability of the considered meteorological parameters influenced the atmospheric stability classes, enabling a greater understanding of the atmospheric conditions under which the most reliable correlations between OMI and surface NO_2 data were found in 2017 and 2018. The monthly average OMI NO_2 densities ranged from 1.73×10^{15} to 2.3×10^{15} $molec \cdot cm^{-2}$ and from 1.70×10^{15} to 2.6×10^{15} $molec \cdot cm^{-2}$ in 2017 and 2018, respectively. Their correlation with monthly average surface NO_2 concentrations was greater in Mexicali (0.39 and 0.55 in 2017 and 2018, respectively) than in Calexico (0.20 and 0.42 in 2017 and 2018, respectively). The variability of surface concentrations due to their transport in the atmosphere was not considered; nevertheless, the meteorological parameters observed at specific points reliably explained turbulence and convective phenomena. The highest correlations between OMI and surface NO_2 concentrations were obtained during the second semester of each year due to lower variation in the daily maximum and minimum NO_2 concentrations. The Pasquill-Gifford classification was more sensitive and enabled the highest correlations in 2017 to be detected under unstable atmospheric conditions (A, A–B); determination coefficients of 0.48 and 0.23 were found for Calexico and Mexicali, respectively. The Monin-Obukhov classification performed better for 2018 (A); under these conditions, determination coefficients of 0.36 and 0.35 were found for Calexico and Mexicali, respectively. The correlations are obtained in this way because the OMI data present limitations when compared to the surface concentrations, particularly during the daytime period where the effects of convective turbulence are present in an urban arid zone. The decreasing trend of solar radiation and wind speed during October–November 2017 and of temperature and friction velocity during October–December 2018 favored a similar pattern of behavior between OMI and surface NO_2 concentrations. In conclusion, different atmospheric schemes explain better the satellite data behavior because of the NO_2 variability not only was it affected by atmospheric local conditions, but also had an impact for the synoptic phenomena of winter storms and cold fronts, which represent an opportunity area for future research. The methods applied and results obtained herein enable a better understanding of the representativeness of OMI NO_2 data in arid border zones with extreme meteorological conditions.

ACKNOWLEDGEMENTS

The NO_2 vertical column data used in this study were produced with the Giovanni online data system, developed, and maintained by NASA GES DISC. We also thank CONAGUA and SPABC in Mexicali, Mexico and CARB in California, United States, for providing us with their respective meteorological and air quality data. Finally, we thank Elizabeth Melgoza and Shuming Du from CARB, for their respective support in obtaining the required information and in using the AERMET model.

ORCID

David E. Flores-Jiménez https://orcid.org/0000-0002-3607-9991

REFERENCES

Aliabadi, A.A., Staebler, R.M., de Grandpré, J., Zadra, A. and Vaillancourt, P.A. (2016) Comparison of estimated atmospheric boundary layer mixing height in the Arctic and Southern Great Plains under statically stable conditions: experimental and numerical aspects. *Atmosphere-Ocean*, 54(1), 60–74. https://doi.org/10.1080/07055900.2015.1119100.

Asharafi, K. and Hoshyaripour, A. (2010) A model to determine atmospheric stability and its correlation with CO concentration. *International Journal of Civil and Environmental Engineering*, 2, 83–88.

Bei, N., Li, G., Zavala, M., Barrera, H., Torres, R., Grutter, M., Gutiérrez, W., Garcia, M., Ruiz-Suarez, L.G., Ortinez, A., Gutierrez, Y., Alvarado, C., Flores, I. and Molina, L.T. (2013) Meteorological overview and plume transport patterns during Cal-Mex 2010. *Atmospheric Environment*, 70, 477–489. https://doi.org/10.1016/j.atmosenv.2012.01.065.

Boersma, K.F., Eskes, H.J., Veekfind, J.P., Brinksman, E.J., van der, A.R.J., Sneep, M., van den Oord, G.H.J., Levelt, P.F., Stammes, P., Gleason, J.F. and Bucsela, E.J. (2007) Near-real time retrieval of tropospheric NO_2 from OMI. *Atmospheric Chemistry and Physics*, 7, 2103–2118. https://doi.org/10.5194/acp-7-2103-2007.

Boersma, K.F., Jacob, D.J., Bucsela, E.J., Perring, A.E., Dirksen, R., van der Ronald, A., Yantosca, R.M., Park, R.J., Wenig, M.O., Bertram, T.H. and Cohen, R.C. (2008) Validation of OMI tropospheric NO_2 observations during INTEX-B and application to constrain NO_x emissions over the eastern United States and Mexico. *Atmospheric Environment*, 42(19), 4480–4497. https://doi.org/10.1016/j.atmosenv.2008.02.004.

Bonan, G. (2015) *Ecological Climatology*. Cambridge: Cambridge University Press.

Burns, S.P., Horst, T.W., Blanken, P.D. and Monson, R.K. (2012) Using sonic anemometer temperature to measure sensible heat flux in strong winds. *Atmospheric Measurement Techniques Discussions*, 5, 447–469. https://doi.org/10.5194/amt-5-2095-2012.

California Air Resources Board. (n.d.) Available at: https://www.arb.ca.gov/adam/index.html [Accessed 20th February 2020].

Canales-Rodriguez, M., Quintero-Núnez, M., Valdés-Salas, B. and Daessle-Heuser, W. (2015) Distribution and characterization of PM10 in city and valley of Mexicali, Baja California, Mexico. *Journal of Environmental Protection*, 06(1), 25–33. https://doi.org/10.4236/jep.2015.61004.

Cohan, A., Wu, J. and Dabdub, D. (2011) High-resolution pollutant transport in the San Pedro Bay of California. *Atmospheric Pollution Research*, 2(3), 237–246. https://doi.org/10.5094/apr.2011.030.

Comisión Nacional del Agua (CONAGUA). (2017) *Reporte del clima en México. Reporte anual 2017*. Available at: https://smn.conagua.gob.mx/tools/DATA/Climatolog%C3%ADa/Diagn%C3%B3stico%20Atmosf%C3%A9rico/Reporte%20del%20Clima%20en%20M%C3%A9xico/Anual2017.pdf [Accessed 2nd March 2020].

Comisión Nacional del Agua (CONAGUA). (2018) *Reporte del clima en México. Reporte anual 2018*. Available at: https://smn.conagua.gob.mx/tools/DATA/Climatolog%C3%ADa/Diagn%C3%B3stico%20Atmosf%C3%A9rico/Reporte%20del%20Clima%20en%20M%C3%A9xico/Anual2018.pdf [Accessed 3rd March 2020].

Coniglio, M.C., Correia, J., Jr., Marsh, P.T. and Kong, F. (2013) Verification of convection-allowing WRF model forecasts of the planetary boundary layer using sounding observations. *Weather and Forecasting*, 28, 842–862. https://doi.org/10.1175/WAF-D-12-00103.1.

Essa, K.S.M., Embaby, M., Mubarak, F. and Kamel, I. (2013) Estimation of seasonal atmospheric stability and mixing height by using different schemes. *International Journal of Advanced Research*, 1(9), 429–438.

Garcia Cueto, R., Santillán Soto, N., Haro Rincón, Z., Ojeda Benitez, S. and Bojórquez Morales, G. (2015) Parameterization of net radiation in an arid city of northwestern Mexico. *Atmosfera*, 28(2), 71–82. https://doi.org/10.20937/atm.2015.28.02.01.

Garcia, M.A., Sánchez, M.L., de Torre, B. and Pérez, I.A. (2007) Characterisation of the mixing height temporal evolution by means of a laser dial system in an urban area –intercomparison results with a model application. *Annales Geophysicae*, 25(10), 2119–2124. https://doi.org/10.5194/angeo-25-2119-2007.

Garcia-Cueto, O.R., Jáuregui-Ostos, E., Toudert, D. and Tejeda-Martinez, A. (2007) Detection of the urban heat Island in Mexicali, B. C., México and its relationship with land use. *Atmosfera*, 20(2), 111–131.

Garcia-Cueto, O.R., Tejeda-Martinez, A. and Bojórquez-Morales, G. (2009) Urbanization effects upon the air temperature in Mexicali, B.C., México. *Atmósfera*, 22(4), 349–365.

Garcia-Cueto, R., Jáuregui, E. and Tejeda, A. (2004) Energy balance observations in a desert city in northern Mexico. *Proc. Fifth International Conference on Urban Climate, Lodz, Poland, 1–5 September*. Available at: http://meteo.geo.uni.lodz.pl/icuc5/text/O_12_2.pdf. (accessed 3 July 2020).

Grare, L., Lenain, L. and Melville, W.K. (2016) The influence of wind direction on Campbell Scientific CSAT3 and Gill R3-50 sonic anemometer measurements. *Journal of Atmospheric and Oceanic Technology*, 33, 2477–2497. https://doi.org/10.1175/JTECH-D-16-0055.1.

Habeebullah, T.M., Munir, S., Awad, A.H.A.A., Essam, A.M., Seroji, A.R. and Mohammed, A.M.F. (2015) The interaction between air quality and meteorological factors in an arid environment of Makkah, Saudi Arabia. *International Journal of Environmental Science and Development*, 6(8), 576–580. https://doi.org/10.7763/ijesd.2015.v6.660.

Haro Velastegui, A.X., Limáico Nieto, C.T., Perugachi Cahueñas, N. P. and Fernández Parra, M.I. (2018) Evaluación de la estabilidad atmosférica bajo condiciones físicas y meteorólogicas del altiplano ecuatoriano. *Revista Brasileira de Meteorologia*, 33(2), 336–343. https://doi.org/10.1590/0102-7786332015.

Haro-Rincón, Z., Santillán-Soto, N., García-Cueto, R., Ojeda-Benitez, S. and Lambert-Arista, A. (2013) Microclimatic experimentation applied to insulating horizontal coverage in Mexicali, Mexico. *Journal of Environmental Science and Engineering*, A2, 561–568.

Holtslag, A.A.M. and Van Ulden, P. (1983) A simple scheme for daytime estimates of the surface fluxes from routine weather data. *Journal of Climate and Applied Meteorology*, 22(4), 517–529. https://doi.org/10.1175/1520-0450(1983)022%3C0517:ASSFDE%3E2.0.CO;2.

Instituto Nacional de Estadistica y Geografia (INEGI). (2009) *Prontuario de información geográfica municipal de los Estados Unidos Mexicanos*. Mexicali. Clave Geoestadistica 02002. Available at: https://www.inegi.org.mx/contenidos/app/mexicocifras/datos_geograficos/02/02002.pdf [Accessed 10th January 2020].

Jiang, N., Dirks, K.N. and Luo, K. (2013) Effects of local synoptic and large-scale climate conditions on daily nitrogen dioxide concentrations in Auckland, New Zealand. *International Journal of Climatology*, 34(6), 1883–1897. https://doi.org/10.1002/joc.3808.

Kelly, K.E., Jaramillo, I.C., Quintero-Núñez, M., Wagner, D.A., Collins, K., Meuzelaar, H.L.C. and Lighty, J.S. (2010) Low-wind/high particulate matter episodes in the Calexico/Mexicali region. *Journal of the Air & Waste Management Association*, 60 (12), 1476–1486. https://doi.org/10.3155/1047-3289.60.12.1476.

Kim, H.C., Lee, P., Judd, L., Pan, L. and Lefer, B. (2016) OMI NO_2 column densities over North American urban cities: the effect of satellite footprint resolution. *Geoscientific Model Development*, 9(3), 1111–1123. https://doi.org/10.5194/gmd-9-1111-2016.

Laughner, J.N., Zare, A. and Cohen, R.C. (2016) Effects of daily meteorology on the interpretation of space-based remote sensing of NO_2. *Atmospheric, Chemistry and Physics*, 16, 15247–15264. https://doi.org/10.5194/acp-16-15247-2016.

Malek, E., Davis, T., Martin, R.S. and Silva, P.J. (2006) Meteorological and environmental aspects of one of the worst national air pollution episodes (January 2004) in Logan, Cache Valley, Utah, USA. *Atmospheric Research*, 79(2), 108–122. https://doi.org/10.1016/j.atmosres.2005.05.003.

Mendoza, A., Chandru, S., Hu, Y., Ana, Y. and Armistead, G. (2011) Chapter 13: Modeling the dynamics of air pollutants: trans-boundary impacts in the Mexicali-Imperial Valley border region. *Book: Advanced Air Pollution. Dr. Farhad Nejadkoorki (Ed.), ISBN: 978-953-307-511-2, InTech*, (1), 213–238. https://doi.org/10.5772/16695.

Montero, G., Coronado, M.A., Garcia, C., Campbell, H.E., Montes, D.G., Torres, R., Pérez, L., León, J.A. and Ayala, J.R. (2018) Chapter 4: Wheat straw open burning: emissions and impact on climate change. Fahad, S., Basir, A. & Adnan, M., *Global Wheat Production*. (1 London: InTech Open), 67–78. https://doi.org/10.5772/intechopen.76031.

Mues, A., Rupakheti, M., Münkel, C., Lauer, A., Bozem, H., Hoor, P., Butler, T. and Lawrence, M.G. (2017) Investigation of the mixing layer height derived from ceilometer measurements in the Kathmandu Valley and implications for local air quality. *Atmospheric Chemistry and Physics*, 17(13), 8157–8176. https://doi.org/10.5194/acp-17-8157-2017.

Mungaray-Moctezuma, A. and Calderón Ramirez, J.A. (2015) Road infrastructure and mobility of consumption in the Mexicali-Imperial Valley border area. *Estudios Fronterizos, Nueva Época*, 16(32), 117–133.

Oke, T.R. (1988) The urban energy balance. *Progress in Physical Geography*, 12(4), 471–508. https://doi.org/10.1177/030913338801200401.

Paine, R.J. (1987). *User's guide to the CTDM Meteorological Preprocessor (METPRO) Program*. EPA-600/8–88-004 (NTIS No. BP 88–162102). Research Triangle Park, NC: U.S. Environmental Protection Agency. Available at: https://www3.epa.gov/ttn/scram/userg/regmod/ctdmmetprepug.pdf

Paraschiv, S., Constantin, D.E., Paraschiv, S.L. and Voiculescu, M. (2017) OMI and ground-based in-situ tropospheric nitrogen dioxide observations over several important European cities during 2005–2014. *International Journal of Environmental Research and Public Health*, 14(11), 1415. https://doi.org/10.3390/ijerph14111415.

Rivera, C., Stremme, W., Barrera, H., Friedrich, M.M., Grutter, M., Garcia Yee, J., Torres Jardon, R. and Ruiz Suarez, L.G. (2015) Spatial distribution and transport patterns of NO_2 in the Tijuana-San Diego area. *Atmospheric Pollution Research*, 6(2), 230–238. https://doi.org/10.5094/apr.2015.027.

Rivera, C., Stremme, W. and Grutter, M. (2013) Nitrogen dioxide DOAS measurements from ground and space: comparison of zenith scattered sunlight ground-based measurements and OMI data in Central Mexico. *Atmosfera*, 26(3), 401–414. https://doi.org/10.1016/s0187-6236(13)71085-3.

Rodriguez Valdés, D., Quintero, S., Yosdany González, J., Cuesta Santos, O. and Sánchez Diaz, A. (2015) Variación de la estabilidad y altura de la capa de mezcla en la Ciudad de Pinar del Rio. Su relación con condiciones sinópticas. *Revista Brasileira De Meteorologia*, 30(1), 1–15. https://doi.org/10.1590/0102-778620140014.

Salcido, A., Ana-Teresa, C.-M., Carreón-Sierra, S., Castro, T., Peralta, O., Rogelio-Sebastián, S.-G., Hernández-Flores, N., Gustavo-Adolfo, T.-F. and Marco-Antonio, M.-F. (2020) Estimations of the Mexicali Valley (Mexico) mixing height. *Atmosphere*, 11(5), 1–26. https://doi.org/10.3390/atmos11050505.

San Diego County Air Pollution Control District (SDAPCD). (2012) *Redesignation request and maintenance plan for the 1997 national ozone standard for San Diego county*. Available at: https://www.sdapcd.org/content/dam/sdc/apcd/PDF/Air%20Quality%20Planning/8_Hour_O3_Maint-Plan.pdf [].

Sánchez-Duque, A., Bautista, F., Goguitchaichvili, A., Cejudo-Ruiz, R., Reyez-López, J.A., Solis-Dominguez, F.A. & Morales-Contreras, J.J. (2015) Evaluación de la contaminación ambiental a partir del aumento magnético en polvos urbanos. Caso de estudio en la ciudad de Mexicali, México. *Revista Mexicana de Ciencias Geológicas*, 32, 501–513. http://www.scielo.org.mx/pdf/rmcg/v32n3/2007-2902-rmcg-32-03-00501.pdf.

Schaap, M., Kranenburg, R., Curier, L., Jozwicka, M., Dammers, E. and Timmermans, R. (2013) Assesing the sensitivity of the OMI-NO_2 product to emission changes across Europe. *Remote Sensing*, 5, 4187–4208. https://doi.org/10.3390/rs5094187.

Secretaria de Protección al Ambiente, Baja California (SPABC). (2011a) *PROAIRE 2011–2020*. Available at: https://www.gob.mx/cms/uploads/attachment/file/69289/12_ProAire_Mexicali.pdf [Accessed 7th February 2020].

Secretaria de Protección al Ambiente, Baja California (SPABC). (2011b) *Monitoreo de calidad del aire*. Available at: http://www.spabc.gob.mx/calidad-del-aire/ [Accessed 11th January 2020].

Shaw, W. J., Pekour, M.S., Coulter, R.L. Martin, R.J. and Walters, J. T. (2007) The daytime mixing layer observed by radiosonde profiler, and lidar during MILAGRO. *Atmospheric Chemistry and*

Physics Discussions, 7(5): 15025–15065. https://doi.org/10.5194/acpd-7-15025-2007
Sillman, S. (1999) The relation between ozone, NOx and hydrocarbons in urban and polluted rural environments. *Atmospheric Environment*, 33, 1821–1845.
Simpson, M., Raman, S., Lundquist, J.K. and Leach, M. (2007) A study of the variation of urban mixed layer heights. *Atmospheric Environment*, 41(33), 6923–6930. https://doi.org/10.1016/j.atmosenv.2006.08.029.
Szep, R., Reka, K., Attila, K., Szende, T. and Mihaela, E.C. (2017) Study of air pollution and atmospheric stability in Ciuc Basin - Romania. *Revista de Chimie*, 68(8), 1763–1767. https://doi.org/10.37358/rc.17.8.5760.
Turtos Carbonell, L., Capote Mastrapa, G., Fonseca Rodriguez, Y., Alvarez Escudero, L., Sanchez Gacita, M., Bezanilla Morlot, A., Borrajero Montejo, I., Meneses Ruiz, E. and Pire Rivas, S. (2013) Assessment of the weather research and forecasting model implementation in Cuba addressed to diagnostic air quality modeling. *Atmospheric Pollution Research*, 4(1), 64–74. https://doi.org/10.5094/apr.2013.007.
United States Environmental Protection Agency (US-EPA). (2019) *AERMOD model formulation and evaluation*. Available at: https://www3.epa.gov/ttn/scram/models/aermod/aermod_mfed.pdf [Accessed 18th November 2019].
Vanoye, A.Y. and Mendoza, A. (2009) Mesoscale meteorological simulations of summer ozone episodes in Mexicali and Monterrey, Mexico: analysis of model sensitivity to grid resolution and parameterization schemes. *Water, Air, & Soil Pollution: Focus*, 9(3–4), 185–202. https://doi.org/10.1007/s11267-009-9205-2.
Villanueva-Solis, J. (2017) Urban heat Island mitigation and urban planning: the case of the Mexicali, B. C. Mexico. *American Journal of Climate Change*, 6(1), 22–39. https://doi.org/10.4236/ajcc.2017.61002.
Wallace, J. and Kanaroglou, P. (2009) The sensitivity of OMI-derived nitrogen dioxide to boundary layer temperature inversions. *Atmospheric Environment*, 43(22–23), 3596–3604. https://doi.org/10.1016/j.atmosenv.2009.03.049.
Wu, N. and Chen, X. (2012) Two photon dissociation dynamics of NO_2 and $NO_2 + H_2O$. *The Journal of Physical Chemistry A*, 116 (25), 6894–6900. https://doi.org/10.1021/jp3029825.
Yu, L., Zhang, Z., Zhou, M., Zhong, S., Lenschow, D., Hsu, H., Wu, H. and Sun, B. (2010) Validation of ECMWF and NCEP-NCAR reanalysis data in Antarctica. *Advances in Atmospheric Sciences*, 27(5), 1151–1168. https://doi.org/10.1007/s00376-010-9140-1.
Yuval, T.T., Raz, R., Levi, Y., Levy, I. and Broday, D.M. (2020) Emissions vs. turbulence and atmospheric stability: a study of their relative importance in determining air pollutant concentrations. *Science of the Total Environment*, 733, 139300. https://doi.org/10.1016/j.scitotenv.2020.139300.

How to cite this article: Flores-Jiménez DE, García-Cueto OR, Santillán-Soto N, López-Velázquez JE, Camargo-Bravo A. Influence of mixing height and atmospheric stability conditions on correlation of NO_2 columns and surface concentrations in a Mexico-United States border region. *Atmos Sci Lett*. 2021;e1024. https://doi.org/10.1002/asl.1024